Extension of the Method of Ellipses to Determining the Orientation of Long, Semi-flexible Fibers in Model 2- and 3-dimensional Geometries

John Thomas Hofmann

Dissertation submitted to the faculty of the Virginia Polytechnic Institute and State University in partial fulfillment of the requirements for the degree of

Doctor of Philosophy

in

Macromolecular Science and Engineering

Donald G. Baird, Chair

Scott W. Case

Richey M. Davis

Stephen M. Martin

Abby R. Whittington

September 5th, 2013

Blacksburg, VA

Keywords: Fiber Reinforce Polymer Composites, Short Glass Fibers, Long Glass Fibers, Fiber Orientation Distribution, Injection Molding, Method of Ellipses, Fiber Flexibility

Extension of the Method of Ellipses to Determining the Orientation of Long, Semi-flexible Fibers in Model 2- and 3-dimensional Geometries

John Thomas Hofmann

(ABSTRACT)

The use of fiber-reinforced polymer composites formed via injection molding is of increasing interest due to their superior mechanical properties as compared to those of the polymer matrix alone. These mechanical properties, however, are strongly dependent on the fiber length and orientation distributions within a molded part. As such, there is a need to understand and model the orientation evolution of chopped fibers in flow in order to accurately simulate the final fiber orientation distribution within injection molded parts. As a result of this, accurate and reliable experimental measurement of fiber orientation is needed.

Within this research, the application and validity of the Method of Ellipses for determining the orientation of long, semi-flexible glass fibers within injection molded composites has been investigated. A fiber suspension with an average length of approximately 3.9 mm was the focus of this study and assumed to be representative of commercial distributions. A novel method to quantify fiber curvature was developed and utilized to show that flexibility in center-gated disc and the end-gated plaque samples was minimal on average for the selected fiber length distribution. Thus, it was determined that the Method of Ellipses was applicable when utilized to obtain reliable orientation data for the selected long glass fiber suspension and within the chosen geometries that exhibit 1-, 2-, and 3-dimensional velocity fields. However, a modified image

analysis width was found to be necessary in regions of highly aligned fibers, due to the increase in ellipse size and the need to reduce the number of partial objects and thus minimize error. This allowed for a direct comparison of the experimental orientation behavior of short and long glass fibers within the center-gated disc and the end-gated plaque, as well as the effect of the orientation distributions on the global modulus of the part.

Original Contributions

The following are considered to be significant original contributions to this research:

- Extension and validation of the Method of Ellipses for determining the experimental orientation distributions of long, semi-flexible glass fibers within injection molded composites via the primary modification of altering the image analysis region.

- Developed a novel method to quantify the experimental extent of fiber curvature within injection molded composites using optical microscopy and image analysis of 2-dimensional cross-sectional areas.

- Ascertained the experimental components of the end-to-end tensor, **R**, via adaptation of the Method of Ellipses and analysis of the "top" view plane (i.e. the r-θ plane) as opposed to the conventional through-thickness inspection plane (i.e. the r-z plane).

- Obtained a thorough compilation of experimental orientation data for short and long glass fibers within the end-gated plaque, including within complex flow regimes such as in the sprue and gate regions, and evaluated the effect of the fiber orientation distribution within a complex geometry on the distribution of mechanical properties within the part.

Format of Dissertation

This dissertation is written in manuscript format. Chapters 3, 4, and 5 are self-contained papers that are to be submitted for journal publication. Each paper separately describes the experiments, results and discussion, and conclusions relative to each chapter. With the exception of Chapter 2, the review of literature, the figures and tables are presented after the reference section of each chapter.

The experimental center-gated disc orientation data utilized in Chapter 3 and Chapter 5 is located in Appendix B. The end-gated plaque orientation data utilized in Chapter 4 and Chapter 5 can be found in Appendix C-D.

Acknowledgments

I would first like to thank my supervisor and advisor, Dr. Donald G. Baird, for his guidance, insight, and continuous encouragement throughout my research project. Dr. Baird's constructive criticism and constant support provided me with the motivation to strive to continually improve both my research and myself as an individual.

Additionally, I want to extend my gratitude to the Virginia Tech community and the Macromolecules and Interfaces Institute. I would also like to thank Dr. Carlos Suchicital and the Department of Materials Science and Engineering, who graciously provided access to laboratory space and equipment making this research possible. I would also like to thank Dr. Ellis, for allowing me to utilize laboratory equipment which greatly improved the quality and efficiency of my results. Moreover, this work would not have been possible without the gracious financial support of the National Science Foundation, the Department of Energy and Oak Ridge National Laboratory, General Motors, and the Institute for Critical Technologies and Applied Science (ICTAS) at Virginia Tech.

I would also like to thank the members of the polymer processing laboratory at Virginia Tech for their collaboration and for being a constant sounding board over the years. The many discussions and ideas were extremely beneficial to the progress of this project. Specifically, I would like to thank Kevin Meyer and Mark Cieslinksi, as well as Gregorio Velez-Garcia for his guidance and help during my first year at Virginia Tech.

Finally, I would like to thank Katherine for her ongoing support and encouragement. Without her, this dissertation would not have been possible and I will be forever grateful.

Thank you all!

Table of Contents

List of Figures

List of Tables

Chapter 1 : Introduction

1.1: Fiber Reinforced Polymers

The addition of fibers to a polymer matrix can lead to increased mechanical properties of a part and numerous benefits. First, these benefits include increased strength to weight ratio, stiffness, and flexural modulus [1-2]. Second, with sufficient mechanical reinforcement fiber polymer composites (FRPs) can rival the performance and cost effectiveness of metallic materials used to construct parts for similar purposes [3], partially due to the relative low cost of glass fibers [4]. Third, the added reinforcing fibers can lead to a significant increase in creep endurance for long fibers due to the addition of a load-supporting fiber network [2, 5]. Fourth, long glass fibers have been shown to impart enhanced mechanical benefits including improved impact toughness as compared to short glass fiber counterparts [6-7]. Short and long carbon fiber injection molded composites have also been investigated due to their higher reinforcing potential [8]. Finally, the above listed commercial benefits of glass fiber FRPs are all obtainable while still maintaining the benefit of being melt processable, and thus the capability of utilizing commercial processes such as injection molding and compression molding [3, 6-7]. As a result, automotive, aerospace, and structural applications routinely utilize glass fiber reinforced polymer composites. However, the magnitude of such mechanical benefits is highly dependent on not only the polymer matrix and fiber material used, but also on processing conditions and final fiber lengths and orientations within an injection molded part.

1.2: Orientation Theory

For injection molded parts, the details of the mold design, including gate type location and cavity thickness, as well as processing parameters, such as mold temperature and injection speed, will influence the evolution of fiber orientation as the mold is filled to generate a part.

Ultimately, if fiber evolution in flow is well understood mold design can be modified and optimized in order to obtain a desired final fiber orientation and thus mechanical strength improvement. Thus, there is a desire to model and understand the orientation evolution kinetics of fibers in flow.

The bulk of orientation models that have been developed to date are applicable for short, rigid glass fibers [9-11]. Theoretical work in this field dates back to the work of Jeffery [9] who solved the dynamics of a high aspect particle of an infinitely dilute suspension subjected to a flow field. More recent modifications to this model have focused on more closely accounting for realistic fiber orientation behavior, including isotropic rotary diffusion, anisotropic diffusion, and delayed orientation kinetics [10-15]. The results have allowed for models that are capable of predicting the orientation kinetics of short, rigid fibers within multiple test geometries with some accuracy [11, 16].

However, there is limited work regarding the prediction of the orientation evolution of concentrated long, semi-flexible fibers [17-19]. Strautins and Latz [20] proposed a model referred to as the Bead-Rod model that is applicable for semi-flexible fibers within a dilute suspension. Subsequent modifications have allowed for the extension of the Bead-Rod model to non-dilute fiber suspensions [19, 21]. However, while initial studies using the Bead-Rod model in non-dilute suspensions have shown some agreement between predicted and experimental orientation data further improvements to the model may be beneficial in order to improve the results.

1.3: Experimental Methods to Quantify Orientation

The primary reason to obtain experimental values of orientation is for comparison to predictions of fiber orientation calculated via numerical simulation packages and to ultimately aid in mold design and optimization. While numerous experimental techniques have been used to qualitatively observe the orientation of fibers within injection molded FRPs, including optical microscopy, scanning electron microscopy, sonic acoustic microscopy, and computed tomography [22-27], the bulk of the studies in the literature have focused on using the Method of Ellipses (MoE) to quantify fiber orientation [16, 23, 28-30]. The MoE is based upon fibers behaving as rigid rods in flow and thus has been primarily applicable for short, rigid glass fibers.

While the orientation of short glass fibers has been extensively studied [28, 31-34], only several recent studies have utilized the traditional MoE in order to evaluate the orientation of long fibers [17, 35]. Furthermore, few efforts have been made to ascertain the true nature and effect of the flexibility of long glass fiber systems, particularly when the average fiber length is significantly greater than 1 mm. Composites produced via injection molding will exhibit a distribution of post-processing fiber lengths with a long tail in the high fiber lengths which can be fitted by either a lognormal or Weibull function [17, 36]. Due to this fiber length distribution, previous works detailing the orientation of "long" fibers with average lengths close to 1 mm in reality consist primarily of short, rigid fibers and thus do not truly represent the nature of semi-flexible fibers [17, 36]. Some authors have suggested that the experimental orientation of flexible fibers can be quantified by "segmenting" the fiber into linear segments based on similar efforts that deal with micromechanical modeling [37]. Furthermore, Nguyen et al. [17] applied the MoE to long, semi-flexible fibers without modification and with results that suggest that the method may work in some cases but may not be applicable in general. However, no known

validation of the MoE for use specifically with long, semi-flexible fibers is known to have been completed.

1.4: Summary of Objectives

The primary goal of this research is to evaluate how the orientation state of long, semi-flexible fibers is quantified. Additionally, this research attempts to further investigate and quantify the flexibility that long fibers may exhibit during flow and processing in an effort to modify and tailor experimental methods for use specifically with long fibers. To accomplish these goals, three primary research objectives have been formulated:

1. Ascertain under what conditions the Method of Ellipses (MoE) can be extended and applied directly for long, semi-flexible glass fibers that possess a length distribution that is typical of fiber lengths seen commercially. This will be completed by investigation of the orientation of fibers within 1-dimensional idealized simple shear flow, 2-dimensional axisymmetric flow, and simple 3-dimensional flow. Additionally, this work will aim to identify any potential issues with the MoE when applied directly to long glass fibers and to identify any potential modifications to the method that may improve performance of the method when applied specifically for semi-flexible glass fibers.

2. Determine how the experimental fiber orientation distributions vary between short and long glass fiber composites that possess lengths similar to those typically seen commercially, and identify if any significant differences are observed within two basic flows: the center-gated disc and the end-gated plaque.

3. Evaluate the experimental fiber orientation distributions of short and long glass fibers within complex geometries by examining the purely 3-dimensional flow field within the end-gated plaque including the sprue and gate region. Furthermore, this study will evaluate how the mechanical properties are affected when a part exhibits a complex fiber orientation distribution that varies not only with part thickness and length but also with part width.

1.5 References

1. Truckenmüller, F. and Fritz, H.G. "Injection Molding of Long Fiber-Reinforced Thermoplastics: A Comparison of Extruded and Pultruded Materials with Direct Addition of Roving Strands." *Polymer Engineering & Science* **31** (18) (1991): 1316-1329.
2. Silverman, E.M. "Effect of Glass Fiber Length on the Creep and Impact Resistance of Reinforced Thermoplastics." *Journal of Polymer Composites* **8** (1) (1987): 8-15.
3. Keshtkar, M., et al. "Rheological Properties and Microstructural Evolution of Semi-Flexible Fiber Suspensions under Shear Flow." *J. Rheol* **54** (2) (2010): 197-222.
4. Guo, R., et al. "Rheology of Fiber Filled Polymer Melts: Role of Fiber-Fiber Interactions and Polymer-Fiber Coupling." *Polymer Engineering & Science* **45** (3) (2005): 385-399.
5. Toll. "Elastic Compression of a Fiber Network." *Journal of applied mechanics* **62** (1) (1995): 223.
6. Thomason, J.L. "The Influence of Fibre Length and Concentration on the Properties of Glass Fibre Reinforced Polypropylene: 5. Injection Moulded Long and Short Fibre Pp." *Composites: Part A* **33** (2002): 1641-1652.
7. Hassan, A., et al. "Tensile, Impact and Fiber Length Properties of Injection-Molded Short and Long Glass Fiber-Reinforced Polyamide 6,6 Composites." *Journal of Reinforced Plastics and Composites* **23** (9) (2004): 969-986.
8. Hassan, A.B., et al. "The Properties of Injection Molded, Short and Long Carbon Fiber Reinforced Polyamide 6,6 Composites." *Annual Technical Conference - Society of Plastics Engineers* **59th (Volume 2)** (2001): 2017-2021.
9. Jeffery, G.B. "The Motion of Ellipsoidal Particles Immersed in a Viscous Fluid." *Proc. R. Soc. Lond. A* **102** (1922): 161-179.
10. Folgar, F. and Tucker, C.L. "Orientation Behavior of Fibers in Concentrated Suspensions." *Journal of Reinforced Plastics and Composites* **3** (2) (1984): 98-119.
11. Phelps, J.H. and III, C.L.T. "An Anisotropic Rotary Diffusion Model for Fiber Orientation in Short- and Long-Fiber Thermoplastics." *Journal of Non-Newtonian Fluid Mechanics* **156** (2009): 165-176.
12. Sepehr, M. "Comparison of Rheological Properties of Fiber Suspensions with Model Predictions." *Journal of polymer engineering* **24** (6) (2004): 579.
13. Eberle, A.P.R., et al. "Fiber Orientation Kinetics of a Concentrated Short Glass Fiber Suspension in Startup of Simple Shear Flow." *Journal of Non-Newtonian Fluid Mechanics* **165** (2010): 110-119.
14. Huynh, H.M. "Improved Fiber Orientation Predictions for Injection-Molded Composites." University of Illinois at Urbana-Champaign. (2001).
15. Wang, J., et al. "An Objective Model for Slow Orientation Kinetics in Concentrated Fiber Suspensions: Theory and Rheological Evidence." *J. Rheol.* **52** (5) (2008): 1179-1200.
16. Vélez-García, G. "Experimental Evaluation and Simulations of Fiber Orientation in Injection Molding of Polymers Containing Short Glass Gibers." Macromolecular Science and Engineering, Virginia Polytechnic Institute and State University. Blacksburg, VA (2012).
17. Nguyen, B.N., et al. "Fiber Length and Orientation in Long-Fiber Injection-Molded Thermoplastics – Part I: Modeling of Microstructure and Elastic Properties." *Journal of Composite Materials* **42** (10) (2008): 1003-27.

18. Ortman, K.C., et al. "Transient Shear Flow Behavior of Concentrated Long Glass Fiber Suspensions in a Sliding Plate Rheometer." *Journal of Non-Newtonian Fluid Mechanics* **166** (16) (2011): 884-895.
19. Kevin C. Ortman, J. "Assessing an Orientation Model and Stress Tensor for Semi-Flexible Glass Fibers in Polypropylene Using a Sliding Plate Rheometer: For the Use of Simulating Processes " Virginia Tech. (2011).
20. Strautins, U. and Latz, A. "Flow-Driven Orientation Dynamics of Semiflexible Fiber Systems." *Rheol Acta* **46** (2007): 1057-1064.
21. Ortman, K. "Prediction of Fiber Orientation in the Injection Molding of Long Fiber Suspensions." *POLYMER COMPOSITES* **33** (8) (2012): 1360-1367.
22. Kawamura, M., et al. "Unambiguous Determination of 3d Fiber Orientation Distribution in Thermoplastic Composites Using Sam Image of Elliptical Mark and Interference Fringe." *Journal of Composite Materials* **39** (4) (2005): 287-299.
23. Hine, P.J., et al. "Measuring the Fiber Orientation and Modelling the Elastic Properties of Injection-Moulded Long-Glass-Fiber-Reinforced Nylon." *Composites Science and Technology* **53** (1994): 125-131.
24. Regnier, G., et al. "A Simplified Method to Determine the 3d Orientation of an Injection Molded Fiber-Filled Polymer." *Polymer Engineering and Science* **48** (2008): 2159-2168.
25. Averous, L., et al. "Evolution of the Three-Dimensionai Orientation Distribution of Glass Fibers in Injected Lsotactic Polypropylene." *Polymer Engineering & Science* **37** (2) (1997): 329-337.
26. Eberhardt, C. and Clarke, A. "Fibre-Orientation Measurements in Short-Glass-Fibre Composites. Part I: Automated, High-Angular-Resolution Measurement by Confocal Microscopy." *Composites Science and Technology* **61** (2001): 1389-1400.
27. Shen, H., et al. "Direct Observation and Measurement of Fiber Architecture in Short Fiber-Polymer Composite Foam through Micro-Ct Imaging." *Composites Science and Technology* **64** (2004): 2113-2120.
28. Vélez-García, G.M., et al. "Unambiguous Orientation in Short Fiber Composites over Small Sampling Area in a Center-Gated Disk." *Composites Part A: Applied Science and Manufacturing* **43** (1) (2012): 104-113.
29. Clarke, A.R., et al. "A Novel Technique for Determining the 3d Spatial Distribution of Glass Fibres in Polymer Composites." *Composites Science and Technology* **55** (1995): 75-91.
30. Bay, R.S. and III, C.L.T. "Stereological Measurement and Error Estimates for Three-Dimensional Fiber Orientation." *Polymer Engineering & Science* **32** (4) (1992): 240-252.
31. Bay, R.S. and III, C.L.T. "Fiber Orientation in Simple Injection Moldings. Part I: Theory and Numerical Methods." *Polymer Composites* **13** (4) (1992): 317-331.
32. Bay, R.S. and III, C.L.T. "Fiber Orientation in Simple Injection Moldings. Part Ii: Experimental Results." *Polymer Composites* **13** (4) (1992): 332-341.
33. Hine, P.J., et al. "Hydrostaticaiiy Extruded Giass-Fiber-Reinforced Polyoxymethylene. I: The Development of Fiber and Matrix Orientation." *Polymer Composites* **17** (5) (1996): 720-729.
34. Vincent, M., et al. "Description and Modeling of Fiber Orientation in Injection Molding of Fiber Reinforced Thermoplastics." *Polymer* **46** (17) (2005): 6719-6725.
35. Lafranche, E., et al. "Injection Moulding of Long Glass Fibre Reinforced Polyamide 6-6: Guidelines to Improve Flexural Properties." *eXPRESS Polymer Letters* **1** (7) (2007): 456-466.
36. Chin, W.-K., et al. "Effects of Fiber Length and Orientation Distribution on the Elastic Modulus of Short Fiber Reinforced Thermoplastics." *Polymer Composites* **9** (1) (1988): 27-35.

37. Bapanapalli, S. and Nguyen, B.N. "Prediction of Elastic Properties for Curved Fiber Polymer Composites." *Polymer Composites* **29** (5) (2008): 544-550.

Chapter 2 : Review of the Literature

2.1 Glass Fiber Reinforced Polymers

The addition of fibers to a polymer matrix can lead to increased mechanical properties of a part, including increased strength to weight ratio, stiffness, and flexural modulus [1-2]. However, the magnitude of such mechanical benefits is highly dependent on not only the polymer matrix and fiber material used, but also on processing conditions and the final fiber length and orientation distributions within the part. This subsection will detail the various classifications of Fiber Reinforced Polymer composites (FRPs) based on fiber concentration and fiber length, as well as common methods of commercial FRP production. Additional subsections will detail the current efforts in modeling the orientation evolution behavior of fibers in flow, as well as the experimental techniques used to quantify fiber orientation.

2.1.1 Classifications of Composites

This section will discuss the common methods of classifying FRPs as found in the literature. First, classification based on fiber concentration regimes will be discussed, as well as the metric for differentiating between dilute, semi-dilute, and concentrated fiber suspensions. Second, composite classification based upon fiber length will be detailed, including the length threshold utilized to differentiate short and long glass fibers.

2.1.1.1 Concentration Regimes

The first classification of fibers identified in the literature is based upon the specific concentration regime of the fiber suspension, as originally defined by Doi and Edwards [3]. They considered a suspension of fibers with n fibers per unit volume and with each fiber

possessing a uniform length, L, and diameter, d. The volume fraction, ϕ, of fibers in the suspension can thus be described by Eq. 2.1:

$$\phi = \frac{\pi n L^3}{4a_r^2} \qquad 2.1$$

Here a_r is the fiber aspect ratio and is defined as $a_r = L/d$.

Three concentration regimes were defined by Doi and Edwards in terms of the fiber volume fraction and aspect ratio. These regimes are labeled as *dilute*, *semi-dilute*, and *concentrated*. A fiber suspension is said to be within the *dilute* regime if a single fiber is in no way affected by the presence of other fibers. A single fiber in a *dilute* suspension cannot be affected by any type of interactions from adjacent fibers, including inter-particle hydrodynamic forces and direct fiber-fiber interactions. In other words, a single fiber can only "see" itself. For this statement to be true, the average distance between two adjacent fibers must be greater than the average length, L, of the fibers themselves. Therefore, n (Eq. 2.1) is limited in that it must be less than $1/L^3$. As a result, Eq. 2.1 reduces to:

$$\phi < \frac{\pi}{4a_r^2} \qquad 2.2$$

Since a_r is the dominating term in the above expression, the order of magnitude of ϕ must be less than a_r^{-2} for a fiber suspension to be considered dilute.

Within the *semi-dilute* regime, the presence of a fiber is translated to its adjacent fibers, but primarily only via hydrodynamic interactions and only weakly through physical fiber-to-fiber contacts. For such interactions to be possible, n must be greater than $1/L^3$. However, the average distance between adjacent fibers must still be greater than the fiber diameter, d, so that the suspension is still considered to be semi-dilute. As such, both a lower and upper limit on ϕ exist. This upper limit, however, depends on whether the fiber suspension is randomly or perfectly

aligned. In these two scenarios, n is constrained to be $<< 1/(dL^2)$ and $<< 1/(d^2L)$, respectively. These limits can be expressed in terms of ϕ and a_r as $\phi << a_r^{-1}$ for the randomly aligned suspension, and $\phi << \pi/4$ for the perfectly aligned suspension.

Direct fiber-fiber interactions and contact are present within *concentrated* systems. These inter-fiber interactions are obtained beyond the upper limit of the *semi-dilute* regime, i.e. when $\phi \geq a_r^{-1}$. High volume fractions within this regime can result in suspensions in which chopped fibers have a potential to preferentially align and to form clusters while in flow [3]. As a result of this clustering and high rate of inter-fiber interactions, flow within the concentrated regime is the most complicated to both predict and to experimentally evaluate.

2.1.1.2 Length Regimes of Glass Fiber Composites

Similar to how the fiber aspect ratio was used to classify the concentration regimes, the average fiber length, L, can be used to classify fibers based as either "short" or "long" fibers. Glass fibers with typical diameters are classified as "short" when their average length is < 1 mm [4]. Similarly, glass fibers are classified as "long" for average lengths > 1 mm [4]. Experimentally, the primary qualitative difference between the two classifications is that short fibers behave as rigid rods during processing, while long fibers may exhibit flexibility and curvature [5]. This fiber flexibility has been quantified by a dimensionless group known as the fiber effective stiffness, S_{eff} as introduced by Switzer and Klingenberg [6]:

$$S_{eff} = \frac{E_\gamma \pi}{64 \eta_m \dot{\gamma} a_r^4} \qquad 2.3$$

Here, E_γ is defined as the Young's modulus of the fiber, η_m is matrix viscosity, and $\dot{\gamma}$ is the shear rate. From this expression, it can be seen that as the aspect ratio increases, the effective stiffness

of the fiber decreases. As a result, fibers with increased length and thus high aspect ratios are *more* flexible. An order of magnitude increase in average fiber length (i.e. from 0.300 mm to 3.000 mm, or from "short" to "long"), with all other parameters held constant will result in fibers being four orders of magnitude more flexible. Thus, it can be seen that long glass fibers are substantially more flexible than their short fiber counterparts.

In addition to increased flexibility for long fibers, the potential effects of Brownian motion must be discussed. For fiber suspensions, the effects of Brownian motion can be evaluated by inspecting the ratio of the relative advection magnitude to the Brownian motion magnitude, or the dimensionless Peclet number, *Pe*, where D_r is the isotropic rotational diffusivity [7]:

$$Pe = \frac{\dot{\gamma}}{D_r} \qquad 2.4$$

For $Pe \leq 1.0$, Brownian motion is not a negligible quantity, as $D_r > \dot{\gamma}$. However, as $\dot{\gamma}$ becomes greater than D_r, and $Pe >> 1.0$, Brownian motion becomes negligible. By using this analysis, it has previously been seen that for a population of glass fibers with lengths of 10 microns that Brownian motion becomes negligible [8]. Therefore, it can safely be assumed that long glass fiber suspensions are not affected by Brownian motion due to initial and post-processing average fiber lengths in excess of 1.0 mm and as a result significantly smaller values of D_r .

In order to determine the concentration regime or whether a fiber population is classified as either long or short, information about the Fiber Length Distribution (FLD) is required. Typically, in commercially processed parts such as those made via injection molding or compression molding, the final population of fibers will have a distribution of fiber lengths. Typically, the FLD will have a concentration or "peak" in the "short" fiber range, with a long "tail" extending into higher fiber lengths. Mathematically the FLD is often represented by either

a Weibull [9-11] or log-normal distribution [11-12], as shown in Eqs. 2.5 and 2.6, respectively. In Eq. 2.5, *p(l)* is the probability density function of fiber length, *l*, while *b* and *c* are shape parameters. In Eq. 2.6, *A* is a normalization factor, and σ and μ are shape and location parameters, respectively. For additional derivations and methods, the reader is referred to the literature [9-12]:

$$p(l) = \frac{c}{b}\left(\frac{l}{b}\right)^{c-1} e^{-(l/b)^c} \tag{2.5}$$

$$p(l) = \frac{A}{l\sigma\sqrt{2\pi}} \exp\left(-\frac{\left(\log l - \mu\right)^2}{2\sigma^2}\right) \tag{2.6}$$

The FLD must be experimentally measured so as to be able to calculate the *average* fiber length. Much work has been done to construct methods of experimentally measuring the FLD [9-12]. Typically, the number average, L_n, and the weight average, L_w, length are reported by calculating the first and second moments of the FLD, respectively, by using various available experimental techniques [13]. These average lengths as calculated via Eqs. 2.7 and 2.8. are commonly used to describe the fiber suspension as a whole.

$$L_n = \frac{\sum_i n_i L_i}{\sum_i n_i} \tag{2.7}$$

$$L_w = \frac{\sum_i n_i L_i^2}{\sum_i n_i L_i} \tag{2.8}$$

For glass fiber suspensions, it can then be determined if the population should be treated as short and thus rigid, or long and thus flexible, allowing for subsequent fiber characterization.

2.1.2 Fiber Orientation

Short fibers (< 1mm in length for glass) behave as rigid rods in flow, and the configuration of such a fiber can be visualized in the x_1-x_2-x_3 three-dimensional space according to Figure 2.1. The orientation vector, ***p***, is aligned along the backbone of the rigid fiber and contains a complete description of the orientation state. The vector ***p*** is constructed in a generic coordinate system as shown in Eqs. 2.9 - 2.12 and is useful for summarizing the orientation state of a single fiber. The methods for evaluating the orientation state of a population of fibers will be explained in further detail in a later Section 2.3.

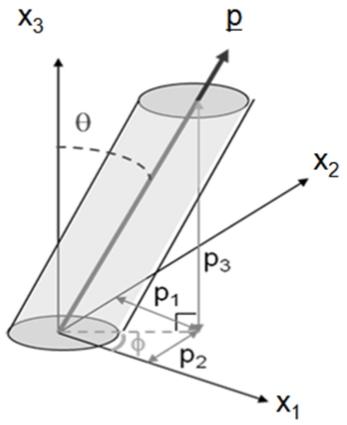

Figure 2.1. Characterization of a rigid fiber in the x_1-x_2-x_3 3-dimensional space by the orientation vector, ***p***.

$$\mathbf{p} = p_1\delta_1 + p_2\delta_2 + p_3\delta_3 \tag{2.9}$$

$$p_1 = \sin\theta\cos\phi \tag{2.10}$$

$$p_2 = \sin\theta\sin\phi \tag{2.11}$$

$$p_3 = \cos\theta \qquad 2.12$$

Long glass fibers have the ability to exhibit flexibility and curvature during processing and as such cannot be represented by a rigid rod. Due to this increased flexibility, a simple orientation vector ***p*** in the x_1-x_2-x_3 space similar to the one in Figure 2.1 is insufficient and incapable of describing the complete orientation state of a single, long glass fiber both theoretically as well as experimentally. Figure 2.2 shows a representation of a long glass fiber, as well as the inherent difficulties presented in trying to define an overall orientation state of such a complex fiber by a singular description such as an orientation vector. As a result, some authors have described the orientation of a semi-flexible fiber by utilizing an end-to-end vector, as described in additional detail in Section 2.2.2. Because of this flexibility, rather than describing the fiber by terms such as "orientation," it is more accurate to refer to the state of a long fiber's *configuration*.

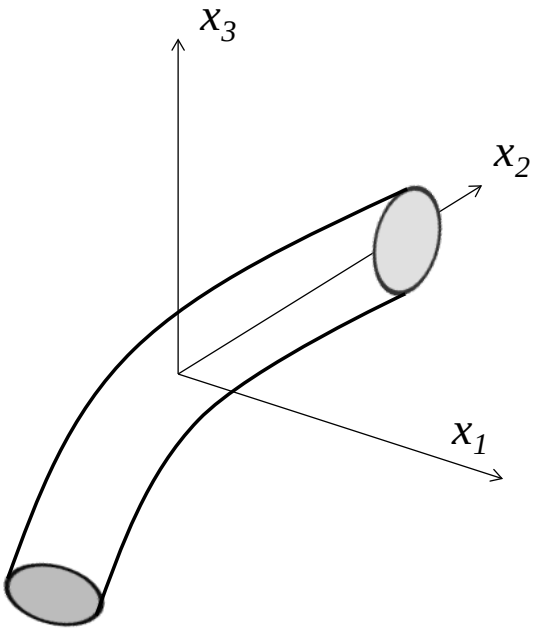

Figure 2.2. A long, flexible fiber with a random configuration.

2.1.3 Production of Glass Fiber Reinforced Materials

The commercial production of long fiber FRPs begins with compounding glass fibers and a polymer resin. The most common method of completing this commercially is via pultrusion [1, 14-15]. In pultrusion, strands of glass fibers that have been sized to have average diameters of approximately 10-12 microns are first chemically treated with a coupling agent in order to improve adhesion between the inorganic fibers and an organic polymer resin [16]. These continuous glass fiber bundles are then passed through a bath of polymer resin, where they are encapsulated with polymer and subsequently pulled through a die to form a strand. The resulting strands of polymer-coated glass fibers are subsequently dried and then cut into the desired lengths by a pelletizer. These discontinuous pellets typically will have lengths on the order of millimeters, with short and long glass fibers typically having pellet lengths of less than 1 mm and approximately 13 mm, respectively [17-18]. While it is possible to compound glass fibers and polymer resin via extrusion, it has been shown that the pultrusion process is preferred due to superior final fiber characteristics [19]. Furthermore, it is worth noting that it is possible to compound fibers and resin while simultaneously molding a final part, but with mixed results as to the effectiveness of this method [20-21].

To form a final composite part, these pellets are subsequently processed by using commercial methods such as injection or compression molding, resulting in attrition of the pellets and a final, post-processing Fiber Length Distribution (FLD) within the molded FRP. While the behavior of these fibers has been studied somewhat in compression molding [22-25], the majority of efforts have involved injection molding [26], primarily due to the many benefits of injection molding

including relatively low cost, ease of production of complex parts, and ability to tailor many processing parameters [27-33]. The majority of fiber length attrition has been found to occur in the screw itself [9]. Furthermore, research has shown that using a low-shear type screw as well utilizing a low compression ratio, a slow injection rate, and minimal back pressure breakage will result in less fiber breakage, and thus superior mechanical properties of the final composite part [34-35].

2.2 Evolution of Fiber Orientation in Flow

A complete and accurate mathematical understanding of the evolution of fiber orientation in flow is an ongoing area of research. If fiber orientation in flow is well understood and can be modeled, the commercial advantages of FRPs can be optimized by tailoring injection mold design so as to obtain a desired final, post-processing fiber length and orientation state. In this section, a review of continuum-based models of fiber orientation evolution in flow will be summarized, beginning with research into the flow behavior of rigid particles. A discussion of modifications necessary for flexible fiber systems as well as an overview of the models of suspension stress will follow.

2.2.1. Orientation Evolution Kinetics for Rigid Fibers

For glass fibers, it is common to express the configuration of a population of rigid fibers by using a singular orientation tensor, rather than individual orientation vectors for each fiber. Two such tensors, $\mathbf{A}$ and $\mathbf{A_4}$, are defined as the second and fourth moment of the orientation vector, respectively. These tensors are constructed by utilizing the orientation vector **p,** as defined previously in Figure 2.1 and the probability density function, ψ, as shown in Eqs. 2.13 and 2.14.

$$\mathbf{A} = \oint \mathbf{pp}\,\psi(\mathbf{p},t)d\mathbf{p} \tag{2.13}$$

$$\mathbf{A}_4 = \oint \mathbf{pppp}\,\psi(\mathbf{p},t)d\mathbf{p} \tag{2.14}$$

The orientation tensor, **A**, is typically utilized to describe the orientation state of a population of fibers, as described by Advani and Tucker [36]. By definition, the trace components of **A** always sum to 1. As such, the orientation tensor of a purely randomly orientated population of fibers would result in the trace components (i.e. A_{11}, A_{22}, and A_{33}) all with a value equal to 1/3. If, on the other hand, the entire population was perfectly aligned in a primary axis direction, the value of that particular trace component would be equal to exactly 1, while all other components of the tensor would be exactly zero. Experimentally, **A** is seen by inspecting a cross section of a fiber-polymer composite, as described by Hine et al. [37] and detailed further in Section 2.3.

2.2.1.1 Jeffery's Model

Work to understand particle motion in a flow field dates back to Jeffery's model for a neutrally-buoyant, ellipsoid-shaped particle in a dilute suspension [38]. In essence, Jeffery's model describes the generalized motion of a vector, such as **p**, with respect to time:.

$$\frac{D\mathbf{p}}{Dt} = \mathbf{W}\cdot\mathbf{p} + \lambda\left[\mathbf{D}\cdot\mathbf{p} - \mathbf{p}\left(\mathbf{p}\cdot\mathbf{D}\cdot\mathbf{p}\right)\right] \tag{2.15}$$

Here, λ is a parameter describing the ellipticity of the particle, while **W** and **D** represent the vorticity tensor and rate of strain tensor, respectively. Expressions for these tensor quantities are shown in Eqs. 2.16 and 2.17, respectively, where $\nabla v = \sum_i \sum_j \delta_i \delta_j \partial v_j / \partial x_i$.

$$\mathbf{W} = \frac{1}{2}\left[\left(\nabla v\right)^t - \nabla v\right] \tag{2.16}$$

$$\mathbf{D} = \frac{1}{2}\left[\left(\nabla v\right)^{t} + \nabla v\right] \qquad 2.17$$

For fibers, it is possible to express Jeffery's model as a function of the particle's aspect ratio, ξ, as defined in Eq. 2.18, and by using **A** and $\mathbf{A_4}$. The resulting Jeffery's model for fiber orientation evolution in a continuum sense is thus constructed by multiplying Eq. 2.15 by **p** and integrating over $\psi d\theta d\phi$, with the result shown in Eq. 2.19:

$$\xi = \frac{\left(a_r{}^2 - 1\right)}{\left(a_r{}^2 + 1\right)} \qquad 2.18$$

$$\frac{D\mathbf{A}}{Dt} = \mathbf{W}\cdot\mathbf{A} - \mathbf{A}\cdot\mathbf{W} + \xi\left(\mathbf{D}\cdot\mathbf{A} + \mathbf{A}\cdot\mathbf{D} - 2\mathbf{D}:\mathbf{A}_4\right) \qquad 2.19$$

For rods such as short, rigid fibers, ξ is seen to reduce to 1.0. It is worth noting, however, that the fourth order orientation tensor requires a closure approximation in order mathematically express the $\mathbf{A_4}$ tensor in terms of the second order orientation tensor **A**.

2.2.1.2 Closure Approximations

A variety of approximations have been studied to express $\mathbf{A_4}$ in terms of **A** by using various types of polynomial closures. Previous work on closure approximations includes an orthotropic fitted closure approximation (ORF) as introduced by Cintra and Tucker [39]. ORF is sufficient for predicting simple homogeneous and nonhomogeneous flows, but encounters non-physical oscillations when utilized for simple shear and radial diverging flows. As a result, approximations known as the ORW and ORW3 were proposed by introducing fitted flow data

over all orientation states and similar shear flow regions as that seen in radial diverging flow [39]. The ORW and especially ORW3 closure approximations outperform the ORF approximations, particularly for nonhomogeneous, radial diverging flows. The orthotropic fitted closures are also referred to as "eigenvalue-based optimal fitting," or EBOF, because they require the computation of the eigenvalues of the second order orientation tensor. As a result, however, EBOF closures require a considerable amount of computational time [40].

The initial invariant-based closure approximation developed by Verleye and Dupret [41] utilized natural closure values by using analytical solutions and the least square fitting process, and as such became known as NAT. However, the NAT requires minimal computational time as it does not require the calculation of eigenvalues. The NAT closure results in good transient behavior but has several limitations including a slight inaccuracy of steady state predictions, as well as possessing singularities [42].

In an effort to combine the accuracy of the EBOF closures while eliminating the singularity inherent to the NAT closure while still maintaining the computational efficiency of invariant-based closure approximations, the Invariant-Based Optimal Fitting closure (IBOF) was developed by Chung and Kwon [40]. The IBOF closure was able to maintain computational efficiency by relying on principal invariants, rather than needing to calculate eigenvalues and transform the coordinate system for tensor components. IBOF was tested for homogeneous, unsteady, and nonhomogeneous radial diverging flow and found to behave as accurately as the EBOF closures for all tested flow fields. At the same time, IBOF computational times were roughly only 30-40% of the required times for the EBOF closures to converge on a solution [40]. The reduction in computational time without the sacrifice of computational accuracy makes IBOF an ideal closure approximation.

2.2.1.3 Folgar-Tucker Model

While Jeffery was able to predict that an ellipsoid particle would align in the flow direction of a dilute suspension as λ approaches 1.0, the work of Folgar and Tucker has extended this model to include application to non-dilute systems [43]. This was accomplished by the addition of a term to account for isotropic rotary diffusion in hopes of accounting for fiber-fiber interactions that occur in semi-dilute and concentrated suspensions. In Eq. 2.20, C_I is a rotary diffusion coefficient which is determined both analytically and experimentally, while $\boldsymbol{I}$ is the identity tensor.

$$\frac{D\mathbf{A}}{Dt} = \mathbf{W}\cdot\mathbf{A} - \mathbf{A}\cdot\mathbf{W} + \xi\left(\mathbf{D}\cdot\mathbf{A} + \mathbf{A}\cdot\mathbf{D} - 2\mathbf{D}:\mathbf{A}_4\right) + 2C_I\dot{\gamma}\left(\mathbf{I} - 3\mathbf{A}\right) \qquad 2.20$$

The Folgar-Tucker model has been found to perform reasonably well in predicting the orientation of short fibers [44-45]. However, the Folgar-Tucker model has been seen to over predict the rate of short fiber orientation evolution for concentrated suspensions [46-48].

2.2.1.4 The "Slip" Parameter

In order to correct the over-prediction of the rate of fiber orientation exhibited by the Folgar-Tucker model, a delay parameter was introduced in order to more accurately represent the orientation kinetics. Originally introduced by Sepehr et al. [47], this delay parameter – also known as the "slip" parameter – was incorporated into the Folgar-Tucker model as shown in Eq. 2.21 [49]:

$$\frac{D\mathbf{A}}{Dt} = \alpha\left(\mathbf{W}\cdot\mathbf{A} - \mathbf{A}\cdot\mathbf{W} + \xi\left(\mathbf{D}\cdot\mathbf{A} + \mathbf{A}\cdot\mathbf{D} - 2\mathbf{D}:\mathbf{A}_4\right) + 2C_I\dot{\gamma}\left(\mathbf{I} - 3\mathbf{A}\right)\right) \qquad 2.21$$

This slip parameter, α, has a value between 0 and 1 and diminishes the rate of fiber orientation. Eberle et al. [50] used orientation predictions at the startup of flow for concentrated short fiber suspensions in order to show that the addition of the slip parameter slows the predicted orientation evolution to steady state. As a result, the predicted values of orientation with the slip parameter include more closely match the measured experimental values. It is worth noting that the slip parameter, α, is roughly equivalent to the strain reduction factor (SRF), κ, originally introduced by Huynh et al. [48] and implemented as a modification to the Folgar-Tucker model in a similar fashion by Wang et al. [51].

2.2.1.5 Reduced Strain Closure Model

Wang et al. [51] introduced a strain reduction factor (SRF), κ, in order to slow the orientation kinetics of the fourth order orientation tensor in a fashion that does not violate objectivity. The authors claimed that modifications similar to the one shown above in Eq. 2.21 violate objectivity by also reducing the terms containing the vorticity tensor by the reduction factor. As a result of this, such models are not invariant under rigid-body rotation, and as such could be insufficient in predicting orientation states in non-simple flow fields. Therefore, Wang et. al. developed a new model by modifying only the growth rates of the eigenvalues of the orientation tensor by the addition of the strain reduction factor, κ, but by excluding any modifications to the rotation rate expressions for the eigenvectors. By doing this, the model is able to achieve nearly the same steady orientation states as the previous models but with slower kinetics that more closely resemble the behavior of fibers in flow [51]. The resulting model was referred to as the reduced-strain closure (RSC) model, and is summarized in Eqs. 2.22 - 2.24, where $\mathbf{L_4}$ and $\mathbf{M_4}$ are defined as shown, and λ and $\mathbf{e_i}$ are the eigenvalues and eigenvectors of $\mathbf{A}$, respectively:

$$\frac{D\mathbf{A}}{Dt} = \mathbf{W}\cdot\mathbf{A} - \mathbf{A}\cdot\mathbf{W} + \xi\left\{\mathbf{D}\cdot\mathbf{A} + \mathbf{A}\cdot\mathbf{D} - 2\left[\mathbf{A}_4 + \left(1+\kappa\right)\left(\mathbf{L}_4 - \mathbf{M}_4 : \mathbf{A}_4\right)\right] : \mathbf{D}\right\} + 2\kappa C_I \dot{\gamma}\left(\mathbf{I} - 3\mathbf{A}\right) \tag{2.22}$$

$$\mathbf{L}_4 = \sum_{i=1}^{3} \lambda_i \left(e_i e_i e_i e_i\right) \tag{2.23}$$

$$\mathbf{M}_4 = \sum_{i=1}^{3} \left(e_i e_i e_i e_i\right) \tag{2.24}$$

2.2.1.6 Anisotropic Rotary Diffusion Model

A later addition to the Folgar-Tucker model was made by Phelps and Tucker [52], who attempted to more closely predict the actual nature of fiber-fiber interactions. While previous work has been completed to model orientation in a non-isotropic fashion [53-55], the most recent efforts have focused on an alteration to the C_I term in order to enable diffusion in a non-isotropic fashion. This has been done by expressing the rotary diffusion in terms of a tensorial quantity, **C**. As a result, this improved model has become known as the anisotropic rotary diffusion (ARD) model [52]. The ARD model improves upon predictions of orientation for short fiber composites as compared to previous models such as the Folgar-Tucker or RSC models [52]. However, it does not provide sufficient results to be able to accurately predict final fiber orientations and mechanical properties of long fiber composites [9]. The present ARD model is summarized in brief in Eqs. 2.25 and 2.26, and explained in further detail by Phelps and Tucker [52].

$$\dot{\mathbf{A}}^{\mathrm{ARD}} = \left(\mathbf{W}\cdot\mathbf{A} - \mathbf{A}\cdot\mathbf{W}\right) + \xi\left(\mathbf{D}\cdot\mathbf{A} - \mathbf{A}\cdot\mathbf{D} - 2\mathbf{A}:\mathbf{D}\right) + \dot{\gamma}\left[2\mathbf{C}' - 2\left(\mathrm{tr}\,\mathbf{C}'\right)\mathbf{A} - 5\left(\mathbf{C}'\cdot\mathbf{A} + \mathbf{A}\cdot\mathbf{C}'\right) + 10\mathbf{A}:\mathbf{C}'\right] \tag{2.25}$$

$$\mathbf{C}' = b_1\mathbf{I} + b_2\mathbf{A} + b_3\mathbf{A}^2 + \frac{b_4}{\dot{\gamma}}\mathbf{D} + \frac{b_5}{\dot{\gamma}^2}\mathbf{D}^2 \qquad 2.26$$

2.2.2 Orientation Evolution Kinetics for Flexible Rods

Due to the flexibility of long fibers, the previously described orientation models such as the Folgar-Tucker model may be insufficient at predicting the orientation evolution of long fibers. However, because the potential mechanical benefits of long fiber composites are superior to those of short fibers, it is necessary to expand orientation studies to long fiber evolution. However, there have been limited efforts in this area of research. The progress to date is summarized in the following section.

2.2.2.1 Characterization and the Bead-Rod Model

One of the first known continuum-based models to account for the flexible nature of long fibers was introduced by Strautins and Latz [45]. This model for semi-flexible fibers has been termed the "bead-rod" model, as it will be referred to here, based on its origination in polymer theory[45, 56]. The basis for the bead-rod model comes from a reevaluation of how one defines the configuration of a long, semi-flexible fiber. For short fibers (Figure 2.1), the fiber is represented by a single vector, due to the fiber's rigidity. For semi-flexible fibers, however, Strautins and Latz proposed using a pair of orientation vectors. To do this, a fiber of total length L is segmented it into two sections of equal length l_b equal to $L/2$. These two half-segments with orientation of **p** and **q**, or "rods," are connected to one another through a central pivot point, or "bead," as shown in Figure 2.3. The two rods in the representative fiber also have beads at the ends, and are connected by not only the central pivot point, which they may flex or bend about, but also by a restorative potential, k, attached to both rods. This restorative potential is similar to

a spring constant. As the value of *k* approaches infinity, the two rod segments lose the ability to flex and become rigid, while as the value of *k* approaches 0 the fiber becomes infinitely flexible. Additionally, it is worth noting that the two-rod schematic presented in Figure 2.3 can theoretically be extended to any number of $2n + 1$ beads and $2n$ rods. However, for ease of presenting the mathematics of the model in the following paragraphs, only the two-rod structure presented in Figure 2.3 will be discussed here.

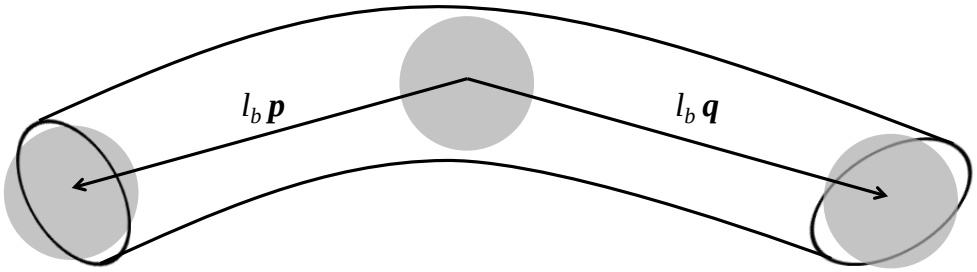

Figure 2.3. A representation of a long, semi-flexible fiber as depicted using two "rods," with orientation vectors **p** and **q**, and three "beads."

By using the representation of fiber configuration as shown in Figure 2.3, Strautins and Latz subsequently developed the necessary assumptions required in order to describe the orientation evolution of a long, semi-flexible fiber. In Figure 2.3, it is first assumed that $\mathbf{p} \approx -\mathbf{q}$. In other words, the central "pivot" bead of the fiber must be exactly at the halfway point of the total fiber length. Furthermore, this model is assumed to be only applicable for dilute suspensions which consist of fibers that are not infinitely flexible with a limited extent of curvature such as has been found previously for long glass fibers [57]. Due to the dilute assumption, no fiber-fiber interactions are possible, simplifying the mathematical derivations. Additionally, a quadratic closure approximation was utilized for similar mathematical simplification reasons.

The authors then derived the orientation model by forming three moments of the **p** and **q** vectors. This includes the second moment of the orientation distribution function of **p**, denoted as **A** and similar to the expression see previously in rigid rod theory (Eq. 2.13). Similarly, the second moment of the orientation distribution function of **p** and **q** is constructed by forming a mixed product of the **p** and **q** orientation vectors and the distribution function, ψ, and denoted **B**. Finally, the first moment of the distribution function of the orientation vector **p** is constructed and denoted **C**. The orientation tensors **A**, **B**, and **C** are summarized in Eqs. 2.27 - 2.29, respectively. However, it is worth noting that the first moment of the distribution function of **p** would be equivalent to the first moment of the distribution function of **q**, due to **p** ≈ **-q**, and the selection of **p** was the convention chosen by the authors. It is worth noting that **C** is a non-zero term in the case of the bead-rod model, whereas the first moment of the distribution function as discussed previously for the rigid rod case vanishes.

$$\mathbf{A} = \int\int \mathbf{pp}\,\psi(\mathbf{p},\mathbf{q},t)\,d\mathbf{p}d\mathbf{q} \tag{2.27}$$

$$\mathbf{B} = \int\int \mathbf{pq}\,\psi(\mathbf{p},\mathbf{q},t)\,d\mathbf{p}d\mathbf{q} \tag{2.28}$$

$$\mathbf{C} = \int\int \mathbf{p}\,\psi(\mathbf{p},\mathbf{q},t)\,d\mathbf{p}d\mathbf{q} \tag{2.29}$$

The authors subsequently derived the necessary orientation functions of the system using Eqs. 2.27-2.29, which results in three material derivative equations for the evolution of **A**, **B**, and **C** as shown in Eqs. 2.30- 2.33. For additional mathematical derivation, the reader is referred to Strautins and Latz [45].

$$\frac{D\mathbf{A}}{Dt} = \left(\mathbf{W}\cdot\mathbf{A} - \mathbf{A}\cdot\mathbf{W}\right) + \left(\mathbf{D}\cdot\mathbf{A} + \mathbf{A}\cdot\mathbf{D} - \left(2\mathbf{D}:\mathbf{A}\right)\mathbf{A}\right) + \frac{l_b}{2}\left[\mathbf{C}\mathbf{m} + \mathbf{m}\mathbf{C} - 2\left(\mathbf{m}\cdot\mathbf{C}\right)\mathbf{A}\right] - 2k\left[\mathbf{B} - \mathbf{A}\ \mathrm{tr}\left(\mathbf{B}\right)\right] \tag{2.30}$$

$$\frac{D\mathbf{B}}{Dt} = \left(\mathbf{W}\cdot\mathbf{B} - \mathbf{B}\cdot\mathbf{W}\right) + \left(\mathbf{D}\cdot\mathbf{B} + \mathbf{B}\cdot\mathbf{D} - \left(2\mathbf{D}:\mathbf{A}\right)\mathbf{B}\right) + \frac{l_b}{2}\left[\mathbf{C}\mathbf{m} + \mathbf{m}\mathbf{C} - 2\left(\mathbf{m}\cdot\mathbf{C}\right)\mathbf{B}\right] - 2k\left[\mathbf{A} - \mathbf{B}\ \mathrm{tr}\left(\mathbf{B}\right)\right] \tag{2.31}$$

$$\frac{D\mathbf{C}}{Dt} = \nabla v^t\cdot\mathbf{C} - \left(\mathbf{A}:\nabla v^t\right)\mathbf{C} + \frac{l_b}{2}\left[\mathbf{m} - \mathbf{C}\left(\mathbf{m}\cdot\mathbf{C}\right)\right] - k\mathbf{C}\left[1 - \mathrm{tr}\left(\mathbf{B}\right)\right] \tag{2.32}$$

$$\mathbf{m} = \sum_{i=1}^{3}\sum_{j=1}^{3}\sum_{k=1}^{3}\frac{\partial^2 v_i}{\partial x_j \partial x_k} A_{jk}\mathbf{e}_i \tag{2.33}$$

The bead-rod model, however, is not without limitations. First, the bead-rod model is only applicable for infinitely dilute fiber suspensions [45]. This is problematic and insufficient for predicting the behavior of fiber suspensions typically utilized commercially which typically have fiber concentrations of 10-40 wt% [16, 58]. Second, the hydrodynamic contributions to flexibility quantized by the vector **m** as shown in Eq. 2.33 are formed by the vector component dyads, $\mathbf{e_i}$, and the summation over the indices *ijk*. Therefore, flexibility as a result of flow will only exist in this model when the second-order spatial derivatives of the velocity term in Eq. 2.33 are non-zero. As a result, no flow-induced flexibility will be predicted for scenarios involving "simple" flow, such as in simple shear. Finally, while simulations of the original bead-rod model by Strautins and Latz [45] demonstrated an increased flow-alignment of long fibers as compared to the short fiber model of Folgar and Tucker [43], no substantiated comparison to actual orientation data was performed in their study.

Subsequently, Ortman et al. [59] suggested several modifications to the original bead-rod model to more closely resemble the behavior of long, concentrated, semi-flexible fiber suspensions. The first modification made was to make the model applicable to non-dilute systems. This was accomplished by adding an isotropic rotary diffusion term, similar to that of Folgar and Tucker [43], so that the model could be extended from dilute and to apply to semi-dilute and concentrated suspensions. Secondly, Ortman further incorporated the "slip" parameter discussed previously, α, in order to more accurately represent the reduced orientation kinetics of both short and long fibers. These modifications are seen below in Eqs. 2.34 - 2.37. Furthermore, Ortman et al. suggested the use of an additional bending term denoted as K_{ijk} (Eq. 2.37). This additional bending term accounts for additional causes of inducing flexibility that result from direct fiber-to-fiber contacts present in non-dilute suspensions, but was not directly explored in the author's work (i.e. K_{ijk} was set equal to 0 for the purpose of their work). As a result of these modifications, this modified version of the bead-rod model is capable of predicting fiber flexing as a function of not only hydrodynamic effects but also as a result of rotary diffusion as shown below:

$$\frac{D\mathbf{A}}{Dt}=\alpha\begin{bmatrix}\left(\mathbf{W}\cdot\mathbf{A}-\mathbf{A}\cdot\mathbf{W}\right)+\left(\mathbf{D}\cdot\mathbf{A}+\mathbf{A}\cdot\mathbf{D}-\left(2\mathbf{D}:\mathbf{A}\right)\mathbf{A}\right)\\ ...-6C_I\dot{\gamma}\left(\mathbf{A}-\frac{1}{3}\mathbf{I}\right)+\frac{l_b}{2}\left[\mathbf{Cm}+\mathbf{mC}-2\left(\mathbf{m}\cdot\mathbf{C}\right)\mathbf{A}\right]\\ ...-2k\left[\mathbf{B}-\mathbf{A}\ \mathrm{tr}\left(\mathbf{B}\right)\right]\end{bmatrix} \tag{2.34}$$

$$\frac{D\mathbf{B}}{Dt}=\alpha\begin{bmatrix}\left(\mathbf{W}\cdot\mathbf{B}-\mathbf{B}\cdot\mathbf{W}\right)+\left(\mathbf{D}\cdot\mathbf{B}+\mathbf{B}\cdot\mathbf{D}-\left(2\mathbf{D}:\mathbf{A}\right)\mathbf{B}\right)-4C_I\dot{\gamma}\mathbf{B}\\ ...+\frac{l_b}{2}\left[\mathbf{Cm}+\mathbf{mC}-2\left(\mathbf{m}\cdot\mathbf{C}\right)\mathbf{B}\right]-2k\left[\mathbf{A}-\mathbf{B}\ \mathrm{tr}\left(\mathbf{B}\right)\right]\end{bmatrix} \tag{2.35}$$

$$\frac{D\mathbf{C}}{Dt}=\alpha\begin{bmatrix}\nabla v^t\cdot\mathbf{C}-\left(\mathbf{A}:\nabla v^t\right)\mathbf{C}+\frac{l_b}{2}\left[\mathbf{m}-\mathbf{C}\left(\mathbf{m}\cdot\mathbf{C}\right)\right]\\ ...-k\mathbf{C}\left[1-\mathrm{tr}\left(\mathbf{B}\right)\right]-2C_I\dot{\gamma}\mathbf{C}\end{bmatrix} \tag{2.36}$$

$$\mathbf{m} = \sum_{i=1}^{3}\sum_{j=1}^{3}\sum_{k=1}^{3}\left(\frac{\partial^2 v_i}{\partial x_j \partial x_k} + K_{ijk}\right) A_{jk}\mathbf{e}_i \qquad 2.37$$

Additionally, Ortman et al. [59] suggested that the configuration state of a long, semi-flexible fiber could be considered by utilizing an end-to-end vector. The end-to-end vector is equivalent to a connecting vector from the two end-points of a semi-flexible fiber, denoted as **(p – q)**, and shown in Figure 2.4:

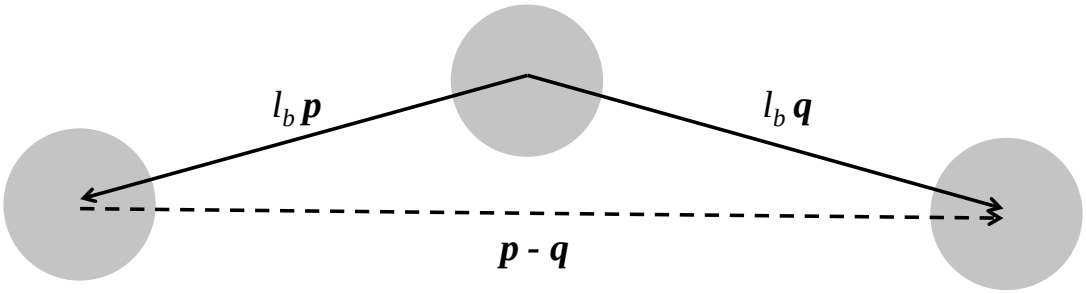

Figure 2.4. Representation of the end-to-end vector, **p** – **q**.

This vector was subsequently used to form an orientation tensor, **r**, which is the second moment of the orientation distribution function of the end-to-end vector. A normalized, dimensionless form of **r** was constructed and denoted **R**. These relationships are summarized in Eqs. 2.38 - 2.40, where l_b is the fiber half-length as originally defined in Figure 2.3.

$$\mathbf{r} = \int\int l_b^{\,2}(\mathbf{p}-\mathbf{q})(\mathbf{p}-\mathbf{q})\psi(\mathbf{p},\mathbf{q},t)\,d\mathbf{p}d\mathbf{q} \qquad 2.38$$

$$\mathbf{r} = 2l_b^{\,2}(\mathbf{A}-\mathbf{B}) \qquad 2.39$$

$$\mathbf{R} = \frac{\mathbf{r}}{\mathrm{tr}(\mathbf{r})} = \frac{\mathbf{A}-\mathbf{B}}{1-\mathrm{tr}(\mathbf{B})} \qquad 2.40$$

When inspecting Eq. 2.40, it can be seen that as the radius of fiber curvature reduces to zero, i.e. as the tensor **B** reduces to zero, the normalized end-to-end tensor **R** similarly reduces to the original orientation tensor **A**. Because it is not necessarily best to describe long glass fibers in terms of their orientation [60], utilizing the end-to-end **R** tensor may be preferable to describe the general configuration state of a population of long, semi-flexible fibers.

2.2.3 Stress Models

A model for the stress tensor of a suspension is necessary due to the closely coupled nature of the fluid stress and fiber orientation equations discussed previously, and possibly for simulation of injection molding. Therefore, rheology can be utilized in order to obtain parameters within the orientation model and to subsequently predict the evolution of fiber orientation in flow as previously demonstrated [60]. Research to understand and accurately model the stress of suspensions has been ongoing for many years [24, 61-64] . Many of the recent approaches for a suspension of particles model the total stress of the system, $\boldsymbol{\sigma}$, via a linear combination of stresses from both the suspending matrix and the particles themselves. To do this, the isotropic pressure, P, the viscosity of the matrix, η_m, and a term to account for the stresses of the particles, $\boldsymbol{\tau_p}$, are included as shown in Eq. 2.41. It is worth noting that η_m is calculated by using an empiricism for viscosity, depending on whether the fluid is Newtonian or non-Newtonian [27].

$$\boldsymbol{\sigma} = -P\mathbf{I} + 2\eta_m \mathbf{D} + \boldsymbol{\tau}_\mathbf{p} \tag{2.41}$$

For a fiber suspension, the term accounting for the stress of the particles in Eq. 2.41 can be expanded. This results in the general form as shown in Eq. 2.42 [65]:

$$\boldsymbol{\sigma} = -P\mathbf{I} + 2\eta_m \mathbf{D} + 2\eta_m \phi \left\{ a\mathbf{A}_4 : \mathbf{D} + b\left(\mathbf{D}\cdot\mathbf{A} + \mathbf{A}\cdot\mathbf{D}\right) + c\mathbf{D} + f\mathbf{A}D_r \right\} \qquad 2.42$$

where the volume fraction of the fibers within the suspension has been accounted for via ϕ. In Eq. 2.42, D_r is the rotary diffusivity related to Brownian motion [7], while *a*, *b*, *c*, and *f* are geometric shape factors. It can be seen that this expression includes the fourth order orientation tensor, $\mathbf{A_4}$, and as such requires a closure approximation similar to those described previously. For long glass fibers, the aspect ratio is large while Brownian motion is negligible. As a result of this *b*, *c*, and D_r can be set equal to 0, and Eq. 2.42 is seen to reduce to Eq. 2.43 [66], where *N* is a parameter that accounts for fiber stress and is a function of both fiber concentration and aspect ratio.

$$\boldsymbol{\sigma} = -P\mathbf{I} + 2\eta_m \left\{ \mathbf{D} + N\mathbf{A}_4 : \mathbf{D} \right\} \qquad 2.43$$

A second approach to reducing Eq. 2.42 results in a form similar to that of Eq. 2.43, while still accounting for the fiber volume fraction, ϕ, as shown in Eq. 2.44 and originally presented by Lipscomb et al. [67]:

$$\boldsymbol{\sigma} = -P\mathbf{I} + 2\eta_m \left\{ \mathbf{D} + + c_1\phi\mathbf{D} + N\mathbf{A}_4 : \mathbf{D} \right\} \qquad 2.44$$

Here, c_i incorporates the enhancement in stress due to the presence of high aspect ratio of fibers. However, similar to the model presented in Eq. 2.43, this expression is only valid for semi-dilute suspensions, and little work has been done to study the stress of highly concentrated fiber suspensions.

While some research has focused on using *N* as a fitting parameter, significant effort has been expended to theoretically determine values for *N* using a variety of methods for concentrated suspensions [8]. This work dates back to Batchelor et al. [62], who suggested an empirical form based on the number of fibers per unit volume, *n*, as shown in Eq. 2.45 and 2.46:

$$N = \frac{\pi n L^3}{6\ln\left(2L/D\right)}\left(\frac{1+0.64\varepsilon}{1-1.50\varepsilon}+1.659\varepsilon^2\right) \tag{2.45}$$

$$\varepsilon = \frac{1}{\ln\left(2\mathrm{L}/\mathrm{D}\right)} \tag{2.46}$$

The above expression was subsequently modified by Dinh and Armstrong [61] to be applicable to semi-dilute suspensions, as shown in Eq. 2.47, depending on whether the fibers within the suspension were randomly oriented (Eq. 2.48) or uniformly aligned (Eq. 2.49).

$$N = \frac{\pi n L^3}{6\ln\left(2h/D\right)} \tag{2.47}$$

$$\text{random orientation:} \quad h = \frac{1}{nL^2} \tag{2.48}$$

$$\text{aligned orientation:} \quad h = \frac{1}{\sqrt{nL}} \tag{2.49}$$

While the majority of research concerning the modeling of suspension stress has revolved around the use of short fibers, Ortman et al. [17, 60] suggested several modifications to account for the semi-flexible nature of long glass fibers. A term derived from the bending potential function within the bead-rod model and the restorative potential, *k*, was added to the suspension stress model due to the non-zero average fiber bending angle. As a result, when incorporating the additional stress resulting from fiber bending, the total stress within a long, semi-flexible fiber suspension becomes,

$$\boldsymbol{\sigma}_{\mathbf{BR}} = \boldsymbol{\sigma} + c_3\eta_m k\frac{3\phi a_r}{2}\left[\mathbf{B} - \mathbf{A}\ \mathrm{tr}\left(\mathbf{B}\right)\right] \tag{2.50}$$

where **A** and **B** were defined in Eqs. 2.27 and 2.28, respectively, while $\boldsymbol{\sigma}$ was defined previously in Eq. 2.41. Additionally, in Eq. 2.50, c_3 is defined as a parameter to quantify the extent of fiber-fiber interactions present within a non-dilute suspension. While this parameter allows for this

model to be extended to non-dilute suspensions, unlike the previously discussed models such as that by Lipscomb et al. [67], the c_3 parameter was limited to a theoretical value of c_3 = 1 by Ortman et al. [59]

Eq. 2.50 can further be modified to include the second moment of the end-to-end vector of the bead-rod model, **R**, as previously detailed and shown in Eq. 2.40. The resulting modification is shown below in Eq. 2.51:

$$\boldsymbol{\sigma}_{\mathbf{BR}} = \boldsymbol{\sigma} + c_3 \eta_m k \frac{3\phi a_r}{2} \frac{\mathrm{tr}(\mathbf{r})}{2l_b^{\,2}} (\mathbf{A} - \mathbf{R}) \tag{2.51}$$

It is worth noting that as the radius of fiber curvature goes to zero and the fiber becomes rigid, **R** is seen to reduce to **A**, and thus the expression for suspension stress similarly simplifies to that of the rigid rod suspension. On the contrary, as fiber flexibility increases the distance between the two ends of the fiber will decrease, which will result in an increase in the magnitude of the suspension stress accordingly.

Additionally, Ortman et al. suggested an alternative empirical modification to the stress theory proposed by Lipscomb (Eq. 2.44) in order to more closely model the suspension stresses as a function of deformation rate. The basis of this modification was to replace both fitting parameters, c_1 and N, with the weighting functions f_1 and f_2, respectively. These modifications are summarized below in Eqs. 2.52 - 2.54, where the weighting function f_1 and f_2 are a function of the shear rate and the invariants of **A** (Eqs. 2.55 - 2.57), respectively.

$$\sigma_{\mathrm{mod}} = -P\mathbf{I} + 2\eta_m \{\mathbf{D} + f_1 \phi \mathbf{D} + f_2 \mathbf{A}_4 : \mathbf{D}\} \tag{2.52}$$

$$f_1 = \begin{cases} \dfrac{c_1}{\dot{\gamma}_{\min}} & \text{for} \quad \dot{\gamma} \le \dot{\gamma}_{\min} \\ \dfrac{c_1}{\dot{\gamma}^b} & \text{for} \quad \dot{\gamma} > \dot{\gamma}_{\min} \end{cases} \tag{2.53}$$

$$f_2 = c_2 I_A II_A III_A \tag{2.54}$$

$$I_A = \mathrm{tr}\left(\mathbf{A}\right) = 1 \tag{2.55}$$

$$II_A = \frac{1}{2}\left[\mathrm{tr}\left(\mathbf{A}\right)^2 - \mathrm{tr}\left(\mathbf{AA}\right)\right] \tag{2.56}$$

$$III_A = \det\left(\mathbf{A}\right) \tag{2.57}$$

The above expression for f_1 allows for a prediction of the viscosity of the suspension to be shear thinning in excess of what is predicted for the matrix alone as commonly observed experimentally, where c_1 and b are fitting parameters. It can be seen that if b is set equal to zero, the expression for f_1 simplifies to that of Lipscomb's model. Furthermore, it can be seen that f_1 is largest for low values of $\dot{\gamma}$, but is limited by a minimal value of $\dot{\gamma}$ (i.e. $\dot{\gamma}_{\min}$) in order to prevent the expression for f_1 from approaching infinity as the shear rate approaches zero. In essence, the f_1 term accounts for a potential steady-state stress enhancement due to the direct contacts between fibers, in addition to the hydrodynamic enhancement in stress as a result of the added volume fraction of fibers to the suspension. Similarly, the above expression for f_2 allows for the proper prediction of experientally seen stress overshoots that are unable to be predicted by Lipscomb's model (Eq. 2.44) and incorporates the fitting parameter c_2. The use of the invariants of the orientation tensor were chosen as weighting functions due to the fact that they represent scalar quantities that are entirely dependent on the orientation state of the fibers within the system and are not affected by the coordinate choice for the system. However, the authors conceded that other functions involving the invariants of **A** may also be applicable. Therefore, Eqs. 2.51 and 2.52, combined with the above expressions for f_1 and f_2, are used to form a modified stress tensor that has been shown to more accurately predict the experimentally

observed rheological responses of long fiber suspensions as compared to the rigid rod model, as shown in Eq. 2.58:

$$\sigma_{\text{BR-mod}} = -P\mathbf{I} + 2\eta_m\left\{\mathbf{D} + f_1\phi\mathbf{D} + f_2\mathbf{A}_4 : \mathbf{D}\right\} + c_3\eta_m k\frac{3\phi a_r}{2}\frac{\text{tr}(\mathbf{r})}{2l_b^{\,2}}(\mathbf{A} - \mathbf{R}) \qquad 2.58$$

2.2.4 Simulation of Fiber Orientation Evolution

In order to predict the evolution of fiber orientation within a mold the flow field within the geometry must be known. The mass and momentum conservation equations for isothermal flow are summarized in Eqs. 2.59 and 2.60:

$$\frac{D\rho}{Dt} = \frac{\partial\rho}{\partial t} + v\cdot\nabla\rho = -\rho(\nabla\cdot v) \qquad 2.59$$

$$\rho\frac{Dv}{Dt} = \rho\frac{\partial v}{\partial t} + \rho v\cdot\nabla v = \nabla\cdot\boldsymbol{\sigma} \qquad 2.60$$

where t is time, v is the fluid velocity, ρ is the fluid density, and $\boldsymbol{\sigma}$ is the stress tensor. The differential equations in Eqs. 2.59 and 2.60 can be used to solve for the velocity field within a selected geometry when combined with a set of initial conditions and assumptions such as the condition of incompressibility:

$$\nabla\cdot v = 0 \qquad 2.61$$

The description of the fluid velocity as given in Eqs. 2.59-2.61must be combined with the the orientation tensor model (i.e. Eq. 2.21) and the model of the suspension stress (Eq. 2.58) in order to predict fiber orientation evolution in flow. This results in a system of coupled equations which can be solved in order to predict the evolution of fiber orientation [68]. However, many studies in the literature have solved this system of equations by using a decoupled approach by

assuming that the rheology of the fiber suspension is primarily dependent on only the rheology of the neat polymer matrix, and by directly substituting the velocity field into the orientation equations [69-70]. Additionally, it has been shown that the resulting predictions can be improved when the actual inlet orientation at an injection molded part's gate is used as the initial conditions for the simulation rather than using an assumption about the initial orientation [71].

The mathematical complexity in the balance equations is typically simplified by using the Hele-Shaw flow approximation in order to reduce the problem from 2-dimensional to 1.5-dimensional flow and to simplify the calculations of the velocity field. The Hele-Shaw simplification is based upon the lubrication approximation, and allows for the balance equations governing flow to be approximated as similar to pressure-driven flow within a narrow gap between two parallel plates. The result of this simplification is demonstrated in Figure 2.5.

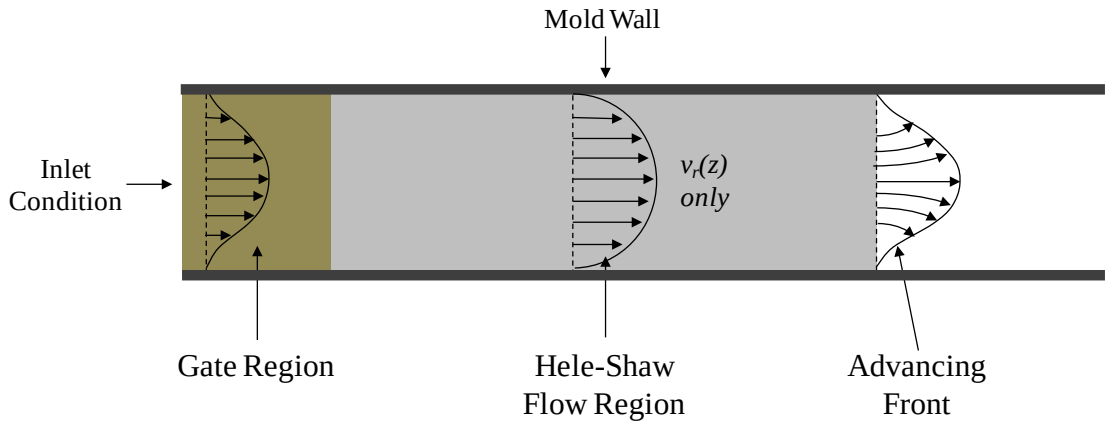

Figure 2.5. Representation of the Hele-Flow approximation.

Typically, most studies in the literature have been primarily concerned with predicting and measuring orientation in the well-developed region of Hele-Shaw flow while neglecting the majority of flow effects of the gate and advancing front regions.

Additional methods which have shown to be effective for short fibers include simulation of fiber evolution by using finite element analysis (FEA) [65, 69, 72] and a pseudo-concentration

method (PCM) to treat the air and polymer as a continuum in order to identify the exact melt front profile [65]. Additionally, a sophisticated technique known as the particle simulation method (PSM) has been used to model a fiber as an array of spheres to some success for short fibers [73-75], including for the prediction of fiber fracture [76].

2.3 Experimental Techniques for Observing Fiber Orientation

The previously presented models can lead to simulations of expected fiber orientations in flow, such as that seen within an injection mold while a part is being formed. Currently, predictions are somewhat limited to simple test geometries. However, the ultimate goal is to be able to understand flow and orientation evolution of not only short fibers but also long fibers in complex flow regimes, so as to be able to tailor and optimize mold design to impart favorable fiber orientations and thus mechanical benefits. As a result, it is necessary to obtain experimental orientation values of fiber orientation in order to compare with predicted values obtained as a result of the previously discussed stress models. A summary of how values of fiber orientation distribution are observed and the experimental methods used to determine the components of the orientation tensor are detailed in the following sections.

2.3.1 Method of Ellipses (MoE)

A technique known as the Method of Ellipses (MoE) is a common experimental approach used to extract the required information from a Fiber Reinforced Polymer composite (FRP) in order to quantify the orientation state of a population of fibers via calculation of the components of the orientation tensor, **A** [77]. In general, the basic concept of the MoE is to qualitatively evaluate the 2-dimensional microstructure of a fiber-reinforced composite using some form of

visual inspection such as optical microscopy, followed by image processing in order to gain a more detailed understanding of the global orientation of fibers within the part. Through careful sample preparation and techniques, which will be detailed further in Section 2.3.2, a portion of the x_1-x_2 plane of an FRP can be acquired via imaging. Figure 2.6 shows an example of an inspection plane featuring the polymer matrix (i.e. the grey background) and the white elliptical projections corresponding to each glass fiber crossing the chosen inspection plane. The MoE subsequently allows for quantitative 3-dimensional fiber orientation data to be reconstructed from the 2-dimensional projections of the ellipses in the image according to the definition of a rigid fiber as discussed previously in Section 2.1 and as depicted in Figure 2.1.

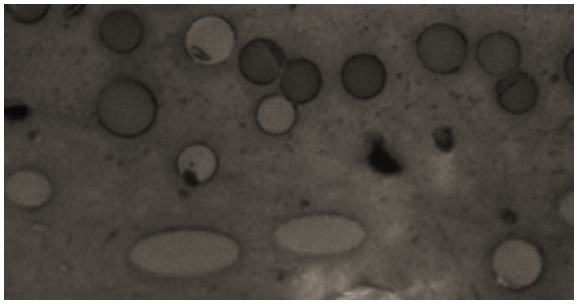

Figure 2.6. Example of a segment of the x_1-x_2 plane within an injection molded sample showing the polymer matrix (grey background) and elliptical projections of fibers (white ellipses).

The MoE is based upon an assumption that each fiber within the sample behaves as a rigid rod in flow (Figure 2.1) and that the orientation vector can be reconstructed for each ellipse in an inspection plane by using the definition of $\boldsymbol{p}$ given in Eqs. 2.9-2.12. In order to do this, a series of parameters must be measured directly from each fiber ellipse. The spatial definition of these parameters is given in Figure 2.7 and include the vertical and horizontal center of mass (v_c and h_c, respectively), as well as the in-plane, or azimuthal, angle, ϕ. Additionally, the minor and

major ellipse axes, *m* and *M*, respectively, are measured and are subsequently used to calculate the out-of-plane, or zenith, angle, θ (Figure 2.1), as defined in Eq. 2.62:

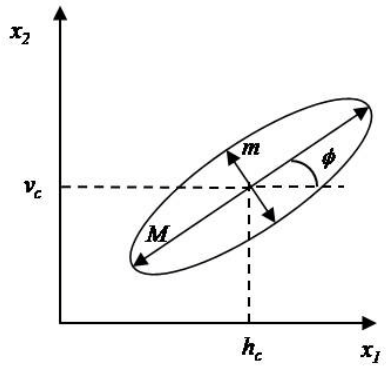

Figure 2.7. Elliptical parameters obtained from the x_1-x_2 plane.

$$\theta = \cos^{-1}\left(\frac{m}{M}\right) \qquad 2.62$$

For a population of fibers, however, as shown in Figure 2.6, it is more convenient to calculate the components of the orientation tensor, **A**. The **A** tensor can be expressed in its most simplistic format by the expectation of the dyadic product of ***p***, as shown in Eq. 2.63:

$$\mathbf{A} = \left\langle p_i p_j \right\rangle \qquad 2.63$$

A weighting function was developed by Bay and Tucker [78] and is used to compensate for visual bias in the calculation of the average components of the orientation tensor, A_{ij}. The addition of a weighting term is necessary because when preparing a sample and cutting an inspection plane it is statistically more likely to cut across a fiber than it is to cut down the length of a fiber. As such, experimentally it is more likely to see near-circular cross sections of fibers, indicative of fibers that are aligned highly transverse to the inspection plane. Therefore, more emphasis should be placed on elongated ellipses with high out-of-plane inclination where the

fibers approach being parallel to the plane of inspection. The expression for A_{ij} is thus modified to include this weighting function, as depicted in Eq. 2.64:

$$A_{ij} = \frac{\sum \left(A_{ij}\right)_n F_n}{\sum F_n} \tag{2.64}$$

Here, the weighting function, F_n, is a function of the out-of-plane fiber angle, θ. While several methods of calculating F_n are available [78], the expression is typically chosen based upon a critical angle of θ, θ_c, as shown in Eq. 2.65. As the angle of inclination approaches $\pi/2$, fibers become perfectly aligned parallel within the inspection plane and the elliptical projections exhibit the profile of a rectangle which can be accurately measured. Therefore, F_n becomes a function only of the fiber's diameter, d, for all angles larger than θ_c, while the expression remains a function of θ for all lesser angles (Eq. 2.66).

$$\theta_c = \cos^{-1}\left(\frac{d}{L}\right) \tag{2.65}$$

$$F_n = \begin{cases} \dfrac{1}{L_n \cos\theta_n + L_n \sin\theta_n} & \theta < \theta_c \\ \dfrac{1}{d_n} & \theta > \theta_c \end{cases} \tag{2.66}$$

The MoE has been utilized in a number of studies to evaluate and quantify the orientation state of short glass fiber FRPs [18, 72, 79-81] because of its numerous benefits. First, the MoE has the ability to accurately determine the local orientation state of a population of fibers, regardless of material choice of the matrix or fiber, so long as the fibers behave as rigid rods in flow. In addition, typically an image analysis width, also referred to in the literature as a "bin" width, of only 700 microns has been found to minimize statistical error for short glass fibers [18, 79], allowing for a quick and efficient calculation of the components of the orientation tensor

with good repeatability [82]. It is worth noting, however, that error is seen to increase when the bin width is reduced to the length scale of a short fiber [83]. Furthermore, the MoE is readily adaptable to various types of parts, including injection molded parts and to parts made within a sliding plate rheometer [59]. Finally, the MoE is capable of being automated in order to calculate components of the orientation tensor by scanning large image analysis widths containing up to 1 million fibers, and one such automation is known as the Leeds Analyzer [84-85].

2.3.1.1 Fiber Orientation Distribution (FOD)

For injection molded parts, the MoE is used to quantify a "through-thickness" orientation profile referred to as the Fiber Orientation Distribution (FOD). Typically for an injection molded part, the x_1-x_2 plane is chosen so that the flow direction is represented as the x_1-direction while the thickness of the part is represented by the x_2-direction, respectively. Furthermore, the x_3-direction is referred to as the "neutral" or "transverse" direction. This allows the orientation data to be presented in such a way as to depict how the orientation quantitatively changes as a function of part thickness from regions of high shear (i.e. near the mold walls) to regions of high extension (i.e. near the midplane of the part). Because predicted values of the orientation tensor vary not only as a function of flow but also as a function of part thickness, the FOD is a convenient mechanism for comparison of experimental to predicted values.

2.3.1.2 Ambiguity

One primary concern when using the MoE is the problem of ambiguity [78], which results from the fact that each 2-dimensional ellipse detected within the x_1-x_2 plane can represent a fiber

inclined in two possible directions. Figure 2.8 depicts the problem of ambiguity and shows that a single ellipse could represent a fiber with orientation of either ϕ or $\phi + \pi$. The ambiguity in the angle of ϕ results in uncertainty in the calculation of the off-diagonal components of the orientation tensor containing the neutral or transverse x_3-direction (i.e. A_{13} and A_{23}). The remaining components of the orientation tensor – A_{11}, A_{22}, A_{33}, and A_{12} – are calculated explicitly in the x_1-x_2 plane and are identical regardless of the ambiguity of ϕ. Several experimental methods have been developed to mitigate the problem of ambiguity and will be detailed further in Section 2.3.2 [79, 86].

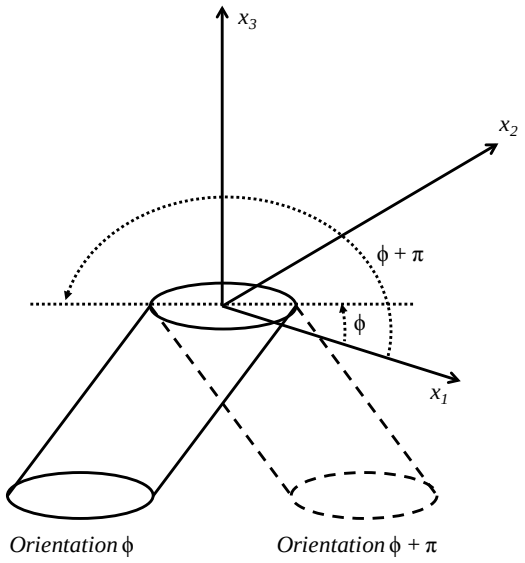

Figure 2.8. Representation of the out-of-plane angle ambiguity showing that ϕ may be equal to either π or π + 180°.

2.3.1.3 Limitations of the MoE

While the primary drawback of ambiguity within the MoE can be negated with proper sample preparation and technique, additional limitations of the method do exist. First, many techniques require slow and time consuming sample preparation or the use of expensive and

highly specialized equipment, depending on the method of sample preparation chosen as detailed further in Section 2.3.2. Additionally, two primary sources of error are resolution of the images used for analysis and user error during sample preparation [78]. Moreover, while a major benefit of the MoE is that it can be automated or semi-automated, it is necessary to construct computerized subroutines in order to do so. Finally, depending on the quality of images obtained, the quantitative image analysis can take considerable time and user effort as low quality images are incapable of being analyzed by automated subroutines with any real sense of accuracy. Historically, care must be taken to discard cut fibers that measure less than one-half of an ellipse during analysis, as these "special ellipses" typically increase error in the measurement which further increases image analysis time [78, 87].

While the above-mentioned limitations are all operational or technique-based, an additional drawback of the MoE is its extension to long, semi-flexible fibers. Because long fibers have the ability to exhibit flexibility and curvature via bending, it is questionable as to how or even if the MoE can be applied directly as is to long glass fiber composites. Previous work by Bay and Tucker has shown that fibers exhibiting small curvature of $L/2r \ll 1$ have little effect on the measurement, where L and r are the fiber length and radius of curvature, respectively. While some studies have evaluated the orientation of long glass fibers using the MoE no formal evaluation of the validity of the method is known to have been completed [9, 88-89].

2.3.2 Experimental Techniques

This following section will discuss the variety of methods and techniques available to experimentally observe qualitative fiber orientation. First, one of the most common techniques available to qualitatively observe fiber orientation via optical microscopy will be summarized in

detail. Additional methods such as Scanning Electron Microscopy (SEM), Scanning Acoustic Microscopy (SAM), and multiple-sectioning methods will be subsequently detailed. In all cases, the benefits and limitations inherent to each specific method will be summarized.

2.3.2.1 Optical Microscopy

Optical microscopy is a common method employed to observe experimental fiber orientation within a fiber-reinforced composites due to its numerous benefits. These benefits include the use of cost-effective and readily available equipment, primarily an optical microscope, as well as the ability to automate or semi-automate the sample preparation procedure. An optical microscope can be used to obtain an image of a fiber-matrix surface that shows a 2-dimensional projection of each fiber crossing through the chosen inspection plane, allowing for ready calculation of the components of the orientation tensor as detailed in Section 2.3.1. Because of these benefits, this method has been employed by a number of studies in the literature [79-80, 83, 90-91]. Furthermore, optical microscopy allows for imaging of a sample surface at high magnification of 20X or greater, resulting in extremely high-quality images that allow for straightforward quantitative analysis. However, in order to image an FRP at high magnification using an optical microscope with sufficient resolution to differentiate between fiber and matrix, careful and time-consuming preparation of the sample is required. A standardized preparation procedure specifically for use with fiber-reinforced polymer composites [92] begins with identification of the inspection line known as the sampling region. This sampling region is then cut, marked, and mounted so that it can be prepared for imaging by using polishing and plasma etching. These steps are detailed in brief in the following subsections and in detail by Velez-Garcia et al [92].

2.3.2.1(a) Cutting and Mounting of the Sampling Region

After identification of a sampling region within an FRP, the first step in the preparation procedure is to cut, mark, and mount the selected area. Because this method is frequently used to examine the fiber orientation within injection molded parts which are typically large, it is necessary to cut a small section for analysis. This must be completed by using a slow speed saw that removes the sampling region via abrasion. This is necessary for several reasons. First, this is done primarily to mitigate both fiber breakage and changes in fiber orientation that are possible if aggressive cutting techniques were to be utilized. Secondly, using a slow speed diamond saw (i.e. Model 650 Low Speed Diamond Blade Saw, South Bay Technologies, San Clemente, CA, USA) results in fibers which maintain their circular cross-section due to minimal degradation from cutting, which leads to reduced margins of error during subsequent image processing and quantification of orientation. The sampling region is cut from a larger part as shown in Figure 2.9(a), and a tridimensional marker is affixed to the line of interest for later identification. The resulting sampling region (Figure 2.9(b)) is subsequently hot-mounted in an acrylic resin using a compression press (i.e. Simplimet 2 Mounting Press, Buehler Co, Lake Bluff, IL, USA). The result is a sample “puck” that consists of cured resin with the sampling region encapsulated with the inspection plane perpendicular to the mounting surface as detailed by Velez-Garcia et al. [92]. This allows for subsequent grinding and polishing of the sample.

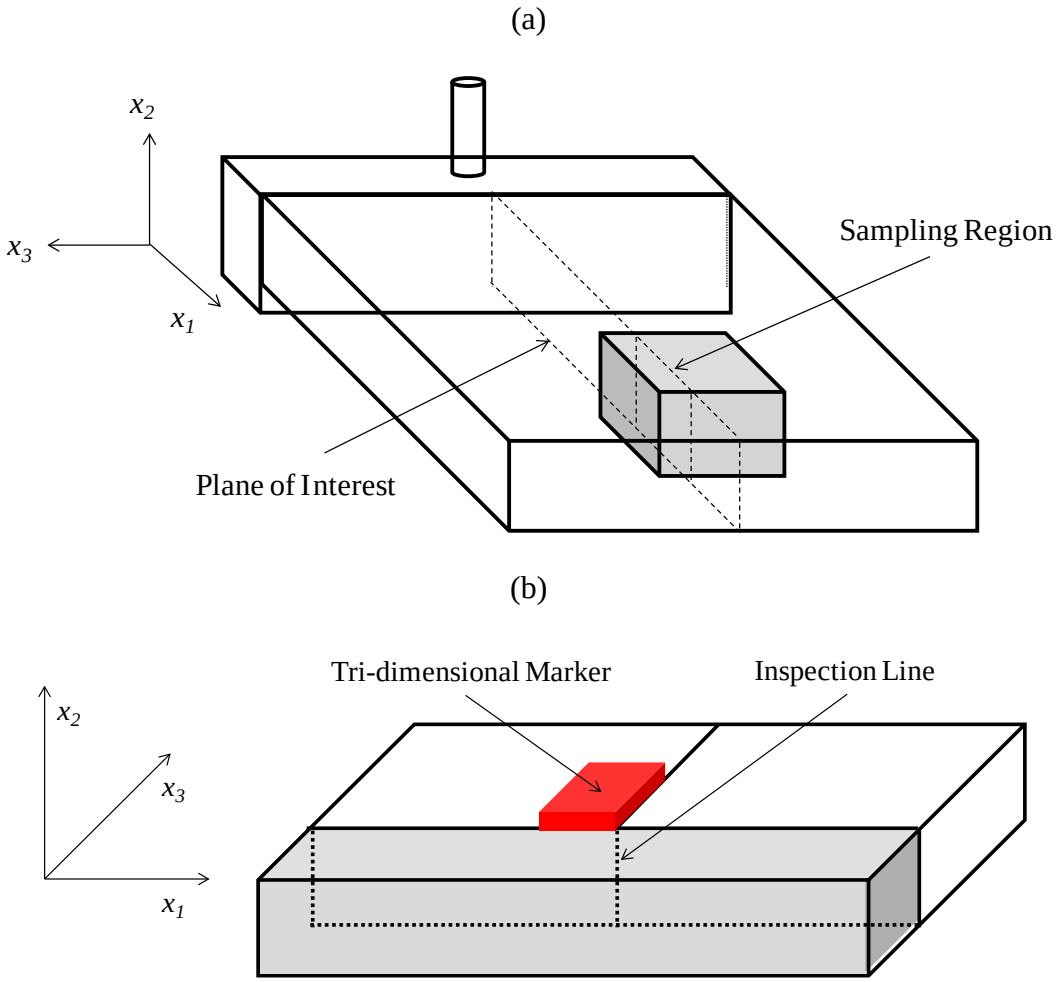

Figure 2.9. Diagram showing (a) the location of an example sampling region in a larger part along a specific plane of interest, and (b) the sampling region once cut from the part showing the location of tridimensional marker that identifies the plane of interest and the inspection line.

2.3.2.1.(b) Grinding and Polishing

To further remove potentially damaged material from the cutting process and to prepare the sampling region as a smooth surface for imaging, grinding is used [92]. Grinding consists of two phases beginning with the use of an automated high-speed wet-belt grinder (BG-32 dual belt grinder; LECO, St. Joseph, MI, USA). The use of the wet-belt grinder with 120- and

subsequently 180-grit abrasive paper results in a quick and efficient removal of the bulk of the excess region adjacent to the sampling plane identified by the grey region in Figure 2.9 (b). The second phase of grinding is completed by hand using a wet-hand roll grinder (HandiMet® 2 Roll Grinder; Buehler Co, Lake Bluff, IL, USA) and a progression of 240-, 320-, 400-, and 600-grit abrasive paper in order to reach the plane of interest as identified by the tridimensional marker attached prior to mounting. However, it is worth noting that uneven grinding of the sampling puck results in images being acquired over a non-desired plane. Therefore, it is critical to ensure that material is removed from the sampling puck in an even fashion during grinding so that the sampling plane remains perpendicular to the preparation surface. This is done by frequently rotating the angle between the sampling puck and the abrasive paper in 90° increments and by frequent visual inspection during the grinding phase [92].

After grinding, the sampling puck is polished to a smooth surface in order to expose the microstructure of the matrix-fiber composite [92]. This is done by using a polishing cloth (Final Finish Cloth; Precision Surface International Inc, Houston, TX. USA) and a progression of alumina slurries of reducing particle size. Careful technique must be applied in order to obtain optimal elliptical footprints of all cut fibers crossing the inspection plane during later imaging using an optical microscope. A semi-automatic single-mount polishing machine (MiniMet 1000 grinder/polisher; Buehler Co, Lake Bluff, IL, USA) allows for precise control of polishing parameters such as down force and rotations per minute. A single sample puck must be polished for a minimum of 120 minutes using a progression of 5-, 1-, and 0.05-micron particle size slurries of alumina (Precision Surface International Inc, Houston, TX. USA). Additional particle sizes of 3- and 0.3-microns can be incorporated into the progression for even more precise polishing control. The result of the polishing procedure is a fiber-matrix interface along the

inspection line with readily identifiable borders between the fibers and matrix with no irregularities observed at the edge of the fiber footprints at 20X magnification [92], as demonstrated in Figure 2.6.

2.3.2.1.(c) Etching

However, plasma etching in an oxygen-rich environment is necessary prior to imaging in order to provide increased contrast enhancement between fibers and the matrix of the inspection plane [92], as well as to allow for unambiguous determination of the components of the orientation tensor [79]. This step of preparation is necessary because the inherent contrast between the fibers and matrix of the polished surface alone is not sufficient for subsequent image analysis and calculation of the components of the orientation tensor. Plasma etching achieves an increase in contrast by uniformly removing a small layer of the polymer matrix and by causing the fibers to protrude from the surface [83, 93], as shown in Figure 2.10.

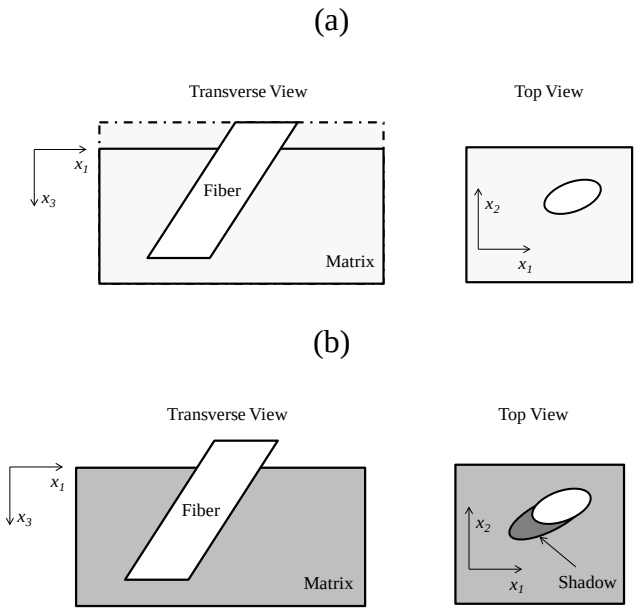

Figure 2.10. Transverse view of a fiber-matrix sample (a) before, and (b) after plasma etching.

This results in a clear distinction between fibers and matrix, as well as ready identification of the "shadow" necessary for unambiguous calculation of the components of the orientation tensor [79]. It has been found that approximately 40 minutes of etching using a radio frequency plasma cleaner (Plasma Prep™ II; SPI Supplies, West Chester, PA, USA) is sufficient for polybutylene terephthalate (PBT) or polypropylene (PP), while a minimum of 60 minutes of etching time is necessary for polyamide 6 [92].

2.3.2.1.(d) Image Acquisition via Optical Microscopy

After sample preparation, an optical microscope can be used to collect high resolution images that can subsequently be used to calculate the components of the orientation tensor for the sampling plane of interest. Care must be taken in order to ensure proper magnification and uniform illumination in order to reduce systematic errors and to obtain images with optimal fiber-matrix contrast. A magnification of 20X provides minimal errors due to pixilation of the image [85, 94], while still maintaining the efficiency of reduced imaging time as compared to higher magnifications [78, 95]. Similarly, auto-focusing algorithms available on optical microscopes with advanced features (i.e. Nikon Eclipse LV100, NIS-Elements Basic Research Software, version 3.10) are essential to obtain sharp contrast across large imaging regions. Finally, the use of a motorized stage and image-stitching software is important for the efficient scanning of large regions of interest and to expedite the image acquisition process [95].

2.3.2.2 Scanning Electron Microscopy

Scanning Electron Microscopy (SEM) is an alternative approach for collecting images of the fiber-matrix inspection plane that comes with numerous advantages. The basic approach of SEM

is similar to that described for optical microscopy in which a sample is polished an imaged at high magnification [13, 96]. Grey-scale images are captured via SEM and can be processed using image analysis and the MoE in order to determine the orientation state of the fibers within the sample. The traditional SEM method, however, allows for a notable improvement in the contrast between the polymer matrix and the reinforcing fibers, allowing for well-defined and easily recognizable interfaces. Furthermore, SEM allows for the determination of unambiguous components of the orientation tensor by applying two thresholds to the image of high and low voltage tension, which allows for the receding "shadow" of the fiber to be recognized, indicating the proper in-plane angle without the necessity of plasma etching the sample. Regnier et al. further improved the SEM method by examining fiber orientation on a 45°-oblique plane with respect to the flow direction, reducing the error and obtaining improved results [97]. However, these benefits can only be obtained by the use of sophisticated and expensive SEM equipment, and without eliminating the majority of the tedious polishing preparation procedures as described for optical microscopy. As such, evaluation of samples via optical microscopy is still preferred by the majority of works in the literature.

2.3.2.3 Scanning Acoustic Microscopy

Scanning Acoustic Microscopy (SAM) is a recent technique used in the analysis of fiber orientation [98]. The SAM method consists of a similar approach as that of optical microscopy and SEM where a chosen inspection plane of an FRP imaged using SAM. The resulting image is converted to binary and the edges are detected in order to calculate the ellipse parameters necessary to quantify the orientation state of the fibers according to the MoE. However, the SAM imaging technique produces "fringes" associated with the elliptical projection of each fiber

that are similar to the "shadows" seen after plasma etching and described previously. These fringes are due to echoes that are reflected by the fibers receding into the matrix. Overlaying these fringes onto the binary image during image analysis allows for unambiguous determination of the components of the orientation tensor [99]. A representation of these ellipses is shown in Figure 2.11, where the "fringes" depict the angle at which the fiber recedes into the polymer matrix and the proper measurement of the in-plane angle, ϕ. The SAM method has been shown to be effective for use with up to 30 wt% glass fiber reinforced injection molded plaques [99].

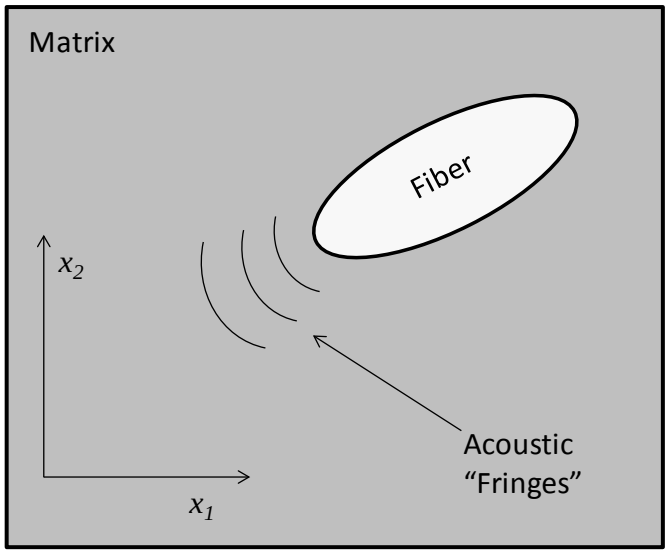

Figure 2.11. Representation of an ellipse in the x_1-x_2 plane showing the "fringes" observed using the SAM method that are used to identify the proper angle of ϕ.

There are numerous advantages of the SAM method for use in evaluating the orientation state of a population of fibers. Unlike the previous methods discussed, the SAM approach is able to obtain the unambiguous components of the orientation tensor in a completely non-destructive fashion and requires no sample preparation such as polishing or plasma etching [99]. Because of this, considerably less time is required to analyze a sample, and it is even possible to analyze

samples with uneven surfaces [100]. The SAM method also has the ability to reveal sub-surface characteristics, including variation in elastic properties [86]. Finally, known test patterns of fiber alignment have been tested using the SAM method and show excellent agreement between theoretical and actual fiber orientation [100]. The calculated error of using SAM is roughly half of the error of SEM, while applying an easier and simpler method [99]

However, there are numerous drawbacks that hinder SAM from widespread use. First, the use of specialized SAM equipment is required in order to obtain the above mentioned benefits [86, 99]. Furthermore, fibers with out-of-plane angles of > 71°, i.e. fibers highly transverse to the inspection plane, do not yield fringes and thus the ambiguity problem remains for these fibers [99]. Thus, the SAM method is unlikely to be a successful method for use with FRPs that exhibit a high extent of transverse-to-flow fiber alignment.

2.3.2.4 Confocal Laser Scanning Microscopy

Confocal Laser Scanning Microscopy (CLSM) is an alternative method available for use to determine the FOD. CLSM allows a semi-transparent part to be optically sectioned in a non-destructive manner in order to quantify the orientation state of the sample [85]. The application of two imaging thresholds allows the CLSM method to obtain two parallel cross sections of the sample by "looking below the surface" [37], similar to the procedure ustilized by SEM. As a result, each individual fiber can be tracked into the inspection plane to a depth of approximately 10 microns in order to eliminate the problem of ambiguity [85]

There are numerous advantages of the CLSM. The primary benefit is the reduction of sample preparation time due to the nondestructive nature of the method [77, 85]. Secondly, the CLSM approach can be automated, similar to the Leeds system for Optical Microscopy, in order

to accurately determine the 3-dimenionsal fiber orientation distribution of a large population of fibers quickly and efficiently [85, 101]. Additionally, the high resolution of images possible via CLSM results in a high level of accuracy of the method, especially when compared to the error inherent to the optical microscopy method alone is utilized without accounting for the "shadows" produced via plasma etching [94]. Finally, the method of CLSM can be used to observe the inherent waviness of fibers, the local radii of fiber curvature, torsion, and to identify local clustering of fibers [84].

However, several major drawbacks accompany the CLSM method. The primary limitation of the CLSM method is due to the requirement to "look below the surface" in order to obtain unambiguous components of the orientation tensor which requires the FRP be limited to a low volume fraction of reinforcing fibers [77]. Additionally, a "semi-transparent" matrix is required for this method, which is not always possible depending on the application(s) of the part(s) being analyzed [85]. Finally, the use of specialized and expensive CLSM equipment could potentially limit this method from more widespread use [77]

2.3.2.5 Computed Tomography

X-ray micro-computed tomography, or Micro-CT, is a novel method that has been used in recent studies to characterize the microstructure variation of an FRP [102]. In the Micro-CT method, x-rays are used to create a cross section of a desired sample. By altering the angle of the incident x-rays, a cross section can be constructed from all possible angles from around a 3-dimenionsal sampling region. The collection of these cross sections can then be combined together using sophisticated computerized algorithms and a 3-dimensional representation of the entire sample can be constructed. Micro-CT has been applied to evaluate the orientation of

strands of fibers in woven fabric and can be extrapolated for use with fiber-reinforced composites samples [102].

The Micro-CT method possesses numerous advantages when used to characterize fiber orientation. First and foremost, Micro-CT is an entirely nondestructive method with no tedious sample preparation required [11, 102]. Secondly, because a complete 3-dimensional model is constructed via the x-ray cross sections, including all fibers within the polymer matrix, the use of Micro-CT allows for the simultaneous calculation of both the FLD and the FOD. This benefit eliminates the need for the use of traditional methods of calculating the FLD [13], and allows for the FLD to be determined from the actual part being characterized. Furthermore, the error associated with the Micro-CT method has shown to be statistically insignificant when compared to the error obtained during traditional image processing via optical microscopy [102]. Finally, Micro-CT has shown to be a promising technique for use with fiber-reinforced foam materials, which would otherwise be destroyed and rendered immeasurable by techniques such as optical microscopy due to the required sample polishing [11].

However, several major drawbacks may potentially hinder the further development of the Micro-CT method in the future. Because the method constructs a complete 3-dimensional model of the entire sample, current studies have only evaluated samples of low fiber weight percents of 5 wt% or less. It is expected that increasing fiber wt% to ranges typically seen in industrial applications of 30-40 wt% would result in a decrease in image resolution and an exponential increase in noise and associated error during quantification of orientation [11]. Additionally, this method requires the use of specialized and expensive Micro-CT equipment. Finally, this method is unable to differentiate between materials with similar atomic densities due to the use of x-ray cross-sectioning. As such, it is necessary for the materials of the polymer matrix and the

reinforcing fibers to be chosen accordingly in order to ensure contrast in the completed 3-dimensional model [11].

2.3.2.6 Magnetic Anisotropy

Magnetic anisotropy is defined as "the dependence of the internal energy on the direction of spontaneous magnetization" by Watanabe et al. [103] and is a novel technique that can be used to characterize the orientation state of ferromagnetic fibers within an FRP. In this method, a specimen is placed on a stationary platform situated between two magnets. The angles of the ferrous fibers within the sample will induce a torque on the sample platform as a result of the magnetic field. This torque can then be directly measured and used to determine the orientation parameters using complex mathematical equations as detailed by Watanabe et al. [103]. The use of magnetic anisotropy has been shown to be a viable technique by the comparison of theoretical and experimental torque measurements for samples with known fiber orientations [104].

However, the disadvantages of the magnetic anisotropy method potentially outweigh the benefits. While the choice of composite matrix is less of a factor, the use of magnetic isotropy requires a FRP to possess identically-sized ferromagnetic particles or fibers as the reinforcing agent [103]. This results in a narrow choice of possible fiber materials, limiting the application of this method. Furthermore, a uniform particle size distribution is difficult if not impossible when production methods such as injection molding are employed, further reducing the applications of magnetic anisotropy. Finally, while tedious sample preparation is not required, the need for specialized equipment and complex mathematics to convert the torque measurements to a description of the 3-dimensional orientation state may potentially prevent magnetic anisotropy from more widespread use in the future [103-104].

2.3.2.7 Multiple-Sectioning Method

Zak et al. [87] proposed an approach based upon optical microscopy but with modifications to produce unbiased orientation data and to resolve the in-plane ambiguity problem. This approach is known as the method of multiple sections. The multiple-sectioning method consists of four primary steps. First, a chosen sampling area of a FRP is prepared via the method described above for optical microscopy by cutting, mounting, grinding, and polishing. It is worth noting that plasma etching is not used. After polishing, the sample is imaged using an optical microscope, and the MoE is used to evaluate orientation data. Second, the identical sampling area is polished for a second time to a depth of one tenth of the average fiber length. Third, the sample is imaged for a second time, and the MoE is once again utilized to calculate orientation data. Finally, the two "section" images are used to identify matching fiber ellipse pairs by using the initial layer to predict the fiber location in the second, lower layer. By doing this, the problem of in-plane ambiguity can be solved without the necessity of expensive and specialized plasma etching equipment. Subsequent polishing and imaging steps can be completed to obtain additional "section" images that can be used to further improve the results and to reduce error.

However, the method of multiple sections does come with several key limitations. First, the required time is almost double that of the traditional optical microscopy method due to the fact that multiple polishing steps are necessary in order to unambiguously determine the components of the orientation tensor. Furthermore, using multiple sections to solve for in-plane ambiguity requires an extremely precise determination of the amount of material removed during the additional polishing step(s). To accurately predict where fibers should be in successive image sections, a magnitude of accuracy of less than 1 micron is required between layers [87]. Finally,

the additional polishing step(s) require a minimum of material to be removed [92], and as such there will be a limitation of this method when applied to fiber populations with low average lengths. For extremely small average fiber lengths, the depth between polishing sections could approach the same order of magnitude of the fibers themselves, thus eliminating ellipse pairs and the ability to solve for the in-plane angle.

2.3.2.8 Miscellaneous Methods and Techniques

A variety of additional sample preparation methods and analysis techniques are found in the literature but are rarely used in practice. While such methods will be briefly mentioned below, the reader is referred to the individual references for additional detail as these methods fall outside the scope of this work. These methods include the use of tracer fibers [105], where a small wt% of opaque tracer fibers are added to a glass fiber reinforced composite with a transparent matrix that matches the index of refraction of glass fibers. The opaque tracer fibers can then be observed in a rapid, automated, and non-destructive fashion and assumed to be representative of the orientation state of the entire fiber population. Furthermore, several authors have extended the work of studying the orientation of fibers within an FRP in order to evaluate the matrix molecular orientation. Hine et al. [37] showed that wide-angle x-ray diffraction (WAXD) can be used to quantify the orientation of the matrix for uni-and biaxial composites as previously demonstrated by Lim et al. [106]. Birefringence has also been used in order to study the matrix molecular orientation as demonstrated by Folkes et al. [107] and has shown that the molecular orientation of the matrix is only affected by very high fiber volume fractions. Additionally, less common analytical techniques have been evaluated and include the use of Clustering Methods as a computational tool to quantify orientation during image processing as

explained in detail by Kawamura et al. [100]. Additionally, a global anisotropy parameter known as the Mean Intercept Length (MIL), which is typically used to evaluate the microstructure of biological and geological structures such as bone, has been shown to be useful for evaluating short fiber composites, as demonstrated by Bernasconi et al. [108]. For additional detail and information on these methods and techniques, the reader is referred to the literature [37, 100, 105, 108-109].

2.4 Fiber Orientation Studies

Studies detailing the experimental characterization of fiber orientation are required in order to evaluate the effectiveness and as the basis for improving the available models. As such, experimental quantification of fiber orientation has been an emphasis in the literature for the last several decades as orientation evolution models are continuously improved. The following section will summarize the major orientation studies to date, beginning first with a description of the typical test geometries used. Then, the experimental results of short glass fiber orientation studies will be discussed. The limited and recent advances in the field to analyze the orientation of long glass fiber composites will subsequently be detailed. Finally, the effect of FOD and FLD on mechanical properties of an FRP will be briefly described.

2.4.1 Geometries

Geometries of injection molded parts selected for prediction of theoretical fiber orientation and for characterization of experimental orientation data must meet several main criteria. First, overly complex geometries lead to overly complex orientations upon filling, making complete parts such as car dashboards not suitable for modeling purposes at this point in time due to

inherent difficulties in the modeling equations. As such, parts with 2-dimensional flow fields are ideal while some of the more simplistic 3-dimensional configurations are possible. Second, a part that features a uniform cross section is ideal for both modeling and experimental characterization because it allows the orientation to be visualized as a function of the through-thickness of the part itself, allowing for a ready comparison between predicted and measured data. This is possible for parts with 2-dimensional velocity profiles and a select subset of 3-dimensional flows. Third and finally, the part geometry must have a constant through-thickness and generally flat profile in order to allow for experimental evaluation of orientation. This is necessary due to most of the experimental methods such as optical microscopy requiring a polishing procedure of a flat cross section in order to experimentally evaluate orientation. Therefore, parts with 2-dimensional geometries or predominantly 2-dimensoinal flow fields are similarly ideal.

The first geometry frequently chosen for study in the literature is the Center-Gated Disc (CGD), as shown in Figure 2.12. The CGD is formed by polymer melt flowing from the extruder down the length of the "sprue." The melt then turns into the flow cavity of the disc, filling radially in all directions simultaneously. This geometry has been an ideal choice for predicting and measuring experimental fiber orientation due to the fact that the CGD is axisymmetric. Therefore, the flow field is 2-dimensional and varies only with disc thickness, z, and radius, r, resulting in slightly simplified orientation prediction equations. Traditionally, experimental characterization of orientation within the CGD has been completed along a line of constant θ. Many studies have evaluated orientation within the well-developed flow regime between approximately 20-80% of the disc radius, while neglecting orientation effects near the flow cavity inlet and near the flow front.

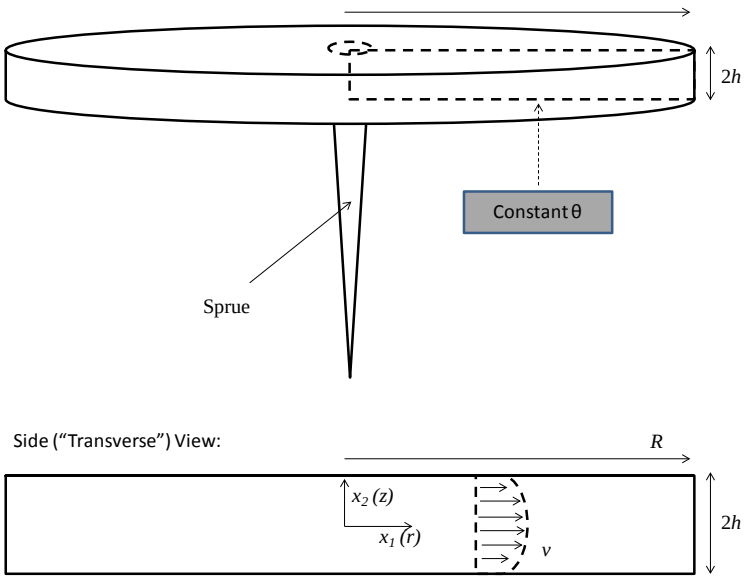

Figure 2.12. Geometry of the Center-Gated Disc (CGD) and respective coordinate system.

The second geometry often used in the literature is the End-Gated Plaque (EGP), as defined in Figure 2.13. The EGP consists of a rectangular mold cavity that is filled by polymer melt entering from the sprue and gate at one end. This geometry is also frequently referred to in the literature as a "film gated strip" [80]. The EGP is a more advanced geometry than the CGD due to the fact that the axisymmetric benefit is lost and a truly 3-dimensional velocity field begins to dominate, particularly near the regions of the plaque close to the side walls (i.e ± w), as well as near the gate region. Traditionally, most of the studies available have investigated the orientation in the region of well-developed flow, while neglecting the effects of the gate region and the front, similar to studies of the CGD. Furthermore, the majority of the studies in the literature have only evaluated orientation along the "center line" (i.e. w = 0). The few studies that have branched away from the center line have done so mostly in a qualitative fashion and have only shown that the orientation near the side walls tends to be more parallel to the flow direction [81, 110].

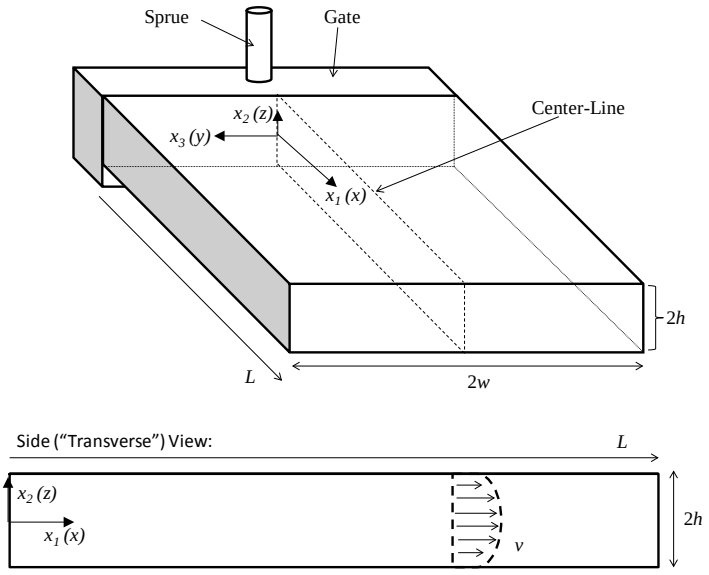

Figure 2.13. Geometry of the End-Gated Plaque (EGP) and respective coordinate system.

2.4.2 Short Glass Fibers

The initial emphasis on the experimental evaluation of fiber orientation revolves around short fibers due to their well-defined definition of rigid orientation evolution (Figure 2.1) as well as being commercially available and utilized for several decades. Many early works detail the orientation state of fibers in a more qualitative fashion, prior to the implementation of the orientation tensor [107, 109, 111-117]. Some of the more detailed early studies include Folgar and Tucker [43], who first predicted in 1984 the evolution of orientation of short, rigid fibers within a simple shear flow using Eq. 2.20. Their experimental results compare favorably with the predicted steady-state distributions at certain locations in the mold. Advani and Tucker [118] expanded this work in 1990 to complete an experimental characterization of orientation study for a molded rectangular plaque similar to the EGP. Experimentally, they found that the orientation of fibers is highly aligned in the flow direction (i.e. the 1-direction) near the top and bottom mold walls. Near the mid-plane of the part, however, the fibers were predominantly aligned transverse

to flow (i.e. in the 3-direction). This multi-layered structure of orientation with noticeably different orientation behaviors in regions of high shear and high extension has since become known as the core-shell structure, as shown in Figure 2.14, where *z/h* is the dimensionless through-thickness of the part. Typically, *z/h* = +1.0 represents the part "top" or sprue side, while *z/h* = -1.0 represents the part "bottom." Advani and Tucker [36, 118] showed that the predictions of orientation via finite element analysis agreed well with experimental results, except for near the frontal flow region. The authors found that the error increased near the fountain flow region due to the models inability to accurately calculate the proper velocity field.

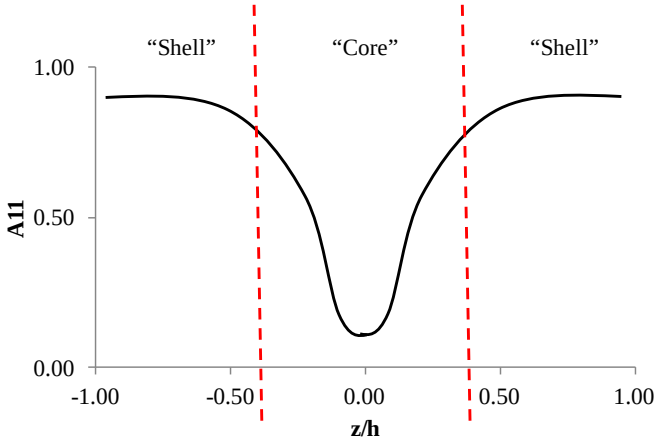

Figure 2.14. Representation of the predicted core-shell structure of the A_{11} component of the orientation tensor.

In 1992, Bay and Tucker [80] extended the experimental studies further so as to evaluate the CGD and EGP test geometries. The authors chose to evaluate the orientation of 43 wt% SGF in a matrix of Nylon 6,6, with average post-processing fiber length and diameter of 210 and 11 microns, respectively. The experimental results show that both geometries exhibit a multi-

layered structure similar to previous studies. It was found that fibers in the core region of the EGP orient randomly in-plane, while the core region fibers of the CGD align predominantly transverse to flow. The associated predictions for this study [70] predict these layers very well. However, the models predicted a core region that was smaller than experimentally observed with a transition to the shell region too close to the mid-plane.

Subsequent studies concentrated efforts to further evaluate and understand the EGP geometry. Gupta and Wang [110] completed and experimental study of SGF within an EGP and confirmed the core-shell results as previously detailed. Additionally, however, Gupta and Wang [110] detailed orientation near the gate region and near the front. They showed that the fibers tend to align along the flow-direction in the gate region due to converging flow effects of the polymer melt passing through the narrow sprue and small gate region. Conversely, the authors found that fibers tend to align transverse to flow near the frontal region due to the diverging flow effect of the fountain region. Chang et al. [119] investigated the multi-layered orientation structure in more detail. The authors were able to find that the structure actually consists of an additional "skin" layer found extremely close to the mold walls. This skin layer forms as a result of thermal effects of the high-temperature polymer melt coming into contact with the lower-temperature mold surface. As such, processing parameters such as fill time could play an important role in final fiber orientation distributions. Additional work by Lee at al. [90] further confirmed that the core-shell structure is seen at multiple percentages of flow along the center line of a film-gated strip. Lee utilized a "dog bone" geometry, which is similar to an EGP, and was able to show that the core-shell structure develops and evolves as the distance away from the gate increases, with the core and shell regions becoming more well-defined at high percentages of mold fill. Furthermore, Lee et al. confirmed that the error between predicted orientatoins and

experimental results increases near the front due to the complexities of the flow field in the fountain flow region, while predictions in the region of well-developed flow agree favorably with experimental data [90].

Several recent studies of SGF experimental orientation have looked at the resulting FOD data in more detail and further attempted to improve the experimental techniques used to obtain orientation data. Hine et al. [83] investigated injection molded EGPs featuring reinforcing transverse ribs. The authors were able to make two important contributions to the field. First, they showed that the FODs within EGP are significantly 3-dimensional, with the FOD developing not only as a function of the flow direction, but also as a function of part width and thickness. This 3-dimensional nature was further compounded by the addition of the reinforcing ribs to the EGP in this specific study. Second, the authors were able to show that the experimental FOD is non-symmetric about the mid-plane of the part. This is of importance due to the fact that historically many studies detailing the prediction of FOD have assumed symmetry and simulated only half of the cavity thickness in an effort to save computational time symmetry. The results of Hine et al. have shown that the accompanying predictions must simulate the complete cavity thickness in order to be able to further improve the models themselves. Velez-Garcia et al. [18, 79] similarly confirmed the asymmetric experimental FOD about the core of an injection molded CGD. Furthermore, Velez-Garcia et al. [79] have applied the MoE via optical microscopy in order to evaluate experimental orientation near the gate region. The results of this study have shown that the inlet fiber orientation is not random in the plane as typically used in many simulation studies reported in the literature. The experimental studies of Hine et al. [83] and Velez-Garcia et al. [79] together have shown that in order to predict accurate orientation data

and improve the predictions of the available models that the complete cavity thickness must be simulated using actual experimental inlet fiber orientations.

2.4.2.1 Effect of Processing Parameters on FLD and FOD

A number of studies in the past several decades have evaluated the effect of processing parameters on the final, post-processing FLD and FOD within injection molded CGDs and EGPs. Bay and Tucker [80] showed that injection time can play an important role in altering the FLD and FOD, while the temperature of the melt and of the mold itself are of little consequence. Chang et al. [119] completed a comprehensive study including the effects of fill time, mold temperature, melt temperature, and ram speed and similarly concluded that mold fill time is the predominant factor in affecting the post-processing FLD and FOD. Furthermore, Chang et al. were able to show that the processing parameters listed above can be manipulated so as to maximize the through-thickness width of the flow-aligned shell region and to minimize the transversely aligned skin and core regions in order to increase the overall strength of the part. Furthermore, Hine et al. [83] showed that the matrix type is of secondary importance to geometry when controlling fiber orientation.

Subsequently, several authors have evaluated the effect of fiber weight percent on both FOD and FLD. Kim et al. [120] showed that predictions and experimental FOD data correlate well at fiber fractions of 30 wt% or less. However, the predictions of orientation at 50 and 70 wt% result in large error due to the increase in inter-fiber interactions. Additionally, Thomason et al. [121] considered the effect of fiber wt% on FLD. The results indicate that increasing initial fiber content is the primary factor in decreasing post-processing weight average fiber length.

One of the more recent studies completed by Sadabadi and Ghasemi [122] features a comprehensive evaluation of numerous processing parameters on the FOD. The authors were able to evaluate the effect of injection flow rate, mold wall temperature, packing pressure, and fiber content on the final, post-processing FOD. It was shown that higher injection flow rates lead to a more well-defined and narrow core region. As a result, this corresponds to a higher tensile modulus in the 1-direction due to an increase in the width of the region of flow-aligned shell region of fibers. Similarly, higher mold temperatures led to a more well-defined and narrow core region and a similar increase in the tensile modulus. However, packing pressure was found to have little to no effect on either FOD or on the resulting tensile modulus. Finally, as the authors increased the fiber wt% from 10 to 30%, the magnitude of the A_{11} component was found to increase. However, as the fiber content was further increased up to 50 wt%, the A_{11} component decreases due to a larger fiber interaction coefficient. The results of this study feature a comparison of experimental and prediction FOD data in two of the cases studied which showed good agreement [122].

2.4.3 Long Glass Fibers

Increasing fiber lengths within FRPs in order to achieve improved mechanical properties has led to a greater emphasis on long fiber research in the recent past. Because less overall work has been devoted to LGF, there is less literature available concerned with LGF. However, typically the same test geometries as utilized for SGF have been evaluated in LGF studies due to the simplified nature of the geometries. Some of the earliest LGF work dates back to Bailey [101], who showed a core-shell structure that develops for LGF as a function of flow and that the FOD can be manipulated by processing parameters such as injection speed, temperature, and holding

pressure. Wu et al. [35] showed that the gate dimensions and the injection rate, while important in controlling the final FOD, were also the most critical factors in avoiding LGF attrition during processing. Wu showed that using a low compression ratio, injection rate, and back pressure are ideal for maintaining maximum final, post-processing fiber length. Finally, Patel et al. [123] showed that evaluating the orientation through the thickness of a part at greater distances from the gate leads to a higher frequency of fibers crossing the inspection plane. The authors attributed this to either an increase in fiber breakage or possibly even to a tendency of fibers to cluster transverse to flow near to the front, similar to what was described by Gupta and Wang [110] for SGF.

One of the first efforts to quantify the orientation state of LGF using the orientation tensor was that of Hine et al. in 1994 [81]. Hine et al. investigated the orientation of fibers in an injection molded EGP along multiple flow locations at 20, 50, and 80% of mold fill along the center-line of the plaque. The results of the study showed that the core region of transversely aligned fibers became quantitatively more pronounced at larger percentages of flow, similar to findings for SGF. Furthermore, Hine et al. also investigated orientation behavior near the side wall of the mold at approximately 50% of mold fill and showed that there is a high alignment of fibers in the flow direction near the side wall and that no clearly defined core-shell structure is present like that which is seen along the centerline.

Only several recent studies have utilized the traditional MoE in order to quantitatively evaluate the orientation of long fibers [9, 88]. A study by Nguyen et al. [9] evaluated the orientation of long fibers for both a center-gated disc (along a line of constant theta), as well as for an end-gated plaque (along the center line of the plaque), while Lafranche et al. [88] concentrated on only the center-line of the end-gated plaque geometry. Nguyen et al.

concentrated their efforts on the orientation analysis of a sampling region approximately 40% from the mold gate for both geometries. Lafranche et al., however, primarily only discussed orientation results at a location roughly 15% of the flow direction from the gate. Both studies utilized the application of the MoE by "segmenting" curved fibers into a series of linear segments, based on a similar method used in the finite element analysis of micromechanical modeling of fibers [57]. However, this method only takes into consideration fibers that are visibly seen to present curvature in the chosen analysis plane and ignores ellipses that appear linear in the selected 2-dimensional image, but could exhibit unknown curvature in the 3-dimensional part. Furthermore, many of the recent investigations of long fibers both in orientation and mechanical properties have focused on fibers with post-processing average lengths within the 1-2 mm range [9, 89]. Therefore, many of the fibers evaluated in these studies were short fibers (i.e. $L < 1$ mm), due to the distribution of fiber lengths, and as such the orientation distributions observed were similar to profiles exhibited by SGF [9-10]. As a result, no formal validation of the MoE for application to long fiber systems is known to have been carried out.

Increased length and flexibility may potentially lead to limitations when attempting to extend the traditional MoE to long fibers. First, an increased fiber length may affect the minimally required sampling size selection, primarily as a result of the exclusion of fibers in the data due to fiber breakage and the increased appearance of partial objects as a result of an application of a too narrow image selection region. Second, because of the increased flexibility, a significant number of fibers may be bent and, hence, a question is raised as to whether the elliptical footprint of said fibers truly represents the average orientation and whether the orientation tensor $\boldsymbol{A}$ can be adapted to long fiber systems.

2.4.4 Mechanics of Composites

Using various micromechanical approaches it is possible to calculate and predict theoretical mechanical properties of an injection molded FRP in order to see the effect of the FLD and FOD [9, 57]. Long glass fibers have the ability to form lace-like mat structures due to their flexibility and ability to exhibit curvature, which greatly increases the melt strength and solid state thermo-mechanical properties [124]. As a result, an increase in the average fiber length and the FLD results in an increase in strength of a part up to a certain level [35]. At identical fiber diameter and loading, a LGF FRP will give a significant improvement in tensile strength, flexural strength, modulus, and impact resistance over a SGF counterpart [121]. It is possible to increase the mechanical properties of a SGF composite by reducing the fiber diameter, but not to the levels possible for LGF [121]. Thomason details the predicted and experimental mechanical data for SGF which shows good agreement [121]. Hassan et al. [14, 19] quantified the effect of increasing fiber length on the mechanical properties and showed that LGF FRPs result in a 17-23% reduction in fracture strain. However, this reduction in fracture strain is accompanied by an improvement in tensile strength and modulus of 16-28% and 18-31%, respectively. Hassan noted that the improved impact properties of LGF FRPs should be attributed to increased fiber diameter, and as such the aspect ratio of the fibers should be considered for prediction of mechanical properties rather than length alone. Finally, however, recent studies have shown that predictions of mechanical properties of LGF FRPs are insufficient when compared to predictions possible for SGF counterparts [9].

Initial fiber pellet length and weight percentage also plays a major role in determining the resulting FOD and FLD and thus the mechanical performance of a part. Patel et al. [123] evaluated the effect of initial fiber pellet length and showed that tensile and flexural properties

increased with fiber length up to 9-mm, followed by a decrease in properties for longer initial lengths. The impact strength similarly increased with increasing fiber length. It was found that the average final, post-processing fiber length of the 9-mm initial pellet lengths was longer than for initial pellets of 3-, 6-, or 12-mm in length [123]. Longer residual, post-processing fiber lengths have been found to improve performance on notched impact tests [125], and as such are ideal for improving mechanical properties. However, drastically increasing the initial fiber pellet length can result in FOD profiles that have amplified heterogeneity and anisotropy, while increasing initial fiber weight percent up to 50 wt% does not greatly affect or improve mechanical properties. The primary results of these studies, therefore, show that care must be taken when designing processes and tailoring processing parameters so as to be able to optimize the final mechanical properties of an injection molded part [88].

2.5 Nomenclature

Variable	Definition
$2h$	EGP or CGD total thickness (total z-direction)
$2w$	EGP width (total y-direction)
A	normalization factor
$\mathbf{A}$	second moment of the orientation vector
a	geometric shape factor
$\mathbf{A_4}$	fourth moment of the orientation vector
A_{ij}	components of the orientation tensor
a_r	fiber aspect ratio
B	shape parameter
$\mathbf{B}$	orientation tensor of a flexible fiber
b	geometric shape factor
C	shape parameter
$\mathbf{C}$	orientation tensor of a flexible fiber
c	geometric shape factor
c_3	parameter to quantify fiber-fiber interactions
C_I	rotary diffusion coefficient
D	fiber diameter
$\mathbf{D}$	rate of strain tensor
D_r	isotropic rotational diffusivity
$\boldsymbol{e_i}$	eigenvectors of $\mathbf{A}$
E_γ	Young's modulus of a fiber
f	geometric shape factor
$f(l)$	probability density function of l
f_1	weighting functions
f_2	weighting functions
f_{eff}	effective fiber stiffness

FLD	Fiber Length Distribution
F_n	ellipse weighting function
FOD	fiber orientation distribution
FRP	fiber-reinforced polymer
h_c	horiztonal center of mass of a fiber
I	identity tensor
k	restorative fiber potential
K_{ijkl}	bending term
L	fiber length
L	EGP flow length (total x-direction)
l_b	half of the fiber length, $L/2$
LGF	long glass fiber
m	minor ellipse axis
M	major ellipse axis
N	number of fibers per unit volume
N	fiber stress
$\boldsymbol{P}$	orientation vector of a rigid fiber
P	isotropic pressure
$p(l)$	probability density function of l
Pe	Peclet number
$\boldsymbol{q}$	additional orientation vector of a flexible fiber
r	end-to-end orientation tensor
R	normalized end-to-end tensor
r	radius of fiber curvature
r	CGD flow direction, i.e. 1-direction
R	CGD total flow direction (r-direction)
SGF	short glass fiber
V	velocity
v_c	vertical center of mass of a fiber

$\mathbf{W}$	vorticity tensor
x	EGP flow direction, i.e. 1-direction
y	EGP neutral or transverse direction, i.e. 3-direction
z	CGD thickness direction, i.e. 2-direction
z	EGP thickness direction, i.e. 2-direction
z/h	dimensionless through-thickness of a part
A	"slip" parameter
Γ	shear rate
η_m	matrix viscosity
η_m	viscosity of the matrix
θ	zenith or out-of-plane fiber angle
θ	CGD neutral or transverse direction, i.e. 3-direction
θ_c	critical out-of-plane angle
K	strain reduction factor
λ	eigenvalues of $\mathbf{A}$
M	location parameter
ξ	particle aspect ratio
Σ	shape parameter
σ	total stress of the system
τ_p	stress of the particles in a system
Φ	fiber volume fraction
ϕ	azimuthal or in-plane fiber angle
Ψ	probability density function of l

2.6 References

1. Truckenmüller, F. and Fritz, H.G. "Injection Molding of Long Fiber-Reinforced Thermoplastics: A Comparison of Extruded and Pultruded Materials with Direct Addition of Roving Strands." *Polymer Engineering & Science* **31** (18) (1991): 1316-1329.
2. Silverman, E.M. "Effect of Glass Fiber Length on the Creep and Impact Resistance of Reinforced Thermoplastics." *Journal of Polymer Composites* **8** (1) (1987): 8-15.
3. Doi, M. and Edwards, S.F. *The Theory of Polymer Dynamics*. New York: Oxford [Oxfordshire] : Clarendon Press ; New York : Oxford University Press, 1988. (1988).
4. Crosby, J.M. "Long-Fiber Molding Materials " *Thermoplastic Composite Materials* (1991): 139-165.
5. Thomasset, J. "Rheological Properties of Long Glass Fiber Filled Polypropylene." *Journal of Non-Newtonian Fluid Mechanics* **125** (1) (2005): 25-34.
6. Switzer III, L.H. and Klingenberg, D.J. "Rheology of Sheared Flexible Fiber Suspensions Via Fiber-Level Simulations." *J. Rheol.* **47** (3) (2003): 759-778.
7. Petrich, M.P. "An Experimental Determination of the Stress-Microstructure Relationship in Semi-Concentrated Fiber Suspensions." *Journal of Non-Newtonian Fluid Mechanics* **95** (2-3) (2000): 101.
8. Eberle, A.P.R. and Baird, D.G. "Obtaining Reliable Transient Rheological Data on Concentrated Short Fiber Suspensions Using a Rotational Rheometer." *J. Rheol.* **53** (5) (2009): 1049-1068.
9. Nguyen, B.N., et al. "Fiber Length and Orientation in Long-Fiber Injection-Molded Thermoplastics – Part I: Modeling of Microstructure and Elastic Properties." *Journal of Composite Materials* **42** (10) (2008): 1003-27.
10. Chin, W.-K., et al. "Effects of Fiber Length and Orientation Distribution on the Elastic Modulus of Short Fiber Reinforced Thermoplastics." *Polymer Composites* **9** (1) (1988): 27-35.
11. Shen, H., et al. "Direct Observation and Measurement of Fiber Architecture in Short Fiber-Polymer Composite Foam through Micro-Ct Imaging." *Composites Science and Technology* **64** (2004): 2113-2120.
12. Pyrz, R. and From, P.S. "Computer Assisted Stereology of Short Fibre Composites. I. Determination of Fibre Length Distribution " *Science and Engineering of Composite Materials (UK)* **8** (3) (1999): 143-158.
13. Averous, L., et al. "Granulometric Characterization of Short Fiberglass in Reinforced Polypropylene. Relation to Processing Conditions and Mechanical Properties." *International Journal of Polymer Analysis and Characterization* **1** (4) (1995): 339-347.
14. Hassan, A., et al. "Tensile, Impact and Fiber Length Properties of Injection-Molded Short and Long Glass Fiber-Reinforced Polyamide 6,6 Composites." *Journal of Reinforced Plastics and Composites* **23** (9) (2004): 969-986.
15. Barkoula, N.M., et al. "Effect of Compounding and Injection Molding on the Mechanical Properties of Flax Fiber Polypropylene Composites." *Journal of Reinforced Plastics and Composites* **29** (9) (2010): 1366-1385.
16. Guo, R., et al. "Rheology of Fiber Filled Polymer Melts: Role of Fiber-Fiber Interactions and Polymer-Fiber Coupling." *Polymer Engineering & Science* **45** (3) (2005): 385-399.
17. Ortman, K. "Prediction of Fiber Orientation in the Injection Molding of Long Fiber Suspensions." *POLYMER COMPOSITES* **33** (8) (2012): 1360-1367.

18. Vélez-García, G. "Experimental Evaluation and Simulations of Fiber Orientation in Injection Molding of Polymers Containing Short Glass Gibers." Macromolecular Science and Engineering, Virginia Polytechnic Institute and State University. Blacksburg, VA (2012).
19. Hassan, A.B., et al. "The Properties of Injection Molded, Short and Long Carbon Fiber Reinforced Polyamide 6,6 Composites." *Annual Technical Conference - Society of Plastics Engineers* **59th (Volume 2)** (2001): 2017-2021.
20. Moriwaki, T. "Mechanical Property Enhancement of Glass Fibre-Reinforced Polyamide Composite Made by Direct Injection Moulding Process." *Composites: Part A* **27A** (1996): 379-384.
21. Sousa, R.A., et al. "Integrated Compounding and Injection Moulding of Short Fibre Reinforced Composites." *Plastics, Rubbers and Composites* **33** (6) (2004): 249-259.
22. Dweib, M.A. and Bradaigh, C.M.O. "Extensional and Shearing Flow of a Glass-Mat-Reinforced Thermoplastics (Gmt) Material as a Non-Newtonian Viscous Fluid." *Composites Science and Technology* **59** (1999): 1399-1410.
23. Dweib, M.A. and Bradaigh, C.M.O. "Compression Molding of Glass Reinforced Thermoplastics: Modeling and Experiments." *Polymer Composites* **21** (5) (2000): 832-845.
24. Gibsona, A.G. and Toll, S. "Mechanics of the Squeeze Flow of Planar Fibre Suspensions." *J. Non-Newtonian Fluid Mech.* **82** (1999): 1-24.
25. Servais, C., et al. "Squeeze Flow of Concentrated Long Fibre Suspensions: Experiments and Model." *J. Non-Newtonian Fluid Mech.* **104** (2002): 165-184.
26. Zainudin, E.S., et al. "Fiber Orientation of Short Fiber Reinforced Injection Molded Thermoplastic Composites: A Review." *Journal of Injection Molding Technology* **6** (1) (2002): 1-10.
27. Baird, D.G. and Collias, D.I. *Polymer Processing : Principles and Design*. Boston [etc.] : Butterworth-Heinemann, cop. 1995 (1995).
28. Bryce, D.M. *Plastic Injection Molding...Manufacturing Process Fundamentals*. Dearborn, MI: Society of Manufacturing Engineers (1996).
29. Bryce, D.M. *Plastic Injection Molding...Mold Design and Construction Fundamentals*. Dearborn, MI: Society of Manufacturing Engineers (1998).
30. Johannaber, F. *Injection Molding Machines: A User's Guide*. Cincinnati: Hanser/Gardner Publications, Inc (1994).
31. Dym, J.B. *Injection Molds and Molding: A Practical Manual*. New York: Van Nostrand Reinhold Company (1987).
32. Olmsted, B.A. and Davis, M.E. *Practical Injection Molding*. New York: Marcel Dekker, Inc (2001).
33. Greener, J. and Wimberger-Friedl, R. *Precision Injection Molding: Process, Materials, and Applicatoins*. Cincinnati: Hanser-Gardner Publications (2006).
34. Tanaka, K., et al. "Injection Molding of Flat Glass Fiber Reinforced Thermoplastics." *International Journal of Modern Physics B: Condensed Matter Physics, Statistical Physics, Applied Physics* **24** (15 & 16 Pt. 1) (2010): 2555-2560.
35. Wu, J.Y., et al. "The Study of Injection Molding of Long Glass Fiber-Reinforced Polyamide." *Annual Technical Conference - Society of Plastics Engineers* **49th** (1991): 2032-2037.
36. Advani, S.G. and Tucker, C.L. "The Use of Tensors to Describe and Predict Fiber Orientation in Short Fiber Composites." *Journal of Rheology* **31** (8) (1987): 751-784.

37. Hine, P.J., et al. "Hydrostaticaiiy Extruded Giass-Fiber-Reinforced Polyoxymethylene. I: The Development of Fiber and Matrix Orientation." *Polymer Composites* **17** (5) (1996): 720-729.
38. Jeffery, G.B. "The Motion of Ellipsoidal Particles Immersed in a Viscous Fluid." *Proc. R. Soc. Lond. A* **102** (1922): 161-179.
39. Cintra, J.S. "Orthotropic Closure Approximations for Flow-Induced Fiber Orientation." *Journal of rheology (New York : 1978)* **39** (6) (1995): 1095.
40. Chung, D.H. and Kwon, T.H. "Invariant-Based Optimal Fitting Closure Approximation for the Numerical Prediction of Flow-Induced Fiber Orientation." *J. Rheol.* **46** (1) (2002): 169-194.
41. Verleye, V.C. and A. Dupret, F. "Numerical Prediction of Fiber Orientation in Complex Composite Injection-Molded Parts." *ASME PUBLICATIONS* **283** (1994): 265.
42. Dupret, F. and Verleye, V. "Modelling the Flow of Fiber Suspensions in Narrow Gaps." *RHEOLOGY SERIES* (8) (1999): 1347-1398.
43. Folgar, F. and Tucker, C.L. "Orientation Behavior of Fibers in Concentrated Suspensions." *Journal of Reinforced Plastics and Composites* **3** (2) (1984): 98-119.
44. Bay, R.S. "Fiber Orientation in Injection Molded Composites: A Comparison of Theory and Experiment." University of Illinois Urbana-Champaign. (1991).
45. Strautins, U. and Latz, A. "Flow-Driven Orientation Dynamics of Semiflexible Fiber Systems." *Rheol Acta* **46** (2007): 1057-1064.
46. Sepehr, M. "Comparison of Rheological Properties of Fiber Suspensions with Model Predictions." *Journal of polymer engineering* **24** (6) (2004): 579.
47. Sepehr, M. "Rheological Properties of Short Fiber Filled Polypropylene in Transient Shear Flow." *Journal of Non-Newtonian Fluid Mechanics* **123** (1) (2004): 19-32.
48. Huynh, H.M. "Improved Fiber Orientation Predictions for Injection-Molded Composites." University of Illinois at Urbana-Champaign. (2001).
49. Eberle, A.P.R., et al. "Using Transient Shear Rheology to Determine Material Parameters in Fiber Suspension Theory." *J. Rheol.* **53** (3) (2009): 685-705.
50. Eberle, A.P.R., et al. "Fiber Orientation Kinetics of a Concentrated Short Glass Fiber Suspension in Startup of Simple Shear Flow." *Journal of Non-Newtonian Fluid Mechanics* **165** (2010): 110-119.
51. Wang, J., et al. "An Objective Model for Slow Orientation Kinetics in Concentrated Fiber Suspensions: Theory and Rheological Evidence." *J. Rheol.* **52** (5) (2008): 1179-1200.
52. Phelps, J.H. and III, C.L.T. "An Anisotropic Rotary Diffusion Model for Fiber Orientation in Short- and Long-Fiber Thermoplastics." *Journal of Non-Newtonian Fluid Mechanics* **156** (2009): 165-176.
53. Fan, X. "A Direct Simulation of Fibre Suspensions." *Journal of Non-Newtonian Fluid Mechanics* **74** (1-3) (1998): 113.
54. Phan-Thien, N. "Folgar-Tucker Constant for a Fibre Suspension in a Newtonian Fluid." *Journal of Non-Newtonian Fluid Mechanics* **103** (2) (2002): 251.
55. Koch, D.L. "A Model for Orientational Diffusion in Fiber Suspensions." *Physics of fluids (1994)* **7** (8) (1995): 2086.
56. Yamakawa, H. *Helical Wormlike Chains in Polymer Solutions*. Springer (Berlin and New York) (1997).
57. Bapanapalli, S. and Nguyen, B.N. "Prediction of Elastic Properties for Curved Fiber Polymer Composites." *Polymer Composites* **29** (5) (2008): 544-550.
58. Ericsson, K.A. "The Two-Way Interaction between Anisotropic Flow and Fiber Orientation in Squeeze Flow." *Journal of rheology (New York : 1978)* **41** (3) (1997): 491.

59. Ortman, K.C., et al. "Transient Shear Flow Behavior of Concentrated Long Glass Fiber Suspensions in a Sliding Plate Rheometer." *Journal of Non-Newtonian Fluid Mechanics* **166** (16) (2011): 884-895.
60. Kevin C. Ortman, J. "Assessing an Orientation Model and Stress Tensor for Semi-Flexible Glass Fibers in Polypropylene Using a Sliding Plate Rheometer: For the Use of Simulating Processes " Virginia Tech. (2011).
61. Dinh, S.M. and Armstrong, R.C. "A Rheological Equation of State for Semiconcentrated Fiber Suspensions." *Journal of Rheology* **28** (3) (1984): 207-227.
62. Batchelor, G.K. "The Stress Generated in a Non-Dilute Suspension of Elongated Particles by Pure Straining Motion." *Journal of fluid mechanics* **46** (04) (1971): 813.
63. Goddard, J.D. "Tensile Behavior of Power-Law Fluids Containing Oriented Slender Fibers." *Journal of rheology (New York : 1978)* **22** (6) (1978): 615.
64. Shaqfeh, E.S.G. "The Hydrodynamic Stress in a Suspension of Rods." *Physics of fluids. A, Fluid dynamics* **2** (1) (1990): 7.
65. Chung, D.H. and Kwon, T.H. "Numerical Studies of Fiber Suspensions in an Axisymmetric Radial Diverging Flow: The Effects of Modeling and Numerical Assumptions." *J. Non-Newtonian Fluid Mech.* **107** (2002): 67-96.
66. Hand, G.L. "A Theory of Anisotropic Fluids." *Journal of fluid mechanics* **13** (01) (1962): 33.
67. Lipscomb, G.G. and Denn, M.M. "The Flow of Fiber Suspensions in Complex Geometries." *Journal of Non-Newtonian Fltid Mechanics* **26** (1988): 297-325.
68. Akbar, S. and Altan, M.C. "On the Solution of Fiber Orientation in Two-Dimensional Homogeneous Flows." *Polymer Engineering & Science* **32** (12) (1992): 810-822.
69. VerWeyst, B.E. and III, C.L.T. "Fiber Suspensions in Complex Geometries: Flow/Orientation Coupling." *The Canadian Journal of Chemical Engineering* **80** (2002): 1093-1106.
70. Bay, R.S. and III, C.L.T. "Fiber Orientation in Simple Injection Moldings. Part I: Theory and Numerical Methods." *Polymer Composites* **13** (4) (1992): 317-331.
71. Velez-Garcla, G.M., et al. "Simulation of Orientation in Injection Molding of High Aspect Ratio Particle Thermoplastic Composites." *The Society of Rheology 80th Annual Meeting* (2008): 42-44.
72. Vincent, M., et al. "Fibre Orientation Calculation in Injection Moulding of Reinforced Thermoplastics." *J. Non-Newtonian Fluid Mech.* **73** (1997): 317-326.
73. Yamamoto, S. and Matsuoka, T. "Dynamic Simulation of Microstructure and Rheology of Fiber Suspensions." *Polymer Engineering & Science* **36** (19) (1996): 2396-2403.
74. Yamamoto, S. and Matsuoka, T. "Dynamic Simulation of Rod-Like and Plate-Like Particle Dispersed Systems." *Computational Materials Science* **14** (1999): 169-176.
75. Yamamoto, S. and Matsuoka, T. "Dynamic Simulation of Fiber Suspensions in Shear Flow." *J. Chem. Phys.* **105** (5) (1995): 2254-2260.
76. Yamamoto, S. and Matsuoka, A. "Dynamic Simulation of Flow-Induced Fiber Fracture." *Polymer Engineering & Science* **35** (12) (1995): 1022-1030.
77. Clarke, A.R., et al. "A Novel Technique for Determining the 3d Spatial Distribution of Glass Fibres in Polymer Composites." *Composites Science and Technology* **55** (1995): 75-91.
78. Bay, R.S. and III, C.L.T. "Stereological Measurement and Error Estimates for Three-Dimensional Fiber Orientation." *Polymer Engineering & Science* **32** (4) (1992): 240-252.

79. Vélez-García, G.M., et al. "Unambiguous Orientation in Short Fiber Composites over Small Sampling Area in a Center-Gated Disk." *Composites Part A: Applied Science and Manufacturing* **43** (1) (2012): 104-113.
80. Bay, R.S. and III, C.L.T. "Fiber Orientation in Simple Injection Moldings. Part Ii: Experimental Results." *Polymer Composites* **13** (4) (1992): 332-341.
81. Hine, P.J., et al. "Measuring the Fiber Orientation and Modelling the Elastic Properties of Injection-Moulded Long-Glass-Fiber-Reinforced Nylon." *Composites Science and Technology* **53** (1994): 125-131.
82. McGrath, J.J. and Wille, J.M. "Determination of 3d Fiber Orientation Distribution in Thermoplastic Injection Molding." *Composites Science and Technology* **53** (1995): 133-143.
83. Hine, P.J. and Duckett, R.A. "Fiber Orientation Structures and Mechanical Properties of Injection Molded Short Glass Fiber Reinforced Ribbed Plates." *Polymer Composites* **25** (3) (2004): 237-254.
84. Clarke, A.R. and Eberhardt, C. "Automated Acquisition and 3d Reconstruction of Glass Fiber Misalignments and Local Curvatures Using Confocal Microscopy." *European Conference on Composite Materials: Science, Technologies and Applications, 8th* **3** (1998): 269-274.
85. Eberhardt, C. and Clarke, A. "Fibre-Orientation Measurements in Short-Glass-Fibre Composites. Part I: Automated, High-Angular-Resolution Measurement by Confocal Microscopy." *Composites Science and Technology* **61** (2001): 1389-1400.
86. Lisy, F., et al. "Application of Scanning Acoustic Microscopy to Polymeric Materials." *Journal of Applied Polymer Science* **52** (1994): 329-352.
87. Zak, G., et al. "Estimation of Three-Dimensional Fibre-Orientation Distribution in Short-Fibre Composites by a Two-Section Method." *Journal of Composite Materials* **35** (2001): 316-339.
88. Lafranche, E., et al. "Injection Moulding of Long Glass Fibre Reinforced Polyamide 6-6: Guidelines to Improve Flexural Properties." *eXPRESS Polymer Letters* **1** (7) (2007): 456-466.
89. Wang, J., et al. "Shear Induced Fiber Orientation, Fiber Breakage and Matrix Molecular Orientation in Long Glass Fiber Reinforced Polypropylene Composites." *Materials Science and Engineering A* **528** (2011): 3169-3176.
90. Lee, K.S., et al. "Measurement and Numerical Simulation of Three-Dimensional Fiber Orientation States in Injection-Molded Short-Fiber-Reinforced Plastics." *Journal of Applied Polymer Science* **88** (2003): 500-509.
91. Zhu, Y.T., et al. "Determination of Non-Symmetric 3-D Fiber-Orientation Distribution and Average Fiber Length in Short-Fiber Composites." *Journal of Composite Materials* **31** (13) (1997): 1287-1301.
92. Vélez-García, G.M., et al. "Sample Preparation and Image Acquisition Using Optical-Reflective Microscopy in the Measurement of Fiber Orientation in Thermoplastic Composites." *J Microscopy-Oxford.* (Accepted (2012)):
93. Mlekusch, B. "Thermoelastic Properties of Short-Fibre-Reinforced Thermoplastics." *Composites Science and Technology* **59** (1999): 911-923.
94. Eberhardt, C., et al. "Fibre-Orientation Measurements in Short-Glass-Fibre Composites—Ii: A Quantitative Error Estimate of the 2d Image Analysis Technique." *Composites Science and Technology* **61** (2001): 1961-1974.
95. Davidson, N.C. "Large-Area, High-Resolution Image Analysis of Composite Materials." *Journal of microscopy (Oxford)* **185** (2) (1997): 233-242.

96. Averous, L., et al. "Evolution of the Three-Dimensionai Orientation Distribution of Glass Fibers in Injected Lsotactic Polypropylene." *Polymer Engineering & Science* **37** (2) (1997): 329-337.
97. Regnier, G., et al. "A Simplified Method to Determine the 3d Orientation of an Injection Molded Fiber-Filled Polymer." *Polymer Engineering and Science* **48** (2008): 2159-2168.
98. Kawamura, M., et al. "Measurement of Three Dimensional Fiber Orientation Distribution in Fiber Reinforced Thermoplastics Using Scanning Acoustic Microscopy." *Seikei Kako* **9** (11) (1997): 913-919.
99. Kawamura, M., et al. "Unambiguous Determination of 3d Fiber Orientation Distribution in Thermoplastic Composites Using Sam Image of Elliptical Mark and Interference Fringe." *Journal of Composite Materials* **39** (4) (2005): 287-299.
100. Kawamura, M., et al. "An Analysis of 3d Fiber Orientation Distribution Using a Clustering Method in Image Processing." *Seikei Kako* **15** (3) (2003): 224-231.
101. Bailey, R. and Rzepka, B. "Fiber Orientation Mechanisms for Injection Molding of Long Fiber Composites." *International Polymer Processing* **6** (1) (1991): 35-41.
102. Desplentere, F., et al. "Micro-Ct Characterization of Variability in 3d Textile Architecture." *Composites Science and Technology* **65** (2005): 1920-1930.
103. Watanabe, Y. "Evaluation of Fiber Orientation in Ferromagnetic Short-Fiber Reinforced Composites by Magnetic Anisotropy." *Journal of Composite Materials* **36** (8) (2002): 915-923.
104. Watanabe, Y. and Fujii, T. "Experimental Study on Magnetic Torque Measurement to Estimate Fiber Orientation in Fe-Fiber-Reinforced Composites." *Jpn. J. Appl. Phys* **42** (2003): 391-393.
105. Ranganathan, S. and Advani, S.G. "Characterization of Orientation Clustering in Short-Fiber Composites." *Journal of Polymer Science: Part B: Polymer Physics,* **28** (1990): 2651-2672.
106. Lim, S., et al. "Wide Angle X-Ray Diffraction Investigations of Orientation of Chopped Fibers in Fabricated Thermoplastic Parts." *Advances in Polymer Technology* **8** (3) (1988): 325-334.
107. Folkes, M.J. and Russell, D.A.M. "Orientation Effects During the Flow of Shortfibre Reinforced Thermoplastics." *Polymer* **21** (1980): 1252-1258.
108. Bernasconi, A., et al. "Local Anisotropy Analysis of Injection Moulded Fibre Reinforced Polymer Composites." *Composites Science and Technology* **68** (2008): 2574-2581.
109. Folkes, M.J. and Potts, H.A. "A Rapid Technique for Observing Fibre Orientation in Carbon Fibre-Reinforced Thermoplastics." *Journal of Materials Science Letter 4* (1985): 105-110.
110. Gupta, M. and Wang, K.K. "Fiber Orientation and Mechanical Properties of Short-Fiber-Reinforced Injection-Molded Composites: Simulated and Experimental Resuits." *Polymer Composites* **14** (5) (1993): 367-382.
111. Malzahn, J.C. and Schultz, J.M. "Transverse Core Fiber Alignment in Short-Fiber Injection-Molding." *Composites Science and Technology* **25** (1986): 187-192.
112. Darlington, M.W. and McGinley, P.L. "Fibre Orientation Distribution in Short Fibre Reinforced Plastics." *Journal of Materials Science Letters* **10** (1975): 906-910.
113. Bright, P.F., et al. "A Study of the Effect of Injection Speed on Fibre Orientation in Simple Mouldings of Short Glass Fibre-Filled Polypropylene." *Journal of Materials Science* **13** (1978): 2497-2506.

114. Kamal, M.R., et al. "Measurement of Fiber and Matrix Orientations in Fiber Reinforced Composites." *Polymer Composites* **7** (5) (1986): 323-329.
115. Vincent, M. and Agassant, J.F. "Experimental Study and Calculations of Short Glass Fiber Orientation in a Center Gated Molded Disc." *Polymer Composites* **7** (2) (1986): 76-83.
116. Darlington, M.W. and Smith, A.C. "Some Features of the Injection Molding of Short Fiber Reinforced Thermoplastics in Center Sprue-Gated Cavities." *Polymer Composites* **8** (1) (1987): 16-21.
117. Fischer, G. and Eyerer, P. "Measuring Spatial Orientation of Short Fiber Reinforced Thermoplastics by Image Analysis." *Polymer Composites* **9** (4) (1988): 297-304.
118. Advani, S.G. and III, C.L.T. "A Numerical Simulation of Short Fiber Orientation in Compression Molding." *Polymer Composites* **11** (3) (1990): 164-173.
119. Chang, S.-H., et al. "Manufacturing Process Optimization of Short Glass Fiber Reinforced Polycarbonate Composites in Injection Molding." *Journal of Reinforced Plastics and Composites* **19** (2000): 301-321.
120. Kim, E.G., et al. "A Study on Fiber Orientation During the Injection Molding of Fiber-Reinforced Polymeric Composites (Comparison between Image Processing Results and Numerical Simulation)." *Journal of Materials Processing Technology* **111** (2001): 225-232.
121. Thomason, J.L. "The Influence of Fibre Length and Concentration on the Properties of Glass Fibre Reinforced Polypropylene: 5. Injection Moulded Long and Short Fibre Pp." *Composites: Part A* **33** (2002): 1641-1652.
122. Sadabadi, H. and Ghasemi, M. "Effects of Some Injection Molding Process Parameters on Fiber Orientation Tensor of Short Glass Fiber Polystyrene Composites (Sgf/Ps)." *Journal of Reinforced Plastics and Composites* **26** (17) (2007): 1729-1741.
123. Patel, V.N., et al. "Studies on Long Glass Fibre Reinforced Polyamide-6 Composites." *International Journal of Plastics Technology* **10** (1) (2006): 614-623.
124. Bush, S.F. "Long Glass Fibre Reinforcement of Thermoplastics. Experimental and Theoretical Results for Injection and Blow Moulding, Sheet and Pipe Extrusion." *International Polymer Processing* **14** (3) (1999): 282-290.
125. Thomason, J.L. "The Influence of Fibre Length, Diameter and Concentration on the Impact Performance of Long Glass-Fibre Reinforced Polyamide 6,6." *Composites: Part A* **40** (2009): 114-124.

Chapter 3 : Application and Evaluation of the Method of Ellipses for Measuring the Orientation of Long, Semi-Flexible Fibers

3.1 Abstract

The Method of Ellipses is a common experimental technique utilized to quantitatively determine the orientation state of a population of rigid fibers within a fiber-polymer composite. In this research, the validity of applying the Method of Ellipses to long, semi-flexible fiber systems in which the majority of fibers are flexible is discussed. The components of the orientation tensor were first determined for a composite formed by a homogenous, simple shear field. The minimum acceptable image analysis width, or bin width, for the selected geometry was found to be approximately 5.5 mm, or 1.4 times the average fiber length. This modified bin width was then used to determine the orientation at multiple percentages of flow within an injection-molded, center-gated disc, and compared to orientation values obtained utilizing the traditional, 0.7-mm bin width. The results show that the traditional, 0.7-mm bin width is sufficient for analysis of the center-gated geometry. This fortuitous result is attributed to the axisymmetric nature of the center-gated geometry, and the highly transverse fiber alignment seen within the samples, especially at moderate to high percentages of flow. In more complex flows it is expected that the conventional bin width will not apply.

Keywords: glass fibers; injection molding; fiber-reinforced composites; fiber orientation;

3.2 Introduction and Background

The term "long fiber" is used here to describe fibers that exhibit bending or curvature during flow and thus during processing such as injection molding. The extent which a fiber will bend in the presence of flow, or its "flexibility," is dependent on both its material properties as well as the strength of the flow field. The effective stiffness of a fiber in a viscous medium, as defined by Switzer and Klingenberg, S^{eff}, shows that increasing the aspect ratio, a_r, results in fibers with an increased flexibility [1]. In Eq. 3.1, E is the Young's Modulus of the fiber, η_m is the viscosity of the matrix, γ is the shear rate, and a_r is equal to L/d, where L and d are the fiber length and diameter, respectively. As Eq. 3.1 shows fiber flexibility is highly dependent on a_r.

$$S^{eff} = \frac{E\pi}{64\eta_m \gamma a_r^4} \qquad 3.1$$

Glass fibers are differentiated into two separate classes based upon their mechanical properties which are highly dependent on fiber length [2]. Glass fibers of less than 1 mm in length are categorized as "short" and thus rigid, while those greater than 1 mm are considered to be "long" and thus flexible [2]. In particular, it has been observed that the modulus of glass fiber thermoplastic composites increases with increasing fiber length up to about 1 mm, and then it plateaus [2]. The tensile strength and impact modulus, on the other hand, continue to rise up with length to about 10 mm. In terms of aspect ratio, short glass fibers typically have values of a_r of approximately 20-50, while long glass fibers have values of approximately 60 or higher. Glass fibers with lengths greater than 1 mm are thought to be somewhat flexible and prone to bending during processing as discussed later in this paper.

The final-processing length and spatial orientation of fibers within fiber reinforced polymer (FRP) composites both play a key role in the mechanical enhancement of the final material. As a

result, these topics of study have become important areas of research for industries such as automotive and aerospace. In general, the addition of reinforcing fibers to a polymer matrix results in improved stiffness, impact toughness, and increased strength as compared to the matrix alone [3-4]. Long fiber FRPs, however, have improved properties relative to their short fiber counterparts, while still maintaining the benefit of being melt processable [5-6]. Furthermore, a FRP composite's properties and microstructure are dependent not only on fiber length but also on fiber orientation.

Previous work to predict the evolution of fiber orientation dates back to Jeffery's model for a rigid, massless fiber in a dilute solution [7]. Jeffery's model has since been modified to include an isotropic rotary diffusion term to account for fiber interactions, and thus be applicable for non-dilute suspensions [8]. Furthermore, the addition of an evolution delay parameter has allowed for a better agreement between the predicted and measured orientation of short fibers [9-10]. Recent work has included the extension of the model to long fiber systems [11].

Short fibers behave as rigid rods in flow, and their orientation is denoted by a vector parallel to the direction of the fiber, $\boldsymbol{p}$, as shown in Figure 3.1. Short fibers are able to rotate and/or translate in the x_1-x_2-x_3 three-dimensional space, but typically do not flex or bend. The x_1 direction is typically synonymous with the flow direction within an injection molded part, while the x_2 direction is typically synonymous with the through-thickness direction of the part. The vector $\boldsymbol{p}$ can be expressed in terms of the azimuthal, or "in-plane" angle, φ, and the zenith, or "out-of-plane" angle, θ, as shown in Eqs. 3.2 - 3.5:

$$\mathbf{p} = p_1\delta_1 + p_2\delta_2 + p_3\delta_3 \qquad 3.2$$

$$p_1 = \sin\theta\cos\phi \tag{3.3}$$

$$p_2 = \sin\theta\sin\phi \tag{3.4}$$

$$p_3 = \cos\theta \tag{3.5}$$

The orientation of a population of fibers, however, is typically described by utilizing an orientation tensor, ***A***. The probability of finding a fiber of a particular orientation is represented by the probability density function, $\psi(\mathbf{p})$. The use of tensors to describe second and fourth moments of orientation has been previously described [12], and is shown in Eqs. 3.6 - 3.7. These orientation tensors have the benefit of always being symmetric and with a trace equal to one. It is worth noting that the fourth order tensor shown in Eq. 3.7 requires a closure approximation, such as the invariant-based optimal fitting (IBOF) approximation [13], in order to express $\mathbf{A_4}$ in terms of **A**.

$$\mathbf{A} = \oint \mathbf{pp}\,\psi(\mathbf{p},t)d\mathbf{p} \tag{3.6}$$

$$\mathbf{A_4} = \oint \mathbf{pppp}\,\psi(\mathbf{p},t)d\mathbf{p} \tag{3.7}$$

The primary reason to obtain experimental values of orientation is for comparison to predictions of fiber orientation calculated via numerical simulation packages. For injection molded parts, the details of the mold design, including channel thickness, as well as processing parameters such as injection speed and thus shear rate, will influence the evolution of fiber orientation as the mold is filled to generate a part. Ultimately, if fiber evolution in flow is well understood based on experimental and predicted values, mold design can be modified and optimized in order to obtain a desired final fiber orientation and thus mechanical strength improvement.

The Method of Ellipses (MoE) is a common experimental technique utilized to extract the information from a composite sample necessary to calculate the components of the orientation tensor [14]. This method has been automated, is capable of analyzing large sampling areas, and is known as the Leeds Analyzer [15]. In the MoE, a composite sample of interest is cut and polished using modified metallographic techniques for composite materials[16-17]. Typically, a region of the x_1-x_2 plane of at least 700 microns in width (hereafter referred to as the "traditional" bin width) is selected for analysis [18]. The parameters that define the orientation state of a fiber (Figure 3.1) required for the calculation of the components of $\boldsymbol{A}$ can then be directly measured from the elliptical footprints of each fiber (Figure 3.2a), including the horizontal and vertical center of mass (h_c and v_c, respectively), as well as φ (Figure 3.2b). The zenith angle, θ, can then be calculated by using the ratio of the minor (m) and major (M) elliptical axes, as shown in Eq. 3.8:

$$\theta = \cos^{-1}\left(\frac{m}{M}\right) \tag{3.8}$$

The error associated with application of this method has previously been studied, and found to be minimal with proper application for rigid fiber composites, as detailed by Bay and Tucker [19].

While the orientation of short glass fibers has been extensively studied [18, 20-23], only several recent studies have utilized the traditional MoE in order to evaluate the orientation of long fibers [24-25]. A study by Nguyen et al. [24] evaluated the orientation of long fibers for both a center-gated disc (along a line of constant theta), as well as for an end-gated plaque (along the center line of the plaque), while Lafranche et al. [25] concentrated on only the center line of the end-gated plaque geometry. Nguyen et al. concentrated their efforts on the orientation analysis of a sampling region approximately 40% from the mold gate for both geometries.

Lafranche et al., however, primarily only discussed orientation results at a location roughly 15% of the flow direction from the gate. Both studies utilized the application of the MoE by "segmenting" curved fibers into a series of linear segments, based on a similar method used in the finite element analysis of micromechanical modeling of fibers [26]. However, this method only takes into consideration fibers that are visibly seen to present curvature in the chosen analysis plane and ignores ellipses that appear linear in the selected 2-dimensional image, but could exhibit unknown curvature in the 3-dimensional part. Furthermore, many of the recent investigations of long fibers both in orientation and mechanical properties have focused on fibers with post-processing average lengths within the 1-2 mm range [24, 27]. Therefore, many of the fibers evaluated in these studies realistically consisted mostly of short fibers (i.e. $L < 1$ mm) due to the Weibull distribution of the fiber length distribution (FLD) [24, 28]. As a result, no formal validation of the MoE for application to long fiber systems is known to have been carried out.

Increased length and flexibility may potentially lead to limitations when attempting to extend the traditional MoE to long fibers. First, an increased fiber length may affect the minimally required sampling size selection, primarily as a result of the exclusion of fibers in the data due to fiber breakage and the increased appearance of partial objects as a result of an application of a too-narrow image selection region. Second, because of the increased flexibility, a significant number of fibers may be bent and, hence, a question is raised as to whether the elliptical footprint of said fibers truly represents the average orientation and whether the orientation tensor $\boldsymbol{A}$ can be adapted to long fiber systems.

The goal of the work reported in this paper is twofold. First, our goal is to determine under what potential conditions the Method of Ellipses (MoE) can be applied to evaluate the orientation of long glass fiber composite systems in which the fibers are only mildly flexible.

Second, we aim to determine if any modifications of the MoE are necessary in the case of long fibers, i.e. $L > 1$ mm. This paper will be concerned with any modifications necessary to extend the method for use with long fiber populations with the majority of post-processing fiber lengths greater than the 1 mm threshold. To answer these questions, we focus on flow within both a center-gated disc as well as within a developed homogeneous shear field.

3.3 Experimental Methods

3.3.1 FRP Composite Geometries

To evaluate the orientation of long fibers within FRPs, a series of 30 wt% glass fiber reinforced polypropylene composites [materials provided by Sabic Innovative Plastics] were created using both a sliding plate rheometer and an injection molding of a center-gated disk. in order to study orientation in 1- and 2-dimensional flow fields. The dimensions of the mold used for injection molding center-gated discs had a thickness ($2h$) of 2.00 mm, inner radius (r_i) of 3.00 mm, and outer radius (R) of 55.0 mm (Figure 3.3). Twenty center-gated discs were molded using roughly an 80% short-shot to mitigate frontal wall effects and packing. The resulting discs had an average final inner and outer radius of 3.03 +/- 0.03 mm and 44.8 +/- 2.02 mm, respectively, thickness of 2.03 +/- 0.02 mm, and an average mass of 14.35 +/- 0.98 g. The homogeneous shear sample had dimensions of 436 mm in length, 60 mm in width, and 1.5 mm in thickness, and was created using a sliding plate rheometer [11]. The number average post-processing fiber length and diameter was determined to be 3.901 mm and 14.5 μm, respectively, using methods described elsewhere [11, 22]. This corresponds to a post-processing average aspect ratio of approximately 270. Additionally, the fiber length distribution appears to be fitted by a Weibull distribution, as frequently reported in the literature [24, 28], and as such the

majority of post-processing fiber lengths in this study are greater than the 1 mm threshold for distinguishing long from short fibers.

3.3.2 Processing Methods

The homogeneous shear samples analyzed in this study were created using the method previously described by Ortman et al. [11]. In this method, 15-mm long pellets of previously extruded 30 wt% reinforced polypropylene strands were randomly aligned in the x_1-x_3 plane of a rectangular mold, with the x_1- and x_3-directions representing the shearing and transverse(but in the shear plane) directions, respectively, and then compression molded at 180 °C for 15 minutes. The resulting sample was 254 mm in length, 60 mm in width, and 1.5 mm in thickness. The sample length was increased to 436 mm after processing at 180 °C in the sliding plate rheometer, using a shear rate of 0.4 s^{-1} and 120 strain units in order to obtain a similar final fiber length distribution as that seen within the injection molded parts.

Pellets containing glass fibers of 13 mm in length, as received, were dried in an oven overnight at 79 °C prior to injection molding. The melt temperature profile of the injection molding machine [Arburg Allrounder, Model 221-55-250] was set to 190/210/210 °C within the feed, compression, and metering zones, respectively, while the mold temperature was held at 79 °C. Using a backpressure of approximately 20 MPa, the center-gated discs as described above were molded using a fill time of 2.00 seconds. Each disc remained in the mold for 20 minutes prior to removal in order to minimize warping. Furthermore, the first ten discs molded were discarded in order to ensure the machine had reached an equilibrium state.

3.3.3 Sample Preparation

Representative discs and sheared samples were selected and prepared for analysis as follows. For the center-gated disc, samples were chosen for inspection at 0, 10, 40, and 90% of fill (Figure 3.3), while a single, central location was selected from the significantly larger homogeneously sheared sample. All of the selected points of interest were cut via abrasion by using a low-speed diamond blade saw in order to minimize sample and fiber degradation. After cutting, each center-gated disc and homogenous shear inspection point measured 5.5 and 13.75 mm in width, respectively. Each sample was subsequently mounted in a thermoplastic resin, and the x_1-x_2 plane (Figure 3.1) was polished using modified metallurgical methods [16-17]. The samples were then plasma etched for approximately 40 minutes in an oxygen-rich environment to increase the contrast between the glass fibers and the polypropylene matrix, as well as to allow for unambiguous determination of the components of the orientation tensor [18]. Finally, the prepared samples were imaged using a reflective optical microscope with a motorized stage and image-stitching software (Nikon Eclipse LV100, NIS-Elements Basic Research Software, version 3.10).

3.3.4 Orientation Measurements

The resulting images were analyzed for fiber orientation measurements with in-house generated Matlab functions using a similar procedure as that applied to short fiber systems and described thoroughly by Vélez-Garcia et al. [18]. First, the image was converted to its binary form, and the edges between each fiber ellipse and the polymer matrix were automatically detected. The parameters that defined the orientation state of each fiber (Figure 3.2b) were subsequently measured for all ellipses in the population. A manual inspection and confirmation of the automatically selected ellipses followed prior to inputting the data into Excel for analysis

and calculation of the components of the orientation tensor as originally defined in Eq. 3.6. It is worth noting that a weighting function as developed by Bay and Tucker [19] was utilized in this calculation in order to correct for fiber orientation angle and visual bias within the chosen inspection plane. Thus, the orientation components for each inspection component were calculated according to Eqs. 3.9 and 3.10:

$$A_{ij} = \frac{\sum_n \left(p_i p_j \right)_n L_n F_n}{\sum_n L_n F_n} \tag{3.9}$$

$$F_n = \begin{cases} \dfrac{1}{L_n \cos\left(\theta_f\right)_n + d_n \sin\left(\theta_f\right)_n} & \theta_f < \theta_c \\ \dfrac{1}{d_n} & \theta_f > \theta_c \end{cases} \tag{3.10}$$

where p is defined in Figure 3.1, L_n is the fiber length, F_n is the weighting function for the n-th fiber in the sample area [20], θ_f is the out-of-plane fiber angle (Figure 3.1) , and θ_c is the critical fiber angle equal to $\cos^{-1}(d/L)$. A minimum of 350 fibers was analyzed at each inspection point across the entire thickness of the part, with the orientation profiles split into 13 vertical "bins" of 2h/13 in height in order to visualize the through-thickness orientation profile of each sample. A total of 5 replicate samples were analyzed and good repeatability of inter-disc measurements was seen.

3.4 Results and Discussion

In order to evaluate the validity of the MoE when used to determine orientation in long fiber FRPs, it is useful to look at the basic qualitative observations when the method is applied to short fibers and then to potential complications with the extension to long fibers. Then, the extension

of the MoE to long fibers within a simplistic steady shear flow will aid in understanding orientation both qualitatively and quantitatively in a one-dimensional velocity field where minimal fiber curvature is seen in the traditional inspection plane. Subsequent extension of this discussion to a more complicated two-dimensional flow will include some criteria for the valid application of the MoE for long fiber systems based on geometry and location, as well as to verify the previous use of the MoE in similar studies in the literature.

While short fibers behave as rigid rods in flow, long, semi-flexible fibers, however, present inherent difficulties in evaluation of their orientation as a result of the potential bending due to increased length and aspect ratio. Long fibers can exhibit significant fiber curvature in the r-θ plane, as shown in Figure 3.4(a). Increased fiber length also leads to an increase in inter-fiber interactions, with the potential for increased clustering (Figure 3.4b). These complications result in questions as to whether the MoE can be applicable to semi-flexible fiber systems in which the majority of fibers are longer than 1 mm. Furthermore, it is possible that the extent of fiber curvature and clustering as shown in Figure 3.4 is at least partially dependent on the flow geometry. As such, defining potential conditions for the valid application of the MoE is subsequently discussed.

A long fiber suspension was deformed in a homogeneous shear field in order to evaluate orientation using the MoE. This geometry was chosen due to the fact that a uniform value of A_{11} is expected both across the thickness of the sample and along the shearing direction, as well as because minimal fiber curvature is experimentally seen in the traditional inspection plane even in highly flow aligned regions. A large segment of the x_1-x_2 plane was polished and imaged (Figure 3.5), where x_1 and x_2 represent the shearing direction and part thickness (also the direction of the shear gradient), respectively. The MoE was used to determine the components

of the orientation tensor beginning with analysis of only the central 1.375 mm of the image (Figure 3.6). The width of the image considered was subsequently increased and reanalyzed in 1.375 mm increments, until ultimately the entire 13.75-mm wide sample was included. As the width of the image analyzed increased from 1.375 to 13.75 mm (Figure 3.7), the A_{11} profile became more uniform across the thickness of the part, and approached a nearly level profile about the line of $A_{11} \approx 0.75$. This value coincides with the orientation value found by Ortman et al. [11] using the same processing parameters and while studying the evolution of orientation at the startup of steady shear flow. A plot of the standard deviation of A_{11} as a function of the width of image analyzed (Figure 3.8) shows that deviation dropped off significantly with increasing width. When only small portions of the image are analyzed increased levels of deviation are attributed to an increase in the quantity of partial ellipses aligned in the shear direction that cross beyond the dimensions of the horizontal image analysis width and are thus discarded from the data, as seen in Figure 3.6. The deviation reaches a minimum and roughly constant value by inclusion of approximately 5.5 mm of the total image, or approximately 1.4 times the average fiber length, due to a decrease in the percentage of highly elongated ellipses that are discarded from the data. This 5.5-mm bin width was determined to be the minimum accepted analysis region for determination of reliable orientation data for long fibers in such a 1-dimensional flow and is hereafter referred to as the "modified" bin width.

The modified bin width determined from the homogenous shear sample was subsequently applied to the 2-dimensional flow geometry, the center-gated disc, and the resulting orientation data were compared to values obtained using the traditional, 700-μm bin width. At all sample locations evaluated (Figure 3.3), minimal difference is seen in the data for the two bin widths for the A_{rr} component of the orientation tensor across the entire sample thickness, as shown in

Figure 3.9(a-d). Furthermore, the majority of all data points have magnitudes less than 0.6, and the profile develops a broad and shallow shape by a high percentage of fill. This is contrary to the well-defined traditional core and shell structure observed in short fiber systems [18, 21-23]. Qualitatively, this difference in profile shape and magnitude can be seen when visually inspecting a selected portion of a center-gated disc at 40% of the flow, as shown in Figure 3.10. The highly transverse alignment of the majority of fibers is readily seen, as is the minimal presence of the shell region of highly flow aligned fibers near the top and bottom walls. As a result, little benefit is obtained when the modified bin width is applied for calculation of the A_{rr} component, especially when considering the additional computational time necessary for larger images.

For long fibers in either a 1- or 2-dimensional flow, negligible fiber curvature was experimentally seen in the traditional inspection plane, as shown in Figure 3.6 and Figure 3.10, respectively. Thus, it can be inferred that the fiber curvature that does occur must be mostly constrained to the x_1-x_3 plane (i.e. the r-θ plane) and, therefore, is unable to be investigated via the traditional view. The highly transverse fiber alignment seen both qualitatively and quantitatively in the selected center-gated geometry (Figure 3.9 and Figure 3.10) implies that the majority of the x_1-x_3 curvature may be about the central axis of the disc for this fiber length distribution, and thus minimal curvature should be present at higher radii of flow. This claim can be further justified by examining calculated values of the effective stiffness parameter (Eq. 3.1). The value of S_{eff} is seen experimentally to increase on average by a factor of approximately 32 from the gate of the center-gated disc to 90% of flow. This is primarily attributed to a drop in shear rate at higher percentages of mold fill, which has been calculated to have experimental average values of approximately 893 and 29 s^{-1} at 0% and 90% of flow, respectively.

Furthermore, fibers that exhibit minimal curvature have previously been found to have little effect on the measurement as long as the condition presented in Eq. 3.11 is satisfied, as described by Bay and Tucker [19], where L is the fiber length and r is the fiber radius of curvature.

$$\frac{L}{2r} \ll 1.0 \tag{3.11}$$

On average Eq. 3.11 will hold true for disc radii greater than approximately 20 mm, or roughly 40% of the flow for this selected center-gated geometry and FLD. Therefore, the MoE may predict incorrect values of orientation when applied to long fibers at extremely low percentages of fill, but may be accurate for determining orientation at moderate fill percentages and above, as has been reported in the literature previously [24]. Furthermore, our findings (Figure 3.10) suggest a minimal presence of clustering in the traditional view for the selected center-gated geometry, except at very high percentages of fill (>95%), which may be attributed to frontal and fountain flow effects.

Additional evidence to suggest that the traditional bin width is acceptable within the center-gated geometry can be seen when analyzing the A_{rz} component of the orientation tensor, as shown in Figure 3.11. Expansion of the image analysis width results in larger differences in measured values of orientation, particularly near the entry region (Figure 3.11a). This effect was attributed to the orientation rapidly changing near the gate and because the bin at this location can only be expanded into increased values of r, rather than symmetrically about the line of inspection. Furthermore, the maximum magnitude of A_{rz} at larger percentages of fill is less than 0.05. As a result, this quantity is more sensitive to adjustments in image analysis width, and the application of the modified width actually smoothes out the orientation profile, possibly obscuring the local values. As such, the application of the traditional bin width both in this and previous studies has been shown to be sufficient for use in the center-gated geometry.

The effect of bin width on the resulting orientation data is expected to become more noticeable when performing analysis on more complicated flow geometries. The center-gated geometry has the benefit of being axisymmetric, and as such results in exhibiting minimal fiber curvature at moderate to high fill percentages due to the highly transverse alignment for the fiber length investigated. The lack of the traditional shell region of flow aligned fibers near the walls allows for sufficient data to be acquired utilizing the traditional bin width due to a minimal presence of partial ellipses that cross beyond the width of the images. However, before stating that the traditional bin width is applicable to all geometries, expansion to geometries that involve 3-dimensional flow should be studied. Extension of this method to long fiber FRPs with geometries that include diverging flow such as the end-gated plaque should be evaluated due to the potential to exhibit sections of highly flow aligned fibers. If parts do exhibit these highly flow aligned regions, as in the case of the homogenous shear sample presented previously (Figure 3.5 through Figure 3.8), the application of the MoE will be limited due to an increase in partial ellipses with application of the traditional bin width. Thus, the extension of this work to the end-gated geometry will be the subject of a future publication.

3.5 Conclusions

In this chapter, we have discussed the application of the traditional Method of Ellipses, as well as the goal of extending its use to the determination of orientation of long, semi-flexible fibers. A homogeneous shear field was used to determine the minimum accepted bin width of 5.5 mm for predominantly shear-aligned fibers with an average fiber length of 3.901 mm.

Orientation was subsequently evaluated at multiple percentages of flow for a center-gated disc using both the traditional and modified bin width, with little difference seen in the two data sets. Fiber curvature was found to be constrained to primarily the r-θ plane for all discs evaluated, and combined with the highly transverse fiber alignment seem, it was concluded to be about the central disc axis on average. Therefore, the traditional MoE was found to be sufficient for application to the center-gated disc with no modifications, particularly for high percentages of flow (i.e. > 40%). Finally, research is currently underway to continue this work to include evaluation of orientation in complex parts that feature 3-dimenionsal flow and, therefore, the potential to exhibit areas of highly flow-aligned fibers in order to define further classifications for the valid application of the MoE to long fiber composites.

3.6 Acknowledgments

The financial support from the National Science Foundation through grant number CMMI-0853537 and the Institute for Critical Technology and Applied Science (ICTAS) is gratefully acknowledged. In addition, the authors would like to thank the department of Material Science and Engineering at Virginia Tech for use of laboratory space and equipment for carrying out the fiber orientation measurements

3.7 References

1. Switzer III, L.H. and Klingenberg, D.J. "Rheology of Sheared Flexible Fiber Suspensions Via Fiber-Level Simulations." *J. Rheol.* **47** (3) (2003): 759-778.
2. Crosby, J.M. "Long-Fiber Molding Materials " *Thermoplastic Composite Materials* (1991): 139-165.
3. Truckenmüller, F. and Fritz, H.G. "Injection Molding of Long Fiber-Reinforced Thermoplastics: A Comparison of Extruded and Pultruded Materials with Direct Addition of Roving Strands." *Polymer Engineering & Science* **31** (18) (1991): 1316-1329.

4. Silverman, E.M. "Effect of Glass Fiber Length on the Creep and Impact Resistance of Reinforced Thermoplastics." *Journal of Polymer Composites* **8** (1) (1987): 8-15.
5. Hassan, A., et al. "Tensile, Impact and Fiber Length Properties of Injection-Molded Short and Long Glass Fiber-Reinforced Polyamide 6,6 Composites." *Journal of Reinforced Plastics and Composites* **23** (9) (2004): 969-986.
6. Thomason, J.L. "The Influence of Fibre Length and Concentration on the Properties of Glass Fibre Reinforced Polypropylene: 5. Injection Moulded Long and Short Fibre Pp." *Composites: Part A* **33** (2002): 1641-1652.
7. Jeffery, G.B. "The Motion of Ellipsoidal Particles Immersed in a Viscous Fluid." *Proc. R. Soc. Lond. A* **102** (1922): 161-179.
8. Folgar, F. and Tucker, C.L. "Orientation Behavior of Fibers in Concentrated Suspensions." *Journal of Reinforced Plastics and Composites* **3** (2) (1984): 98-119.
9. Eberle, A.P.R., et al. "Fiber Orientation Kinetics of a Concentrated Short Glass Fiber Suspension in Startup of Simple Shear Flow." *Journal of Non-Newtonian Fluid Mechanics* **165** (2010): 110-119.
10. Wang, J., et al. "An Objective Model for Slow Orientation Kinetics in Concentrated Fiber Suspensions: Theory and Rheological Evidence." *J. Rheol.* **52** (5) (2008): 1179-1200.
11. Ortman, K.C., et al. "Transient Shear Flow Behavior of Concentrated Long Glass Fiber Suspensions in a Sliding Plate Rheometer." *Journal of Non-Newtonian Fluid Mechanics* **166** (16) (2011): 884-895.
12. Advani, S.G. and Tucker, C.L. "The Use of Tensors to Describe and Predict Fiber Orientation in Short Fiber Composites." *Journal of Rheology* **31** (8) (1987): 751-784.
13. Chung, D.H. and Kwon, T.H. "Invariant-Based Optimal Fitting Closure Approximation for the Numerical Prediction of Flow-Induced Fiber Orientation." *J. Rheol.* **46** (1) (2002): 169-194.
14. Clarke, A.R., et al. "A Novel Technique for Determining the 3d Spatial Distribution of Glass Fibres in Polymer Composites." *Composites Science and Technology* **55** (1995): 75-91.
15. Eberhardt, C. and Clarke, A. "Fibre-Orientation Measurements in Short-Glass-Fibre Composites. Part I: Automated, High-Angular-Resolution Measurement by Confocal Microscopy." *Composites Science and Technology* **61** (2001): 1389-1400.
16. Vélez-García, G. "Experimental Evaluation and Simulations of Fiber Orientation in Injection Molding of Polymers Containing Short Glass Gibers." Macromolecular Science and Engineering, Virginia Polytechnic Institute and State University. Blacksburg, VA (2012).
17. Vélez-García, G.M., et al. "Sample Preparation and Image Acquisition Using Optical-Reflective Microscopy in the Measurement of Fiber Orientation in Thermoplastic Composites." *J Microscopy-Oxford.* (Submitted (2012)):
18. Vélez-García, G.M., et al. "Unambiguous Orientation in Short Fiber Composites over Small Sampling Area in a Center-Gated Disk." *Composites Part A: Applied Science and Manufacturing* **43** (1) (2012): 104-113.
19. Bay, R.S. and III, C.L.T. "Stereological Measurement and Error Estimates for Three-Dimensional Fiber Orientation." *Polymer Engineering & Science* **32** (4) (1992): 240-252.
20. Bay, R.S. and III, C.L.T. "Fiber Orientation in Simple Injection Moldings. Part I: Theory and Numerical Methods." *Polymer Composites* **13** (4) (1992): 317-331.
21. Bay, R.S. and III, C.L.T. "Fiber Orientation in Simple Injection Moldings. Part Ii: Experimental Results." *Polymer Composites* **13** (4) (1992): 332-341.
22. Hine, P.J., et al. "Hydrostaticaiiy Extruded Giass-Fiber-Reinforced Polyoxymethylene. I: The Development of Fiber and Matrix Orientation." *Polymer Composites* **17** (5) (1996): 720-729.

23. Vincent, M., et al. "Description and Modeling of Fiber Orientation in Injection Molding of Fiber Reinforced Thermoplastics." *Polymer* **46** (17) (2005): 6719-6725.
24. Nguyen, B.N., et al. "Fiber Length and Orientation in Long-Fiber Injection-Molded Thermoplastics – Part I: Modeling of Microstructure and Elastic Properties." *Journal of Composite Materials* **42** (10) (2008): 1003-27.
25. Lafranche, E., et al. "Injection Moulding of Long Glass Fibre Reinforced Polyamide 6-6: Guidelines to Improve Flexural Properties." *eXPRESS Polymer Letters* **1** (7) (2007): 456-466.
26. Bapanapalli, S. and Nguyen, B.N. "Prediction of Elastic Properties for Curved Fiber Polymer Composites." *Polymer Composites* **29** (5) (2008): 544-550.
27. Wang, J., et al. "Shear Induced Fiber Orientation, Fiber Breakage and Matrix Molecular Orientation in Long Glass Fiber Reinforced Polypropylene Composites." *Materials Science and Engineering A* **528** (2011): 3169-3176.
28. Chin, W.-K., et al. "Effects of Fiber Length and Orientation Distribution on the Elastic Modulus of Short Fiber Reinforced Thermoplastics." *Polymer Composites* **9** (1) (1988): 27-35.

3.8 Figures

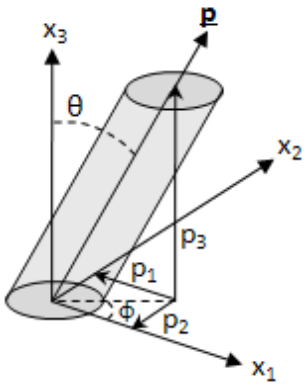

Figure 3.1 Short, rigid fiber denoted by the vector ***p***.

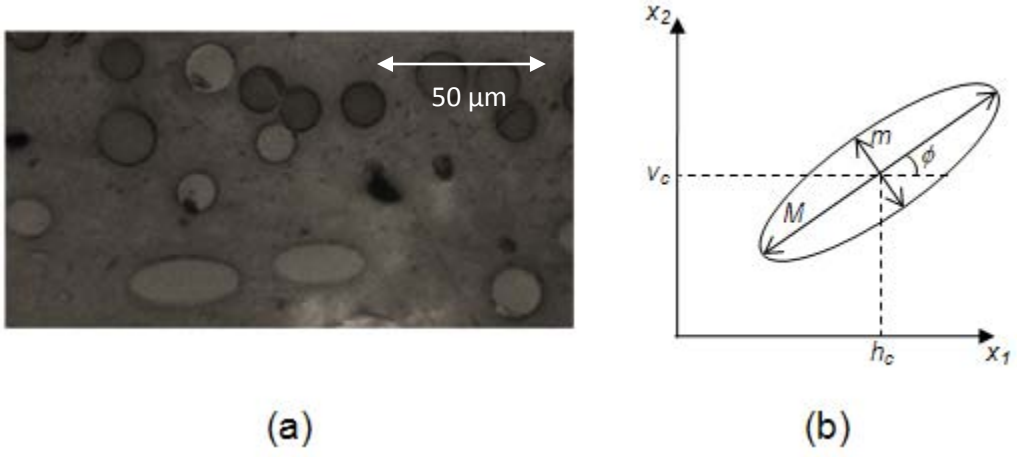

Figure 3.2. Example of (a) a segment of the x_1-x_2 plane, and (b) the required parameters for calculation of the second moment of orientation, as measured for each ellipse.

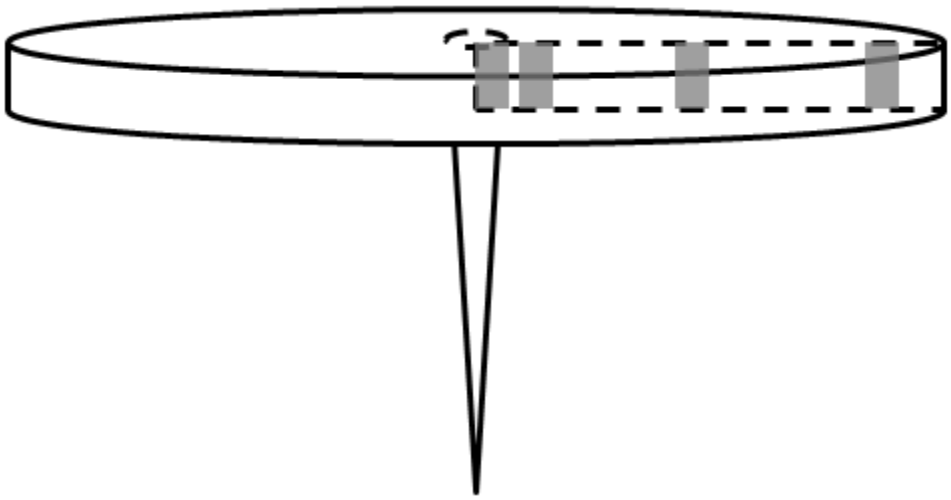

Figure 3.3. Location of sampling regions within the center-gated disc geometry at 0, 10, 40, and 90% of fill.

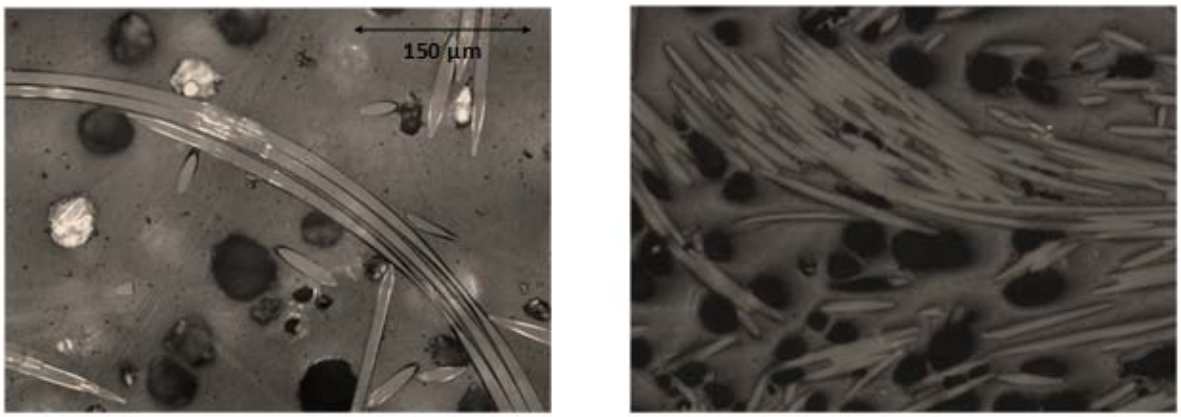

Figure 3.4. Example of (a) curvature and (b) clustering of long fibers, as seen in the r-θ plane of a center-gated disc at high percentages (>95%) of fill. Note: the black, circular regions are voids within the composite.

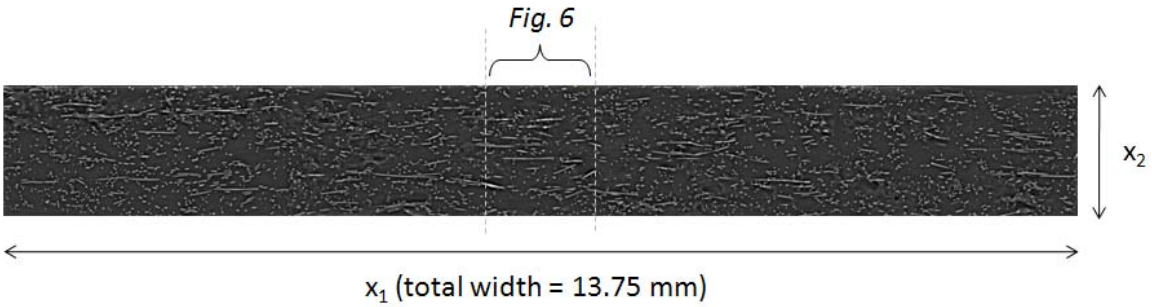

Figure 3.5. Entire image from the homogeneous shear sample.

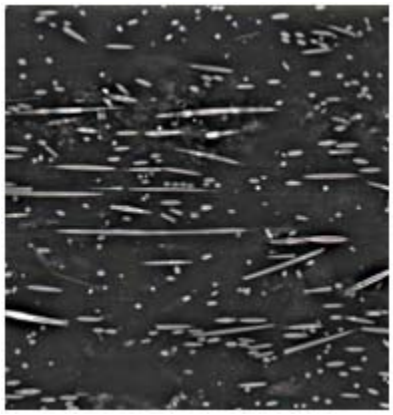

Figure 3.6. Central 1.375-mm wide segment from the homogeneous shear sample.

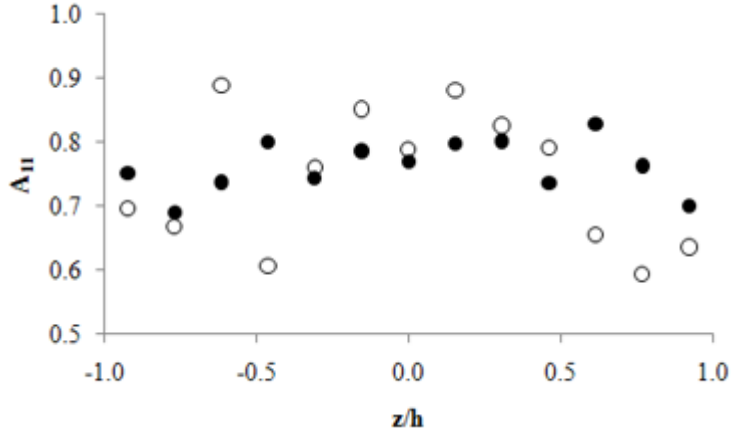

Figure 3.7. Through thickness orientation (A_{11}) when analyzing (o) central 1.375 mm and (•) entire 13.75 mm of the image width.

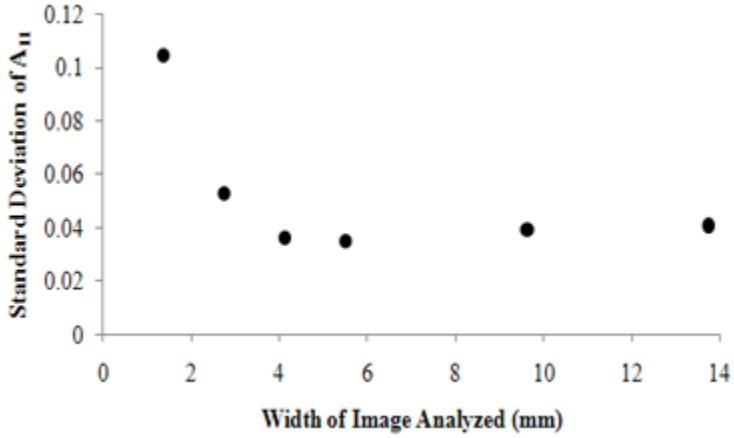

Figure 3.8. Standard deviation as a function of image width analyzed

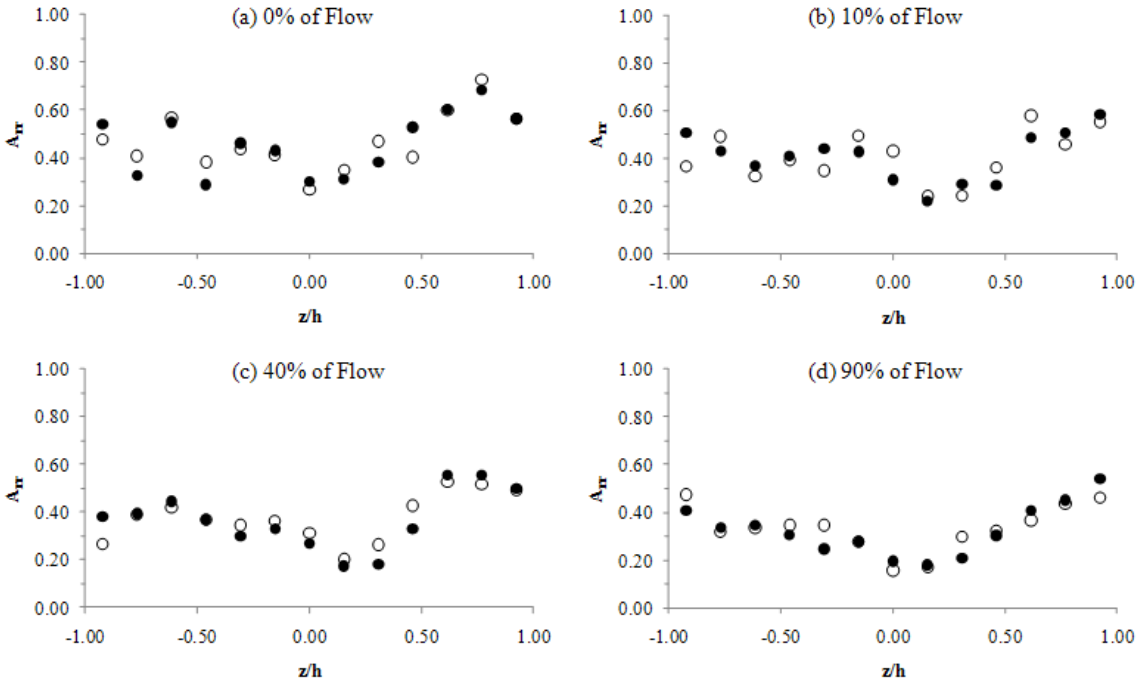

Figure 3.9. A_{rr} component of the orientation tensor for a center-gated disc for application of both (o) 0.7 mm and (•) 5.5 mm bin width, for (a) 0, (b) 10, (c) 40, and (d) 90% of flow.

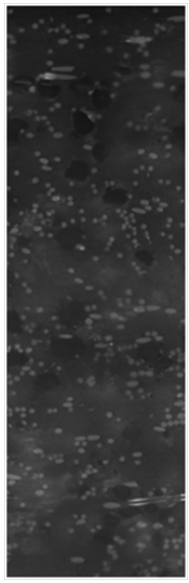

Figure 3.10. Representative image of the *r-z* plane of a long fiber center-gated disc at 40% of flow, showing the lack of a well-defined core-shell structure typically seen for short fiber samples [18, 20-23]. Image dimensions: 0.700 by 2.00 mm. Flow is to the right.

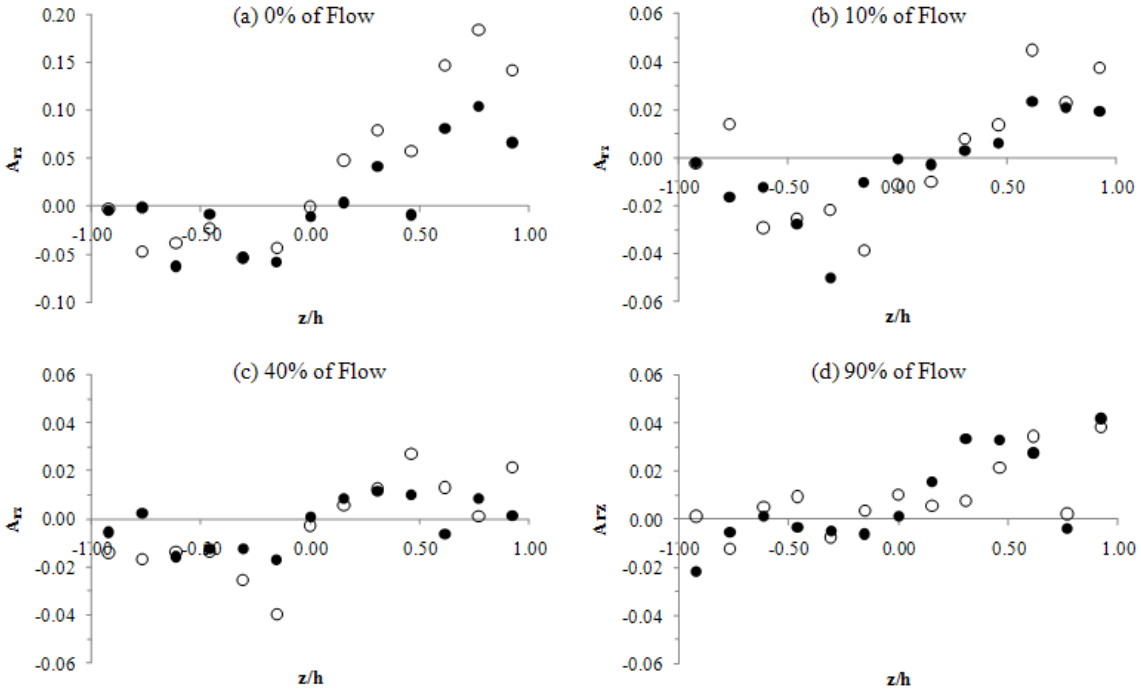

Figure 3.11. A_{rz} component of the orientation tensor for a center-gated disc for application of both (o) 0.7 mm and (•) 5.5 mm bin width, for (a) 0, (b) 10, (c) 40, and (d) 90% of flow.

Chapter 4 : Extension of the Method of Ellipses to Determining the Orientation of Long, Semi-Flexible Fibers Generated in 3-Dimensional Flow

4.1 Abstract

The effect of the increased flexibility and curvature of long glass fibers with an average aspect ratio of 300 on the validity of the Method of Ellipses (MoE), a method for measuring rigid fiber orientation, has been evaluated. The extent of fiber flexibility in various regions within injection molded composites was quantified by the development of a novel method designed to ascertain the average experimental radius of fiber curvature. This effort focused on flow in the axisymmetric center-gated disc, as well as that in the end-gated plaque, a geometry which exhibits a fully 3-dimensional velocity profile and a resulting complex fiber orientation distribution. In both geometries investigated, it was found that in regions of well-developed flow and low shear, fiber curvature is minimal and the traditional MoE is valid. Within the more complex end-gated plaque, however, fiber flexibility was found to be more prevalent near the gate and entry region of the part. Additionally, a method was developed to obtain the experimental components of the second moment of the end-to-end vector, R_{ij}, in order to verify experimental orientation data obtained by utilizing the traditional MoE. Using this method, it was determined that even in regions of fiber curvature the traditional method of ellipses is still applicable provided that the previously ascertained modified image analysis width is utilized. It is worth noting, however, that this is valid for the selected fiber length distribution under investigation, which is expected to closely resemble the distribution of fiber lengths observed in commercially produced parts. As average fiber length and hence flexibility increases then modifications to the Method of Ellipses may become more significant.

Keywords: long glass fibers; fiber orientation; injection molding; fiber curvature;

4.2 Introduction and Background

The desire to obtain stronger and more lightweight materials has led to considerable research in the area of fiber-reinforced polymer composites (FRPs). FRPs possess superior mechanical properties such as increased strength-to-weight ratio, stiffness, and fracture toughness as compared to the neat matrix alone [1-3]. Additionally, it has been shown that an increase in the fiber aspect ratio, a_r, defined as the fiber length divided by the fiber diameter, typically corresponds to an increase in the mechanical properties, especially impact toughness, of a part [4]. Due to the fact that long fiber suspensions remain melt processable and thus capable of utilizing commercial production techniques including injection molding, FRPs are commonly utilized in a number of applications including the automotive industry [5-6]. However, the mechanical properties of a part are strongly dependent on both the length and orientation of the reinforcing fibers within the composite [7-8]. It is, therefore, desirable to study the theoretical and experimental fiber orientation evolution under flow and thus processing in order to be able to optimize injection mold design so as to impart a desirable final fiber orientation distribution.

Research concerning the experimental and predicted orientation evolution of glass fibers in the filling of injection molded parts has been ongoing over the last several decades, and has focused on two classes of composite materials based on average fiber length [9]. Glass fiber with lengths of less than 1.0 mm are commonly said to be “short” and are assumed to behave as rigid rods in flow [9]. Short glass fibers (SGF) have the ability to translate and rotate in 3-dimensional space but not to flex or bend. SGF have been the focus of a number of recent studies, including the application of the Method of Ellipses (MoE) to determine the experimental orientation distribution within injection molded parts [10-12]. Fibers longer than 1.0 mm in length, however, are said to be “long” [9]. Long glass fibers (LGF) have the ability to not only

translate and rotate in 3-dimensional space but also are capable of exhibiting flexibility and curvature during flow and, hence, in processing such as injection molding. It is worth noting that the threshold in length that differentiates short and long glass fibers arises primarily due to the mechanical properties of a composite and the correlation between an increase in fiber aspect ratio, a_r, and a resulting increase in modulus up to a length of approximately 1 mm for glass fibers [9, 13]. Furthermore, this 1-mm threshold in length that differentiates short and long glass fibers may also be discussed in terms of aspect ratio, defined as the fiber length divided by the fiber diameter [9]. For an average fiber diameter of 13.5 microns, which is typical of commercial fibers, this threshold corresponds to an aspect ratio of approximately 75.

Due to the potential to exhibit flexibility, the "Bead-Rod" Model has been proposed by Strautins and Latz [14] to model the orientation evolution of LGF in dilute suspensions. In the Bead-Rod Model, a long fiber is represented by a series of rigid rods connected by beads (Figure 4.1). The individual rod segments have the ability to pivot or "flex" about the beads, allowing for the flexibility of the fiber to be captured via the model. Similar to the rigid rod approach originally developed by Folgar and Tucker [15] and utilized for SGF, a series of orientation tensors can be derived for a flexible fiber (Figure 4.1), as demonstrated in Eq. (4.1) - (4.3) [14]:

$$\mathbf{A} = \int\int \mathbf{pp}\,\psi(\mathbf{p},\mathbf{q},t)\,d\mathbf{p}d\mathbf{q} \tag{4.1}$$

$$\mathbf{B} = \int\int \mathbf{pq}\,\psi(\mathbf{p},\mathbf{q},t)\,d\mathbf{p}d\mathbf{q} \tag{4.2}$$

$$\mathbf{C} = \int\int \mathbf{p}\,\psi(\mathbf{p},\mathbf{q},t)\,d\mathbf{p}d\mathbf{q} \tag{4.3}$$

The Bead-Rod model was subsequently extended to concentrated LGF suspensions by Ortman et al. [16]. The authors suggested a more convenient way to describe the orientation state of a suspension of mildly flexed fibers by use of the end-to-end tensor, **R**, which is formed via the

second moment of the probability distribution of the end-to-end vector, r, as defined in Eq. (4.4) and (4.5):

$$\mathbf{r} = \int\int l_b^2 (\mathbf{p}-\mathbf{q})(\mathbf{p}-\mathbf{q})\psi(\mathbf{p},\mathbf{q},t)\,d\mathbf{p}d\mathbf{q} \tag{4.4}$$

$$\mathbf{R} = \frac{\mathbf{r}}{\mathrm{tr}(\mathbf{r})} = \frac{\mathbf{A}-\mathbf{B}}{\mathbf{1}-\mathrm{tr}(\mathbf{B})} \tag{4.5}$$

It is worth noting that as a long fiber becomes straight (i.e. in the limit of p$\rightarrow$ -q), the expression in Eq. (4.5) is seen to reduce to **R** = **A**. Thus, as the flexibility of a fiber reduces to zero, the rigid rod model for fiber orientation is regained. However, only two studies utilizing the Bead-Rod Model and the end-to-end tensor representation of long glass fiber orientation have been reported in the literature [16-17].

While the experimental orientation of SGF has been studied for several decades by use of the Method of Ellipses (MoE), a recent study by Hofmann et al. [18] focused on the extension and validation of the MoE when applied specifically to long, semi-flexible fibers. This study focused on flow under idealized shear and within the center-gated disc (CGD). The authors found that the MoE was valid within the CGD due to the minimal curvature of long fibers within the geometry by moderate fill percentages due to the predominantly transverse alignment of fibers observed. Meyer et al. [17] subsequently demonstrated the increased validity of the Bead-Rod model within the center-gated geometry for semi-flexible fibers as compared to the performance of the previous rigid-rod models. However, the center-gated disc is still somewhat of an idealized geometry due to its axisymmetric nature. It is, therefore, desirable to extend these efforts to geometries that are more representative of commercial parts in order to assess the validity of the Bead-Rod model for determining orientation in complex flow.

The orientation of long fibers within the end-gated plaque (EGP) is of increasing interest in order to evaluate the validity of the Bead-Rod model in complex flow. This is partially due to the fact that the fully 3-dimensional filling profile exhibited within the EGP is the next step up in complexity from the somewhat-idealized, axisymmetric center-gated disc. The orientation of LGF within the EGP was evaluated in a recent study by Nguyen et al. [8]. While the authors were able to show a good correlation between experimental and predicted orientation results, these studies focused on the experimental orientation along the centerline of the plaque for a fiber suspension with an average length of approximately 1 mm. This average fiber length is not only close to the threshold between short and long fibers, but due to the Weibull distribution of fiber lengths also results in a large portion of fibers with post-processing lengths of less than 1 mm. Additionally, the fact that this study only evaluated fiber orientation along the centerline of the plaque may have been somewhat beneficial due to the fact that the centerline lies along a plane of symmetry and as a result the orientation evolution is somewhat similar to the behavior demonstrated within the more idealized center-gated disc. Evaluation of experimental orientation data within the complex regions of the end-gated plaque was neglected, such as at high percentages of the plaque width near the mold side walls or near the gate and entry region. As such, no formal validation of the Method of Ellipses when applied to long, semi-flexible fibers within the more-complex EGP is known to have been reported.

The goal of this work is twofold. The first goal is to determine if fiber flexibility and curvature is observed in 2- and 3-dimensional injection molded composites with an average fiber length of 3.9 mm, which is a commonly found fiber length for glass systems even in commercial size parts. This will be accomplished by developing an experimental method to quantify the extent of average fiber curvature and to identify regions within injection molded center-gated

discs and end-gated plaques where fiber flexing and bending are prevalent. Second, to identify any modifications that must be made in order to utilize the Method of Ellipses to obtain the components of the orientation tensor for long glass fibers in regions that exhibit considerable fiber flexibility and curvature. A novel experimental method to ascertain the experimental components of the second moment of the end-to-end vector, R_{ij}, will be developed and used to verify experimental orientation data obtained for LGF using the method of ellipses. The modifications to the MoE necessary in order to be applicable to LGF in the end-gated plaque will be discussed, as well as potential limitations of the method.

4.3 Experimental Methods

4.3.1 FRP Composite Geometries

Composite parts consisting of 30 wt% glass fiber-reinforced polypropylene were created using a center and end-gated mold in order to evaluate the orientation of fibers in geometries that exhibit a 2- and fully 3-D velocity profile, respectively. The mold used for the center-gated disc (CGD) (Figure 4.2a) had an inner radius, r_i, of 3.00 mm, and outer radius, R, of 55.0 mm, and a thickness, $2h$, of 2.00 mm. The end-gated plaque (EGP) was composed of both a gate and plaque region (Figure 4.2b). The gate region had a length of 6.33 mm, a height of 6.25 mm, and a width of 80.7 mm, while the plaque region had a length, L, of 77.7 mm, width, $2w$, of 75.0 mm, and height, $2h$, of 1.53 mm, respectively. Both geometries utilized a sprue which had a length of 65.0 mm, and an initial and final radius of 1.45 and 1.75 mm, respectively.

The average post-processing aspect ratio was determined experimentally to be approximately 300, where the aspect ratio is defined as the average fiber length divided by the average fiber diameter. The post-processing number average fiber length and diameter was measured to be

3.901 mm and 13.5 μm, respectively, using the method outlined by Nguyen et al. [8]. It is worth noting that the fiber length distribution (FLD) was ascertained for both geometries under consideration and found to be within statistical agreement. Additionally, the FLD appears to be fitted by a Weibull distribution as previously reported [8, 19].

4.3.2 Processing Methods

A series of center-gated discs and end-gated plaques were formed using an injection molding machine(Arburg Allrounder, Model 221-55-250). This process began by drying long glass fiber polypropylene pellets with an initial length of 13 mm (materials provided by SABIC Innovative Plastics) in an oven at 79 °C overnight prior to processing. The temperature profile of the injection molding machine was set to 190, 210, and 210 °C in the feed, compression, and metering zones, respectively. The mold temperature was held constant at 79 °C. Samples were generated in the center-gated and end-gated geometries described above using a 90% short shot of the mold cavity in order to mitigate packing effects and with a fill time of 2.00 seconds to mitigate nonisothermal effects. The resulting discs and plaques had an average radius of 49.3 ± 2.02 mm and average length of 68.65 ± 1.87 mm, respectively. Each part was left in the closed mold for a period of twenty minutes in order to reduce warparge. Additionally, the first 10 center-gated discs and end-gated plaques were discarded in order to ensure that the machine was operating in an equilibrium state prior to selection of parts for the analysis of fiber orientation.

4.3.3 Sample Preparation and Orientation Measurements

For both geometries being evaluated, a set of five representative parts was selected and prepared for analysis as described below. The chosen inspection areas for both geometries were

at lines of interest of 0, 10, 40, and 90% of mold fill. For the center-gated disc, these samples were prepared for inspection along a line of constant θ, while samples were prepared for the end-gated plaque along lines of interest at 0, 50, and 90% of the half-width of the plaque (Figure 4.2b). For both geometries, two types of samples were prepared at each inspection location. The first type of sample consisted of the traditional inspection plane utilized with the traditional MoE, corresponding to the *r*-*z* and *x*-*z* planes in the CGD and EGP, respectively, and will hereafter be referred to as the "traditional" samples. The second type of sample consisted of the "top" of the part, and corresponded to the *r*-θ and *x*-*y* plane in the CGD and EGP, respectively, and will hereafter be referred to as the "top view" samples. All traditional and top view samples were prepared according to the procedure described in detail by Velez-Garcia et al. [20] and imaged at 20X magnification using an optical microscope equipped with a motorized stage and image-stitching software (Nikon Eclipse LV100, NIS-Elements Basic Research Software, v.3.10). The experimental components of the orientation tensor (**A**) were subsequently computed from the resulting images of the traditional samples using in-house generated Matlab routines using the traditional MoE as previously described by a number of authors [11-12, 18, 21]. Additionally, the experimental components of the end-to-end tensor (**R**) were calculated via analysis of the top view samples according to the novel methods described in detail in the following section.

4.4 Results and Discussion

Prior to discussing the necessary techniques of computing the experimental orientation of long fibers within the end-gated plaque, it is first beneficial to reexamine the center-gated disc in order to verify prior experimental orientation results obtained using the traditional Method of

Ellipses [18]. This section will detail the development of novel methods to experimentally quantify the extent of fiber curvature as well as to aid in assessing the validity of prior applications of the traditional MoE. The center-gated geometry will be first examined due to its more idealized nature and utilized as a proof of concept prior to extension of these novel methods to the more complex end-gated plaque.

4.4.1 Center-Gated Disc

In order to assist in verifying prior experimental results, a novel method of ascertaining and quantifying the extent of experimental fiber curvature within the CGD was developed. It is desirable to be able to quantify the extent of fiber curvature due to previous efforts by Bay and Tucker [22] that have shown that the curvature of single fiber will have a minimal effect on the measurement of orientation if the relationship in Eq. (4.6) is valid:

$$\frac{L}{2\rho} \ll 1 \tag{4.6}$$

where L is the fiber length, and ρ is the radius of fiber curvature. It is worth noting that as the radius of fiber curvature goes to infinity, and thus as the fiber becomes rigid, the left-hand side of the expression in Eq. (4.6) reduces to zero. Based on the predominantly planar alignment of fibers within channel flow, it is expected that the majority of all fiber curvature will similarly be constrained in a planar fashion. Therefore, within the center-gated disc, it is expected that fiber curvature will be constrained to the r-θ plane, rather than the r-z inspection plane corresponding to the traditional MoE. Therefore, a novel method has been developed in which the r-θ plane of the CGD, which hereafter is referred to as the "top view," is polished and imaged using similar techniques as those defined previously by Velez-Garcia et al. [20]. An example top view image is presented in Figure 4.3, and shows not only the predominantly planar alignment of fibers but

also demonstrates that the extent of curvature may be measured by assuming that a flexed fiber lies along the circumference of an imaginary circle. The fiber length and radius of fiber curvature, ρ, can, therefore, be measured for each individual fiber. This technique may be extended to a population of fibers at any given location in order to ascertain the average radius of curvature and subsequently to calculate the average magnitude of the expression previously defined in Eq. (4.6).

The newly developed Top View Curvature method was applied to the center-gated disc at multiple percentages of flow and through-thickness of the part. At each inspection location (10, 40, and 90% of R), a minimum of 150 fibers was analyzed in the r-θ plane using semi-automated Matlab routines and the fiber length and curvature were recorded. The resulting average values of Eq. (4.6) were computed at each location at multiple locations through the thickness of the disc and are summarized in Table 4.1. The data shows that along the mid-plane of the part (z/h = 0.0), there is minimal fiber curvature on average, likely due to the minimal velocity gradient in this region. Near the mold side wall, however, as $z/h \rightarrow \pm 1.0$, curvature is seen to increase, particularly near the gate and entry region of the part, likely attributed to increased shear and extensional deformation, but also possibly due to compression as a result of the entry geometry and the stagnation point at the end of the sprue and gate regions. However, the results suggest that on average, the expression in Eq. (4.6) holds true throughout the majority of the center-gated geometry and confirms previous assumptions of only mildly flexed fibers within the channel flow of the center-gated disc.

Modification of the Top View Curvature (TVC) method has led to the development of the Top View Method of Ellipses (TVMoE) in order to obtain experimental orientation data directly from the r-θ plane. This was done in an effort to directly compare top view orientation data to

results obtained via the traditional inspection plane and MoE. It is possible to obtain orientation data from the r-θ plane for several reasons. First, the center-gated disc is a geometry which exhibits a through-thickness, *2h*, which is less than the average fiber length, *L*. Second, the inlet geometry results in fibers aligned along the axis of the sprue initially and primarily along the streamlines of the filling profile of the part, which leads to a primarily planar orientation state initially within the disc cavity. As a result, fiber curvature has been found experimentally to be predominantly confined to the r-θ plane and minimal on average throughout the geometry. Thus, a bead-rod configuration can be used to describe mildly flexed fibers exhibiting constant curvature by segmenting the fiber into a series of rigid rods, as shown in Figure 4.4. The resulting end-to-end vector, **r**, may then be used to construct the end-to-end orientation tensor, **R.**

It is, therefore, possible to utilize the TVMoE in order to determine the experimental components of the end-to-end tensor (R_{ij}) for direct comparison to the orientation components obtained using the traditional MoE (A_{ij}). This has been completed at multiple percentages of flow and through-thickness positions and can be compared directly to previous orientation data obtained using the traditional MoE through the thickness of the disc, as shown in Figure 4.5. The results show good agreement in orientation data computed using the two methods at all locations of flow and through-thickness positions evaluated. These findings further verify the validity of the traditional MoE within the center-gated geometry for long glass fibers but also confirm the previous conclusion of the presence of minimal fiber curvature within the CGD as discussed in a prior study by Hofmann et al. [18], which concluded that the primary fiber alignment is about the circumference of the disc and as a result minimal curvature was experimentally observed. These findings are possibly due to the specific fiber length distribution under investigation here, which represents a typical FLD observed in commercially produced

parts. While the average fiber length has been observed to be approximately 3.9 mm in this study, there still remains a large percentage of fibers that exhibit lengths of less than 1 mm, the threshold between short and long fibers. Thus, while fiber length and the potential to exhibit flexibility must be accounted for in the simulation of orientation evolution, experimentally there is not much effect on the measurement due to curvature only being possible for a small ratio of the total fiber population in the selected regions evaluated. Finally, these findings show a proof of concept of both the TVC and TVMoE methods within the CGD and leads to the expectation that these methods may be extended in order to verify the validity of the traditional MoE within the more complicated end-gated plaque.

4.4.2 End-Gated Plaque

The end-gated plaque was selected for subsequent analysis using the methods developed in the previous section in order to validate the experimental techniques utilized to obtain orientation data in a complex geometry that exhibits a fully 3-dimensional filling profile. Similar to the CGD, the EGP is primarily a channel flow geometry with a gap thickness that is less than the average fiber length and an initial entry fiber orientation distribution which is primarily planar and that may result in a predominantly planar alignment of fibers with minimal vertical orientation through the thickness of the part. However, the end-gated geometry exhibits a more complex filling profile, as shown in Figure 4.6. Due to the location of the gate within the EGP, the mold cavity fills with an irregular advancing front at extremely low mold fill percentages (Figure 4.6a). This is likely due to the larger cross-sectional area of the gate region which results in a higher transverse velocity within the gate region than the initial entry velocity within the plaque cavity itself. Thus, a significantly varying initial fiber orientation distribution is expected

throughout the width of the geometry. This is contrary to the filling profile of the CGD, which fills uniformly in all directions simultaneously due to the location of the gate and the axisymmetric nature of the geometry.

The TVC method developed in the previous section has been extended to the EGP in order to ascertain the effect of the more complex geometry on the experimental extent of fiber curvature at various locations within the plaque. The results along lines of 0, 50, and 90% of plaque width at multiple percentages of the filling direction are summarized in Table 4.2 through Table 4.4 for a constant through-thickness values of z/h = 0.00, 0.50, and 0.90 and compare favorably with the data discussed previously for the center-gated disc. Near the mid-plane of the part at z/h = 0.00 (Table 4.2) and z/h = 0.50 (Table 4.3), minimal curvature was observed within the plaque cavity, with the exception of near the advancing front at 90% of flow. Increased fiber curvature in this region may be attributed to the fountain flow effects and formation of a skin region along the mold surface during the forming of the part. Additionally, the extent of fiber curvature is increased in the shell region near the mold side walls ($y/w \rightarrow \pm 1.0$) in the region of high shear rate (Table 4.4). This is particularly observed near the gate and entry region of the plaque, in regions of flow that exhibit a high shear and extensional rates due to the previously discussed complex initial filling profile of the EGP (i.e. at 10% of flow or less). It is worth noting, however, that within the gate region, the primary velocity component is in the transverse or y-direction (Figure 4.2b). As the suspension approaches the stagnation point at the end of the gate region (i.e. as $y/W \rightarrow \pm 1.0$), the velocity component rapidly transitions to the x -direction as the fluid enters the mold cavity. This results in a complex velocity profile with components in the x-, y-, and z-directions and may result in a non-planar fiber orientation state within the gate region. As a result, the current TVC method is currently unable to quantitatively assess the extent of

fiber curvature within this complex region due to the likelihood that the assumption of predominantly planar flow will not be valid in the gate.

The Top View Curvature results within the End-Gated Plaque may be utilized in order to provide insight into the potential limitations of the MoE. The findings discussed above appear to indicate minimal fiber curvature is observed within the selected system, and that on average Eq. (4.6) holds true throughout the majority of the geometry at the locations evaluated. It is possible, therefore, to relate these experimental curvature results to values of the effective flexibility parameter, originally defined by Switzer and Klingenberg [23]:

$$f^{eff} = \frac{64\eta_m \dot{\gamma} a_r^{\ 4}}{E\pi} \tag{4.7}$$

where η_m is the matrix viscosity, $\dot{\gamma}$ is the shear rate, E is the modulus of the fiber, and a_r is the fiber aspect ratio. As f^{eff} is seen to increase with increasing shear rate, it is expected that fiber flexibility will similarly increase in not only complex flow regimes such as the within the advancing front, but in general flow regions in which the second invariant of the rate of deformation tensor has a larger magnitude than in the selected regions of investigation within this study. The current top view curvature results provide evidence to verify this statement, with the highest experimental fiber flexibility being observed close to the gate (i.e. at 10% of flow) and the mold walls (i.e. at z/h = 0.90) (Table 4.4). At this location in the geometry, the value of f^{eff} is calculated to be approximately 6.00 x 10^5 for this particular system. However, regions of flow of less than 10% and at through-thickness values greater than 0.90 z/h will exhibit an increase in the second invariant of the rate of deformation tensor. Therefore, these results suggest a potential "upper bound" on the effective flexibility parameter for the given system, in that locations within the geometry which exhibit a f^{eff} of greater than 6.00 x 10^5 may lead to a breakdown of the traditional MoE due to increased fiber flexibility.

While the above results initially suggest that the traditional MoE may be valid above 10% of flow within the EGP, similar to previous efforts that focused on the CGD, an additional consideration must be made during analysis of fiber orientation in the regions of high shear near the mold side walls. In regions of high plaque width near the mold side wall (Figure 4.2b), there is significantly increased shear throughout the thickness of the geometry due to the proximity to the mold side wall. This results in an increase in highly flow-aligned fibers near the side wall. Thus, application of the traditional MoE and the traditional image analysis region of 700 μm results in an increase in partial ellipses within the image, as demonstrated in Figure 4.7. This leads to an error in computation of the components of the orientation tensor due to the necessity of discarding the partial ellipses corresponding to fibers which cross beyond the edges of the image [22]. Therefore, it is necessary to utilize a modified image analysis width in these regions that exhibit high shear rates. The derivation of a modified image analysis width of 5.500 mm has been previously described in detail by Hofmann et al. [18] and previously been shown to be valid within the center-gated disc when fiber curvature is negligible. This allows for the computation of reliable orientation data for long, semi-flexible glass fibers within the EGP, including in the regions of highly shear-aligned fibers near the side wall, by application of the traditional MoE and the previously ascertained modified image analysis width.

The flow-direction component of the orientation tensor (A_{xx}) is shown at multiple percentages of plaque width at 10, 40, and 90% of flow in Figure 4.8. Similar to the prior discussion of orientation data within the CGD, the values of the orientation tensor (A_{ij}) computed using the traditional MoE and the modified image analysis width are expected to be valid based on the previously discussed findings of minimal fiber curvature in the selected areas of inspection. The results show that a generally higher alignment of fibers along lines of 50%

and 90% of width throughout the length of the plaque. Along the centerline, however, the orientation distribution develops into a shell-core-shell profile by moderate fill percentages at 40% of flow (Figure 4.8b). By 90% of flow (Figure 4.8c) the core region is significantly wider and broader than traditionally seen in short fiber composites, suggesting a predominantly transverse fiber alignment along the centerline near the advancing front. The data in Figure 4.8 demonstrates the necessity to account for fiber orientation both experimentally and in simulations away from the more ideal centerline of the part due to the widely varying fiber orientation distribution observed within the end-gated plaque and the expected impact this will have on the mechanical properties of the part.

Finally, similar to the CGD, the Top View Method of Ellipses was subsequently applied to the EGP in an effort to verify the experimental orientation data by a direct comparison of experimental A_{ij} and R_{ij} data. The results along planes of interest of 0% and 90% of plaque width are shown in Figure 4.9 and Figure 4.10, respectively. Throughout the geometry, good agreement between the two data sets is observed, particularly along the centerline. This data not only confirms the previously discussed orientation data (Figure 4.8), but also provides additional evidence to verify the previous conclusions regarding minimal fiber curvature within the EGP. As a result, this work has verified the application of the traditional MoE and the modified image analysis width (or bin width) within the selected system and for the fiber length distribution under investigation here, particularly within regions of the geometry which exhibit a maximum fiber flexibility defined by f_{eff} = 6.00 x 10^5. It is worth noting, however, that the variance associated with the Top View Method of Ellipses (R_{ij}) is increased as compared to the previously discussed CGD data. This is likely attributed to the more complex EGP geometry resulting in a

slightly higher variance of fiber curvature throughout the geometry, particularly in the region of high shear flow near the mold side wall, as well as extensional flow near the advancing front.

4.5 Conclusions

In this chapter, the effect of long glass fiber flexibility and curvature on the validity of the method of ellipses within 2- and 3-dimensional geometries was investigated. The extent of average fiber flexibility within injection molded center-gated discs and end-gated plaques was quantified using a novel experimental approach designed to ascertain the average radius of fiber curvature. Within the center-gated disc, fiber flexibility and curvature was seen to be minimal through the geometry, likely attributed to a predominantly transverse orientation state for the fiber system under investigation. Within the end-gated plaque, however, curvature was seen to be more prevalent close to the gate and entry region of the part. In both geometries, fiber curvature was seen to increase in close proximity to the top and bottom mold walls, attributed to not only the increased velocity gradient in this region but also due to the effects of the advancing front and the resultant skin formation due to the fountain flow effect.

Additionally, an experimental technique to ascertain the components of the second moment of the end-to-end tensor, R_{ij}, was developed. A comparison of experimental A_{ij} and R_{ij} data showed good agreement in both geometries at the locations evaluated. In the end-gated plaque, the MoE has been shown to be valid for computing the components of the orientation tensor for long fibers with an average fiber length of 3.9 mm. However, the application of modified image analysis width was shown to be necessary due to the increase in fiber length and the presence of highly shear aligned fibers near the mold side walls. Finally, discussion of potential limitations of the MoE by relating the experimental findings of this work to values of the effective flexibility

parameter was included. Although bending and flexing was observed in the EGP, the MoE was still applicable to the systems of length distribution used in this study. It is suspected as the FLD is kept more narrow and a higher ratio of long fibers is maintained then the modified method may be more significant.

4.6 Acknowledgments

The financial support from the Department of Energy and Oakridge National Lab through grant number 4000122683 is gratefully acknowledged. In addition, the authors would like to thank the department of Material Science and Engineering at Virginia Tech for use of laboratory space and equipment for carrying out the fiber orientation measurements.

4.7 References

1. Truckenmüller, F. and Fritz, H.G. "Injection Molding of Long Fiber-Reinforced Thermoplastics: A Comparison of Extruded and Pultruded Materials with Direct Addition of Roving Strands." *Polymer Engineering & Science* **31** (18) (1991): 1316-1329.
2. Silverman, E.M. "Effect of Glass Fiber Length on the Creep and Impact Resistance of Reinforced Thermoplastics." *Journal of Polymer Composites* **8** (1) (1987): 8-15.
3. Hassan, A., et al. "Tensile, Impact and Fiber Length Properties of Injection-Molded Short and Long Glass Fiber-Reinforced Polyamide 6,6 Composites." *Journal of Reinforced Plastics and Composites* **23** (9) (2004): 969-986.
4. Thomason, J.L. "The Influence of Fibre Length, Diameter and Concentration on the Impact Performance of Long Glass-Fibre Reinforced Polyamide 6,6." *Composites: Part A* **40** (2009): 114-124.
5. Hine, P.J. and Duckett, R.A. "Fiber Orientation Structures and Mechanical Properties of Injection Molded Short Glass Fiber Reinforced Ribbed Plates." *Polymer Composites* **25** (3) (2004): 237-254.
6. Hassan, A.B., et al. "The Properties of Injection Molded, Short and Long Carbon Fiber Reinforced Polyamide 6,6 Composites." *Annual Technical Conference - Society of Plastics Engineers* **59th (Volume 2)** (2001): 2017-2021.
7. Fu, S.-Y. and Lauke, B. "Effects of Fiber Length and Fiber Orientation Distributions on the Tensile Strength of Short-Fiber-Reinforced Polymers." *Composites Science and Technology* **56** (1996): 1179-1190.
8. Nguyen, B.N., et al. "Fiber Length and Orientation in Long-Fiber Injection-Molded Thermoplastics – Part I: Modeling of Microstructure and Elastic Properties." *Journal of Composite Materials* **42** (10) (2008): 1003-27.
9. Crosby, J.M. "Long-Fiber Molding Materials " *Thermoplastic Composite Materials* (1991): 139-165.
10. Eberhardt, C. and Clarke, A. "Fibre-Orientation Measurements in Short-Glass-Fibre Composites. Part I: Automated, High-Angular-Resolution Measurement by Confocal Microscopy." *Composites Science and Technology* **61** (2001): 1389-1400.
11. Hine, P.J., et al. "Measuring the Fiber Orientation and Modelling the Elastic Properties of Injection-Moulded Long-Glass-Fiber-Reinforced Nylon." *Composites Science and Technology* **53** (1994): 125-131.
12. Vélez-García, G.M., et al. "Unambiguous Orientation in Short Fiber Composites over Small Sampling Area in a Center-Gated Disk." *Composites Part A: Applied Science and Manufacturing* **43** (1) (2012): 104-113.
13. Chen, C.H. and Cheng, C.H. "Effective Elastic Moduli of Misoriented Short-Fiber Composites." *International journal of solids and structures* **33** (17) (1996): 2519-2539.
14. Strautins, U. and Latz, A. "Flow-Driven Orientation Dynamics of Semiflexible Fiber Systems." *Rheol Acta* **46** (2007): 1057-1064.
15. Folgar, F. and Tucker, C.L. "Orientation Behavior of Fibers in Concentrated Suspensions." *Journal of Reinforced Plastics and Composites* **3** (2) (1984): 98-119.
16. Ortman, K. "Prediction of Fiber Orientation in the Injection Molding of Long Fiber Suspensions." *POLYMER COMPOSITES* **33** (8) (2012): 1360-1367.
17. Meyer, K.J., et al. "Initial Conditions for Simulating Glass Fiber Orientation in the Filling of Center-Gated Disks." *Composites Part A: Applied Science and Manufacturing* (2013):

18. Hofmann, J.T., et al. "Application and Evaluation of the Method of Ellipses for Measuring the Orientation of Long, Semi-Flexible Fibers." *POLYMER COMPOSITES* (2013):
19. Chin, W.-K., et al. "Effects of Fiber Length and Orientation Distribution on the Elastic Modulus of Short Fiber Reinforced Thermoplastics." *Polymer Composites* **9** (1) (1988): 27-35.
20. Velez-Garcia, G., et al. "Sample Preparation and Image Acquisition Using Optical-Reflective Microscopy in the Measurement of Fiber Orientation in Thermoplastic Composites." *Journal of Microscopy* **248** (1) (2012): 23-33.
21. Bay, R.S. and III, C.L.T. "Fiber Orientation in Simple Injection Moldings. Part Ii: Experimental Results." *Polymer Composites* **13** (4) (1992): 332-341.
22. Bay, R.S. and III, C.L.T. "Stereological Measurement and Error Estimates for Three-Dimensional Fiber Orientation." *Polymer Engineering & Science* **32** (4) (1992): 240-252.
23. Switzer III, L.H. and Klingenberg, D.J. "Rheology of Sheared Flexible Fiber Suspensions Via Fiber-Level Simulations." *J. Rheol.* **47** (3) (2003): 759-778.

4.8 Figures

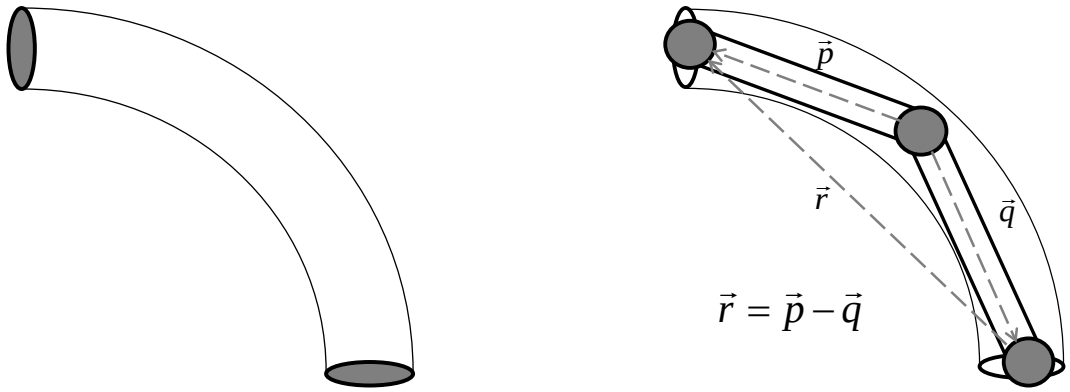

Figure 4.1. Representation of a (a) semi-flexible fiber and the (b) bead-rod model.

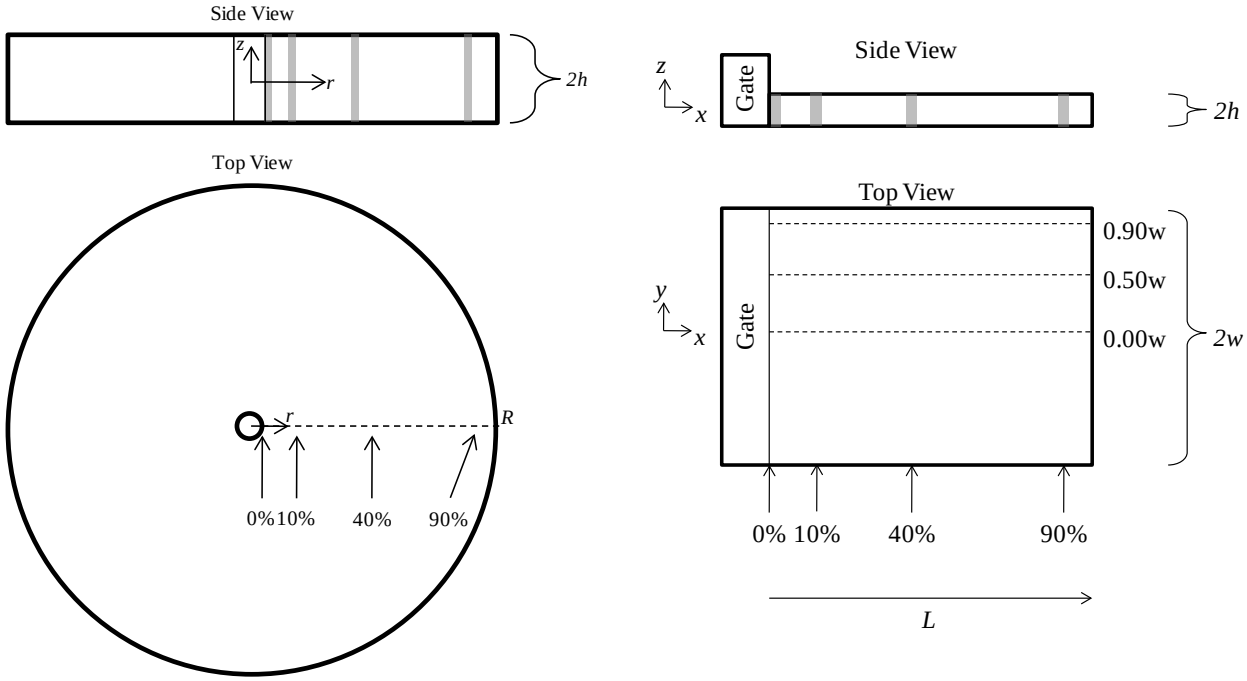

Figure 4.2. The selected geometries and sampling locations for the (a) Center-Gated Disc (CGD), and the (b) End-Gated Plaque (EGP).

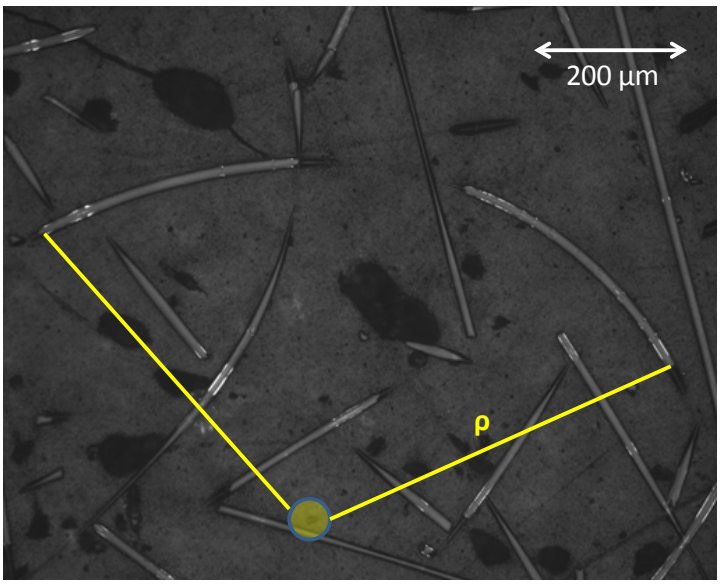

Figure 4.3. The Top View Fiber Curvature method showing a curved fiber in the r-θ plane at 10% of R and 0.9 z/h, and the radius of curvature, ρ, required to superimpose the bent fiber along the circumference of a circle.

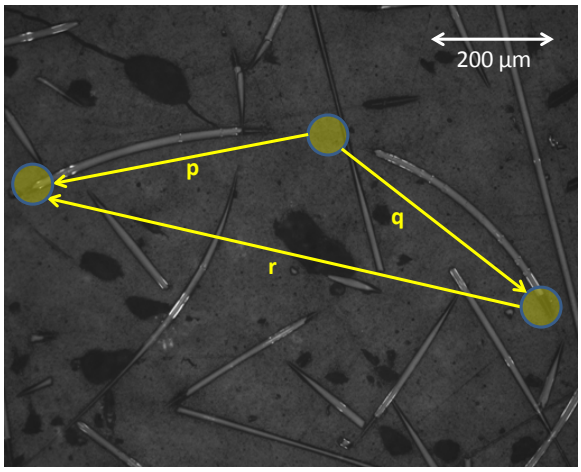

Figure 4.4. The Top View Method of Ellipses to determine the components of the end-to-end tensor, R, by representing a bent fiber in the r-θ plane by bead-rod configuration.

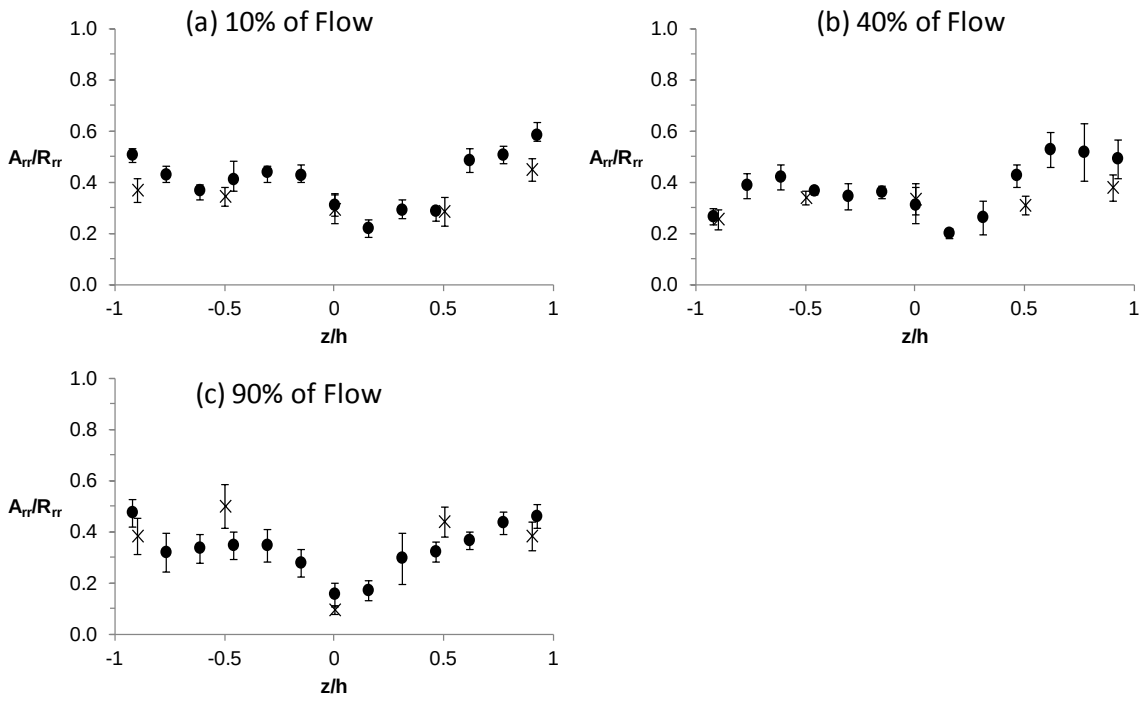

Figure 4.5. Flow-direction orientation data within the center-gated disc computed using the traditional method of ellipses (A_{rr}), and the top view method of ellipses (R_{rr}), for (a) 10%, (b) 40%, and (c) 90% of mold fill. The traditional method of ellipses data (A_{rr}) is represented by the filled circles (●), while the top view method of ellipses data is represented by the x's (X).

(a) (b)

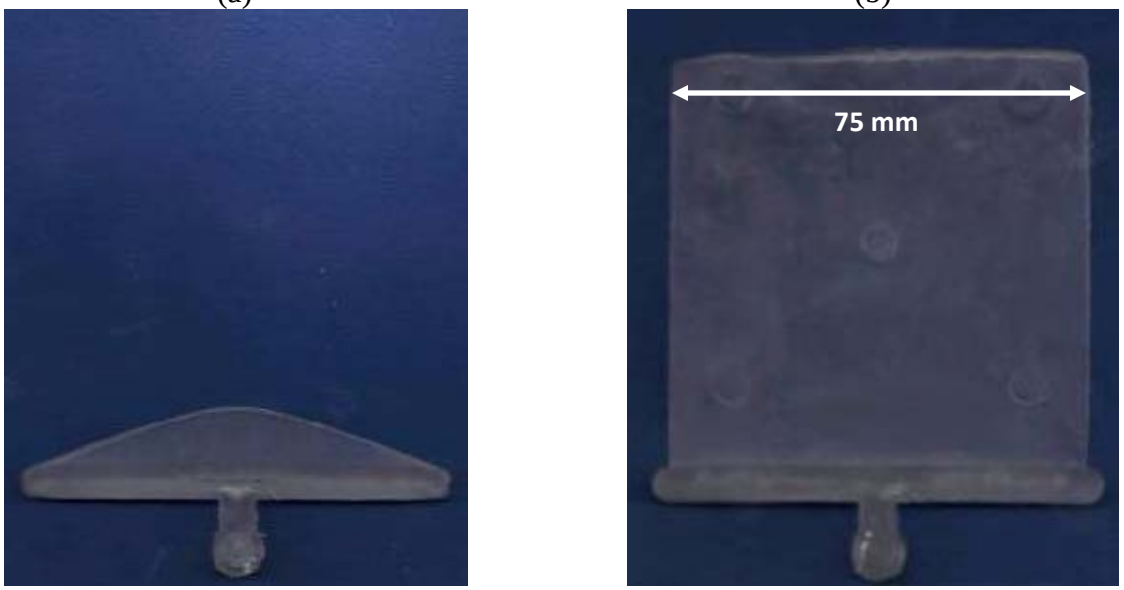

Figure 4.6. A filling profile of an EGP showing the *x-y* plane of a (a) 10% and (b) 90% short-shot fill, respectively.

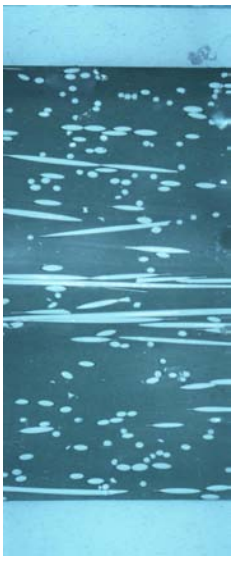

Figure 4.7. The 700-μm image analysis width utilized with the traditional method of ellipses, showing a large percentage of long fibers cross beyond the image analysis region along an inspection plane of 90% of plaque width and 40% of mold fill.

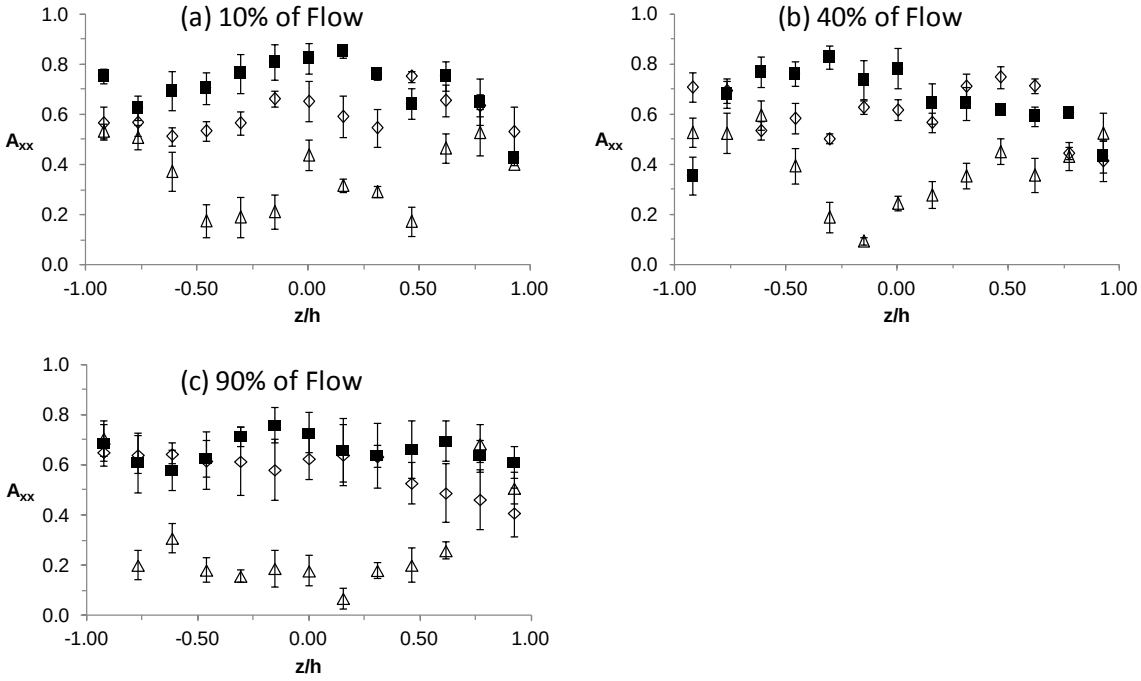

Figure 4.8. Flow-direction orientation data within the end-gated computed using the traditional method of ellipses with the modified image analysis width at (a) 10%, (b) 40%, and (c) 90% of mold fill. The triangles (Δ) represent orientation data at 0% of plaque width (i.e. along the plaque centerline), the diamonds (◊) represent orientation data at 50% of plaque width, and the filled squares (▪) represent orientation data at 90% of plaque width.

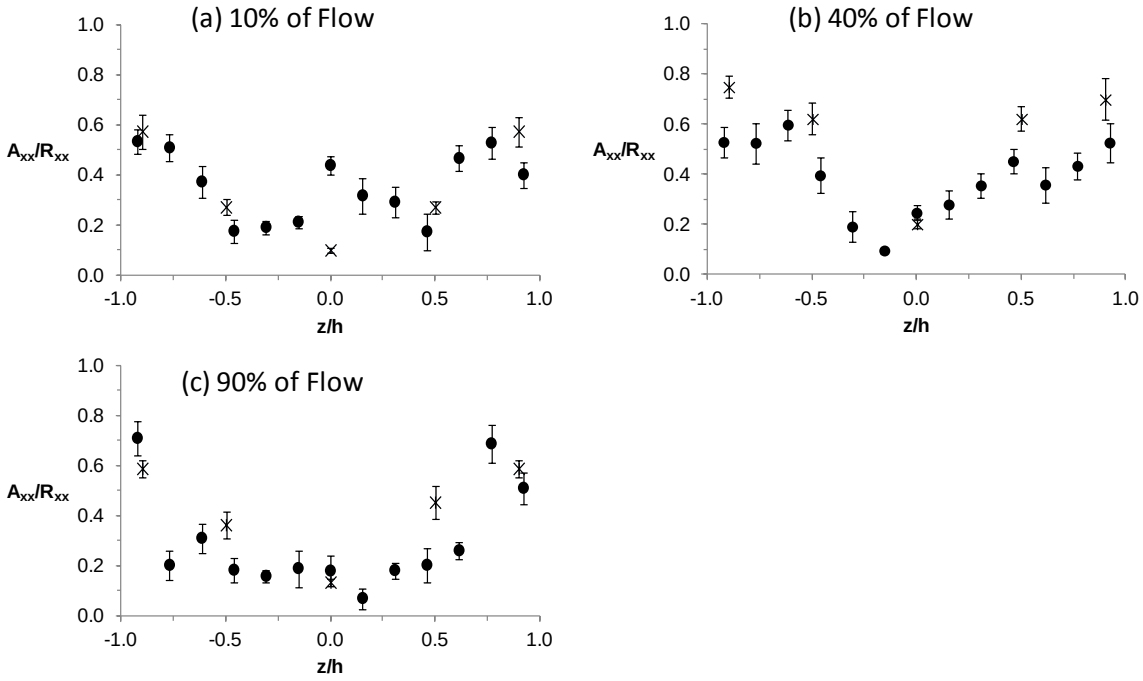

Figure 4.9. Flow-direction orientation data along the centerline of the end-gated plaque computed using the traditional method of ellipses and the modified image analysis region (A_{xx}), and the top view method of ellipses (R_{xx}), for (a) 10%, (b) 40%, and (c) 90% of mold fill. The traditional method of ellipses data (A_{xx}) is represented by the filled circles (●), while the top view method of ellipses data is represented by the x's (X).

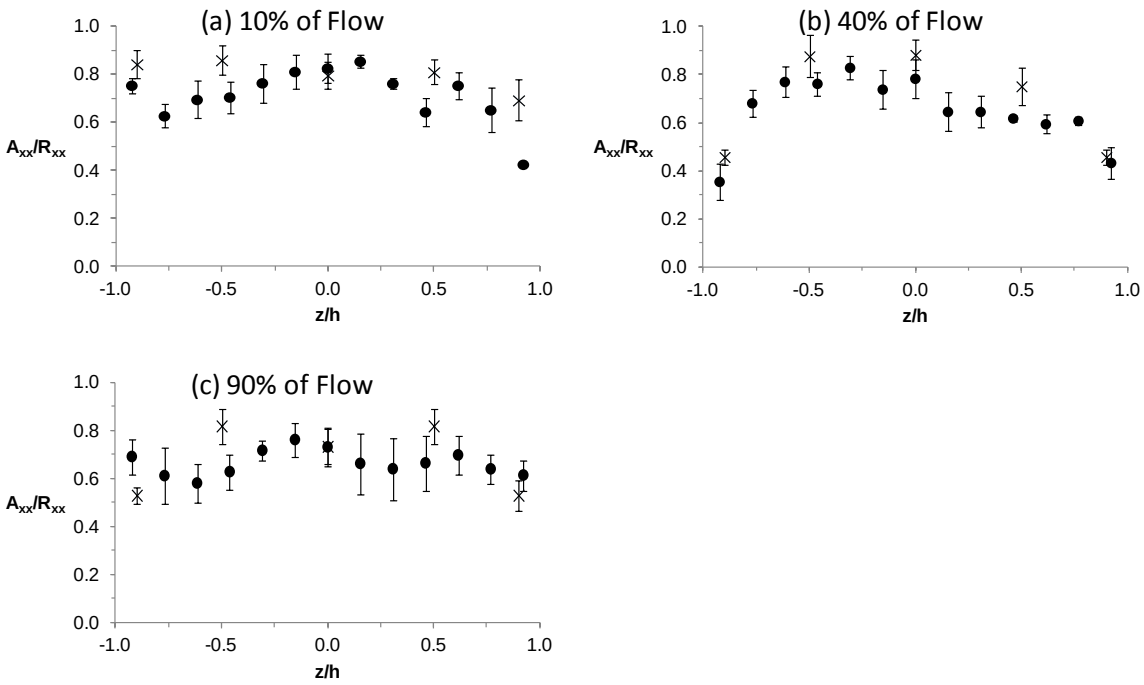

Figure 4.10. Flow-direction orientation data within the end-gated plaque at 90% width computed using the traditional method of ellipses and the modified image analysis width (A_{xx}), and the top view method of ellipses (R_{xx}), for (a) 10%, (b) 40%, and (c) 90% of mold fill. The traditional method of ellipses data (A_{xx}) is represented by the filled circles (●), while the top view method of ellipses data is represented by the x's (X).

Table 4.1. Average values of L/2r at various locations within the center-gated disc as function of flow length and through-thickness

	10% R	40% R	90% R
0.9 z/h	0.17	0.10	0.12
0.5 z/h	0.13	0.11	0.10
0.0 z/h	0.00	0.02	0.09

Table 4.2. Average values of L/2r at various locations within the end-gated plaque at a through-thickness of 0.0 z/h, as function of flow length and plaque width

	10% L	40% L	90% L
0.0w	0.06	0.04	0.13
0.5w	0.03	0.07	0.11
0.9w	0.08	0.06	0.10

Table 4.3. Average values of L/2r at various locations within the end-gated plaque at a through-thickness of 0.5 z/h, as function of flow length and plaque width

	10% L	40% L	90% L
0.0w	0.08	0.05	0.13
0.5w	0.09	0.08	0.08
0.9w	0.07	0.01	0.09

Table 4.4. Average values of L/2r at various locations within the end-gated plaque at a through-thickness of 0.9 z/h, as function of flow length and plaque width

	10% L	40% L	90% L
0.0w	0.11	0.12	0.21
0.5w	0.20	0.07	0.09
0.9w	0.11	0.14	0.07

Chapter 5 : Evaluation of the Orientation Distribution of Long Glass Fibers in 2- and 3-Dimensional Test Geometries and the Effect on Modulus

5.1 Abstract

The effect of orientation distributions of long, semi-flexible fibers on the resulting modulus of injection molded parts has been evaluated. A long glass fiber suspension with a post-processing average length of approximately 3.9 mm was selected for analysis in model 2- and 3-dimensional test geometries. Experimental and predicted orientation distributions were obtained within the center-gated disc and the end-gated plaque at multiple percentages of flow and width. The Bead-Rod model for semi-flexible fibers was shown to more closely agree with experimental orientation data throughout both test geometries as compared to the previously developed rigid rod model. The simulated and experimental orientation data were coupled with composite laminate theory and utilized to predict the modulus of the parts, and subsequently compared to experimentally obtained values of modulus. The results demonstrate good agreement between predicted and actual modulus for long, semi-flexible fiber-reinforced composites with an average length of 3.9 mm. On average, the Bead Rod model for semi-flexible fibers simulated orientation distribution data coupled with laminate ply theory has been shown to more closely predict the resulting modulus of the parts.

Keywords: Fiber composites; injection molding; long glass fiber; fiber orientation distribution; bead-rod model; modulus;

5.2 Introduction

The addition of reinforcing fibers to a polymer matrix has been seen to result in improved mechanical properties as compared to the neat polymer matrix alone. Specifically, studies have shown that the addition of chopped glass fibers to a polymer matrix results in an increase in stiffness, strength to weight ratio, and fracture toughness, dependent on the final orientation of fibers within a molded part [1-3]. Additionally, an increase in fiber aspect ratio, defined as the fiber length divided by the fiber diameter, generally is related to an increase in the magnitude of the enhancement of mechanical properties [2, 4-5]. Because chopped glass fiber composites remain melt processable, they can be processed by commercially available techniques such as injection or compression molding, and are thus highly desirable for applications in a range of industries but especially the automotive industry.

The experimental and predicted mechanical properties of injection-molded composites has been investigated due to the strong dependence of these properties on the final fiber orientation within the part [6-7]. Chin et al. [6] applied a simulated laminate plate model to short fiber reinforced composites in order to utilize the through-thickness Fiber Orientation Distribution (FOD) to predict the elastic modulus of the composite. A later study by Hashemi et al. [7] evaluated the type of gate and location within an end-gated geometry on the fracture toughness of the final part. In several more recent studies the effect of a number of other processing parameters on the final mechanical properties of injection molded ASTM dogbones, including Fiber Length Distribution (FLD), average fiber aspect ratio, fiber wt%, and compounding procedure have been evaluated [2, 4-5, 8]. However, the above studies focused primarily on short glass fiber (SGF) composites and lacked a correlation of fiber orientation evolution models to the measured mechanical properties.

For short, rigid glass fibers, tensors are often utilized to describe the orientation state of a concentrated population of fibers [9], as defined in Eq. (5.1) and Eq. (5.2):

$$\mathbf{A} = \oint \mathbf{pp}\,\psi(\mathbf{p},t)d\mathbf{p} \tag{5.1}$$

$$\mathbf{A_4} = \oint \mathbf{pppp}\,\psi(\mathbf{p},t)d\mathbf{p} \tag{5.2}$$

Here, $\mathbf{A}$ and $\mathbf{A_4}$ represent the second and fourth moment of the fiber orientation vector, $\mathbf{p}$, respectively, while $\psi(\mathbf{p},t)$ is defined as the probability density function. The origin of these tensors can be traced back to the work of Jeffery [10], who developed a model for a rigid, massless ellipsoid in an infinitely dilute suspension. It is worth noting that the fourth order orientation tensor, $\mathbf{A_4}$, can be expressed in terms of $\mathbf{A}$ by utilizing a closure approximation. The effectiveness of a number of closure approximations have been evaluated, including the invariant-based optimal fitting (IBOF) approximation [11]. Additionally, these orientation tensors possess the benefit of always being symmetric and with the requirement that the trace is always equal to exactly one. More recently, Jeffery's model was extended for use with concentrated suspensions by Folgar and Tucker [12]. As a result, it has been utilized in a number of studies evaluating the theoretical and experimental orientation evolution of SGF in injection molded composites [13-16].

For long glass fibers, however, a more sophisticated model known as the Bead-Rod model is under consideration for predicting long fiber orientation due the necessity to capture the effects of fiber flexibility [17-18]. The Bead-Rod model, as initially described by Strautins and Latz for semi-flexible fibers [19], segments a flexed fiber into a series of rigid rods connected by beads. The rods may flex or pivot about these beads in order to capture the flexibility of the fiber. For mildly-flexed long fibers, a representation consisting of 3 beads and 2 rods has been utilized with

the rod segments represented by the orientation vectors **p** and **q**, respectively. Using a similar approach as the rigid rod model based on the work of Jeffery [10] and extended to concentrated suspensions by Folgar and Tucker [12], two of orientation tensors are derived:

$$\mathbf{A} = \int\int \mathbf{pp}\,\psi(\mathbf{p},\mathbf{q},t)\,d\mathbf{p}d\mathbf{q} \tag{5.3}$$

$$\mathbf{B} = \int\int \mathbf{pq}\,\psi(\mathbf{p},\mathbf{q},t)\,d\mathbf{p}d\mathbf{q} \tag{5.4}$$

Here, **A** is similar to the orientation tensor previously defined (Eq. (5.3), while **B** represents bending by quantifying the extent at which the orientation vectors **p** and **q** are non-parallel to one another. However, a more concise way to represent this orientation data is by use of the second moment of the orientation distribution of the end-to-end vector, **p** - **q**:

$$\mathbf{r} = \int\int l_b^2\,(\mathbf{p}-\mathbf{q})(\mathbf{p}-\mathbf{q})\,\psi(\mathbf{p},\mathbf{q},t)\,d\mathbf{p}d\mathbf{q} \tag{5.5}$$

where l_b is defined as one-half of the fiber length. Eq. (4.4) may be normalized to obtain the end-to-end tensor, **R**:

$$\mathbf{R} = \frac{\mathbf{r}}{\mathrm{tr}(\mathbf{r})} = \frac{\mathbf{A}\text{-}\mathbf{B}}{\mathbf{1}\text{-}\,\mathrm{tr}(\mathbf{B})} \tag{5.6}$$

It is worth noting that as the flexibility of a fiber reduces to zero the expression in Eq. (5.6) simplifies to R = A, and the rigid rod model discussed previously is regained.

The desire to optimize the mechanical properties of long glass fiber-reinforced injection molded parts, which are related to fiber orientation, has led to considerable investigation into the comparison of experimental long glass fiber orientation data to numerical simulations of fiber orientation evolution during processing via the rigid and Bead Rod models [20-22]. While many prior works have focused on predicting the orientation evolution of short, rigid glass fibers, only a few works have investigated the simulation of orientations of long glass fibers, which provide far superior mechanical properties as previously discussed [2, 4-5]. Ortman et al. [23] and

Meyer et al. [22] recently investigated the predicted and actual orientation distributions of long glass fibers within the center-gated disc. Both authors found that the Bead-Rod model exhibits superior performance when simulating the orientation evolution of long, semi-flexible fibers as compared to the previous rigid-rod model as originally introduced by Folgar and Tucker [12]. More recent efforts by Meyer et al. [24] have extended orientation predictions to the end-gated plaque, a fully three-dimensional geometry which has previously been shown to exhibit a complex filling profile and a complex fiber orientation distribution [25]. The authors similarly found that the Bead-Rod model is far superior for predicting the orientation evolution of long glass fibers which have the ability to exhibit flexibility and curvature.

In a recent study Nguyen et al. [20] investigated the predicted and experimental fiber orientation distribution and modulus within long glass fiber-reinforced center-gated discs and end-gated plaques. The authors observed good agreement between the predicted and experimental results for both orientation and modulus. However, several aspects of this study must be discussed. First, this study only focused on evaluating the orientation distribution along the centerline of the plaque and neglected the experimental orientation behavior in the more complex flow areas away from the plane of symmetry along the centerline of the end-gated mold. Second, the average fiber length within this study was close to 1 mm, the threshold between short and long glass fibers. Because of the Weibull distribution of fiber lengths, a large percentage of the fibers in this study were below the threshold of 1 mm, and, therefore, the fibers were considered to be short and thus rigid. Furthermore, the fact that many fibers had lengths of less than 1 mm may provide some insight into the good agreement between predicted values of orientation in the selected geometries by use of the rigid rod orientation model and experimental orientation data. As such, there has been no comprehensive report of the orientation distribution

of a long glass fiber suspension with a fiber length distribution more representative of that which is seen commercially, for regions of flow far from the centerline of the end-gated plaque and near the mold side walls or within the complex gate region of the geometry, nor the effect on modulus in these regions.

More recent efforts by Hofmann et al. [25] have focused on the extension and validation of the Method of Ellipses to obtaining experimental orientation data for long glass fibers within center- and end-gated test geometries for which the average fiber length is approximately 4 mm. The authors determined that within the selected geometries and for the given fiber length distribution with an average length of 4 mm, that the traditional Method of Ellipses was valid provided that the modified image analysis width was utilized in regions of highly aligned fibers. This was primarily attributed to the observation that only a small fraction of fibers exhibited curvature throughout the geometry on average due to the specific fiber length distribution and processing conditions, and, therefore, fiber bending only mildly influences the fiber orientation distribution. However, to date there has been no correlation between either the experimental or the predicted orientation data and the resulting mechanical properties of the selected test geometries for a long glass fiber distribution with an average length of approximately 4 mm.

The goal of this paper is to provide a thorough and comprehensive evaluation of the experimental and predicted orientation distribution of long, semi-flexible glass fibers within the center-gated disc and the end-gated plaque and the effect on modulus. This will be accomplished by evaluating both the predicted and experimental values of fiber orientation at multiple percentages of plaque length and width, including in the regions of complex flow near the mold side walls. The simulated and experimental orientation data will be coupled with lamination theory to calculate the predicted global modulus of the composites in regions of widely varying

fiber orientation. Thus, this work aims to ascertain whether the mechanical properties of select model test geometries can be accurately predicted for a long glass fiber which exhibits a fiber length distribution representative of that which is typically observed commercially and with an average length of approximately 4 mm. Finally, experimental values of modulus are reported and utilized to evaluate the accuracy of the predictions.

5.3 Experimental Conditions

5.3.1 FRP Composite Geometries

Center-gated discs (CGD) and end-gated plaques (EGP) were formed for the experimental evaluation of fiber orientation using 30 weight percent long glass fiber in a polypropylene matrix (LNP Verton MV006S) provided by Sabic Innovation Plastics. Both geometries had a sprue length of 65mm with an initial radius of 1.45mm and a final radius at the gate of 1.75mm. The center-gated disc (Figure 5.1) had an initial, r_i, and final radius, R, of 3.00 and 55.0 mm, respectively, and a thickness, $2h$, of 2.00 mm. The end-gated plaque consisted of a gate and plaque region (Figure 5.2). The gate region of the plaque has dimensions of 80.68mm (width) by 6.25mm (height) by 6.33mm (length) and the mold region of the plaque has dimensions of 75.05mm (width) by 1.55mm (height) by 77.65mm (length).

5.3.2 Processing Methods

An injection molding machine was utilized to mold a series of center-gated discs and end-gated plaques. The temperatures of the feed, compression and metering zones within the injection molding machine (Arburg Allrounder, Model 221-55-250) were set to 190 °C, 210 °C, and 210 °C, respectively, while the mold temperature was held constant at 79 °C. The plaques

were molded using a fill time of 2.00 seconds with a backpressure of approximately 20 MPa. Additionally, both mold geometries were filled using a 90% short shot in order to mitigate any potential packing effects. The resulting discs had an average final radius of 50.8 ± 2.03 mm, while the plaques had an average final length of 68.65 ± 1.87 mm. Furthermore, all parts were left to cool in the closed mold for a period of twenty minutes prior to removal in order to reduce warping. It is worth noting that the first 10 parts molded of each geometry were discarded in order to ensure that the injection molding machine was operating at an equilibrium state.

5.3.3 Fiber Length Distribution Determination

The fiber length distribution (FLD) was determined to verify that the average lengths of the fibers in the end-gated plaque were indeed in the long fiber regime that is typically defined as $L > 1$ mm. Methods described by Nguyen et al. [20] were used to determine the fiber length distribution of approximately 2000 fibers. The method involved taking a representative sample of the suspension of the injection-molded sample and burning off the polymer matrix in a high temperature furnace leaving only the glass fiber mat behind. A small amount of epoxy resin was applied to the glass fiber matrix to secure a population of fibers and any fibers not secured to the epoxy were carefully removed. The remaining fiber/epoxy sample was returned to the furnace to remove the epoxy and leave only the glass fibers. Finally, the remaining fibers were analyzed through optical techniques in order to determine the experimental FLD. The post-processing number average fiber length and average fiber aspect ratio, a_r, were determined experimentally to be approximately 3.90 mm and 300, respectively, within both the center-gated disc and the end-gated plaque.

5.3.4 Sample Preparation and Experimental Orientation Measurements

A set of five representative plaques were selected and prepared for analysis at multiple locations according to procedure described in detail by Velez-Garcia et al. [26]. The chosen inspection points to obtain experimental values of orientation were 0%, 10%, 40%, and 90% of length of the mold, and along the centerline, 50% of the half-width of the mold, and 90% of the half-width of the mold. After sample preparation via polishing, an optical microscope with a motorized stage and image-stitching software (Nikon Eclipse LV100, NIS-Elemets Basic Research software, v.3.10) was subsequently utilized to image each inspection point at 20X magnification.

The experimental components of the end-to-end orientation tensor (R_{ij}) were subsequently computed using an in-house written Matlab image analysis routine according to the recent findings of Hofmann et al. [25]. In brief, this method consists of the application of a modified form of the traditional Method of Ellipses (MoE) [13]. It has recently been shown that the modified image analysis width determined by Hofmann et al. [27] must be utilized in regions of highly shear-aligned fibers often exhibited in complex geometries which feature regions of high shear, such as the end-gated plaque, where too narrow of an image analysis region results in an increase in partial ellipses and associated error. This modified method allows for the accurate determination of the unambiguous components of the orientation tensor at all inspection points within the center-gated disc and the end-gated plaque [14].

5.3.5 Simulation of Fiber Orientation Evolution

The prediction of fiber orientation in the end-gated plaque was carried out using the decoupled approach to fiber orientation and the two-step solution given by Meyer et al. [18, 28]

First, the finite element method (ANSYS Polyflow®) was used to simulated the neat matrix filling the end-gated plaque geometry. Only the neat matrix was simulated because the fibers are only affected by the drag of the fluid and fiber-fiber collisions. These contributed were taken into account via the slip parameter, κ, and the fiber interaction coefficient, C_I, in the equations of orientation. For the neat matrix, a Generalized Newtonian Fluid relation was chosen to represent the stress tensor using the empirical Carreau-Yasuda model for viscosity. The fluid was tracked through the domain solving the transport equation for the fluid fraction on a fixed mesh.

The second step in the solution of fiber orientation was to utilize the velocity fields and the velocity gradients obtained in the previous step in order to solve a set of non-linear ordinary differential equations in order to compute the components of the orientation tensor. The strain reduction model, proposed by Sepehr et al. [29] and Eberle et al. [30] was used for rigid fiber orientation distribution calculations, while the modified bead-rod model proposed by Ortman et al. [17]was used for the semi-flexible fiber calculations. The ordinary differential equations were solved using a variable step size backwards difference implementation of the Kopfenstein-Shampine family of numerical differentiation formulas [31].

5.3.6 Prediction of Modulus

The relationship between stress and strain within a material may be expressed using the generalized Hooke's law and the use of the stiffness tensor, c_{ijkl}:

$$\sigma_{ij} = c_{ijkl}\varepsilon_{kl} \tag{5.7}$$

This stiffness tensor, also commonly referred to as the stiffness matrix, is a function of not only the material choice of the matrix and filler, but also of the fiber length and orientation distribution within an injection-molded composite. If the spatial distribution of fiber orientations

within an injection molded part is known, the stiffness tensor may be computed at any location and subsequently utilized in order to predict the global modulus of via laminate ply theory [6].

The computation of the global mechanical properties of an injection molded composite begin with derivation of the stiffness matrix for a unidirectional, chopped fiber composite having a uniform aspect ratio of *l/d*, defined as $C^{*}_{ijkl}\left(l/d\right)$. This expression is obtained according to the Eshelby-Mori-Tanaka method, as described elsewhere [32]. This expression is subsequently modified in order to account for the distribution of fiber lengths observed in real parts. This is done by multiplying the expression by the probability distribution of fiber length, $p\left(l\right)$, and integrating in order to determine the stiffness matrix of a unidirectional fiber composite that consists of a distribution of fiber lengths as defined in Eq. (5.8):

$$C_{ijkl} = \frac{\int_{0}^{\infty} C^{*}_{ijkl}\left(l/d\right) p\left(l\right) dl}{\int_{0}^{\infty} p\left(l\right) dl} \tag{5.8}$$

In addition to a fiber length distribution, an injection molded part will contain a distribution of final, post-processing orientations which will vary as a function of part length, width, and thickness. The orientation averaging method is utilized in order to account for the varied orientation states of fibers within an injection molded composite, by first calculating the invariants of Eq. (5.8), denoted as B_i [9, 33]. Using these invariants, as well as the components of the orientation tensor, A_{ij}, the stiffness matrix of a composite with a distribution of both fiber lengths and orientations can be calculated at any location within the part, as defined in Eq. (5.9):

$$\bar{\bar{C}}_{ijkl} = B_1 A_{ijkl} + B_2\left(A_{ij}\delta_{kl} + A_{kl}\delta_{ij}\right) + B_3\left(A_{ik}\delta_{jl} + A_{il}\delta_{jk} + A_{jl}\delta_{ik} + A_{jk}\delta_{il}\right) + B_4\left(\delta_{ij}\delta_{kl}\right) + B_5\left(\delta_{ik}\delta_{jl} + \delta_{il}\delta_{jk}\right) \tag{5.9}$$

It is worth noting that the expression in Eq. ((5.9) may also be expressed in terms of the end-to-end orientation vector, **R**.

The global mechanical response of an injection molded part consisting of a distribution of both fiber lengths and orientations can thus be predicted at any location by utilizing laminate ply theory. In this method, the composite is simulated as a series of stacked lamina plies of uniform thickness. Each ply will consist of fibers with some calculated or experimentally determined orientation distribution. Eq. (5.9) can then be utilized in order to compute the stiffness tensor of each ply at any location within the composite using the corresponding through-thickness orientation data. The global mechanical properties of a composite consisting of a stacked sequence of "simulated" lamina plies through the thickness of the part can then be computed using lamination theory.

5.3.7 Evaluation of Modulus

Experimental values of modulus were obtained within the center-gated disc (Figure 5.3) and at several locations within the end-gated plaque (Figure 5.4) featuring widely varying orientation distributions in order to evaluate the effectiveness of the predictions in a fully 3-dimensional geometry. This included ascertaining the flow-direction modulus (E_{11}) along a line of 40% of plaque length, and at 0%, 50%, and 90% of the half-width of the plaque. Additionally, the transverse-to-flow direction modulus (E_{33}) was determined along the center line of the plaque at 10%, 40%, and 90% of plaque length. Predicted values of modulus obtained by utilizing the orientation averaging method and laminate ply theory as described previously were directly

compared to experimentally obtained values of modulus collected using the methodology outlined by ASTM D638 and appropriate dogbone test specimens cut from a population of five end-gated plaques at each respective testing location.

5.4 Results

5.4.1 Fiber Length Distribution

The experimental fiber length distribution (FLD) was measured and is reported in Figure 5.5. The initial average fiber length of 13 mm in the as-received LGF polypropylene pellets was reduced to a number average fiber length of approximately 3.901 mm after processing. From inspection of the data, it can be seen that only a small percentage of the population of fibers are present with lengths of 1-mm or less. Because this is the traditional threshold that differentiates short and long glass fibers, the system under investigation is seen to consist predominantly of fibers which have the ability to exhibit flexibility and curvature during flow. Additionally, the data exhibits a long tail in the higher fiber length region, and is well-represented by a Weibull distribution as several authors have previously reported [6, 20]. The parameters for the Weibull distribution (as defined in Eq. (5.10)) were estimated using the method of least squares to be $b = 4.04$ and $c = 2.87$:

$$p(l) = \frac{c}{b}\left(\frac{l}{b}\right)^{c-1} e^{-(l/b)^c} \tag{5.10}$$

Finally, it is worth noting that the FLD was measured at 40% of flow within both geometries under consideration and the resulting data were found to be within statistical agreement.

5.4.2 Center-Gated Disc

The experimental and predicted values of fiber orientation distribution (FOD) in the center-gated disc at 40% of flow are summarized in Figure 5.6. The experimental data is predominantly planar, with the majority of fibers being aligned in the r-θ plane, and with minimal alignment through the thickness of the part in the z-direction. The FOD exhibits a broad core-shell profile, with a slightly higher alignment near the top and bottom mold walls (i.e. ~~as~~ ~~z~~≠hl.0). However, the overall alignment is highly transverse to flow, with the majority of fibers aligned in the θ-direction. Additionally, Figure 5.6 demonstrates the improved performance of the Bead-Rod model for simulating the orientation evolution of LGF which have an average fiber length of approximately 3.9 mm, as compared to the predictions of the rigid-rod model.

The results presented in Figure 5.6 were utilized to compute the predicted modulus of a center-gated disc based on the predicted and experimental orientation data. The corresponding predictions as well as the experimentally measured modulus are summarized in Table 5.1. The predicted flow-direction modulus computed using the experimental FOD was found to be within the experimental error of the actual modulus of 2.79 GPa. The predicted value of modulus computed using the Bead-Rod FOD, while outside of the error bounds of the actual modulus, shows good agreement. The difference in these two values is primarily attributed to the reduced agreement between the Bead-Rod FOD and the experimental FOD in the regions in close proximity to the mold walls (Figure 5.6). The predicted value of modulus computed via the Rigid-Rod model, however, differs from the actual modulus by roughly 85%. This is due to the significant over-prediction of the shell region of highly flow-aligned fibers within the Rigid-Rod FOD. These findings emphasize the superior performance of the Bead-Rod model in predicting the orientation evolution kinetics during the injection molding of a glass fiber-reinforced center-

gated disc with an average length of 3.9 mm and the ability for the fibers to exhibit flexibility during processing. Moreover, these results propose an inherent accuracy of the experimental orientation data obtained for long glass fibers within this selected test geometry due to the agreement between the predicted and actual modulus data.

5.4.3 End-Gated Plaque

Prior to evaluating quantitative orientation data, it is first useful to discuss the complex flow behavior in the end-gated plaque in a qualitative fashion. Due to the nature of the end-gated geometry, and specifically the location of the centrally-located sprue, a complex initial filling profile is exhibited (Figure 5.7a). The larger cross-sectional area of the gate region running the width of the plaque (Figure 5.2) allows for the gate to fill at a faster rate initially than the plaque cavity itself (Figure 5.7b). This causes an irregular advancing front at low mold fill percentages (Figure 5.7c). This radial advancing front is expected to result in a similar fiber orientation evolution behavior along the plaque center-line as has previously been observed in the center-gated disc [34]. It is expected, however, that this complex filling profile will lead to a complex FOD across the width of the gate region, particularly near the stagnation point near the mold side walls. Furthermore, it is worth noting that this irregular advancing front has been observed to persist until the filling of the plaque cavity is more than approximately 50% complete.

The filling pattern of the EGP, as shown in Figure 5.7 and described in the preceding paragraph, results in a difference in fiber orientation distribution across the width of the geometry far from the gate. Figure 5.8(a) and (b) shows the resulting FOD in the *x*-*z* plane at 40% of mold fill along inspection planes of interest of 0% and 90% of the half-width of the plaque, respectively. It can be seen that along the centerline of the plaque (i.e. at 0% of width)

the FOD qualitatively takes on a similar appearance as that of the center-gated disc, exhibiting a core-shell profile. Near the mold side wall, however (i.e. at 90% of width), the fiber alignment is predominantly in the flow direction, likely due to the increased shear in this region due to the proximity of the mold side wall. It can be expected, therefore, that the global mechanical properties of the composite will vary considerably across the width of the plaque as a result of the drastically changing fiber orientation distribution.

Results for the predicted and experimental components of orientation at 40% of mold flow of the end-gated plaque are shown in Figure 5.9 along inspection planes of interest at 0, 50, and 90% of the half-width, *w*, of the plaque (Figure 5.2). As Figure 5.9(a) demonstrates, the experimental orientation behavior along the centerline of the plaque (i.e. 0% of width) at 40% of mold flow is similar to the FOD observed within the previously discussed CGD. This is primarily due to the fact that the centerline of the EGP lies along a plane of symmetry, resulting in a very broad core-shell profile with the predominant alignment in the transverse or y-direction. At 50 and 90% of plaque width (Figure 5.9b and c, respectively), however, there is a significant increase in fiber alignment in the flow direction due to the increased shear in this region as a result of the proximity to the side wall of the mold. Similar to the center-gated disc, the performance of the Bead-Rod model is seen to be superior to that of the Rigid-Rod model in capturing the trends of fiber orientation in the region of well-developed flow at 40% of mold fill of the end-gated plaque, particularly along the centerline of the plaque (Figure 5.9a).

The effect of this complex fiber orientation distribution on the modulus at various locations across the width of the composite is summarized in Table 5.2, including predicted and experimental values of modulus. Experimentally, the modulus is seen to vary considerably across the width of the plaque, with values of 3.94 GPa and 6.65 GPa along lines of 0% and 90%

of plaque width, respectively. This increase in modulus near the plaque side wall corresponds with the increased fiber alignment in the flow direction (Figure 5.9) due to the majority of added mechanical reinforcement expected in the direction of the axis of the fibers. This experimental orientation data (Figure 5.9) has been used to accurately predict the modulus across the width of the plaque (Table 5.2) with a good correlation of predicted modulus to actual modulus.

Additionally, modulus values were predicted by using the orientation data computed using both the rigid- and semi-flexible fiber models (Figure 5.9). At 0% and 90% of plaque width, the Bead-Rod model data was found to more closely predict the actual modulus of the plaque as compared to the values computed using the Rigid-Rod model data. This was attributed to the improved performance of the Bead Rod model in these selected regions. At 50% of plaque width, however, the predicted modulus obtained using the Bead Rod FOD is less accurate due to a larger disparity between the Bead Rod and experimental orientation distributions (Figure 5.9b).

Finally, predicted and experimental components of the orientation tensor along the centerline of the end-gated plaque are shown in Figure 5.10 at inspection points 10, 40, and 90% of mold flow. The experimental data shows the evolution of a core-shell profile already present by 10% of mold flow (Figure 5.10a). However, by 90% of mold flow (Figure 5.10c), the FOD takes on a predominantly transverse alignment, with a very wide and broad core region, suggesting that the majority of the mechanical enhancement to modulus in this location will be in the transverse- or y-direction. The predictions from the Bead-Rod model once again outperform that of the Rigid-Rod model at 10 and 40% of mold flow. However, it is worth noting that there is minimal difference between the two models and the experimental data at 90% of flow (Figure 5.10c). Therefore, it is likely that the predicted values of modulus supplied via the Bead-Rod model will be vastly superior on average throughout the plaque geometry.

A comparison of predicted vs. actual modulus in the transverse direction at multiple percentages of flow is detailed in Table 5.3. Similar to the trend discussed previously for the flow-direction modulus predictions and data, there is a close agreement between the actual modulus values and the predicted modulus values obtained using the experimental fiber orientation distribution. This agreement provides additional evidence as to the accuracy of the experimental fiber orientation data obtained for long, semi-flexible fibers using the method previously described by Hofmann et al. [25]. It is worth noting, however, that the disparity is slightly larger at 90% of flow, possibly due to the proximity to the advancing front and a more irregular orientation of fibers within the dog bone test specimen.

Values of predicted modulus were computed using the orientation distributions obtained using the rigid- and semi-flexible fiber models (Figure 5.10). Values of the transverse-direction modulus computed using the Bead-Rod FOD more closely agree with the actual modulus at 10% and 40% of flow. This is due to the improved performance of the Bead-Rod model in these regions (Figure 5.10a-b) as compared to the Rigid Rod model, which over-predicts the flow-direction orientation component (A_{11}) and under-predicts the transverse orientation component (A_{33}). At 90% of flow (Figure 5.10c) both models agree favorably with the experimental orientation distribution through the thickness of the part. However, the rigid model exhibits larger values of the transverse orientation component, and thus a larger predicted value of the transverse modulus which agrees well with the value of modulus predicted using the experimental orientation data (Table 5.3).

5.5 Conclusions

In this paper, the fiber orientation distribution observed in the center-gated disc and end-gated plaque has been evaluated, including the resulting effect on the distribution of modulus. A fiber length distribution similar to distributions observed commercially and exhibiting an average length of 3.9 mm has been investigated. Experimental data within the center-gated disc and the end-gated plaque has been reported, showing the improved performance of the Bead-Rod model for simulating orientation evolution for long glass fibers. Additionally, theoretical values of flow- and transverse-direction modulus were calculated at various locations within the center-gated disc and the end-gated plaque by coupling experimental and predicted orientation data with lamination theory. The experimental values of modulus correlate well with the predicted values in both geometries under investigation. In addition, the agreement between the predicted and experimental values of modulus provides a secondary avenue to verify the validity of the experimental fiber orientation data obtained using the method of ellipses and the modified image analysis width. Finally, this work has demonstrated the validity of lamination theory when applied to semi-flexible fibers with an average fiber length of approximately 3.9 mm.

5.6 Acknowledgments

The financial support from the Department of Energy and Oakridge National Lab through grant number 4000122683 is gratefully acknowledged. In addition, the authors would like to thank the department of Material Science and Engineering at Virginia Tech for use of laboratory space and equipment for carrying out the fiber orientation measurements.

5.7 References

1. Silverman, E.M. "Effect of Glass Fiber Length on the Creep and Impact Resistance of Reinforced Thermoplastics." *Journal of Polymer Composites* **8** (1) (1987): 8-15.
2. Hassan, A., et al. "Tensile, Impact and Fiber Length Properties of Injection-Molded Short and Long Glass Fiber-Reinforced Polyamide 6,6 Composites." *Journal of Reinforced Plastics and Composites* **23** (9) (2004): 969-986.
3. Hassan, A.B., et al. "The Properties of Injection Molded, Short and Long Carbon Fiber Reinforced Polyamide 6,6 Composites." *Annual Technical Conference - Society of Plastics Engineers* **59th (Volume 2)** (2001): 2017-2021.
4. Thomason, J.L. "The Influence of Fibre Length, Diameter and Concentration on the Impact Performance of Long Glass-Fibre Reinforced Polyamide 6,6." *Composites: Part A* **40** (2009): 114-124.
5. Thomason, J.L. "The Influence of Fibre Length and Concentration on the Properties of Glass Fibre Reinforced Polypropylene: 5. Injection Moulded Long and Short Fibre Pp." *Composites: Part A* **33** (2002): 1641-1652.
6. Chin, W.-K., et al. "Effects of Fiber Length and Orientation Distribution on the Elastic Modulus of Short Fiber Reinforced Thermoplastics." *Polymer Composites* **9** (1) (1988): 27-35.
7. Hashemi, S. and Koohgilani, M. "Fracture Toughness of Injection Molded Glass Fiber Reinforced Polypropylene." *Polymer Engineering & Science* **35** (13) (1995): 1124-1132.
8. Barkoula, N.M., et al. "Effect of Compounding and Injection Molding on the Mechanical Properties of Flax Fiber Polypropylene Composites." *Journal of Reinforced Plastics and Composites* **29** (9) (2010): 1366-1385.
9. Advani, S.G. and Tucker, C.L. "The Use of Tensors to Describe and Predict Fiber Orientation in Short Fiber Composites." *Journal of Rheology* **31** (8) (1987): 751-784.
10. Jeffery, G.B. "The Motion of Ellipsoidal Particles Immersed in a Viscous Fluid." *Proc. R. Soc. Lond. A* **102** (1922): 161-179.
11. Chung, D.H. and Kwon, T.H. "Invariant-Based Optimal Fitting Closure Approximation for the Numerical Prediction of Flow-Induced Fiber Orientation." *J. Rheol.* **46** (1) (2002): 169-194.
12. Folgar, F. and Tucker, C.L. "Orientation Behavior of Fibers in Concentrated Suspensions." *Journal of Reinforced Plastics and Composites* **3** (2) (1984): 98-119.
13. Hine, P.J., et al. "Measuring the Fiber Orientation and Modelling the Elastic Properties of Injection-Moulded Long-Glass-Fiber-Reinforced Nylon." *Composites Science and Technology* **53** (1994): 125-131.
14. Vélez-García, G.M., et al. "Unambiguous Orientation in Short Fiber Composites over Small Sampling Area in a Center-Gated Disk." *Composites Part A: Applied Science and Manufacturing* **43** (1) (2012): 104-113.
15. Bay, R.S. and III, C.L.T. "Fiber Orientation in Simple Injection Moldings. Part I: Theory and Numerical Methods." *Polymer Composites* **13** (4) (1992): 317-331.
16. Bay, R.S. and III, C.L.T. "Stereological Measurement and Error Estimates for Three-Dimensional Fiber Orientation." *Polymer Engineering & Science* **32** (4) (1992): 240-252.
17. Ortman, K., et al. "Using Startup of Steady Shear Flow in a Sliding Plate Rheometer to Determine Material Parameters for the Purpose of Predicting Long Fiber Orientation." *Journal of Rheology* **56** (4) (2012): 955-981.
18. Meyer, K.J., et al. "Initial Conditions for Simulating Glass Fiber Orientation in the Filling of Center-Gated Disks." *Composites: Part A* **49** (0) (2013): 192-202.

19. Strautins, U. and Latz, A. "Flow-Driven Orientation Dynamics of Semiflexible Fiber Systems." *Rheol Acta* **46** (2007): 1057-1064.
20. Nguyen, B.N., et al. "Fiber Length and Orientation in Long-Fiber Injection-Molded Thermoplastics – Part I: Modeling of Microstructure and Elastic Properties." *Journal of Composite Materials* **42** (10) (2008): 1003-27.
21. Ortman, K. "Prediction of Fiber Orientation in the Injection Molding of Long Fiber Suspensions." *POLYMER COMPOSITES* **33** (8) (2012): 1360-1367.
22. Meyer, K.J., et al. *Composites Part A: Applied Science and Manufacturing* (2013 (Accepted)):
23. Ortman, K.C., et al. "Prediction of Fiber Orientation in the Injection Molding of Long Fiber Suspensions." *Journal of Composite Materials (Accepted)* (2012):
24. Meyer, K.J. (2013 (In Preparation)):
25. Hofmann, J.T., et al. "Extension and Validation of the Method of Ellipses to Long, Semi-Flexible Fibers in Fully 3-Dimensional Flow." (2013 (In Preparation)):
26. Velez-Garcia, G., et al. "Sample Preparation and Image Acquisition Using Optical-Reflective Microscopy in the Measurement of Fiber Orientation in Thermoplastic Composites." *Journal of Microscopy* **248** (1) (2012): 23-33.
27. Hofmann, J.T., et al. "Application and Evaluation of the Method of Ellipses for Measuring the Orientation of Long, Semi-Flexible Fibers." *POLYMER COMPOSITES* (2013):
28. Meyer, K.J., et al. "Prediction of Short Glass Fiber Orientation in the Filling of an End-Gated Plaque." *Composites: Part A* (2013 (Accepted)):
29. Sepehr, M. "Rheological Properties of Short Fiber Filled Polypropylene in Transient Shear Flow." *Journal of Non-Newtonian Fluid Mechanics* **123** (1) (2004): 19-32.
30. Eberle, A.P.R., et al. "Fiber Orientation Kinetics of a Concentrated Short Glass Fiber Suspension in Startup of Simple Shear Flow." *Journal of Non-Newtonian Fluid Mechanics* **165** (2010): 110-119.
31. LFR, S. "The Matlab Ode Suite."
32. Chen, C.H. and Cheng, C.H. "Effective Elastic Moduli of Misoriented Short-Fiber Composites." *International journal of solids and structures* **33** (17) (1996): 2519-2539.
33. Camacho, C.W., et al. "Stiffness and Thermal Expansion Predictions for Hybrid Short Fiber Composites." *POLYMER COMPOSITES* **11** (4) (2004): 229-239.
34. Hofmann, J.T., et al. "Application and Evaluation of the Method of Ellipses for Measuring the Orientation of Long, Semi-Flexible Fibers." *POLYMER COMPOSITES* **34** (3) (2013): 390-398.

5.8 Figures

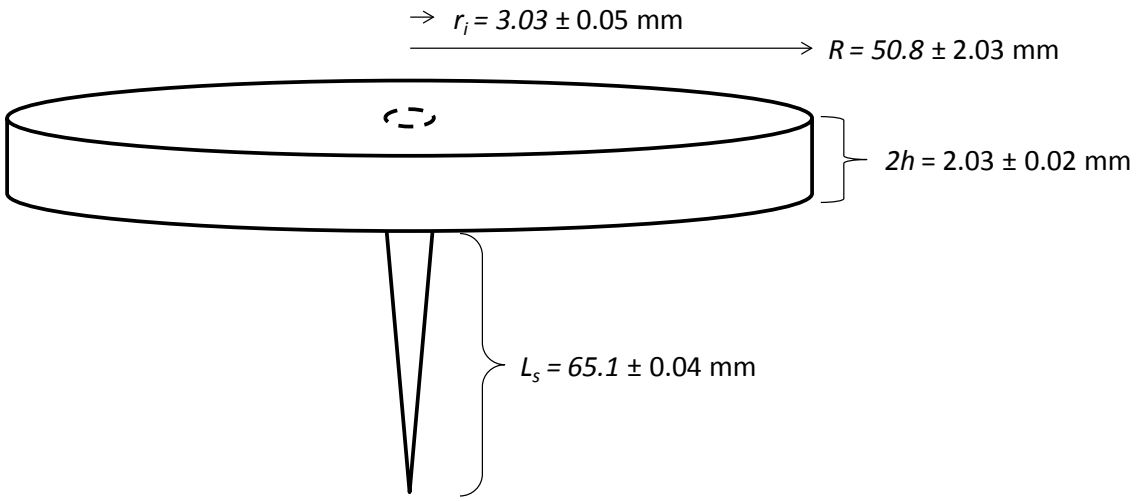

Figure 5.1. The center-gated disc (CGD). The inspection planes for comparing experimental and predicted values of fiber orientation was along a line of constant theta, and 10, 40, and 90% of *L*.

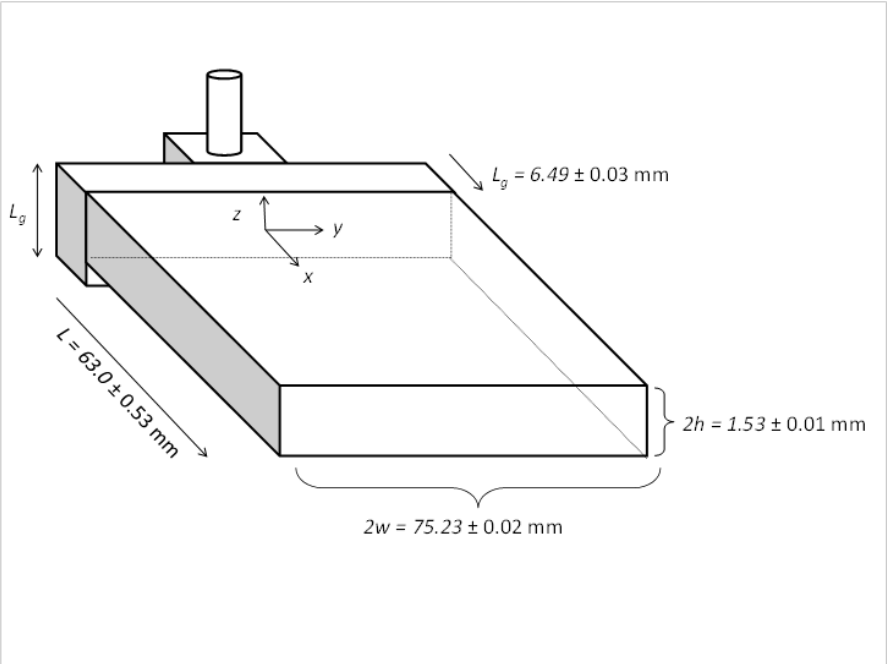

Figure 5.2. The end-gated plaque (EGP). Inspection planes for comparing experimental and predicted values of fiber orientation were located along lines of interest at 0, 50, and 90% of *w*, and 10, 40, and 90% of *L*.

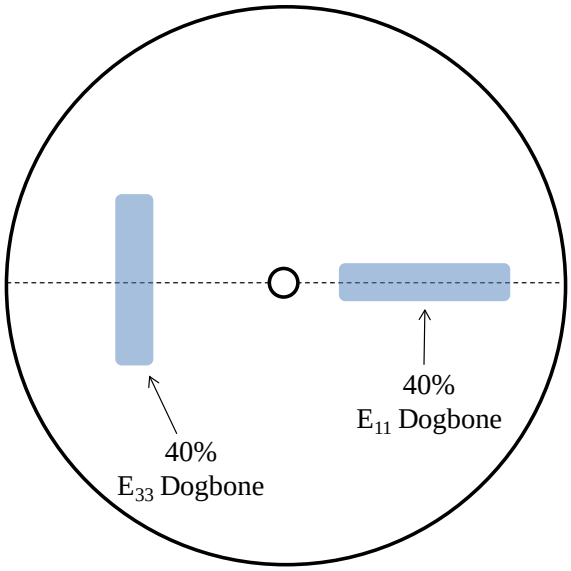

Figure 5.3. Location of the mechanical testing samples for the center-gated disc (E_{11} and E_{33}).

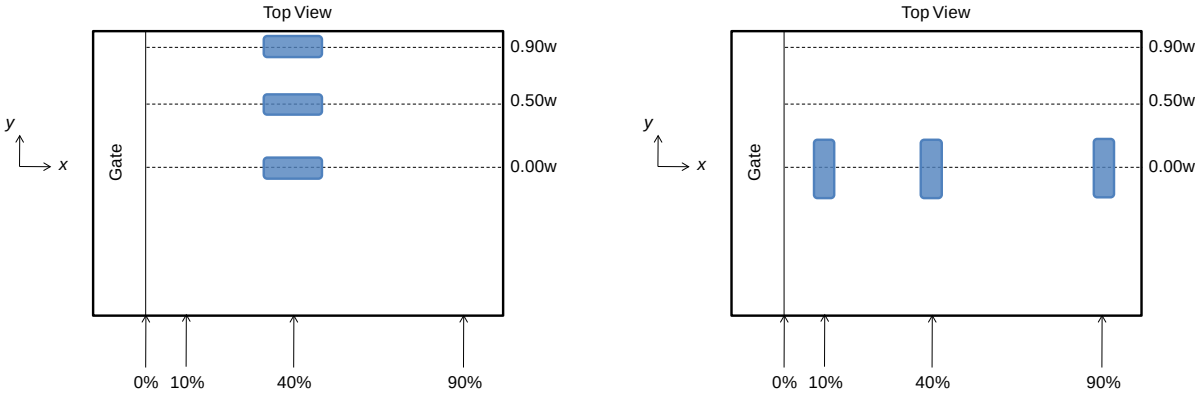

Figure 5.4. Location of mechanical testing samples for the end-gated plaque for (a) E_{11} (i.e. the flow-direction modulus), and (b) E_{33} (i.e. the transverse modulus).

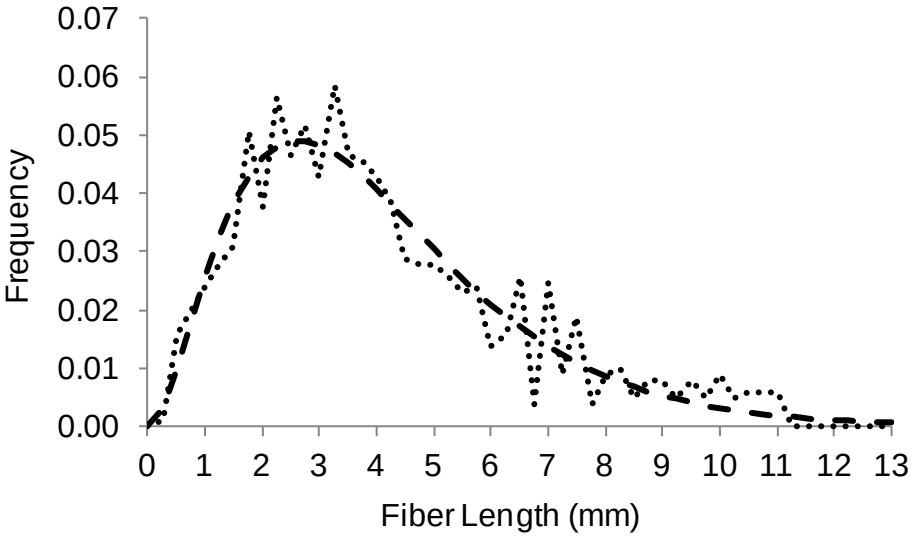

Figure 5.5. Experimental Fiber Length Distribution (FLD) (dotted line) and corresponding Weibull Fit (dashed line).

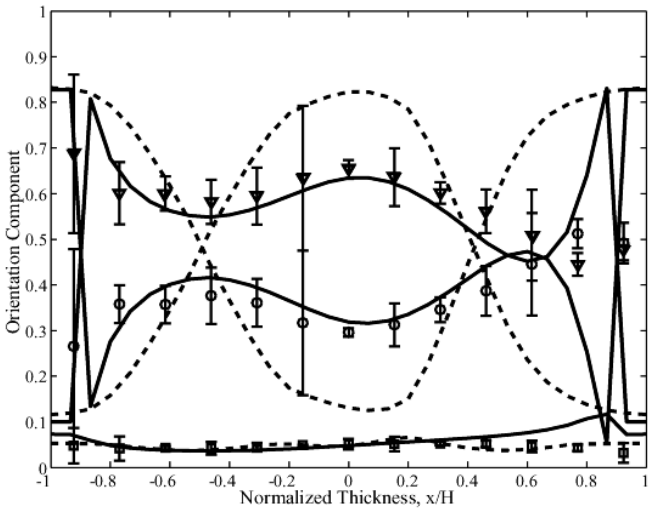

Figure 5.6. Predicted and experimental orientation data within the center-gated disc at 40% of flow, for the rigid rod (----) and bead-rod models (–) for (○) R_{rr}, (∇) $R_{\theta\theta}$, and (▪) R_{zz}.

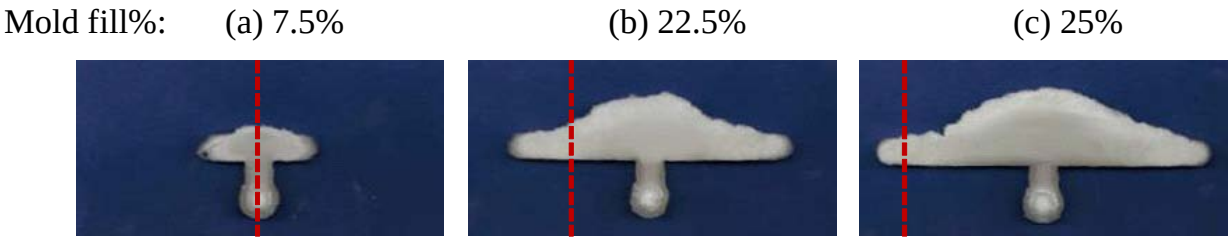

Figure 5.7. Short shots of the end-gated plaque mold displaying the irregular advancing front at low fill percentages. The dashed red lines represent lines of interest at 0, 50, and 90% of plaque width at (a) 7.5, (b) 22.5, and (c) 25% short shots, respectively.

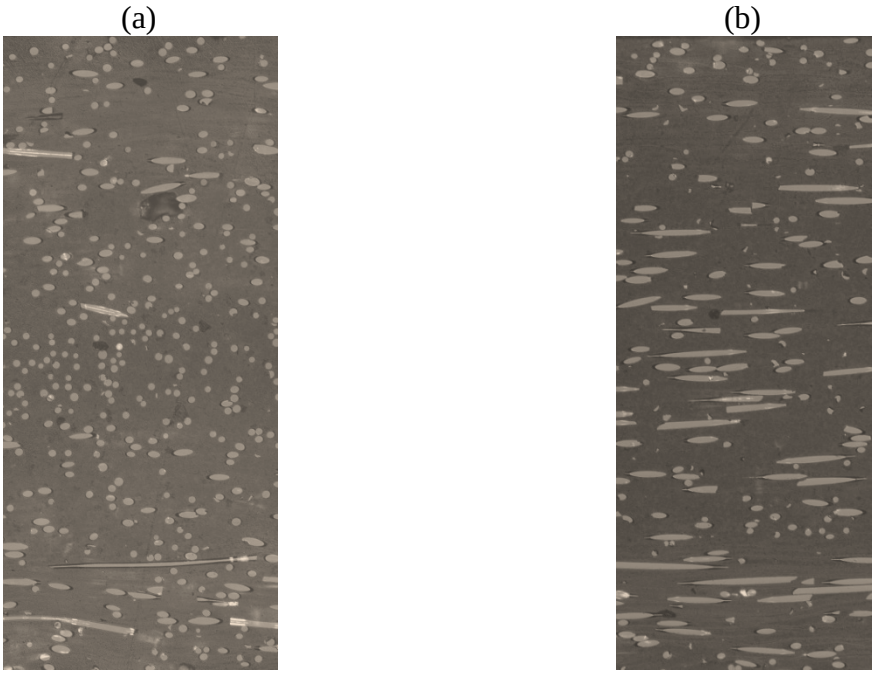

Figure 5.8. A segment of the polished *x*-*z* plane of an EGP at 40% of mold fill along a line of (a) 0%, and (b) 90% of plaque width. Each image has dimensions of 0.70 x 1.53 mm in the *x*- and *z*-directions, respectively.

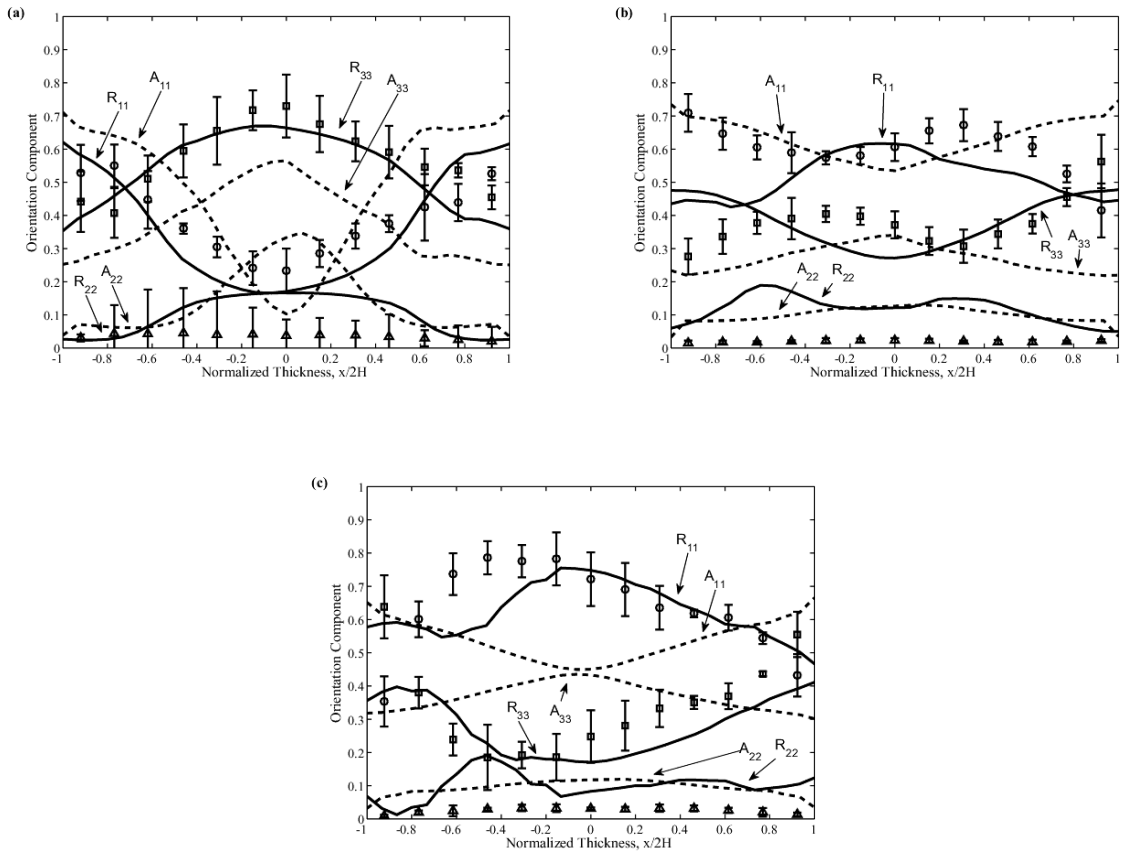

Figure 5.9. Fiber orientation predictions at 40% of the mold fill using the rigid (--) and semi-flexible (-) fiber models compared to experimental data (R_{11} – ○, R_{22} – Δ and R_{33} – □) at (a) 0% of the mold width, (b) 50% of the mold width and (c) 90% of the mold width.

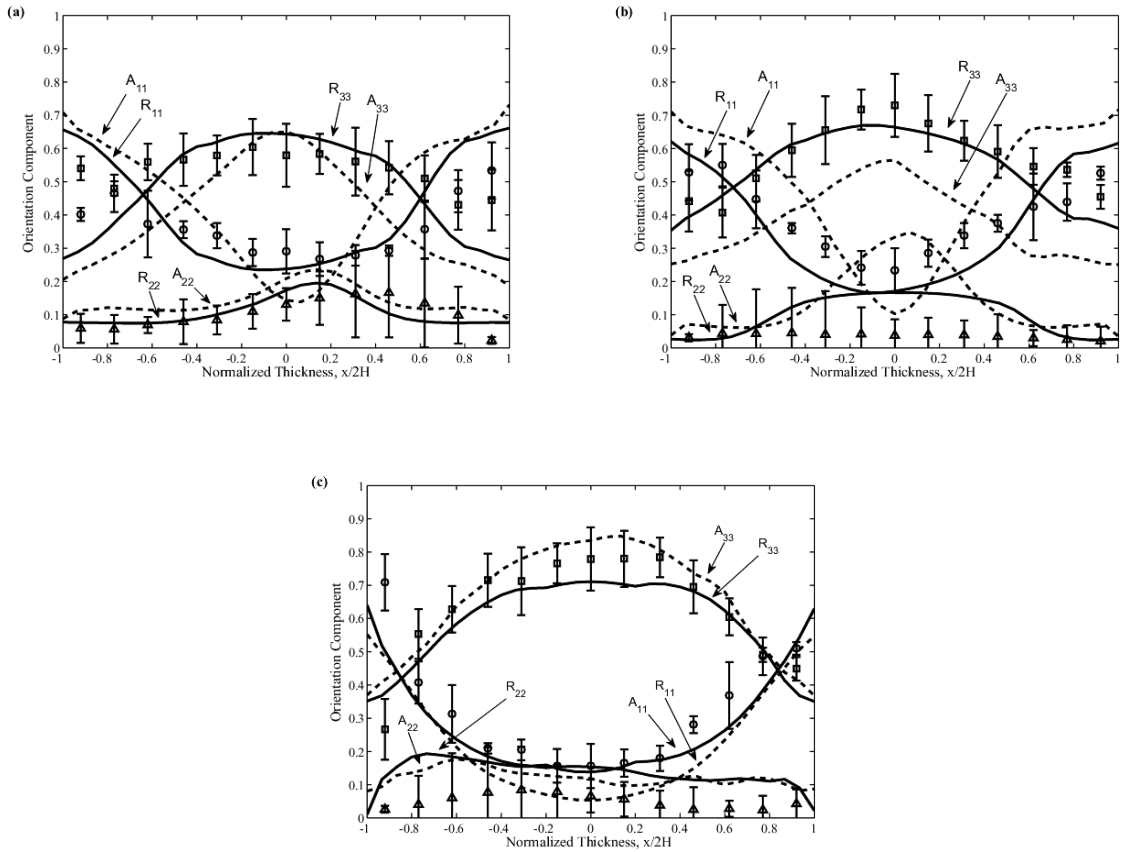

Figure 5.10. Fiber orientation predictions at 0% of the mold width using the rigid (--) and semi-flexible (-) fiber models compared to experimental data (R_{11} – ○, R_{22} – Δ and R_{33} – □) at (a) 10%, (b) 50%, and (c) 90% of the plaque length, *L*.

Table 5.1. Comparison of predicted vs. actual values of flow-direction modulus (E_{rr}, GPa) at 40% of flow of the center-gated disc

	E_{xx} (GPa)
Predicted E_{xx} (Rigid-Rod FOD)	5.155
Predicted E_{xx} (Flexible-Rod FOD)	3.322
Predicted E_{xx} (Experimental FOD)	2.912
Experimental E_{xx}	2.79 ± 0.212

Table 5.2. Comparison of predicted vs. actual values of flow-direction modulus (E_{xx}, GPa) at 40% of flow at multiple percentages of plaque width

	0% of plaque width	50% of plaque width	90% of plaque width
Predicted E_{xx} (Rigid-Rod FOD)	4.62	5.69	4.81
Predicted E_{xx} (Flexible-Rod FOD)	3.74	4.67	5.71
Predicted E_{xx} (Experimental FOD)	3.88	5.78	6.11
Experimental E_{xx}	3.94 ± 0.26	5.41 ± 0.39	6.65 ± 0.44

Table 5.3. Comparison of predicted vs. actual values of transverse-direction modulus (E_{yy}, GPa) at multiple percentages of flow along the centerline

	10% of flow	40% of flow	90% of flow
Predicted E_{yy} (Rigid-Rod FOD)	3.97	3.76	6.21
Predicted E_{yy} (Flexible-Rod FOD)	4.60	4.99	5.43
Predicted E_{yy} (Experimental FOD)	4.93	5.31	6.26
Experimental E_{yy}	4.13 ± 0.37	5.15 ± 0.49	5.57 ± 0.60

Chapter 6 : Conclusions and Recommendations for Future Research

6.1: Conclusions from this Research

The following conclusions encompass the novel contributions resultant from this research corresponding to the objectives as laid out in Chapter 1:

1. The Method of Ellipses (MoE) for measuring rigid fiber orientation was successfully extended to semi-flexible fibers under certain conditions via the primary modification of increasing the width of the image analysis region (also known as the "bin" width) in areas of highly aligned fibers.

   Extension of the method was shown to be valid within the axisymmetric center-gated disc due to the highly transverse alignment of long fibers observed by moderate fill percentages. Within regions of highly flow-aligned fibers, such as within 1-D simple shear or regions of shear-dominated 3-D flow within the end-gated plaque, it was shown that the MoE had to be modified by increasing the image analysis region in order to minimize partial ellipses and decrease error. Minimal fiber curvature was necessary for the valid application of the traditional inspection plane of the Method of Ellipses.

2. The experimental extent of fiber curvature was quantified within samples obtained from injection molded test geometries and demonstrated that flexibility was minimal on average for the selected fiber length distribution, both in terms of the fraction of flexed fibers and in the average extent of curvature.

Development of the top view curvature method has allowed for quantification of the extent of fiber curvature throughout the selected test geometries in order to identify potential limitations of the traditional MoE, such as within the gate and mold entry region. The experimental extent of fiber curvature, however, was shown to be minimal within the channel flow far from the gate and entry region of the injection molded parts and fiber length distribution selected for analysis in this study. As a result, this has allowed for the valid application of the traditional MoE with use of the modified image analysis region.

3. In cases where fiber bending was observed, the experimental components of the end-to-end orientation tensor (R_{ij}) obtained via the Top View Method of Ellipses confirmed the application of the conventional inspection plane of the traditional MoE (A_{ij}), provided that the modified image analysis width was utilized, due to the small percentage of flexed fibers present within the selected system.

A novel technique to ascertain the components of the second moment of the end-to-end orientation tensor, R_{ij}, was developed. This method was utilized to obtain experimental values of R_{ij} at multiple locations within the center-gated disc and the end-gated plaque, both as a function of flow, plaque width, and part through-thickness. A comparison of the experimental A_{ij} and R_{ij} data showed good agreement in both geometries at the selected locations evaluated. The results indicated that while flexibility was present, the average extent of curvature and the fraction of flexed fibers was minimal on average. Thus, the extent of fiber bending within the selected system was shown to have minimal impact on the

computation of the orientation tensor when utilizing the traditional through-thickness inspection plane.

4. The experimental and predicted orientation distributions of long glass fibers were observed to be more broad and uniform through the part thickness with a distinct lack of the traditional core-shell distribution relative to to short, rigid glass fibers which were seen to more readily orient in flow, potentially as a result of a reduced number of inter-fiber interactions and decreased hindrances to orientation evolution kinetics.

   In this research the experimental orientation distributions of both short and long glass fibers were obtained within two basic test geometries, the center-gated disc and the end-gated plaque, were investigated in an effort to ascertain the effect of increased aspect ratio on the experimental fiber orientation distributions ([Appendix]). Within the center-gated disc it was shown that while short glass fibers develop into the well-predicted core-shell profile, long glass fibers exhibit a broader and predominantly transverse distribution, with the majority of the fibers oriented around the circumference of the disc on average. Therefore, minimal fiber curvature is observed in moderate fill percentages of the disc. Within the end-gated plaque, a similar trend is observed along the centerline of the geometry. This was attributed to the fact that the centerline is a plane of symmetry and as such results in a similar filling behavior as that observed within the center-gated disc. However, within the regions of high deformation near the mold side walls, the majority of fibers are seen to align predominantly in the flow direction. In this region, short glass fibers were seen to orient in the flow direction more so than longer fibers, potentially attributed to the reduced number of inter-fiber interactions and

resulting faster orientation evolution kinetics. In addition, fiber orientation was investigated within the most complex flow regimes of the parts, including the sprue and gate ([Appendix]). The results in the complex entry regions have provided a solid foundation for the initial fiber orientation conditions required for the simulation and modeling of fiber orientation evolution in the filling of injection molded parts.

5. Experimental and predicted orientation distributions were coupled with lamination theory to accurately predict the global modulus of long, semi-flexible glass fiber-reinforced composites with the Bead-Rod model predictions of orientation coupled with lamination theory predicting modulus values which were noticeable better than values obtained using the rigid rod model.

Emphasis was placed on evaluating fiber orientation distributions and the result on modulus within the end-gated plaque, a complex geometry which exhibits a fully 3-dimensional flow field. The resulting data ([Appendix]) demonstrated a complex fiber orientation distribution across both the flow direction and the width of the plaque portion of the mold cavity. This complex fiber orientation distribution resulted in a complex distribution of modulus across the width of the plaque. Both experimental and simulated orientation data were utilized to predict the global modulus of the plaque by coupling the data with lamination theory and showed good agreement. Predictions of orientation data provided via the Bead-Rod model were demonstrated to more accurately predict the modulus when coupled with lamination theory as compared to predictions obtained using the simulated Rigid Rod orientation distribution data.

6.2: Recommendations for Future Research

Several key areas of investigation will need to be pursued in order to continue this research, including:

1. Ascertain if the traditional Method of Ellipses will remain valid when applied to long glass fiber-reinforced injection molded parts formed under a variety of processing conditions (fill time, cavity thickness, mold temperature) as the processing conditions may influence fiber configuration and orientation.

   The preceding chapters have discussed the extension of the MoE to long, semi-flexible fibers within the fully 3-dimensional end-gated plaque, including ascertaining the experimental extent of fiber curvature within the geometry. However, the work in this dissertation has focused on the validity of the MoE and developing methods to quantify fiber curvature under a narrow set of injection molding processing parameters. As a result, it will be necessary to continue efforts in this area to assess the validity of the MoE for LGF within the EGP and the resulting mechanical properties of plaques produced under a variety of processing parameters. Specifically, the effect of various processing parameters such as mold dimensions, mold fill time, mold temperature, and fiber fraction will need to be addressed in order to complete a thorough analysis of the MoE.

2. Test the ruggedness of the Bead-Rod Model by obtaining a more thorough set of experimental orientation data from a wide array of processing conditions to compare to simulated orientation distributions.

In order to evaluate the overall performance of the Bead-Rod model for simulation the orientation evolution of long, semi-flexible fibers, it will be necessary to compare simulated and experimental orientation distribution data across a wide array of processing parameters. By doing this, it will be possible to complete a thorough evaluation of the Bead-Rod model and to identify any potential weakness in the model that may be observed dependent on the injection molding parameters.

3. Determine at what point the traditional MoE breaks down and the Top View Method of Ellipses becomes necessary for long glass fibers due to flexibility by increasing average length such that significant curvature will be observed.

   As fiber flexibility increases, the difference in orientation computed using the conventional inspection plane (A_{ij}) and the end-to-end tensor computed using the top view MoE (R_{ij}) will be expected to increase. At some level of flexibility, it will no longer be valid to utilize the conventional inspection plane and the traditional MoE. As such, it will be necessary to evaluate the experimental orientation distribution of long glass fibers when significant fiber curvature is present. Two potential methods may be pursued in order to obtain samples with significant curvature by reexamining the effective flexibility parameter originally defined in Chapter 2. First, increased values of f_{eff} may be obtained by altering the mold fill time to increase the shear rate. However, manipulation of the final, post-processing fiber length distribution may be a more desirable avenue to obtain increased curvature due to the dominance of the aspect ratio in determining the effective flexibility parameter.

4. Investigate the extension and validity of the Method of Ellipses for injection molded composites reinforced with long, discontinuous carbon fibers, including quantifying the experimental extent of fiber curvature, due to the fact that carbon fibers possess an increased modulus when compared to that of glass, but may exhibit increased flexibility.

   Due to the desire to increase mechanical properties of composites, additional research on the use of discontinuous carbon fibers as a filling agent will need to be completed. Carbon fibers possess an axial modulus of approximately three times that of glass while only having approximately half the average diameter [1]. As a result, the aspect ratio of carbon fibers is significantly higher, leading to an increased potential to exhibit flexibility and fiber curvature if length can be mantained. Thus, significant efforts will need to spent on evaluating the extent of this curvature in injection molded composites as well as the effectiveness of Method of Ellipses.

5. Determine if the experimentally observed fiber clustering of long glass fibers is the result of poor dispersion in the screw or rather a phenomenon resultant from preferential fiber alignment during flow and the mold filling process.

   Long glass fiber materials have been shown to exhibit an increase in fiber clustering (Chapter 3), which may have a significant impact on mechanical properties and lead to anisotropy within a molded part. These clusters may be the result of poor dispersion in the screw, or potentially due to a preferential alignment of fibers during flow as the mold is being filled. As a result, research into understanding this phenomenon is necessary in order to be able to

mitigate the formation of clusters in the molding process. Additionally, voids have also been experimentally observed in significant quantities in LGF injection molding composites (Chapter 3) unlike with SGF materials. Predictions of fiber orientation and mechanical properties could be improved by incorporating the presence of voids into the models and simulations for two reasons. First, studies have shown that the increased strength of fiber-reinforced composites is attributed to the effective contact area of the reinforcing fibers with the polymer matrix [2]. Therefore, neglecting the increased presence of voids within LGF composites could result in potentially over predicting the actual mechanical response of the part. Second, a large void content may have an impact on the fiber orientation evolution kinetics, resulting in a disparity between predicted and actual orientation.

6.3: References

1. Chen, C.H. and Cheng, C.H. "Effective Elastic Moduli of Misoriented Short-Fiber Composites." *International journal of solids and structures* **33** (17) (1996): 2519-2539.
2. Kumar, K.S.S., et al. "Effect of Fiber Length and Composition on Mechanical Properties of Carbon Fiber-Reinforced Polybenzoxazine." *Polymers for Advanced Technologies* **19** (2008): 895-904.

Appendix A. Geometries and Dimensions: Center-Gated Disc and End-Gated Plaque

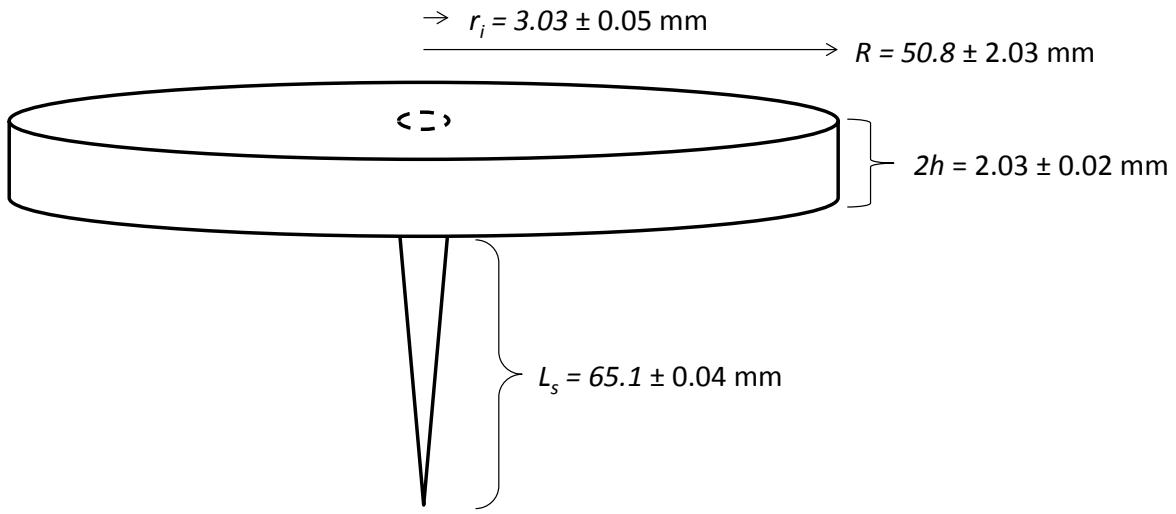

Figure A.1. The Center Gated Disc (CGD) geometry and dimensions.

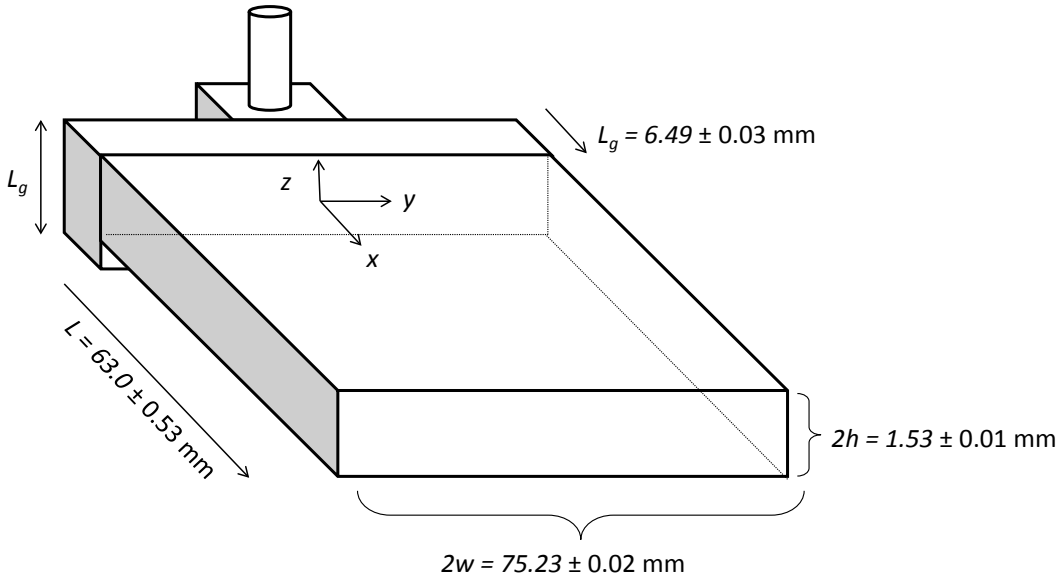

Figure A.2. The End-Gated Plaque (EGP) geometry and dimensions.

Appendix B. Center-Gated Disc Orientation Data (SGF vs. LGF)

Table B.1. Average experimental orientation data and corresponding error within the CGD for short (A_{rr}) and long (R_{rr}) glass fibers at 00 % of flow.

LGF - 0.7 mm z/h			LGF 5.5 mm z/h			SGF		
z/h	Mean	Error	z/h	Mean	Error	z/h	Mean	Error
0.92	0.56	0.09	-0.92	0.54	0.03	0.92	0.70	0.06
0.77	0.73	0.03	-0.77	0.33	0.03	0.75	0.73	0.07
0.62	0.60	0.06	-0.62	0.55	0.04	0.58	0.71	0.06
0.46	0.40	0.05	-0.46	0.29	0.03	0.42	0.67	0.07
0.31	0.47	0.11	-0.31	0.46	0.07	0.25	0.72	0.06
0.15	0.35	0.06	-0.15	0.43	0.05	0.08	0.60	0.06
0.00	0.27	0.04	0.00	0.30	0.03	-0.08	0.33	0.05
-0.15	0.41	0.07	0.15	0.31	0.08	-0.25	0.58	0.06
-0.31	0.44	0.06	0.31	0.38	0.09	-0.42	0.64	0.06
-0.46	0.38	0.04	0.46	0.53	0.08	-0.58	0.64	0.07
-0.62	0.57	0.08	0.62	0.60	0.02	-0.75	0.51	0.07
-0.77	0.41	0.02	0.77	0.68	0.02	-0.92	0.42	0.07
-0.92	0.48	0.04	0.92	0.56	0.12			

Table B.2. Average experimental orientation data and corresponding error within the CGD for short (A_{rr}) and long (R_{rr}) glass fibers at 10% of flow.

LGF - 0.7 mm z/h			LGF 5.5 mm z/h			SGF		
z/h	Mean	Error	z/h	Mean	Error	z/h	Mean	Error
0.92	0.55	0.03	-0.92	0.51	0.03	0.92	0.55	0.06
0.77	0.46	0.03	-0.77	0.43	0.04	0.75	0.78	0.07
0.62	0.58	0.05	-0.62	0.37	0.03	0.58	0.77	0.06
0.46	0.36	0.08	-0.46	0.41	0.07	0.42	0.57	0.06
0.31	0.24	0.08	-0.31	0.44	0.03	0.25	0.48	0.06
0.15	0.24	0.03	-0.15	0.43	0.04	0.08	0.32	0.04
0.00	0.43	0.06	0.00	0.31	0.05	-0.08	0.34	0.04
-0.15	0.49	0.05	0.15	0.22	0.03	-0.25	0.51	0.05
-0.31	0.35	0.03	0.31	0.29	0.04	-0.42	0.61	0.06
-0.46	0.39	0.11	0.46	0.29	0.02	-0.58	0.63	0.07
-0.62	0.33	0.04	0.62	0.48	0.05	-0.75	0.65	0.07
-0.77	0.49	0.05	0.77	0.51	0.04	-0.92	0.59	0.05
-0.92	0.37	0.06	0.92	0.58	0.05			

Table B.3. Average experimental orientation data and corresponding error within the CGD for short (A_{rr}) and long (R_{rr}) glass fibers at 40% of flow.

LGF - 0.7 mm z/h			LGF 5.5 mm z/h			SGF		
z/h	Mean	Error	z/h	Mean	Error	z/h	Mean	Error
0.92	0.49	0.08	-0.92	0.38	0.03	0.92	0.62	0.06
0.77	0.52	0.11	-0.77	0.39	0.03	0.75	0.72	0.07
0.62	0.53	0.07	-0.62	0.45	0.04	0.58	0.86	0.06
0.46	0.43	0.04	-0.46	0.37	0.04	0.42	0.74	0.06
0.31	0.26	0.06	-0.31	0.30	0.04	0.25	0.59	0.06
0.15	0.20	0.02	-0.15	0.33	0.03	0.08	0.30	0.03
0.00	0.31	0.07	0.00	0.27	0.04	-0.08	0.35	0.03
-0.15	0.36	0.02	0.15	0.17	0.03	-0.25	0.67	0.06
-0.31	0.34	0.05	0.31	0.18	0.03	-0.42	0.85	0.06
-0.46	0.37	0.02	0.46	0.33	0.04	-0.58	0.75	0.06
-0.62	0.42	0.05	0.62	0.55	0.04	-0.75	0.76	0.06
-0.77	0.39	0.05	0.77	0.56	0.03	-0.92	0.65	0.05
-0.92	0.27	0.03	0.92	0.50	0.02			

Table B.4. Average experimental orientation data and corresponding error within the CGD for short (A_{rr}) and long (R_{rr}) glass fibers at 90% of flow.

LGF - 0.7 mm z/h			LGF 5.5 mm z/h			SGF		
z/h	Mean	Error	z/h	Mean	Error	z/h	Mean	Error
0.92	0.46	0.05	-0.92	0.41	0.02	0.92	0.74	0.07
0.77	0.44	0.04	-0.77	0.34	0.04	0.75	0.54	0.05
0.62	0.37	0.03	-0.62	0.35	0.02	0.58	0.58	0.07
0.46	0.32	0.04	-0.46	0.30	0.04	0.42	0.64	0.06
0.31	0.30	0.10	-0.31	0.25	0.03	0.25	0.48	0.06
0.15	0.17	0.04	-0.15	0.28	0.03	0.08	0.21	0.02
0.00	0.16	0.05	0.00	0.20	0.05	-0.08	0.22	0.02
-0.15	0.28	0.05	0.15	0.18	0.05	-0.25	0.54	0.06
-0.31	0.35	0.06	0.31	0.21	0.03	-0.42	0.69	0.06
-0.46	0.35	0.05	0.46	0.30	0.04	-0.58	0.59	0.06
-0.62	0.34	0.06	0.62	0.41	0.03	-0.75	0.70	0.06
-0.77	0.32	0.07	0.77	0.45	0.04	-0.92	0.72	0.07
-0.92	0.48	0.05	0.92	0.54	0.02			

Table B.5. Average experimental orientation data and corresponding error within the CGD for short ($A_{r\theta}$) and long ($R_{r\theta}$) glass fibers at 00% of flow.

LGF - 0.7 mm z/h			LGF 5.5 mm z/h			SGF		
z/h	Mean	Error	z/h	Mean	Error	z/h	Mean	Error
0.92	0.14	0.04	-0.92	-0.01	0.01	0.92	0.01	0.01
0.77	0.18	0.05	-0.77	0.00	0.01	0.75	0.08	0.02
0.62	0.15	0.04	-0.62	-0.06	0.02	0.58	0.09	0.02
0.46	0.06	0.02	-0.46	-0.01	0.01	0.42	0.05	0.02
0.31	0.08	0.04	-0.31	-0.05	0.02	0.25	0.06	0.01
0.15	0.05	0.03	-0.15	-0.06	0.02	0.08	0.06	0.01
0.00	0.00	0.03	0.00	-0.01	0.02	-0.08	0.01	0.01
-0.15	-0.04	0.02	0.15	0.00	0.02	-0.25	-0.04	0.01
-0.31	-0.05	0.01	0.31	0.04	0.03	-0.42	0.00	0.01
-0.46	-0.02	0.01	0.46	-0.01	0.02	-0.58	0.01	0.01
-0.62	-0.04	0.01	0.62	0.08	0.02	-0.75	-0.02	0.02
-0.77	-0.05	0.01	0.77	0.10	0.09	-0.92	0.01	0.01
-0.92	0.00	0.01	0.92	0.07	0.03			

Table B.6. Average experimental orientation data and corresponding error within the CGD for short ($A_{r\theta}$) and long ($R_{r\theta}$) glass fibers at 10% of flow.

LGF - 0.7 mm z/h			LGF 5.5 mm z/h			SGF		
z/h	Mean	Error	z/h	Mean	Error	z/h	Mean	Error
0.92	0.04	0.02	-0.92	0.00	0.02	0.92	0.04	0.02
0.77	0.02	0.02	-0.77	-0.02	0.01	0.75	0.04	0.01
0.62	0.04	0.01	-0.62	-0.01	0.01	0.58	0.04	0.01
0.46	0.01	0.01	-0.46	-0.03	0.01	0.42	0.02	0.01
0.31	0.01	0.01	-0.31	-0.05	0.03	0.25	-0.03	0.01
0.15	-0.01	0.01	-0.15	-0.01	0.03	0.08	-0.02	0.00
0.00	-0.01	0.03	0.00	0.00	0.03	-0.08	-0.05	0.00
-0.15	-0.04	0.01	0.15	0.00	0.01	-0.25	-0.06	0.02
-0.31	-0.02	0.02	0.31	0.00	0.00	-0.42	-0.03	0.02
-0.46	-0.03	0.01	0.46	0.01	0.01	-0.58	-0.03	0.00
-0.62	-0.03	0.01	0.62	0.02	0.01	-0.75	-0.01	0.00
-0.77	0.01	0.01	0.77	0.02	0.02	-0.92	-0.04	0.01
-0.92	0.00	0.02	0.92	0.02	0.01			

Table B.7. Average experimental orientation data and corresponding error within the CGD for short ($A_{r\theta}$) and long ($R_{r\theta}$) glass fibers at 40% of flow.

LGF - 0.7 mm z/h			LGF 5.5 mm z/h			SGF		
z/h	Mean	Error	z/h	Mean	Error	z/h	Mean	Error
0.92	0.02	0.02	-0.92	-0.01	0.01	0.92	0.00	0.01
0.77	0.00	0.02	-0.77	0.00	0.01	0.75	-0.01	0.00
0.62	0.01	0.01	-0.62	-0.02	0.00	0.58	0.02	0.00
0.46	0.03	0.01	-0.46	-0.01	0.01	0.42	0.03	0.03
0.31	0.01	0.01	-0.31	-0.01	0.02	0.25	0.01	0.01
0.15	0.01	0.03	-0.15	-0.02	0.02	0.08	0.02	0.01
0.00	0.00	0.02	0.00	0.00	0.02	-0.08	-0.02	0.01
-0.15	-0.04	0.01	0.15	0.01	0.01	-0.25	-0.04	0.01
-0.31	-0.03	0.01	0.31	0.01	0.02	-0.42	-0.02	0.02
-0.46	-0.01	0.02	0.46	0.01	0.01	-0.58	-0.01	0.01
-0.62	-0.01	0.01	0.62	-0.01	0.01	-0.75	0.00	0.01
-0.77	-0.02	0.01	0.77	0.01	0.01	-0.92	-0.05	0.01
-0.92	-0.01	0.01	0.92	0.00	0.01			

Table B.8. Average experimental orientation data and corresponding error within the CGD for short ($A_{r\theta}$) and long ($R_{r\theta}$) glass fibers at 90% of flow.

LGF - 0.7 mm z/h			LGF 5.5 mm z/h			SGF		
z/h	Mean	Error	z/h	Mean	Error	z/h	Mean	Error
0.92	0.04	0.03	-0.92	-0.02	0.01	0.92	-0.03	0.01
0.77	0.00	0.01	-0.77	-0.01	0.01	0.75	-0.04	0.01
0.62	0.03	0.03	-0.62	0.00	0.01	0.58	-0.05	0.03
0.46	0.02	0.01	-0.46	0.00	0.01	0.42	-0.04	0.01
0.31	0.01	0.02	-0.31	0.00	0.01	0.25	-0.02	0.01
0.15	0.01	0.03	-0.15	-0.01	0.01	0.08	-0.01	0.01
0.00	0.01	0.02	0.00	0.00	0.01	-0.08	-0.05	0.01
-0.15	0.00	0.03	0.15	0.02	0.01	-0.25	-0.05	0.01
-0.31	-0.01	0.01	0.31	0.03	0.01	-0.42	-0.02	0.01
-0.46	0.01	0.01	0.46	0.03	0.02	-0.58	-0.01	0.01
-0.62	0.01	0.01	0.62	0.03	0.02	-0.75	0.00	0.01
-0.77	-0.01	0.01	0.77	0.00	0.01	-0.92	0.03	0.01
-0.92	0.00	0.03	0.92	0.04	0.02			

Table B.9. Average experimental orientation data and corresponding error within the CGD for short (A_{rz}) and long (R_{rz}) glass fibers at 00% of flow.

LGF - 0.7 mm z/h			LGF 5.5 mm z/h			SGF		
z/h	Mean	Error	z/h	Mean	Error	z/h	Mean	Error
0.92	0.07	0.03	-0.92	-0.01	0.01	0.92	0.02	0.06
0.77	0.04	0.04	-0.77	0.01	0.01	0.75	0.03	0.08
0.62	0.20	0.04	-0.62	-0.12	0.03	0.58	-0.03	0.06
0.46	0.22	0.02	-0.46	-0.04	0.02	0.42	-0.04	0.08
0.31	0.20	0.03	-0.31	-0.11	0.03	0.25	-0.06	0.07
0.15	0.14	0.03	-0.15	-0.14	0.03	0.08	-0.12	0.07
0.00	0.03	0.02	0.00	0.00	0.05	-0.08	0.03	0.05
-0.15	-0.04	0.02	0.15	0.00	0.03	-0.25	0.07	0.06
-0.31	0.04	0.08	0.31	0.04	0.03	-0.42	0.11	0.07
-0.46	0.04	0.03	0.46	0.02	0.01	-0.58	0.05	0.07
-0.62	0.00	0.02	0.62	0.12	0.02	-0.75	-0.06	0.08
-0.77	-0.10	0.03	0.77	0.08	0.01	-0.92	0.09	0.08
-0.92	0.09	0.02	0.92	0.06	0.06			

Table B.10. Average experimental orientation data and corresponding error within the CGD for short (A_{rz}) and long (R_{rz}) glass fibers at 10% of flow.

LGF - 0.7 mm z/h			LGF 5.5 mm z/h			SGF		
z/h	Mean	Error	z/h	Mean	Error	z/h	Mean	Error
0.92	-0.05	0.04	-0.92	0.00	0.06	0.92	0.08	0.07
0.77	0.06	0.03	-0.77	0.00	0.06	0.75	0.09	0.07
0.62	0.06	0.00	-0.62	-0.02	0.05	0.58	-0.01	0.07
0.46	0.04	0.02	-0.46	-0.06	0.05	0.42	0.06	0.07
0.31	-0.01	0.02	-0.31	-0.07	0.06	0.25	-0.03	0.07
0.15	0.09	0.02	-0.15	-0.02	0.05	0.08	-0.04	0.06
0.00	-0.03	0.02	0.00	-0.02	0.05	-0.08	-0.03	0.06
-0.15	-0.07	0.02	0.15	0.01	0.04	-0.25	0.11	0.07
-0.31	-0.04	0.08	0.31	0.03	0.03	-0.42	0.03	0.09
-0.46	0.02	0.02	0.46	0.05	0.03	-0.58	0.05	0.09
-0.62	-0.07	0.01	0.62	0.08	0.03	-0.75	0.06	0.07
-0.77	0.11	0.02	0.77	0.07	0.02	-0.92	0.10	0.06
-0.92	-0.08	0.02	0.92	0.09	0.03			

Table B.11. Average experimental orientation data and corresponding error within the CGD for short (A_{rz}) and long (R_{rz}) glass fibers at 40% of flow.

LGF - 0.7 mm z/h			LGF 5.5 mm z/h			SGF		
z/h	Mean	Error	z/h	Mean	Error	z/h	Mean	Error
0.92	-0.01	0.01	-0.92	0.01	0.05	0.92	0.05	0.07
0.77	-0.10	0.02	-0.77	0.01	0.05	0.75	0.04	0.07
0.62	0.01	0.03	-0.62	0.00	0.06	0.58	-0.02	0.06
0.46	0.03	0.01	-0.46	-0.01	0.05	0.42	0.00	0.07
0.31	-0.01	0.03	-0.31	-0.02	0.06	0.25	0.06	0.07
0.15	-0.09	0.02	-0.15	0.00	0.05	0.08	-0.10	0.06
0.00	-0.05	0.02	0.00	0.03	0.05	-0.08	-0.10	0.06
-0.15	0.00	0.02	0.15	0.03	0.03	-0.25	0.07	0.07
-0.31	-0.07	0.06	0.31	0.05	0.03	-0.42	0.06	0.06
-0.46	-0.04	0.01	0.46	0.04	0.03	-0.58	0.05	0.07
-0.62	0.03	0.02	0.62	0.04	0.04	-0.75	0.02	0.07
-0.77	0.01	0.02	0.77	0.06	0.04	-0.92	0.05	0.06
-0.92	-0.19	0.02	0.92	0.06	0.05			

Table B.12. Average experimental orientation data and corresponding error within the CGD for short (A_{rz}) and long (R_{rz}) glass fibers at 90% of flow.

LGF - 0.7 mm z/h			LGF 5.5 mm z/h			SGF		
z/h	Mean	Error	z/h	Mean	Error	z/h	Mean	Error
0.92	-0.01	0.03	-0.92	0.00	0.06	0.92	0.10	0.07
0.77	-0.19	0.04	-0.77	0.04	0.04	0.75	-0.03	0.07
0.62	0.05	0.02	-0.62	0.04	0.04	0.58	0.12	0.07
0.46	0.04	0.02	-0.46	0.03	0.04	0.42	0.06	0.07
0.31	0.10	0.03	-0.31	0.02	0.05	0.25	0.05	0.07
0.15	0.08	0.04	-0.15	0.03	0.06	0.08	-0.03	0.05
0.00	0.02	0.05	0.00	0.05	0.05	-0.08	-0.02	0.05
-0.15	0.01	0.01	0.15	0.06	0.04	-0.25	0.06	0.07
-0.31	-0.08	0.07	0.31	0.09	0.03	-0.42	0.00	0.06
-0.46	-0.01	0.03	0.46	0.10	0.03	-0.58	0.06	0.07
-0.62	-0.01	0.03	0.62	0.08	0.04	-0.75	0.11	0.07
-0.77	-0.06	0.03	0.77	0.04	0.05	-0.92	0.04	0.07
-0.92	-0.04	0.01	0.92	0.12	0.03			

A_{22}

Table B.13. Average experimental orientation data and corresponding error within the CGD for short ($A_{\theta\theta}$) and long ($R_{\theta\theta}$) glass fibers at 00% of flow.

LGF - 0.7 mm z/h			LGF 5.5 mm z/h			SGF		
z/h	Mean	Error	z/h	Mean	Error	z/h	Mean	Error
0.92	0.10	0.03	-0.92	0.02	0.01	0.92	0.02	0.06
0.77	0.09	0.02	-0.77	0.04	0.01	0.75	0.04	0.07
0.62	0.07	0.02	-0.62	0.03	0.00	0.58	0.05	0.06
0.46	0.07	0.01	-0.46	0.02	0.01	0.42	0.04	0.07
0.31	0.05	0.01	-0.31	0.05	0.01	0.25	0.03	0.06
0.15	0.05	0.01	-0.15	0.04	0.01	0.08	0.02	0.06
0.00	0.07	0.01	0.00	0.05	0.01	-0.08	0.02	0.05
-0.15	0.04	0.01	0.15	0.04	0.01	-0.25	0.02	0.06
-0.31	0.03	0.01	0.31	0.06	0.02	-0.42	0.02	0.06
-0.46	0.02	0.01	0.46	0.05	0.01	-0.58	0.02	0.07
-0.62	0.02	0.00	0.62	0.04	0.01	-0.75	0.03	0.07
-0.77	0.04	0.01	0.77	0.11	0.04	-0.92	0.02	0.07
-0.92	0.03	0.01	0.92	0.05	0.02			

Table B.14. Average experimental orientation data and corresponding error within the CGD for short ($A_{\theta\theta}$) and long ($R_{\theta\theta}$) glass fibers at 10% of flow.

LGF - 0.7 mm z/h			LGF 5.5 mm z/h			SGF		
z/h	Mean	Error	z/h	Mean	Error	z/h	Mean	Error
0.92	0.02	0.02	-0.92	0.03	0.01	0.92	0.03	0.06
0.77	0.04	0.02	-0.77	0.03	0.01	0.75	0.02	0.07
0.62	0.04	0.02	-0.62	0.04	0.01	0.58	0.03	0.05
0.46	0.05	0.01	-0.46	0.04	0.01	0.42	0.02	0.06
0.31	0.03	0.00	-0.31	0.04	0.01	0.25	0.03	0.06
0.15	0.04	0.01	-0.15	0.04	0.01	0.08	0.02	0.04
0.00	0.03	0.01	0.00	0.05	0.01	-0.08	0.02	0.04
-0.15	0.04	0.01	0.15	0.05	0.02	-0.25	0.03	0.05
-0.31	0.03	0.01	0.31	0.05	0.01	-0.42	0.03	0.06
-0.46	0.04	0.01	0.46	0.05	0.02	-0.58	0.01	0.07
-0.62	0.04	0.01	0.62	0.05	0.02	-0.75	0.01	0.07
-0.77	0.03	0.01	0.77	0.04	0.01	-0.92	0.02	0.05
-0.92	0.04	0.01	0.92	0.04	0.02			

A_{22}

Table B.15. Average experimental orientation data and corresponding error within the CGD for short ($A_{\theta\theta}$) and long ($R_{\theta\theta}$) glass fibers at 40% of flow.

LGF - 0.7 mm z/h			LGF 5.5 mm z/h			SGF		
z/h	Mean	Error	z/h	Mean	Error	z/h	Mean	Error
0.92	0.03	0.01	-0.92	0.03	0.01	0.92	0.02	0.05
0.77	0.05	0.03	-0.77	0.05	0.01	0.75	0.01	0.06
0.62	0.05	0.02	-0.62	0.04	0.01	0.58	0.01	0.06
0.46	0.05	0.02	-0.46	0.05	0.01	0.42	0.04	0.05
0.31	0.05	0.01	-0.31	0.05	0.01	0.25	0.03	0.06
0.15	0.06	0.02	-0.15	0.05	0.01	0.08	0.02	0.04
0.00	0.05	0.01	0.00	0.04	0.01	-0.08	0.02	0.03
-0.15	0.04	0.01	0.15	0.04	0.01	-0.25	0.02	0.06
-0.31	0.05	0.01	0.31	0.05	0.01	-0.42	0.03	0.05
-0.46	0.04	0.01	0.46	0.05	0.02	-0.58	0.02	0.06
-0.62	0.04	0.01	0.62	0.04	0.01	-0.75	0.02	0.06
-0.77	0.04	0.01	0.77	0.04	0.01	-0.92	0.03	0.05
-0.92	0.05	0.01	0.92	0.04	0.01			

Table B.16. Average experimental orientation data and corresponding error within the CGD for short ($A_{\theta\theta}$) and long ($R_{\theta\theta}$) glass fibers at 90% of flow.

LGF - 0.7 mm z/h			LGF 5.5 mm z/h			SGF		
z/h	Mean	Error	z/h	Mean	Error	z/h	Mean	Error
0.92	0.07	0.04	-0.92	0.06	0.01	0.92	0.02	0.06
0.77	0.08	0.04	-0.77	0.06	0.01	0.75	0.03	0.05
0.62	0.09	0.05	-0.62	0.05	0.01	0.58	0.04	0.07
0.46	0.08	0.04	-0.46	0.04	0.01	0.42	0.02	0.06
0.31	0.07	0.02	-0.31	0.05	0.01	0.25	0.02	0.06
0.15	0.06	0.01	-0.15	0.05	0.01	0.08	0.03	0.02
0.00	0.07	0.01	0.00	0.06	0.01	-0.08	0.03	0.02
-0.15	0.05	0.01	0.15	0.06	0.02	-0.25	0.02	0.06
-0.31	0.04	0.00	0.31	0.08	0.01	-0.42	0.03	0.06
-0.46	0.04	0.01	0.46	0.07	0.02	-0.58	0.03	0.06
-0.62	0.04	0.01	0.62	0.08	0.02	-0.75	0.02	0.06
-0.77	0.03	0.01	0.77	0.08	0.03	-0.92	0.03	0.06
-0.92	0.04	0.01	0.92	0.05	0.02			

Table B.17. Average experimental orientation data and corresponding error within the CGD for short ($A_{\theta z}$) and long ($R_{\theta z}$) glass fibers at 00% of flow.

LGF - 0.7 mm z/h			LGF 5.5 mm z/h			SGF		
z/h	Mean	Error	z/h	Mean	Error	z/h	Mean	Error
0.92	0.08	0.04	-0.92	0.04	0.01	0.92	0.01	0.02
0.77	0.06	0.01	-0.77	0.05	0.01	0.75	0.00	0.02
0.62	0.06	0.02	-0.62	0.05	0.01	0.58	0.01	0.03
0.46	0.05	0.03	-0.46	0.04	0.01	0.42	0.01	0.02
0.31	0.06	0.03	-0.31	0.07	0.01	0.25	-0.01	0.02
0.15	0.04	0.03	-0.15	0.06	0.01	0.08	-0.02	0.02
0.00	0.04	0.03	0.00	0.06	0.01	-0.08	-0.02	0.02
-0.15	-0.04	0.02	0.15	0.05	0.01	-0.25	0.00	0.02
-0.31	-0.06	0.01	0.31	0.07	0.02	-0.42	-0.03	0.02
-0.46	-0.04	0.02	0.46	0.04	0.01	-0.58	-0.02	0.02
-0.62	-0.02	0.01	0.62	0.05	0.00	-0.75	-0.01	0.03
-0.77	-0.07	0.03	0.77	0.05	0.01	-0.92	-0.04	0.02
-0.92	-0.01	0.02	0.92	0.05	0.01			

Table B.18. Average experimental orientation data and corresponding error within the CGD for short ($A_{\theta z}$) and long ($R_{\theta z}$) glass fibers at 10% of flow.

LGF - 0.7 mm z/h			LGF 5.5 mm z/h			SGF		
z/h	Mean	Error	z/h	Mean	Error	z/h	Mean	Error
0.92	0.04	0.01	-0.92	0.04	0.00	0.92	0.03	0.02
0.77	-0.01	0.02	-0.77	0.04	0.01	0.75	0.02	0.02
0.62	0.03	0.01	-0.62	0.04	0.01	0.58	0.00	0.02
0.46	0.03	0.01	-0.46	0.05	0.00	0.42	0.02	0.02
0.31	0.02	0.02	-0.31	0.05	0.01	0.25	0.00	0.02
0.15	-0.02	0.02	-0.15	0.05	0.01	0.08	-0.01	0.02
0.00	0.01	0.03	0.00	0.05	0.01	-0.08	-0.01	0.02
-0.15	-0.01	0.01	0.15	0.05	0.01	-0.25	-0.02	0.02
-0.31	-0.01	0.03	0.31	0.05	0.01	-0.42	-0.02	0.02
-0.46	-0.01	0.01	0.46	0.05	0.02	-0.58	-0.02	0.01
-0.62	-0.05	0.01	0.62	0.05	0.01	-0.75	-0.01	0.01
-0.77	0.01	0.02	0.77	0.05	0.01	-0.92	-0.02	0.02
-0.92	-0.03	0.01	0.92	0.05	0.02			

Table B.19. Average experimental orientation data and corresponding error within the CGD for short ($A_{\theta z}$) and long ($R_{\theta z}$) glass fibers at 40% of flow.

LGF - 0.7 mm z/h			LGF 5.5 mm z/h			SGF		
z/h	Mean	Error	z/h	Mean	Error	z/h	Mean	Error
0.92	0.03	0.03	-0.92	0.04	0.00	0.92	0.01	0.02
0.77	0.02	0.02	-0.77	0.05	0.01	0.75	0.00	0.01
0.62	0.02	0.01	-0.62	0.05	0.00	0.58	-0.01	0.01
0.46	0.01	0.01	-0.46	0.05	0.01	0.42	-0.01	0.02
0.31	0.01	0.02	-0.31	0.05	0.01	0.25	-0.02	0.02
0.15	0.01	0.05	-0.15	0.05	0.01	0.08	-0.01	0.01
0.00	-0.02	0.03	0.00	0.05	0.01	-0.08	-0.02	0.01
-0.15	-0.05	0.02	0.15	0.05	0.01	-0.25	-0.02	0.02
-0.31	-0.03	0.02	0.31	0.05	0.01	-0.42	-0.02	0.02
-0.46	-0.05	0.01	0.46	0.06	0.02	-0.58	0.00	0.02
-0.62	-0.03	0.01	0.62	0.05	0.01	-0.75	-0.01	0.01
-0.77	-0.04	0.01	0.77	0.05	0.01	-0.92	-0.03	0.01
-0.92	-0.03	0.04	0.92	0.05	0.01			

Table B.20. Average experimental orientation data and corresponding error within the CGD for short ($A_{\theta z}$) and long ($R_{\theta z}$) glass fibers at 90% of flow.

LGF - 0.7 mm z/h			LGF 5.5 mm z/h			SGF		
z/h	Mean	Error	z/h	Mean	Error	z/h	Mean	Error
0.92	0.03	0.03	-0.92	0.07	0.01	0.92	0.00	0.02
0.77	0.02	0.02	-0.77	0.07	0.01	0.75	0.02	0.02
0.62	0.02	0.04	-0.62	0.06	0.01	0.58	0.01	0.02
0.46	0.02	0.02	-0.46	0.06	0.01	0.42	0.01	0.02
0.31	0.00	0.03	-0.31	0.06	0.01	0.25	0.02	0.02
0.15	0.01	0.05	-0.15	0.06	0.01	0.08	0.02	0.02
0.00	0.03	0.04	0.00	0.07	0.01	-0.08	0.02	0.02
-0.15	0.00	0.04	0.15	0.07	0.01	-0.25	0.01	0.01
-0.31	-0.01	0.01	0.31	0.08	0.01	-0.42	0.01	0.02
-0.46	0.03	0.02	0.46	0.08	0.02	-0.58	-0.01	0.02
-0.62	0.00	0.02	0.62	0.08	0.02	-0.75	0.01	0.02
-0.77	-0.02	0.02	0.77	0.08	0.02	-0.92	0.01	0.02
-0.92	0.01	0.02	0.92	0.07	0.01			

Table B.21. Average experimental orientation data and corresponding error within the CGD for short (A_{zz}) and long (R_{zz}) glass fibers at 00% of flow.

LGF - 0.7 mm z/h			LGF 5.5 mm z/h			SGF		
z/h	Mean	Error	z/h	Mean	Error	z/h	Mean	Error
0.92	0.34	0.09	-0.92	0.44	0.03	0.92	0.28	0.02
0.77	0.18	0.04	-0.77	0.63	0.04	0.75	0.24	0.03
0.62	0.33	0.07	-0.62	0.42	0.04	0.58	0.25	0.03
0.46	0.53	0.05	-0.46	0.69	0.03	0.42	0.30	0.03
0.31	0.48	0.11	-0.31	0.49	0.06	0.25	0.26	0.03
0.15	0.61	0.06	-0.15	0.53	0.06	0.08	0.39	0.01
0.00	0.67	0.05	0.00	0.65	0.03	-0.08	0.65	0.01
-0.15	0.55	0.07	0.15	0.65	0.08	-0.25	0.41	0.02
-0.31	0.53	0.05	0.31	0.56	0.09	-0.42	0.34	0.02
-0.46	0.59	0.04	0.46	0.43	0.08	-0.58	0.35	0.02
-0.62	0.41	0.08	0.62	0.36	0.02	-0.75	0.47	0.02
-0.77	0.55	0.01	0.77	0.21	0.04	-0.92	0.56	0.02
-0.92	0.50	0.03	0.92	0.38	0.13			

Table B.22. Average experimental orientation data and corresponding error within the CGD for short (A_{zz}) and long (R_{zz}) glass fibers at 10% of flow.

LGF - 0.7 mm z/h			LGF 5.5 mm z/h			SGF		
z/h	Mean	Error	z/h	Mean	Error	z/h	Mean	Error
0.92	0.42	0.04	-0.92	0.47	0.03	0.92	0.42	0.02
0.77	0.50	0.03	-0.77	0.54	0.04	0.75	0.20	0.03
0.62	0.38	0.05	-0.62	0.60	0.03	0.58	0.20	0.03
0.46	0.59	0.09	-0.46	0.55	0.07	0.42	0.42	0.02
0.31	0.72	0.08	-0.31	0.52	0.03	0.25	0.51	0.02
0.15	0.72	0.03	-0.15	0.53	0.05	0.08	0.67	0.01
0.00	0.54	0.06	0.00	0.64	0.05	-0.08	0.64	0.01
-0.15	0.47	0.04	0.15	0.73	0.05	-0.25	0.47	0.02
-0.31	0.62	0.03	0.31	0.66	0.05	-0.42	0.38	0.02
-0.46	0.57	0.10	0.46	0.66	0.04	-0.58	0.37	0.01
-0.62	0.63	0.03	0.62	0.47	0.05	-0.75	0.35	0.01
-0.77	0.48	0.05	0.77	0.46	0.04	-0.92	0.40	0.02
-0.92	0.59	0.06	0.92	0.37	0.04			

A_{33}

Table B.23. Average experimental orientation data and corresponding error within the CGD for short (A_{zz}) and long (R_{zz}) glass fibers at 40% of flow.

LGF - 0.7 mm z/h			LGF 5.5 mm z/h			SGF		
z/h	Mean	Error	z/h	Mean	Error	z/h	Mean	Error
0.92	0.48	0.07	-0.92	0.58	0.04	0.92	0.37	0.01
0.77	0.43	0.09	-0.77	0.56	0.03	0.75	0.27	0.01
0.62	0.42	0.06	-0.62	0.52	0.04	0.58	0.14	0.02
0.46	0.52	0.04	-0.46	0.58	0.04	0.42	0.23	0.02
0.31	0.69	0.08	-0.31	0.66	0.04	0.25	0.39	0.02
0.15	0.74	0.02	-0.15	0.62	0.03	0.08	0.69	0.01
0.00	0.64	0.07	0.00	0.70	0.05	-0.08	0.63	0.01
-0.15	0.60	0.02	0.15	0.79	0.04	-0.25	0.31	0.02
-0.31	0.61	0.05	0.31	0.77	0.04	-0.42	0.12	0.03
-0.46	0.59	0.02	0.46	0.62	0.05	-0.58	0.24	0.02
-0.62	0.54	0.04	0.62	0.41	0.05	-0.75	0.22	0.02
-0.77	0.57	0.04	0.77	0.40	0.03	-0.92	0.33	0.02
-0.92	0.69	0.03	0.92	0.46	0.02			

Table B.24. Average experimental orientation data and corresponding error within the CGD for short (A_{zz}) and long (R_{zz}) glass fibers at 90% of flow.

LGF - 0.7 mm z/h			LGF 5.5 mm z/h			SGF		
z/h	Mean	Error	z/h	Mean	Error	z/h	Mean	Error
0.92	0.47	0.05	-0.92	0.53	0.02	0.92	0.25	0.02
0.77	0.48	0.06	-0.77	0.61	0.04	0.75	0.44	0.02
0.62	0.54	0.08	-0.62	0.60	0.02	0.58	0.39	0.02
0.46	0.60	0.04	-0.46	0.65	0.04	0.42	0.34	0.02
0.31	0.63	0.09	-0.31	0.70	0.03	0.25	0.51	0.02
0.15	0.77	0.04	-0.15	0.68	0.03	0.08	0.77	0.01
0.00	0.78	0.04	0.00	0.74	0.04	-0.08	0.76	0.01
-0.15	0.67	0.06	0.15	0.76	0.05	-0.25	0.44	0.02
-0.31	0.61	0.07	0.31	0.71	0.03	-0.42	0.28	0.02
-0.46	0.61	0.05	0.46	0.63	0.05	-0.58	0.39	0.02
-0.62	0.62	0.05	0.62	0.51	0.05	-0.75	0.29	0.02
-0.77	0.65	0.07	0.77	0.47	0.05	-0.92	0.26	0.03
-0.92	0.48	0.04	0.92	0.40	0.02			

Appendix C. End-Gated Plaque Orientation Data (SGF)

Note:	Axx	Axy	Ayy	Azz	Axz	Ayz
	A11	A12	A22	A33	A13	A23

Table C.1. Short glass fiber orientation data (A_{ij}) in the End-Gated Plaque at 0% of width and 0% of flow

z/h	A11	A12	A22	A33	A13	A23
0.92	0.6411	-0.0105	0.0164	0.3425	0.0373	0.0324
0.77	0.5104	0.0111	0.0181	0.4715	0.0512	0.0290
0.62	0.4439	-0.0419	0.0324	0.5236	-0.0250	0.0396
0.46	0.2944	-0.0047	0.0233	0.6824	0.0305	0.0285
0.31	0.2262	0.0598	0.0372	0.7366	0.0796	0.0326
0.15	0.1409	0.0320	0.0375	0.8216	0.0315	0.0320
0.00	0.0508	0.0013	0.0336	0.9157	-0.0067	0.0182
-0.15	0.1073	-0.0247	0.0512	0.8416	-0.0419	0.0465
-0.31	0.2726	-0.0244	0.0453	0.6821	-0.0679	0.0612
-0.46	0.3355	-0.0406	0.0333	0.6312	-0.0411	0.0340
-0.62	0.3061	-0.0216	0.0452	0.6487	-0.0429	0.0477
-0.77	0.4870	-0.0463	0.0197	0.4933	-0.0735	0.0173
-0.92	0.6085	-0.0724	0.0297	0.3618	-0.1537	0.0503

Table C.2. Short glass fiber orientation data (A_{ij}) in the End-Gated Plaque at 0% of width and 10% of flow

z/h	A11	A12	A22	A33	A13	A23
0.92	0.4695	-0.0096	0.0226	0.5079	0.0103	0.0293
0.77	0.6140	0.0297	0.0139	0.3720	0.0660	0.0243
0.62	0.5320	0.0103	0.0318	0.4362	0.0722	0.0448
0.46	0.4439	-0.0138	0.0252	0.5308	-0.0278	0.0416
0.31	0.2617	0.0243	0.0568	0.6815	0.0847	0.0687
0.15	0.3082	0.0461	0.0366	0.6552	0.0650	0.0429
0.00	0.1883	0.0251	0.0307	0.7809	0.0161	0.0317
-0.15	0.2808	0.0122	0.0445	0.6747	-0.0187	0.0397
-0.31	0.4300	-0.0115	0.0320	0.5380	-0.0108	0.0440
-0.46	0.4088	-0.0081	0.0246	0.5667	0.0261	0.0254
-0.62	0.5386	-0.0076	0.0122	0.4492	-0.0249	0.0201
-0.77	0.6604	0.0031	0.0175	0.3221	0.0167	0.0237
-0.92	0.5085	-0.0147	0.0170	0.4745	-0.0187	0.0299

00% of Width – 0, 10% L A_{ij} Error

Table C.3. Short glass fiber orientation data standard error in the End-Gated Plaque at 0% of width and 00% of flow

z/h	A11	A12	A22	A33	A13	A23
0.92	0.0674	0.0209	0.0038	0.0703	0.0262	0.0027
0.77	0.0588	0.0237	0.0074	0.0567	0.1010	0.0125
0.62	0.0327	0.0030	0.0184	0.0482	0.1089	0.0128
0.46	0.0841	0.0040	0.0126	0.0966	0.0184	0.0190
0.31	0.0573	0.0097	0.0135	0.0707	0.0148	0.0011
0.15	0.0277	0.0067	0.0053	0.0329	0.0166	0.0060
0.00	0.0432	0.0012	0.0174	0.0579	0.0054	0.0149
-0.15	0.0217	0.0035	0.0182	0.0324	0.0124	0.0184
-0.31	0.0510	0.0049	0.0178	0.0502	0.0023	0.0233
-0.46	0.0133	0.0224	0.0069	0.0198	0.0082	0.0002
-0.62	0.0808	0.0209	0.0120	0.0722	0.0084	0.0083
-0.77	0.0616	0.0047	0.0115	0.0584	0.0314	0.0010
-0.92	0.0250	0.0126	0.0113	0.0314	0.0299	0.0122

Table C.4. Short glass fiber orientation data standard error in the End-Gated Plaque at 0% of width and 10% of flow

z/h	A11	A12	A22	A33	A13	A23
0.92	0.0700	0.0062	0.0079	0.1244	0.0356	0.0145
0.77	0.0788	0.0048	0.0049	0.0739	0.0040	0.0069
0.62	0.0358	0.0142	0.0040	0.0319	0.0063	0.0082
0.46	0.0338	0.0112	0.0060	0.0388	0.0308	0.0033
0.31	0.0317	0.0075	0.0126	0.0327	0.0154	0.0109
0.15	0.0700	0.0091	0.0037	0.1287	0.0057	0.0011
0.00	0.0635	0.0130	0.0123	0.0755	0.0249	0.0097
-0.15	0.0455	0.0045	0.0071	0.0420	0.0255	0.0086
-0.31	0.0266	0.0117	0.0106	0.0164	0.0235	0.0137
-0.46	0.0800	0.0079	0.0127	0.1088	0.0259	0.0152
-0.62	0.0298	0.0159	0.0055	0.0312	0.0392	0.0079
-0.77	0.0349	0.0131	0.0071	0.0298	0.0652	0.0092
-0.92	0.0569	0.0152	0.0060	0.0629	0.0169	0.0105

00% of Width – 40, 90% L A_{ij} Data

Table C.5. Short glass fiber orientation data (A_{ij}) in the End-Gated Plaque at 0% of width and 10% of flow

z/h	A11	A12	A22	A33	A13	A23
0.92	0.5033	-0.0295	0.0177	0.4791	-0.0541	0.0152
0.77	0.5880	-0.0279	0.0228	0.3892	-0.0415	0.0345
0.62	0.6873	-0.0131	0.0206	0.2921	0.0085	0.0283
0.46	0.6176	-0.0478	0.0327	0.3497	-0.0488	0.0433
0.31	0.4449	-0.0017	0.0175	0.5376	0.0654	0.0322
0.15	0.2701	0.0288	0.0222	0.7078	0.0330	0.0184
0.00	0.0685	-0.0166	0.0378	0.8937	-0.0045	0.0327
-0.15	0.1644	-0.0291	0.0377	0.7979	-0.0341	0.0435
-0.31	0.4665	-0.0239	0.0106	0.5230	-0.1008	0.0187
-0.46	0.5903	-0.0169	0.0129	0.3968	-0.0587	0.0151
-0.62	0.7962	0.0094	0.0139	0.1899	-0.0340	0.0135
-0.77	0.6777	0.0082	0.0399	0.2823	-0.0080	0.0244
-0.92	0.5628	0.0325	0.0398	0.3974	0.0733	0.0316

Table C.6. Short glass fiber orientation data (A_{ij}) in the End-Gated Plaque at 0% of width and 10% of flow

z/h	A11	A12	A22	A33	A13	A23
0.92	0.6928	0.0136	0.0382	0.2690	0.0485	0.0523
0.77	0.4101	-0.0178	0.0505	0.5394	-0.0053	0.0622
0.62	0.6101	-0.0216	0.0440	0.3458	-0.0206	0.0352
0.46	0.5476	-0.0320	0.0492	0.4032	-0.0670	0.0543
0.31	0.3711	0.0122	0.0521	0.5768	0.0297	0.0482
0.15	0.1323	0.0427	0.0692	0.7985	0.0364	0.0415
0.00	0.0518	0.0455	0.0879	0.8603	0.0429	0.0493
-0.15	0.2478	-0.0387	0.0930	0.6592	-0.0160	0.0556
-0.31	0.4057	-0.0581	0.0867	0.5076	-0.0386	0.0959
-0.46	0.6059	-0.0036	0.0277	0.3664	0.0468	0.0403
-0.62	0.5489	0.0177	0.0246	0.4265	0.0370	0.0259
-0.77	0.4368	0.0097	0.0299	0.5333	0.0473	0.0515
-0.92	0.5921	0.0256	0.0354	0.3725	0.0674	0.0523

00% of Width – 40, 90% L A_{ij} Error

Table C.7. Short glass fiber orientation data standard error in the End-Gated Plaque at 0% of width and 40% of flow

z/h	A11	A12	A22	A33	A13	A23
0.92	0.0414	0.0137	0.0142	0.0414	0.0183	0.0021
0.77	0.0231	0.0111	0.0069	0.0242	0.0590	0.0007
0.62	0.0650	0.0208	0.0073	0.0577	0.0595	0.0094
0.46	0.0342	0.0267	0.0043	0.0299	0.0982	0.0004
0.31	0.0422	0.0223	0.0072	0.0480	0.1117	0.0109
0.15	0.0335	0.0124	0.0110	0.0392	0.0336	0.0039
0.00	0.0345	0.0148	0.0069	0.0374	0.0044	0.0025
-0.15	0.0800	0.0205	0.0067	0.1035	0.0026	0.0063
-0.31	0.0302	0.0040	0.0063	0.0361	0.0268	0.0018
-0.46	0.0724	0.0100	0.0096	0.0738	0.0201	0.0008
-0.62	0.0246	0.0171	0.0042	0.0237	0.0061	0.0001
-0.77	0.0839	0.0274	0.0213	0.0765	0.0976	0.0020
-0.92	0.0800	0.0174	0.0226	0.1177	0.0154	0.0151

Table C.8. Short glass fiber orientation data standard error in the End-Gated Plaque at 0% of width and 90% of flow

z/h	A11	A12	A22	A33	A13	A23
0.92	0.0424	0.0088	0.0141	0.0446	0.0176	0.0175
0.77	0.0351	0.0119	0.0234	0.0519	0.0063	0.0322
0.62	0.0980	0.0369	0.0216	0.0870	0.0517	0.0132
0.46	0.0900	0.0057	0.0164	0.0550	0.0368	0.0200
0.31	0.0545	0.0112	0.0191	0.0735	0.0526	0.0117
0.15	0.0220	0.0144	0.0259	0.0438	0.0165	0.0027
0.00	0.0153	0.0124	0.0434	0.0584	0.0080	0.0132
-0.15	0.0551	0.0128	0.0267	0.0904	0.0156	0.0221
-0.31	0.0650	0.0144	0.0184	0.0500	0.0091	0.0045
-0.46	0.0423	0.0047	0.0123	0.0496	0.0050	0.0083
-0.62	0.0850	0.0126	0.0108	0.0850	0.0161	0.0010
-0.77	0.0387	0.0102	0.0119	0.0379	0.0372	0.0145
-0.92	0.0860	0.0116	0.0145	0.0717	0.0656	0.0219

50% of Width – 0, 10% L A_{ij} Data

Table C.9. Short glass fiber orientation data (A_{ij}) in the End-Gated Plaque at 50% of width and 00% of flow

z/h	A11	A12	A22	A33	A13	A23
0.92	0.4319	-0.0056	0.0494	0.5187	-0.0516	0.0617
0.77	0.6519	0.0051	0.0287	0.3194	0.0290	0.0550
0.62	0.4795	0.0585	0.0243	0.4962	0.0793	0.0374
0.46	0.6510	0.0537	0.0300	0.3190	0.0596	0.0389
0.31	0.6326	-0.0050	0.0399	0.3276	0.1484	0.0637
0.15	0.6564	0.0088	0.0446	0.2991	0.0921	0.0714
0.00	0.8001	-0.0215	0.0096	0.1903	-0.0377	0.0241
-0.15	0.7191	0.0091	0.0226	0.2582	0.0655	0.0387
-0.31	0.6875	-0.0149	0.0689	0.2436	-0.0312	0.1009
-0.46	0.5711	-0.0768	0.0601	0.3688	-0.0911	0.0846
-0.62	0.5224	-0.0022	0.0208	0.4568	-0.0832	0.0357
-0.77	0.3720	-0.0270	0.0706	0.5574	-0.0423	0.0943
-0.92	0.2633	-0.0138	0.0532	0.6835	-0.0023	0.0700

Table C.10. Short glass fiber orientation data (A_{ij}) in the End-Gated Plaque at 50% of width and 10% of flow

z/h	A11	A12	A22	A33	A13	A23
0.92	0.3375	0.0091	0.0653	0.5971	0.0214	0.1112
0.77	0.7113	-0.0080	0.0255	0.2632	-0.0963	0.0508
0.62	0.5132	-0.0248	0.0474	0.4395	-0.0438	0.0717
0.46	0.6744	0.0028	0.0532	0.2724	0.0088	0.0736
0.31	0.5895	0.0057	0.0297	0.3809	0.0163	0.0484
0.15	0.6746	-0.0098	0.0243	0.3011	-0.0431	0.0409
0.00	0.6708	-0.0087	0.0348	0.2944	-0.0475	0.0582
-0.15	0.7858	-0.0823	0.0214	0.1928	-0.1772	0.0455
-0.31	0.6290	-0.0454	0.0286	0.3425	-0.1707	0.0513
-0.46	0.6046	-0.0193	0.0324	0.3630	-0.0698	0.0579
-0.62	0.7134	0.0157	0.0195	0.2671	-0.0065	0.0331
-0.77	0.6983	0.0156	0.0390	0.2627	-0.0009	0.0502
-0.92	0.6211	-0.0420	0.0246	0.3543	-0.1716	0.0506

50% of Width – 0, 10% L A_{ij} Error

Table C.11. Short glass fiber orientation data standard error in the End-Gated Plaque at 50% of width and 00% of flow

z/h	A11	A12	A22	A33	A13	A23
0.92	0.0800	0.0171	0.0150	0.0907	0.0145	0.0129
0.77	0.0618	0.0395	0.0131	0.0488	0.1307	0.0093
0.62	0.0600	0.0250	0.0096	0.0600	0.0125	0.0116
0.46	0.0260	0.0467	0.0220	0.0456	0.0753	0.0173
0.31	0.0220	0.0483	0.0065	0.0275	0.0904	0.0178
0.15	0.0357	0.0162	0.0218	0.0440	0.0536	0.0160
0.00	0.0237	0.0119	0.0015	0.0225	0.0792	0.0025
-0.15	0.0381	0.0190	0.0042	0.0387	0.1014	0.0043
-0.31	0.0820	0.0321	0.0347	0.0483	0.0582	0.0201
-0.46	0.0900	0.0161	0.0212	0.0700	0.0021	0.0358
-0.62	0.0600	0.0099	0.0115	0.0750	0.0162	0.0203
-0.77	0.0298	0.0088	0.0500	0.0585	0.0257	0.0512
-0.92	0.0639	0.0093	0.0366	0.0274	0.0194	0.0317

Table C.12. Short glass fiber orientation data standard error in the End-Gated Plaque at 50% of width and 10% of flow

z/h	A11	A12	A22	A33	A13	A23
0.92	0.0730	0.0118	0.0361	0.0375	0.0385	0.0345
0.77	0.0500	0.0061	0.0171	0.0783	0.0249	0.0224
0.62	0.0399	0.0216	0.0129	0.0280	0.0051	0.0148
0.46	0.0336	0.0259	0.0226	0.0124	0.0492	0.0170
0.31	0.0567	0.0088	0.0056	0.0527	0.0236	0.0064
0.15	0.0558	0.0139	0.0062	0.0545	0.0452	0.0017
0.00	0.0274	0.0221	0.0131	0.0241	0.0372	0.0025
-0.15	0.0605	0.0181	0.0067	0.0555	0.0018	0.0163
-0.31	0.0487	0.0295	0.0048	0.0439	0.1089	0.0188
-0.46	0.0641	0.0086	0.0080	0.0576	0.0290	0.0015
-0.62	0.0600	0.0179	0.0129	0.0724	0.0555	0.0146
-0.77	0.0186	0.0411	0.0058	0.0129	0.1125	0.0117
-0.92	0.0294	0.0229	0.0018	0.0303	0.0269	0.0035

50% of Width – 40, 90% L A_{ij} Data

Table C.13. Short glass fiber orientation data (A_{ij}) in the End-Gated Plaque at 50% of width and 50% of flow

z/h	A11	A12	A22	A33	A13	A23
0.92	0.2889	-0.0005	0.0353	0.6758	0.0035	0.0405
0.77	0.7138	0.0026	0.0106	0.2756	-0.0343	0.0271
0.62	0.7174	-0.0161	0.0143	0.2683	-0.0738	0.0320
0.46	0.7149	0.0132	0.0214	0.2637	-0.0276	0.0330
0.31	0.5113	0.0003	0.0271	0.4616	-0.0607	0.0478
0.15	0.6538	-0.0019	0.0173	0.3288	-0.0281	0.0453
0.00	0.6662	-0.0516	0.0460	0.2877	-0.1744	0.0665
-0.15	0.6395	-0.0495	0.0310	0.3295	-0.1393	0.0533
-0.31	0.6839	-0.0136	0.0186	0.2975	0.0465	0.0416
-0.46	0.6117	-0.0168	0.0490	0.3393	0.0311	0.0579
-0.62	0.5251	-0.0291	0.0472	0.4277	-0.0834	0.0554
-0.77	0.6708	-0.0036	0.0223	0.3069	-0.0246	0.0462
-0.92	0.5835	-0.0151	0.0383	0.3782	-0.0430	0.0537

Table C.14. Short glass fiber orientation data (A_{ij}) in the End-Gated Plaque at 50% of width and 90% of flow

z/h	A11	A12	A22	A33	A13	A23
0.92	0.6508	-0.0484	0.0392	0.3100	-0.0260	0.0351
0.77	0.6498	-0.0299	0.0470	0.3032	0.0265	0.0505
0.62	0.6754	-0.0374	0.0281	0.2965	-0.0882	0.0478
0.46	0.7119	-0.0289	0.0078	0.2803	-0.1109	0.0223
0.31	0.7255	-0.0224	0.0104	0.2641	-0.0783	0.0277
0.15	0.6501	-0.0179	0.0197	0.3302	-0.0680	0.0375
0.00	0.5714	0.0276	0.0487	0.3799	0.0009	0.0631
-0.15	0.4810	0.0369	0.0627	0.4563	0.0128	0.0534
-0.31	0.5342	-0.0056	0.1205	0.3453	-0.0306	0.0891
-0.46	0.7020	0.0116	0.0443	0.2536	0.0818	0.0520
-0.62	0.6864	0.0206	0.0155	0.2981	-0.0308	0.0320
-0.77	0.5768	-0.0072	0.0290	0.3942	-0.0056	0.0502
-0.92	0.8249	0.0409	0.0121	0.1630	0.0424	0.0212

50% of Width – 40, 90% L A_{ij} Error

Table C.15. Short glass fiber orientation data standard error in the End-Gated Plaque at 50% of width and 40% of flow

z/h	A11	A12	A22	A33	A13	A23
0.92	0.0299	0.0057	0.0171	0.0470	0.0767	0.0181
0.77	0.0398	0.0142	0.0015	0.0392	0.0307	0.0023
0.62	0.0651	0.0162	0.0038	0.0615	0.0615	0.0025
0.46	0.0241	0.0279	0.0044	0.0197	0.0628	0.0039
0.31	0.0315	0.0104	0.0112	0.0352	0.0442	0.0173
0.15	0.0418	0.0042	0.0050	0.0467	0.0145	0.0034
0.00	0.0065	0.0276	0.0125	0.0140	0.0084	0.0015
-0.15	0.0726	0.0068	0.0103	0.0718	0.0356	0.0067
-0.31	0.0500	0.0193	0.0020	0.0500	0.0615	0.0099
-0.46	0.0101	0.0391	0.0169	0.0210	0.1121	0.0095
-0.62	0.0700	0.0217	0.0187	0.0800	0.0893	0.0262
-0.77	0.0334	0.0193	0.0040	0.0300	0.0702	0.0001
-0.92	0.0290	0.0230	0.0089	0.0253	0.0347	0.0057

Table C.16. Short glass fiber orientation data standard error in the End-Gated Plaque at 50% of width and 90% of flow

z/h	A11	A12	A22	A33	A13	A23
0.92	0.0586	0.0349	0.0159	0.0428	0.0940	0.0033
0.77	0.0315	0.0370	0.0108	0.0420	0.0811	0.0088
0.62	0.0606	0.0178	0.0064	0.0591	0.0872	0.0024
0.46	0.0900	0.0048	0.0011	0.0600	0.0107	0.0031
0.31	0.0541	0.0039	0.0008	0.0535	0.0005	0.0017
0.15	0.0751	0.0209	0.0036	0.0719	0.1217	0.0170
0.00	0.0652	0.0412	0.0097	0.0558	0.0954	0.0186
-0.15	0.0900	0.0398	0.0258	0.0700	0.0659	0.0181
-0.31	0.0675	0.0477	0.0409	0.0500	0.0808	0.0211
-0.46	0.0729	0.0098	0.0164	0.0600	0.1118	0.0096
-0.62	0.0621	0.0072	0.0046	0.0665	0.0172	0.0059
-0.77	0.0600	0.0126	0.0083	0.0500	0.0052	0.0141
-0.92	0.0432	0.0096	0.0039	0.0396	0.0006	0.0040

90% of Width – 0, 10% L A_{ij} Data

Table C.17. Short glass fiber orientation data (A_{ij}) in the End-Gated Plaque at 90% of width and 00% of flow

z/h	A11	A12	A22	A33	A13	A23
0.92	0.3402	-0.0019	0.0130	0.6468	-0.0341	0.0254
0.77	0.5234	-0.0227	0.0111	0.4655	-0.1046	0.0174
0.62	0.7218	-0.0148	0.0272	0.2511	-0.0336	0.0404
0.46	0.8566	-0.0505	0.0155	0.1279	-0.0234	0.0094
0.31	0.8399	0.0125	0.0165	0.1436	-0.0099	0.0208
0.15	0.9578	0.0482	0.0165	0.0257	-0.0342	0.0119
0.00	0.9743	-0.0529	0.0064	0.0193	-0.0852	0.0095
-0.15	0.8975	0.0019	0.0151	0.0874	0.0280	0.0250
-0.31	0.8648	0.0016	0.0155	0.1197	-0.0490	0.0208
-0.46	0.8404	-0.0674	0.0402	0.1194	-0.0721	0.0391
-0.62	0.7384	-0.0266	0.0150	0.2466	-0.0357	0.0374
-0.77	0.5193	-0.0258	0.0307	0.4499	-0.0781	0.0427
-0.92	0.4210	-0.0275	0.0365	0.5425	-0.0163	0.0324

Table C.18. Short glass fiber orientation data (A_{ij}) in the End-Gated Plaque at 90% of width and 10% of flow

z/h	A11	A12	A22	A33	A13	A23
0.92	0.5108	0.0144	0.0300	0.4592	0.0467	0.0423
0.77	0.6276	-0.0008	0.0100	0.3624	-0.0311	0.0229
0.62	0.7492	0.0066	0.0067	0.2441	-0.0381	0.0049
0.46	0.9499	-0.0217	0.0045	0.0456	-0.0678	0.0094
0.31	0.9218	0.0278	0.0059	0.0723	0.0425	0.0169
0.15	0.8747	0.0506	0.0212	0.1040	0.0254	0.0323
0.00	0.8349	0.0830	0.0185	0.1467	0.0818	0.0325
-0.15	0.8063	0.0732	0.0221	0.1716	0.1919	0.0277
-0.31	0.8385	0.0177	0.0106	0.1509	0.0672	0.0286
-0.46	0.8279	0.0183	0.0246	0.1475	0.0419	0.0419
-0.62	0.8105	0.0206	0.0127	0.1768	0.0631	0.0180
-0.77	0.7108	0.0260	0.0115	0.2776	0.1073	0.0220
-0.92	0.3972	0.0378	0.0224	0.5803	0.0011	0.0336

90% of Width – 0, 10% L A_{ij} Error

Table C.19. Short glass fiber orientation data standard error in the End-Gated Plaque at 90% of width and 00% of flow

z/h	A11	A12	A22	A33	A13	A23
0.92	0.0541	0.0156	0.0045	0.0501	0.0635	0.0007
0.77	0.0900	0.0054	0.0061	0.0600	0.0075	0.0022
0.62	0.0700	0.0053	0.0089	0.0700	0.0147	0.0230
0.46	0.0600	0.0401	0.0086	0.0781	0.0634	0.0049
0.31	0.0686	0.0278	0.0080	0.0608	0.0351	0.0125
0.15	0.0072	0.0621	0.0084	0.0096	0.0272	0.0040
0.00	0.0061	0.0272	0.0017	0.0044	0.0422	0.0022
-0.15	0.0660	0.0540	0.0058	0.0620	0.0296	0.0077
-0.31	0.0497	0.0718	0.0081	0.0478	0.0875	0.0090
-0.46	0.0268	0.0892	0.0148	0.0158	0.0860	0.0065
-0.62	0.0156	0.0248	0.0042	0.0194	0.0586	0.0043
-0.77	0.0574	0.0338	0.0124	0.0481	0.0633	0.0103
-0.92	0.0468	0.0431	0.0123	0.0560	0.0656	0.0021

Table C.20. Short glass fiber orientation data standard error in the End-Gated Plaque at 90% of width and 10% of flow

z/h	A11	A12	A22	A33	A13	A23
0.92	0.0077	0.0113	0.0172	0.0219	0.0428	0.0241
0.77	0.0615	0.0178	0.0022	0.0593	0.0560	0.0049
0.62	0.0850	0.0209	0.0056	0.1630	0.0169	0.0010
0.46	0.0033	0.0198	0.0038	0.0028	0.0387	0.0048
0.31	0.0080	0.0297	0.0009	0.0077	0.0617	0.0034
0.15	0.0334	0.0558	0.0115	0.0231	0.1689	0.0161
0.00	0.0416	0.0550	0.0074	0.0343	0.1663	0.0144
-0.15	0.0657	0.0106	0.0084	0.0579	0.0312	0.0120
-0.31	0.0253	0.0065	0.0029	0.0247	0.0255	0.0003
-0.46	0.0097	0.0291	0.0061	0.0075	0.0723	0.0056
-0.62	0.0472	0.0112	0.0040	0.0446	0.0072	0.0065
-0.77	0.0571	0.0093	0.0032	0.0538	0.0008	0.0035
-0.92	0.0448	0.0270	0.0105	0.0521	0.0976	0.0150

90% of Width – 40, 90% L A_{ij} Data

Table C.21. Short glass fiber orientation data (A_{ij}) in the End-Gated Plaque at 90% of width and 40% of flow

z/h	A11	A12	A22	A33	A13	A23
0.92	0.5384	0.0183	0.0375	0.4241	0.0495	0.0654
0.77	0.7879	-0.0191	0.0230	0.1890	-0.1196	0.0497
0.62	0.7344	0.0198	0.0057	0.2599	0.0414	0.0102
0.46	0.8882	0.0073	0.0025	0.1093	0.0417	0.0076
0.31	0.9052	-0.0221	0.0135	0.0813	-0.0503	0.0247
0.15	0.9214	-0.0448	0.0097	0.0689	-0.0671	0.0115
0.00	0.9265	-0.0261	0.0139	0.0596	-0.0173	0.0192
-0.15	0.9022	-0.0096	0.0104	0.0875	-0.0072	0.0190
-0.31	0.8950	-0.0280	0.0157	0.0893	-0.0944	0.0231
-0.46	0.7550	-0.0068	0.0104	0.2346	-0.0374	0.0261
-0.62	0.8034	-0.0066	0.0142	0.1824	-0.0462	0.0158
-0.77	0.8104	-0.0204	0.0092	0.1805	-0.1247	0.0210
-0.92	0.7554	0.0179	0.0124	0.2323	-0.0479	0.0241

Table C.22. Short glass fiber orientation data (A_{ij}) in the End-Gated Plaque at 90% of width and 90% of flow

z/h	A11	A12	A22	A33	A13	A23
0.92	0.6986	-0.0405	0.0241	0.2774	-0.0962	0.0360
0.77	0.6740	-0.0356	0.0206	0.3055	-0.0846	0.0389
0.62	0.7067	-0.0524	0.0337	0.2596	-0.1136	0.0484
0.46	0.6365	-0.0264	0.0375	0.3260	-0.0925	0.0463
0.31	0.7098	0.0405	0.0258	0.2644	-0.0154	0.0288
0.15	0.7083	0.0121	0.0290	0.2627	-0.0062	0.0523
0.00	0.6993	0.0196	0.1137	0.1870	0.0307	0.0805
-0.15	0.7087	0.0527	0.0708	0.2205	0.0142	0.0627
-0.31	0.7766	0.0160	0.0668	0.1566	-0.0790	0.0600
-0.46	0.8129	-0.0513	0.0348	0.1523	-0.1092	0.0418
-0.62	0.7796	0.0103	0.0253	0.1952	-0.0146	0.0373
-0.77	0.8253	-0.0225	0.0026	0.1721	-0.1077	0.0132
-0.92	0.8526	-0.0026	0.0097	0.1377	-0.0338	0.0171

90% of Width – 40, 90% L A_{ij} Error

Table C.23. Short glass fiber orientation data standard error in the End-Gated Plaque at 90% of width and 40% of flow

z/h	A11	A12	A22	A33	A13	A23
0.92	0.0402	0.0211	0.0237	0.0610	0.1018	0.0259
0.77	0.0610	0.0072	0.0117	0.0586	0.0107	0.0001
0.62	0.0915	0.0154	0.0024	0.0907	0.0133	0.0014
0.46	0.0059	0.0071	0.0011	0.0070	0.0023	0.0020
0.31	0.0180	0.0090	0.0088	0.0131	0.0391	0.0079
0.15	0.0246	0.0119	0.0026	0.0221	0.0054	0.0052
0.00	0.0109	0.0118	0.0074	0.0052	0.0278	0.0094
-0.15	0.0233	0.0061	0.0064	0.0223	0.0436	0.0040
-0.31	0.0144	0.0045	0.0092	0.0228	0.0191	0.0050
-0.46	0.0264	0.0206	0.0017	0.0269	0.0343	0.0074
-0.62	0.0697	0.0028	0.0039	0.0676	0.0127	0.0019
-0.77	0.0823	0.0240	0.0043	0.0843	0.0645	0.0013
-0.92	0.0519	0.0195	0.0037	0.0544	0.0637	0.0049

Table C.24. Short glass fiber orientation data standard error in the End-Gated Plaque at 90% of width and 90% of flow

z/h	A11	A12	A22	A33	A13	A23
0.92	0.0633	0.0282	0.0042	0.0644	0.1037	0.0052
0.77	0.0192	0.0167	0.0013	0.0193	0.0461	0.0049
0.62	0.0704	0.0310	0.0041	0.0742	0.0109	0.0068
0.46	0.0150	0.0065	0.0049	0.0196	0.0344	0.0027
0.31	0.0864	0.0101	0.0092	0.0818	0.0107	0.0087
0.15	0.0714	0.0122	0.0056	0.0661	0.0415	0.0136
0.00	0.0763	0.0717	0.0323	0.0479	0.0672	0.0265
-0.15	0.0821	0.0100	0.0157	0.0755	0.0243	0.0177
-0.31	0.0592	0.0061	0.0034	0.0573	0.0017	0.0303
-0.46	0.0496	0.0286	0.0022	0.0501	0.0533	0.0112
-0.62	0.0707	0.0156	0.0029	0.0677	0.0276	0.0088
-0.77	0.0229	0.0032	0.0003	0.0232	0.0092	0.0003
-0.92	0.0222	0.0137	0.0033	0.0192	0.0181	0.0106

Appendix D. End-Gated Plaque Orientation Data (LGF)

Note:	Axx	Axy	Ayy	Azz	Axz	Ayz
	A11	A12	A22	A33	A13	A23

00% of Width – 0, 10% L R_{ij} Data

Table D.1. Long glass fiber orientation data (R_{ij}) in the End-Gated Plaque at 00% of width and 00% of flow

z/h	A11	A12	A22	A33	A13	A23
0.92	0.5985	0.0885	0.0488	0.3527	0.0673	0.0632
0.77	0.3775	0.0469	0.0617	0.5608	0.0424	0.1073
0.62	0.2990	0.1484	0.1739	0.5271	0.1867	0.1189
0.46	0.3698	0.1173	0.0716	0.5586	0.1269	0.0965
0.31	0.4120	0.1544	0.0880	0.4999	0.1819	0.1016
0.15	0.3614	0.1437	0.0957	0.5429	0.1159	0.1248
0.00	0.2289	0.1124	0.0795	0.6916	0.0972	0.1323
-0.15	0.2408	0.0702	0.0727	0.6864	0.1094	0.0964
-0.31	0.1768	0.0458	0.0768	0.7464	0.0835	0.0733
-0.46	0.1139	0.0151	0.0435	0.8427	-0.0090	0.0410
-0.62	0.2119	-0.0045	0.0185	0.7696	0.0244	0.0147
-0.77	0.1756	-0.0173	0.0271	0.7974	-0.0377	0.0073
-0.92	0.6384	-0.0505	0.0231	0.3386	-0.1940	#####

Table D.2. Long glass fiber orientation data (R_{ij}) in the End-Gated Plaque at 00% of width and 10% of flow

z/h	A11	A12	A22	A33	A13	A23
0.92	0.4013	0.0400	0.0584	0.5403	0.0113	0.0409
0.77	0.5279	-0.0058	0.0575	0.4147	0.1001	0.0201
0.62	0.4662	0.0190	0.0514	0.4824	0.1010	0.0280
0.46	0.1738	0.0044	0.0884	0.7377	0.0398	#####
0.31	0.2918	0.0451	0.0881	0.6201	0.0921	0.0850
0.15	0.3173	0.0390	0.1064	0.5763	0.0637	0.0735
0.00	0.4382	-0.0129	0.0839	0.4779	0.0381	0.0240
-0.15	0.2123	0.0211	0.1806	0.6071	0.0112	0.0733
-0.31	0.1912	-0.0212	0.1931	0.6157	0.0271	#####
-0.46	0.1758	0.0395	0.1838	0.6404	-0.0255	0.0994
-0.62	0.3727	-0.0123	0.1666	0.4607	-0.0252	0.0499
-0.77	0.5086	0.0339	0.1059	0.3855	0.0072	0.0598
-0.92	0.5334	-0.0030	0.0221	0.4446	0.0753	0.0085

00% of Width – 0, 10% L R_{ij} Error

Table D.3. Long glass fiber orientation standard error in the End-Gated Plaque at 00% of width and 00% of flow.

z/h	A11	A12	A22	A33	A13	A23
0.92	0.0514	0.0545	0.0417	0.0138	0.0293	0.0293
0.77	0.0640	0.0468	0.0130	0.0554	0.0324	0.0324
0.62	0.0506	0.0379	0.0557	0.0650	0.0547	0.0547
0.46	0.0746	0.0334	0.0058	0.0804	0.0154	0.0154
0.31	0.0600	0.0464	0.0167	0.0978	0.0169	0.0169
0.15	0.0700	0.0336	0.0202	0.1005	0.0404	0.0404
0.00	0.0370	0.0177	0.0114	0.0469	0.0411	0.0411
-0.15	0.0227	0.0135	0.0186	0.0311	0.0239	0.0239
-0.31	0.0270	0.0113	0.0278	0.0434	0.0171	0.0171
-0.46	0.0444	0.0126	0.0113	0.0335	0.0187	0.0187
-0.62	0.0650	0.0085	0.0083	0.0700	0.0107	0.0107
-0.77	0.0550	0.0045	0.0042	0.0800	0.0145	0.0145
-0.92	0.0500	0.0231	0.0030	0.0800	0.0211	0.0211

Table D.4. Long glass fiber orientation standard error in the End-Gated Plaque at 00% of width and 10% of flow.

z/h	A11	A12	A22	A33	A13	A23
0.92	0.0195	0.0210	0.0436	0.0356	0.0136	0.0346
0.77	0.0562	0.0356	0.0432	0.0216	0.0894	0.0221
0.62	0.1004	0.0146	0.0241	0.0550	0.0642	0.0209
0.46	0.0254	0.0205	0.0673	0.0794	0.0419	0.0583
0.31	0.0381	0.0196	0.0437	0.0601	0.0107	0.0209
0.15	0.0411	0.0113	0.0519	0.0846	0.0101	0.0311
0.00	0.0665	0.0490	0.0490	0.0950	0.0198	0.0457
-0.15	0.0506	0.0177	0.0803	0.0600	0.0479	0.0247
-0.31	0.0311	0.0438	0.1303	0.1023	0.0147	0.1128
-0.46	0.0155	0.0513	0.1352	0.0800	0.0310	0.0379
-0.62	0.0869	0.0206	0.1335	0.0700	0.0083	0.0183
-0.77	0.0635	0.0286	0.0859	0.0748	0.0468	0.0173
-0.92	0.0850	0.0082	0.0105	0.0914	0.0502	0.0168

00% of Width – 40, 90% L R_{ij} Data

Table D.5. Long glass fiber orientation data (R_{ij}) in the End-Gated Plaque at 00% of width and 40% of flow

z/h	A11	A12	A22	A33	A13	A23
0.92	0.5255	-0.0024	0.0202	0.4544	0.0548	0.0314
0.77	0.4329	0.0060	0.0152	0.5520	0.1621	0.0216
0.62	0.3580	0.0072	0.0399	0.6020	0.0992	0.0605
0.46	0.4514	0.0261	0.0518	0.4968	0.0986	0.0306
0.31	0.3548	0.0225	0.0206	0.6246	0.1425	0.0265
0.15	0.2786	0.0577	0.0428	0.6786	0.1699	0.0760
0.00	0.2458	0.0368	0.0388	0.7154	0.1173	0.0584
-0.15	0.0951	-0.0060	0.0423	0.8626	0.0812	0.0061
-0.31	0.1906	0.0099	0.0414	0.7680	0.1182	0.0389
-0.46	0.3951	-0.0353	0.0421	0.5629	-0.0079	0.0655
-0.62	0.5970	0.0070	0.0367	0.3663	0.0594	0.0283
-0.77	0.5245	-0.0117	0.0627	0.4128	0.0792	0.0160
-0.92	0.5280	0.0117	0.0306	0.4414	0.0986	0.0219

Table D.6. Long glass fiber orientation data (R_{ij}) in the End-Gated Plaque at 00% of width and 90% of flow

z/h	A11	A12	A22	A33	A13	A23
0.92	0.5096	0.0738	0.0419	0.4485	0.0505	0.0779
0.77	0.6868	0.0366	0.0108	0.3024	-0.0272	0.0212
0.62	0.2604	0.0333	0.0178	0.7218	0.0692	0.0406
0.46	0.2026	0.0224	0.0326	0.7648	-0.0025	0.0473
0.31	0.1815	0.0112	0.0329	0.7856	0.0241	0.0254
0.15	0.0700	0.0097	0.0287	0.9013	0.0402	0.0456
0.00	0.1796	0.0338	0.0759	0.7445	0.0800	0.0852
-0.15	0.1895	0.0993	0.1089	0.7016	0.0437	0.0457
-0.31	0.1585	0.0600	0.0806	0.7609	0.0468	0.0881
-0.46	0.1829	0.0527	0.0989	0.7182	0.0030	0.0684
-0.62	0.3101	0.0063	0.0553	0.6346	-0.0035	0.0165
-0.77	0.2023	-0.0173	0.0394	0.7584	0.0022	0.0040
-0.92	0.7086	-0.0304	0.0258	0.2656	0.0223	0.0056

00% of Width – 40, 90% L R_{ij} Error

Table D.7. Long glass fiber orientation standard error in the End-Gated Plaque at 00% of width and 40% of flow.

z/h	A11	A12	A22	A33	A13	A23
0.92	0.0800	0.0258	0.0071	0.0800	0.0795	0.0109
0.77	0.0554	0.0164	0.0029	0.0560	0.1028	0.0170
0.62	0.0700	0.0155	0.0208	0.0819	0.1246	0.0235
0.46	0.0500	0.0315	0.0190	0.0600	0.0506	0.0256
0.31	0.0500	0.0081	0.0064	0.0700	0.1049	0.0091
0.15	0.0545	0.0045	0.0181	0.0393	0.0577	0.0213
0.00	0.0289	0.0188	0.0045	0.0329	0.0791	0.0168
-0.15	0.0132	0.0115	0.0070	0.0196	0.0695	0.0381
-0.31	0.0600	0.0079	0.0101	0.0862	0.0914	0.0094
-0.46	0.0700	0.0253	0.0160	0.0691	0.1350	0.0298
-0.62	0.0600	0.0157	0.0149	0.0760	0.1007	0.0121
-0.77	0.0800	0.0383	0.0121	0.0880	0.0941	0.0352
-0.92	0.0600	0.0123	0.0107	0.0802	0.1162	0.0073

Table D.8. Long glass fiber orientation standard error in the End-Gated Plaque at 00% of width and 90% of flow.

z/h	A11	A12	A22	A33	A13	A23
0.92	0.0622	0.0415	0.0186	0.0537	0.0839	0.0368
0.77	0.0767	0.0282	0.0054	0.0815	0.1281	0.0070
0.62	0.0353	0.0212	0.0118	0.0459	0.0149	0.0276
0.46	0.0700	0.0151	0.0154	0.0620	0.0330	0.0171
0.31	0.0318	0.0100	0.0161	0.0161	0.0202	0.0153
0.15	0.0413	0.0067	0.0197	0.0441	0.0354	0.0286
0.00	0.0600	0.0179	0.0197	0.0646	0.0372	0.0359
-0.15	0.0727	0.0300	0.0519	0.0500	0.0160	0.0135
-0.31	0.0255	0.0227	0.0259	0.0316	0.0208	0.0367
-0.46	0.0469	0.0300	0.0455	0.0066	0.0595	0.0267
-0.62	0.0600	0.0096	0.0263	0.0556	0.0101	0.0220
-0.77	0.0600	0.0098	0.0303	0.0325	0.0237	0.0142
-0.92	0.0700	0.0317	0.0124	0.0650	0.1123	0.0306

50% of Width – 0, 10% L R_{ij} Data

Table D.9. Long glass fiber orientation data (R_{ij}) in the End-Gated Plaque at 50% of width and 00% of flow

z/h	A11	A12	A22	A33	A13	A23
0.92	0.5390	0.1180	0.0687	0.3923	0.2512	0.0765
0.77	0.5895	0.1250	0.0512	0.3593	-0.0187	0.0709
0.62	0.5351	0.1080	0.0517	0.4131	0.0415	0.0561
0.46	0.5524	0.0716	0.0373	0.4103	0.0255	0.0556
0.31	0.4475	0.1186	0.0573	0.4952	0.1493	0.1021
0.15	0.5683	0.1212	0.0486	0.3832	0.1634	0.0849
0.00	0.7012	0.1383	0.0459	0.2529	0.2371	0.0747
-0.15	0.6353	0.1158	0.0419	0.3228	0.1473	0.0592
-0.31	0.6934	0.1185	0.0413	0.2654	0.1932	0.0592
-0.46	0.4507	0.0426	0.0310	0.5183	0.0201	0.0490
-0.62	0.3777	0.0512	0.0335	0.5888	0.0634	0.0506
-0.77	0.5288	-0.0027	0.0217	0.4495	-0.0863	0.0056
-0.92	0.5043	-0.0056	0.0162	0.4795	-0.1082	0.0070

Table D.10. Long glass fiber orientation data (R_{ij}) in the End-Gated Plaque at 50% of width and 10% of flow

z/h	A11	A12	A22	A33	A13	A23
0.92	0.5313	0.0128	0.0105	0.4582	0.0558	0.0217
0.77	0.6355	-0.0072	0.0187	0.3459	0.0102	0.0289
0.62	0.6562	0.0162	0.0213	0.3225	0.0463	0.0277
0.46	0.7529	0.0228	0.0135	0.2335	0.0315	0.0217
0.31	0.5471	0.0255	0.0096	0.4433	0.0577	0.0216
0.15	0.5919	0.0410	0.0157	0.3924	0.0917	0.0295
0.00	0.6523	0.0348	0.0173	0.3304	0.0704	0.0311
-0.15	0.6626	0.0045	0.0128	0.3245	0.0052	0.0326
-0.31	0.5663	0.0053	0.0263	0.4074	0.0173	0.0328
-0.46	0.5348	-0.0162	0.0229	0.4424	-0.0062	0.0250
-0.62	0.5129	-0.0050	0.0115	0.4757	-0.0312	0.0242
-0.77	0.5684	0.0042	0.0233	0.4083	-0.0283	0.0293
-0.92	0.5661	-0.0036	0.0091	0.4247	-0.0092	0.0255

50% of Width – 0, 10% L R_{ij} Error

Table D.11. Long glass fiber orientation standard error in the End-Gated Plaque at 50% of width and 00% of flow.

z/h	A11	A12	A22	A33	A13	A23
0.92	0.0797	0.0371	0.0211	0.0867	0.0643	0.0111
0.77	0.0899	0.0427	0.0149	0.0953	0.0313	0.0174
0.62	0.1060	0.0357	0.0102	0.1047	0.0305	0.0146
0.46	0.0576	0.0341	0.0075	0.0564	0.0359	0.0167
0.31	0.0632	0.0104	0.0085	0.0595	0.0196	0.0159
0.15	0.0443	0.0152	0.0065	0.0463	0.0534	0.0038
0.00	0.0373	0.0113	0.0058	0.0386	0.0356	0.0077
-0.15	0.0797	0.0314	0.0082	0.0839	0.0740	0.0054
-0.31	0.0189	0.0140	0.0060	0.0213	0.0365	0.0119
-0.46	0.0430	0.0130	0.0068	0.0436	0.0153	0.0094
-0.62	0.0612	0.0091	0.0043	0.0593	0.0321	0.0134
-0.77	0.0781	0.0098	0.0059	0.0762	0.0237	0.0173
-0.92	0.0575	0.0123	0.0067	0.0539	0.0455	0.0100

Table D.12. Long glass fiber orientation standard error in the End-Gated Plaque at 50% of width and 10% of flow.

z/h	A11	A12	A22	A33	A13	A23
0.92	0.1000	0.0079	0.0052	0.0975	0.0400	0.0070
0.77	0.0450	0.0043	0.0051	0.0489	0.0185	0.0056
0.62	0.0635	0.0053	0.0072	0.0571	0.0238	0.0042
0.46	0.0218	0.0153	0.0029	0.0201	0.0277	0.0023
0.31	0.0766	0.0105	0.0034	0.0780	0.0330	0.0045
0.15	0.0845	0.0120	0.0041	0.0851	0.0380	0.0048
0.00	0.0807	0.0122	0.0040	0.0796	0.0342	0.0032
-0.15	0.0328	0.0093	0.0008	0.0323	0.0495	0.0015
-0.31	0.0449	0.0131	0.0028	0.0458	0.0510	0.0027
-0.46	0.0404	0.0144	0.0087	0.0345	0.0298	0.0065
-0.62	0.0371	0.0037	0.0033	0.0359	0.0131	0.0029
-0.77	0.0548	0.0086	0.0122	0.0438	0.0216	0.0094
-0.92	0.0675	0.0113	0.0024	0.0694	0.0625	0.0048

50% of Width – 40, 90% L R_{ij} Data

Table D.13. Long glass fiber orientation data (R_{ij}) in the End-Gated Plaque at 50% of width and 40% of flow

z/h	A11	A12	A22	A33	A13	A23
0.92	0.4149	0.0107	0.0225	0.5626	0.0209	0.0321
0.77	0.4451	0.0035	0.0168	0.5381	-0.0060	0.0270
0.62	0.7142	0.0079	0.0198	0.2660	0.0350	0.0308
0.46	0.7495	0.0108	0.0185	0.2320	0.0375	0.0264
0.31	0.7125	0.0193	0.0132	0.2743	0.0157	0.0245
0.15	0.5680	0.0101	0.0229	0.4091	0.0373	0.0420
0.00	0.6176	0.0443	0.0271	0.3553	0.0273	0.0445
-0.15	0.6284	0.0200	0.0291	0.3425	0.0339	0.0409
-0.31	0.5023	-0.0091	0.0217	0.4760	-0.0143	0.0416
-0.46	0.5844	-0.0091	0.0128	0.4028	-0.0238	0.0262
-0.62	0.5355	-0.0104	0.0193	0.4452	-0.0250	0.0373
-0.77	0.6947	-0.0060	0.0182	0.2871	-0.0215	0.0300
-0.92	0.7090	-0.0091	0.0150	0.2760	-0.0262	0.0270

Table D.14. Long glass fiber orientation data (R_{ij}) in the End-Gated Plaque at 50% of width and 90% of flow

z/h	A11	A12	A22	A33	A13	A23
0.92	0.4107	0.0153	0.0268	0.5625	0.0787	0.0413
0.77	0.4646	0.0072	0.0143	0.5211	0.0142	0.0253
0.62	0.4903	0.0099	0.0182	0.4914	0.0113	0.0260
0.46	0.5299	0.0097	0.0257	0.4444	0.0189	0.0339
0.31	0.6354	-0.0163	0.0178	0.3468	-0.0308	0.0312
0.15	0.6419	0.0074	0.0406	0.3175	-0.0071	0.0349
0.00	0.6274	0.0351	0.0269	0.3456	0.0152	0.0298
-0.15	0.5830	0.0054	0.0192	0.3978	0.0186	0.0304
-0.31	0.6166	-0.0016	0.0398	0.3436	-0.0297	0.0441
-0.46	0.6185	-0.0028	0.0247	0.3569	-0.0159	0.0376
-0.62	0.6464	-0.0081	0.0233	0.3303	-0.0113	0.0359
-0.77	0.6424	0.0179	0.0199	0.3377	0.0623	0.0304
-0.92	0.6528	0.0279	0.0250	0.3222	0.0982	0.0368

50% of Width – 40, 90% L R_{ij} Error

Table D.15. Long glass fiber orientation standard error in the End-Gated Plaque at 50% of width and 40% of flow.

z/h	A11	A12	A22	A33	A13	A23
0.92	0.0816	0.0137	0.0040	0.0808	0.0303	0.0018
0.77	0.0253	0.0069	0.0028	0.0272	0.0217	0.0055
0.62	0.0288	0.0175	0.0070	0.0292	0.0275	0.0073
0.46	0.0439	0.0186	0.0063	0.0432	0.0364	0.0089
0.31	0.0482	0.0137	0.0022	0.0499	0.0257	0.0015
0.15	0.0379	0.0142	0.0061	0.0417	0.0406	0.0077
0.00	0.0416	0.0414	0.0075	0.0409	0.0783	0.0114
-0.15	0.0258	0.0257	0.0060	0.0259	0.0596	0.0074
-0.31	0.0197	0.0180	0.0080	0.0246	0.0731	0.0102
-0.46	0.0617	0.0080	0.0028	0.0624	0.0191	0.0036
-0.62	0.0364	0.0141	0.0034	0.0334	0.0513	0.0016
-0.77	0.0487	0.0116	0.0052	0.0519	0.0296	0.0047
-0.92	0.0568	0.0227	0.0078	0.0543	0.0507	0.0081

Table D.16. Long glass fiber orientation standard error in the End-Gated Plaque at 50% of width and 90% of flow.

z/h	A11	A12	A22	A33	A13	A23
0.92	0.0968	0.0178	0.0061	0.0983	0.0664	0.0098
0.77	0.1199	0.0097	0.0011	0.1196	0.0301	0.0029
0.62	0.1179	0.0057	0.0055	0.1144	0.0044	0.0050
0.46	0.0830	0.0119	0.0103	0.0853	0.0384	0.0077
0.31	0.0448	0.0063	0.0051	0.0424	0.0201	0.0052
0.15	0.1215	0.0063	0.0204	0.1188	0.0271	0.0127
0.00	0.0851	0.0145	0.0080	0.0782	0.0115	0.0061
-0.15	0.1230	0.0051	0.0050	0.1191	0.0059	0.0053
-0.31	0.1370	0.0196	0.0114	0.1267	0.0295	0.0086
-0.46	0.1136	0.0214	0.0130	0.1024	0.0554	0.0129
-0.62	0.0412	0.0226	0.0030	0.0409	0.0545	0.0029
-0.77	0.0749	0.0069	0.0067	0.0725	0.0149	0.0056
-0.92	0.0534	0.0219	0.0062	0.0569	0.0618	0.0060

90% of Width – 0, 10% L R_{ij} Data

Table D.17. Long glass fiber orientation data (R_{ij}) in the End-Gated Plaque at 90% of width and 00% of flow

z/h	A11	A12	A22	A33	A13	A23
0.92	0.7084	0.1627	0.0626	0.2290	0.1182	0.0489
0.77	0.7842	0.1787	0.0524	0.1635	0.2655	0.0628
0.62	0.7692	0.1152	0.0487	0.1821	0.2250	0.0525
0.46	0.5964	0.1185	0.0475	0.3561	0.1163	0.0636
0.31	0.7438	0.1408	0.0660	0.1902	0.1801	0.0537
0.15	0.6732	0.1673	0.0654	0.2613	0.1924	0.0506
0.00	0.6684	0.1464	0.0571	0.2745	0.1242	0.0759
-0.15	0.6835	0.1561	0.0619	0.2546	0.1506	0.0894
-0.31	0.7794	0.0949	0.0295	0.1911	0.1531	0.0448
-0.46	0.5810	0.0415	0.0526	0.3663	-0.0106	0.0449
-0.62	0.8224	0.0002	0.0183	0.1593	-0.0724	0.0127
-0.77	0.6018	0.0244	0.0628	0.3355	-0.1207	0.0612
-0.92	0.4167	0.0158	0.0313	0.5521	0.1898	0.0254

Table D.18. Long glass fiber orientation data (R_{ij}) in the End-Gated Plaque at 90% of width and 10% of flow

z/h	A11	A12	A22	A33	A13	A23
0.92	0.4242	0.0487	0.0283	0.5474	0.1158	0.0444
0.77	0.6508	0.0361	0.0086	0.3406	0.1130	0.0206
0.62	0.7530	0.0561	0.0174	0.2296	0.0821	0.0229
0.46	0.6423	0.0488	0.0377	0.3200	0.0839	0.0328
0.31	0.7609	0.0437	0.0335	0.2056	0.0903	0.0363
0.15	0.8532	0.0449	0.0203	0.1266	0.0472	0.0236
0.00	0.8247	0.0211	0.0229	0.1524	0.0442	0.0292
-0.15	0.8102	0.0440	0.0259	0.1639	0.1096	0.0363
-0.31	0.7632	0.0562	0.0228	0.2139	0.1065	0.0356
-0.46	0.7041	-0.0011	0.0277	0.2682	-0.0115	0.0457
-0.62	0.6940	0.0125	0.0266	0.2793	-0.0413	0.0359
-0.77	0.6260	-0.0111	0.0255	0.3485	-0.0745	0.0362
-0.92	0.7531	-0.0165	0.0071	0.2398	-0.1160	0.0212

90% of Width – 0, 10% L R_{ij} Error

Table D.19. Long glass fiber orientation standard error in the End-Gated Plaque at 90% of width and 00% of flow.

z/h	A11	A12	A22	A33	A13	A23
0.92	0.0496	0.0291	0.0094	0.0543	0.0396	0.0209
0.77	0.0324	0.0203	0.0072	0.0358	0.0225	0.0057
0.62	0.0363	0.0242	0.0140	0.0255	0.0174	0.0128
0.46	0.0596	0.0104	0.0101	0.0544	0.0367	0.0067
0.31	0.0441	0.0089	0.0154	0.0396	0.0136	0.0216
0.15	0.0445	0.0341	0.0107	0.0547	0.0257	0.0142
0.00	0.0842	0.0229	0.0048	0.0875	0.0401	0.0096
-0.15	0.0564	0.0096	0.0109	0.0487	0.0465	0.0178
-0.31	0.0504	0.0200	0.0064	0.0485	0.0355	0.0056
-0.46	0.0916	0.0398	0.0087	0.0856	0.0761	0.0227
-0.62	0.0289	0.0414	0.0045	0.0304	0.0871	0.0155
-0.77	0.0476	0.0298	0.0183	0.0346	0.0959	0.0224
-0.92	0.0461	0.0185	0.0084	0.0449	0.0518	0.0246

Table D.20. Long glass fiber orientation standard error in the End-Gated Plaque at 90% of width and 10% of flow.

z/h	A11	A12	A22	A33	A13	A23
0.92	0.0039	0.0060	0.0081	0.0119	0.0043	0.0069
0.77	0.0923	0.0026	0.0006	0.0929	0.0638	0.0038
0.62	0.0571	0.0182	0.0031	0.0603	0.0251	0.0035
0.46	0.0600	0.0200	0.0201	0.0938	0.0168	0.0107
0.31	0.0232	0.0134	0.0175	0.0057	0.0525	0.0110
0.15	0.0283	0.0239	0.0024	0.0307	0.0451	0.0032
0.00	0.0600	0.0227	0.0113	0.1118	0.0462	0.0154
-0.15	0.0700	0.0470	0.0067	0.0675	0.1201	0.0230
-0.31	0.0800	0.0455	0.0160	0.0753	0.0727	0.0228
-0.46	0.0645	0.0252	0.0035	0.0680	0.0711	0.0029
-0.62	0.0779	0.0013	0.0053	0.0726	0.0250	0.0123
-0.77	0.0494	0.0095	0.0057	0.0437	0.0168	0.0061
-0.92	0.0307	0.0035	0.0040	0.0347	0.0498	0.0016

90% of Width – 40, 90% L R_{ij} Data

Table D.21. Long glass fiber orientation data (R_{ij}) in the End-Gated Plaque at 90% of width and 40% of flow

z/h	A11	A12	A22	A33	A13	A23
0.92	0.4319	0.0157	0.0133	0.5548	0.0635	0.0304
0.77	0.6065	0.0322	0.0220	0.3714	0.0111	0.0298
0.62	0.5930	0.0037	0.0247	0.3823	0.0224	0.0326
0.46	0.6169	0.0107	0.0302	0.3528	0.0208	0.0412
0.31	0.6442	0.0189	0.0393	0.3165	-0.0040	0.0385
0.15	0.6443	-0.0102	0.0269	0.3288	-0.0473	0.0428
0.00	0.7821	-0.0154	0.0219	0.1961	-0.0621	0.0331
-0.15	0.7371	-0.0225	0.0443	0.2186	-0.0537	0.0436
-0.31	0.8276	-0.0137	0.0306	0.1418	-0.0182	0.0319
-0.46	0.7611	-0.0014	0.0236	0.2153	-0.0113	0.0286
-0.62	0.7687	-0.0079	0.0339	0.1974	0.0108	0.0381
-0.77	0.6802	-0.0126	0.0160	0.3038	-0.0625	0.0303
-0.92	0.3532	-0.0080	0.0087	0.6381	-0.0438	0.0166

Table D.22. Long glass fiber orientation data (R_{ij}) in the End-Gated Plaque at 90% of width and 90% of flow

z/h	A11	A12	A22	A33	A13	A23
0.92	0.6125	0.0080	0.0188	0.3687	0.0167	0.0301
0.77	0.6382	0.0068	0.0360	0.3258	-0.0013	0.0399
0.62	0.6962	0.0198	0.0310	0.2728	0.0199	0.0364
0.46	0.6629	-0.0055	0.0226	0.3145	-0.0319	0.0341
0.31	0.6386	0.0103	0.0303	0.3311	0.0319	0.0359
0.15	0.6610	0.0389	0.0295	0.3095	0.0832	0.0378
0.00	0.7295	0.0264	0.0413	0.2291	0.0285	0.0410
-0.15	0.7601	0.0504	0.0347	0.2052	0.0637	0.0379
-0.31	0.7153	0.0552	0.0462	0.2384	0.0668	0.0495
-0.46	0.6265	0.0460	0.0616	0.3119	0.0324	0.0612
-0.62	0.5793	0.0273	0.0519	0.3688	0.0133	0.0532
-0.77	0.6100	-0.0018	0.0198	0.3703	-0.0023	0.0297
-0.92	0.6895	0.0007	0.0136	0.2969	0.0005	0.0235

90% of Width – 40, 90% L A_{ij} Error

Table D.23. Long glass fiber orientation standard error in the End-Gated Plaque at 90% of width and 40% of flow.

z/h	A11	A12	A22	A33	A13	A23
0.92	0.0637	0.0092	0.0057	0.0684	0.0356	0.0055
0.77	0.0177	0.0289	0.0131	0.0069	0.0203	0.0070
0.62	0.0387	0.0179	0.0079	0.0389	0.0393	0.0043
0.46	0.0113	0.0140	0.0087	0.0195	0.0193	0.0069
0.31	0.0658	0.0313	0.0112	0.0564	0.0582	0.0063
0.15	0.0800	0.0328	0.0066	0.0754	0.0806	0.0122
0.00	0.0804	0.0233	0.0034	0.0790	0.0530	0.0079
-0.15	0.0800	0.0202	0.0116	0.0699	0.0274	0.0114
-0.31	0.0485	0.0238	0.0099	0.0401	0.0284	0.0073
-0.46	0.0500	0.0085	0.0043	0.0981	0.0076	0.0057
-0.62	0.0626	0.0036	0.0162	0.0479	0.0056	0.0127
-0.77	0.0539	0.0157	0.0061	0.0478	0.0303	0.0053
-0.92	0.0752	0.0039	0.0039	0.0949	0.0246	0.0041

Table D.24. Long glass fiber orientation standard error in the End-Gated Plaque at 90% of width and 90% of flow.

z/h	A11	A12	A22	A33	A13	A23
0.92	0.0621	0.0103	0.0057	0.0674	0.0176	0.0048
0.77	0.0633	0.0127	0.0106	0.0702	0.0285	0.0063
0.62	0.0806	0.0076	0.0059	0.0758	0.0120	0.0045
0.46	0.1157	0.0193	0.0033	0.1136	0.0362	0.0063
0.31	0.1307	0.0101	0.0021	0.1307	0.0168	0.0046
0.15	0.1269	0.0136	0.0030	0.1295	0.0279	0.0068
0.00	0.0803	0.0277	0.0076	0.0804	0.0498	0.0088
-0.15	0.0699	0.0299	0.0099	0.0635	0.0190	0.0088
-0.31	0.0404	0.0353	0.0104	0.0353	0.0294	0.0101
-0.46	0.0714	0.0328	0.0179	0.0664	0.0401	0.0150
-0.62	0.0805	0.0147	0.0096	0.0760	0.0382	0.0114
-0.77	0.1174	0.0111	0.0042	0.1136	0.0250	0.0048
-0.92	0.0720	0.0108	0.0023	0.0715	0.0234	0.0017

Appendix E. Sprue Orientation Data (SGF vs. LGF)

Note:	Axx	Axy	Ayy	Azz	Axz	Ayz
	A11	A12	A22	A33	A13	A23

SGF – 20% of Sprue Length - A_{ij}

Table E.1. Short glass fiber orientation data (A_{ij}) at 20% of sprue length as a function of dimensionless sprue radius.

r/R	A11	A12	A22	A33	A13	A23
0.00	0.22	0.12	0.61	0.18	0.00	0.01
0.13	0.11	0.09	0.67	0.22	-0.01	0.01
0.27	0.06	0.07	0.77	0.17	-0.01	-0.02
0.40	0.07	0.06	0.77	0.16	0.00	0.02
0.53	0.05	0.05	0.80	0.15	-0.01	-0.02
0.67	0.03	0.03	0.83	0.13	0.00	-0.01
0.80	0.03	0.03	0.85	0.11	-0.01	-0.02
0.93	0.07	0.06	0.69	0.24	0.01	0.01

Table E.2. Short glass fiber orientation data error at 20% of sprue length as a function of dimensionless sprue radius.

r/R	A11	A12	A22	A33	A13	A23
0.00	0.09	0.02	0.03	0.06	0.04	0.02
0.13	0.01	0.02	0.10	0.10	0.09	0.06
0.27	0.02	0.01	0.03	0.02	0.06	0.08
0.40	0.09	0.05	0.10	0.09	0.04	0.05
0.53	0.02	0.01	0.03	0.03	0.04	0.05
0.67	0.03	0.01	0.06	0.05	0.02	0.05
0.80	0.04	0.03	0.09	0.08	0.04	0.06
0.93	0.03	0.02	0.20	0.23	0.02	0.05

SGF – 100% of Sprue Length - A_{ij}

Table E.3. Short glass fiber orientation data (A_{ij}) at 100% of sprue length as a function of dimensionless sprue radius.

r/R	A11	A12	A22	A33	A13	A23
0.00	0.37	0.20	0.26	0.38	-0.01	-0.05
0.13	0.33	0.18	0.34	0.33	0.10	0.07
0.27	0.22	0.19	0.47	0.31	-0.06	-0.08
0.40	0.18	0.11	0.56	0.25	0.10	0.07
0.53	0.06	0.05	0.78	0.16	-0.01	-0.02
0.67	0.04	0.04	0.81	0.15	0.00	-0.01
0.80	0.05	0.04	0.82	0.13	0.00	0.00
0.93	0.03	0.04	0.85	0.12	0.00	-0.01

Table E.4. Short glass fiber orientation data error at 100% of sprue length as a function of dimensionless sprue radius.

r/R	A11	A12	A22	A33	A13	A23
0.00	0.07	0.00	0.02	0.05	0.18	0.16
0.13	0.14	0.02	0.13	0.04	0.15	0.07
0.27	0.09	0.05	0.14	0.08	0.14	0.11
0.40	0.12	0.02	0.20	0.09	0.10	0.04
0.53	0.02	0.02	0.09	0.09	0.02	0.03
0.67	0.01	0.01	0.06	0.06	0.01	0.03
0.80	0.01	0.01	0.04	0.03	0.01	0.02
0.93	0.02	0.02	0.02	0.03	0.01	0.02

LGF – 20% of Sprue Length - R_{ij}

Table E.5. Long glass fiber orientation data (R_{ij}) at 20% of sprue length as a function of dimensionless sprue radius.

r/R	A11	A12	A22	A33	A13	A23
0.00	0.20	0.14	0.57	0.23	0.03	-0.03
0.13	0.17	0.12	0.53	0.31	0.02	-0.06
0.27	0.21	0.17	0.39	0.40	0.00	0.00
0.40	0.12	0.12	0.59	0.28	0.01	0.02
0.53	0.13	0.12	0.43	0.45	0.00	-0.02
0.67	0.09	0.09	0.44	0.47	-0.01	-0.05
0.80	0.06	0.07	0.60	0.34	0.01	-0.02
0.93	0.03	0.03	0.69	0.28	-0.01	0.00

Table E.6. Long glass fiber orientation data error at 20% of sprue length as a function of dimensionless sprue radius.

r/R	A11	A12	A22	A33	A13	A23
0.00	0.02	0.01	0.00	0.02	0.15	0.15
0.13	0.10	0.03	0.21	0.16	0.19	0.13
0.27	0.12	0.11	0.12	0.23	0.21	0.17
0.40	0.05	0.04	0.21	0.19	0.04	0.06
0.53	0.05	0.05	0.13	0.17	0.06	0.10
0.67	0.09	0.07	0.23	0.25	0.09	0.11
0.80	0.05	0.04	0.11	0.07	0.05	0.03
0.93	0.02	0.02	0.05	0.05	0.03	0.05

LGF – 100% of Sprue Length - R_{ij}

Table E.7. Long glass fiber orientation data (R_{ij}) at 20% of sprue length as a function of dimensionless sprue radius.

r/R	A11	A12	A22	A33	A13	A23
0.00	0.38	0.18	0.18	0.44	0.04	0.02
0.13	0.36	0.20	0.20	0.44	0.11	0.04
0.27	0.22	0.16	0.26	0.52	0.11	0.09
0.40	0.29	0.17	0.32	0.38	0.00	-0.01
0.53	0.08	0.09	0.40	0.52	-0.02	-0.04
0.67	0.09	0.10	0.46	0.44	0.01	0.04
0.80	0.17	0.15	0.59	0.24	0.01	0.00
0.93	0.17	0.14	0.61	0.23	-0.01	-0.01

Table E.8. Long glass fiber orientation data error at 100% of sprue length as a function of dimensionless sprue radius.

r/R	A11	A12	A22	A33	A13	A23
0.00	0.36	0.13	0.00	0.36	0.07	0.06
0.13	0.23	0.11	0.13	0.26	0.22	0.14
0.27	0.10	0.07	0.12	0.20	0.09	0.06
0.40	0.14	0.03	0.18	0.09	0.27	0.11
0.53	0.04	0.03	0.03	0.05	0.05	0.06
0.67	0.03	0.02	0.11	0.12	0.04	0.08
0.80	0.06	0.05	0.15	0.11	0.03	0.01
0.93	0.05	0.03	0.09	0.06	0.05	0.01

Appendix F. End-Gated Plaque Gate Orientation Data (SGF vs. LGF)

Note:	Axx	Axy	Ayy	Azz	Axz	Ayz
	A11	A12	A22	A33	A13	A23

Gate: 00% of Width – SGF A_{ij} Data

Table F.1. Short Glass Fiber end-gated plaque gate orientation data (A11) at 00% Width.

A11		x/L_g									
		-0.9	-0.7	-0.5	-0.3	-0.1	0.1	0.3	0.5	0.7	0.9
z/L_g	-0.9	0.810	0.642	0.610	0.511	0.542	0.437	0.397	0.279	0.390	0.430
	-0.7	0.833	0.730	0.702	0.556	0.364	0.260	0.167	0.109	0.126	0.094
	-0.5	0.737	0.831	0.677	0.527	0.427	0.271	0.288	0.078	0.044	0.110
	-0.3	0.600	0.454	0.466	0.408	0.153	0.078	0.110	0.035	0.032	0.037
	-0.1	0.543	0.553	0.529	0.291	0.132	0.102	0.082	0.062	0.046	0.069
	0.1	0.634	0.591	0.379	0.302	0.253	0.165	0.083	0.067	0.054	0.042
	0.3	0.380	0.387	0.453	0.494	0.419	0.219	0.100	0.076	0.055	0.018
	0.5	0.803	0.621	0.616	0.597	0.395	0.328	0.158	0.073	0.061	0.024
	0.7	0.686	0.597	0.522	0.447	0.256	0.291	0.177	0.081	0.048	0.045
	0.9	0.673	0.462	0.528	0.403	0.300	0.186	0.183	0.087	0.070	0.110

Table F.2. Short Glass Fiber end-gated plaque gate orientation data (A12) at 00% Width.

A12		x/L_g									
		-0.9	-0.7	-0.5	-0.3	-0.1	0.1	0.3	0.5	0.7	0.9
z/L_g	-0.9	0.007	-0.022	-0.015	-0.001	-0.041	-0.027	-0.012	0.019	0.009	0.021
	-0.7	0.013	-0.004	-0.001	-0.003	-0.052	-0.017	-0.010	-0.013	-0.002	0.015
	-0.5	-0.086	-0.089	-0.117	-0.063	-0.142	-0.074	-0.105	-0.044	-0.002	0.066
	-0.3	-0.003	-0.044	-0.015	0.057	-0.079	-0.017	-0.111	-0.011	0.013	0.023
	-0.1	0.265	0.148	0.123	0.145	0.050	0.051	0.038	0.012	0.012	0.017
	0.1	0.159	0.123	0.087	0.179	0.110	0.073	0.055	0.004	0.001	0.005
	0.3	0.060	0.094	0.151	0.164	0.118	0.071	0.058	0.032	-0.014	-0.009
	0.5	0.004	0.094	0.098	0.074	0.061	0.074	0.014	0.014	0.009	-0.018
	0.7	-0.025	0.048	0.013	0.032	0.001	0.006	0.005	-0.005	0.000	0.007
	0.9	-0.005	0.026	0.030	0.011	0.008	-0.011	0.002	-0.006	-0.005	0.054

Gate: 00% of Width – SGF A_{ij} Data

Table F.3. Short Glass Fiber end-gated plaque gate orientation data (A22) at 00% Width.

A22		x/L_g									
		-0.9	-0.7	-0.5	-0.3	-0.1	0.1	0.3	0.5	0.7	0.9
z/L_g	-0.9	0.017	0.026	0.015	0.037	0.033	0.038	0.028	0.028	0.040	0.013
	-0.7	0.024	0.028	0.028	0.030	0.087	0.056	0.035	0.034	0.041	0.052
	-0.5	0.058	0.046	0.067	0.052	0.112	0.095	0.079	0.101	0.105	0.161
	-0.3	0.224	0.336	0.199	0.187	0.228	0.231	0.280	0.137	0.143	0.203
	-0.1	0.312	0.233	0.184	0.326	0.293	0.300	0.271	0.249	0.154	0.176
	0.1	0.110	0.128	0.148	0.198	0.183	0.179	0.200	0.181	0.144	0.254
	0.3	0.097	0.082	0.134	0.140	0.117	0.109	0.129	0.155	0.119	0.126
	0.5	0.034	0.060	0.045	0.041	0.062	0.055	0.074	0.096	0.076	0.098
	0.7	0.032	0.022	0.041	0.042	0.051	0.048	0.064	0.034	0.048	0.177
	0.9	0.016	0.036	0.024	0.015	0.050	0.043	0.023	0.032	0.032	0.161

Table F.4. Short Glass Fiber end-gated plaque gate orientation data (A33) at 00% Width.

A33		x/L_g									
		-0.9	-0.7	-0.5	-0.3	-0.1	0.1	0.3	0.5	0.7	0.9
z/L_g	-0.9	0.173	0.332	0.375	0.452	0.425	0.526	0.575	0.692	0.570	0.557
	-0.7	0.143	0.241	0.270	0.414	0.549	0.684	0.798	0.857	0.833	0.854
	-0.5	0.205	0.123	0.256	0.422	0.461	0.634	0.633	0.822	0.851	0.729
	-0.3	0.176	0.210	0.335	0.405	0.619	0.691	0.610	0.827	0.825	0.760
	-0.1	0.145	0.214	0.286	0.383	0.575	0.599	0.647	0.689	0.800	0.755
	0.1	0.256	0.281	0.472	0.499	0.564	0.656	0.717	0.752	0.802	0.704
	0.3	0.523	0.531	0.413	0.366	0.464	0.672	0.771	0.770	0.827	0.856
	0.5	0.163	0.319	0.339	0.362	0.543	0.617	0.768	0.831	0.863	0.878
	0.7	0.281	0.381	0.437	0.511	0.693	0.661	0.758	0.885	0.903	0.778
	0.9	0.310	0.502	0.447	0.582	0.650	0.771	0.794	0.881	0.899	0.728

Gate: 00% of Width – SGF A_{ij} Data

Table F.5. Short Glass Fiber end-gated plaque gate orientation data (A13) at 00% Width.

A13		x/L_g									
		-0.9	**-0.7**	**-0.5**	**-0.3**	**-0.1**	**0.1**	**0.3**	**0.5**	**0.7**	**0.9**
z/L_g	**-0.9**	0.068	-0.057	-0.036	0.043	-0.031	-0.111	0.012	0.044	0.051	0.053
	-0.7	0.044	0.005	0.010	-0.034	-0.095	-0.026	-0.025	-0.019	0.006	-0.006
	-0.5	-0.089	-0.099	-0.128	-0.145	-0.178	-0.109	-0.104	-0.037	-0.009	0.034
	-0.3	0.005	-0.017	-0.025	0.030	-0.046	-0.022	-0.085	-0.009	0.005	0.010
	-0.1	0.038	0.089	0.067	0.059	0.035	0.039	0.010	-0.009	0.012	0.010
	0.1	0.099	0.066	0.025	0.072	0.086	0.054	0.012	0.004	-0.007	0.000
	0.3	0.101	0.127	0.112	0.089	0.083	0.074	0.052	0.023	-0.022	-0.007
	0.5	0.012	0.086	0.130	0.094	0.079	0.107	0.023	0.009	-0.001	-0.020
	0.7	-0.001	0.067	0.056	0.075	0.020	-0.016	-0.005	0.001	-0.001	-0.004
	0.9	0.025	0.062	0.112	0.054	0.029	0.014	0.022	0.002	-0.024	-0.008

Table F.6. Short Glass Fiber end-gated plaque gate orientation data (A23) at 00% Width.

A23		x/L_g									
		-0.9	**-0.7**	**-0.5**	**-0.3**	**-0.1**	**0.1**	**0.3**	**0.5**	**0.7**	**0.9**
z/L_g	**-0.9**	0.031	0.038	0.034	0.047	0.042	0.047	0.037	0.031	0.045	0.023
	-0.7	0.030	0.037	0.040	0.049	0.086	0.053	0.038	0.038	0.047	0.040
	-0.5	0.053	0.036	0.064	0.067	0.108	0.090	0.071	0.082	0.076	0.105
	-0.3	0.110	0.134	0.137	0.152	0.130	0.126	0.160	0.070	0.089	0.121
	-0.1	0.110	0.149	0.115	0.171	0.156	0.179	0.149	0.123	0.085	0.110
	0.1	0.088	0.095	0.099	0.112	0.137	0.137	0.107	0.112	0.098	0.114
	0.3	0.092	0.098	0.112	0.096	0.088	0.094	0.089	0.087	0.073	0.068
	0.5	0.046	0.072	0.054	0.055	0.068	0.064	0.064	0.069	0.057	0.070
	0.7	0.044	0.033	0.051	0.045	0.057	0.053	0.048	0.036	0.041	0.094
	0.9	0.026	0.045	0.043	0.030	0.054	0.044	0.028	0.034	0.033	0.064

Gate: 00% of Width – SGF A_{ij} Error

Table F.7. Short Glass Fiber end-gated plaque gate orientation error (A11) at 00% Width.

A11		x/L_g									
		-0.9	-0.7	-0.5	-0.3	-0.1	0.1	0.3	0.5	0.7	0.9
z/L_g	-0.9	0.006	0.043	0.012	0.041	0.017	0.014	0.023	0.032	0.042	0.001
	-0.7	0.026	0.047	0.057	0.055	0.091	0.071	0.006	0.028	0.023	0.030
	-0.5	0.004	0.022	0.019	0.026	0.060	0.049	0.018	0.034	0.024	0.001
	-0.3	0.039	0.031	0.065	0.095	0.049	0.045	0.030	0.013	0.033	0.015
	-0.1	0.106	0.038	0.049	0.067	0.002	0.039	0.013	0.021	0.034	0.021
	0.1	0.064	0.106	0.086	0.030	0.029	0.013	0.030	0.026	0.014	0.009
	0.3	0.038	0.066	0.022	0.102	0.048	0.038	0.036	0.035	0.014	0.012
	0.5	0.020	0.009	0.006	0.106	0.040	0.007	0.041	0.016	0.007	0.017
	0.7	0.001	0.050	0.109	0.088	0.028	0.053	0.036	0.064	0.006	0.005
	0.9	0.067	0.052	0.011	0.062	0.060	0.076	0.011	0.018	0.001	0.031

Table F.8. Short Glass Fiber end-gated plaque gate orientation error (A12) at 00% Width.

A12		x/L_g									
		-0.9	-0.7	-0.5	-0.3	-0.1	0.1	0.3	0.5	0.7	0.9
z/L_g	-0.9	0.008	0.002	0.007	0.011	0.005	0.015	0.009	0.006	0.005	0.014
	-0.7	0.025	0.012	0.018	0.024	0.037	0.040	0.047	0.007	0.013	0.000
	-0.5	0.008	0.028	0.046	0.036	0.021	0.015	0.008	0.007	0.001	0.018
	-0.3	0.092	0.030	0.026	0.042	0.035	0.000	0.007	0.024	0.016	0.008
	-0.1	0.019	0.040	0.073	0.092	0.027	0.006	0.010	0.014	0.003	0.006
	0.1	0.009	0.004	0.031	0.036	0.004	0.036	0.000	0.000	0.009	0.009
	0.3	0.014	0.012	0.053	0.030	0.009	0.006	0.000	0.019	0.012	0.003
	0.5	0.031	0.038	0.014	0.017	0.006	0.034	0.038	0.014	0.000	0.004
	0.7	0.007	0.015	0.011	0.008	0.003	0.008	0.001	0.007	0.000	0.016
	0.9	0.013	0.010	0.002	0.005	0.012	0.012	0.005	0.015	0.008	0.031

Gate: 00% of Width – SGF A_{ij} Error

Table F.9. Short Glass Fiber end-gated plaque gate orientation error (A22) at 00% Width.											
A22		**x/L_g**									
		-0.9	**-0.7**	**-0.5**	**-0.3**	**-0.1**	**0.1**	**0.3**	**0.5**	**0.7**	**0.9**
z/L_g	**-0.9**	0.006	0.010	0.018	0.046	0.043	0.050	0.024	0.023	0.023	0.022
	-0.7	0.030	0.009	0.038	0.052	0.077	0.048	0.004	0.076	0.000	0.027
	-0.5	0.014	0.001	0.012	0.020	0.006	0.085	0.056	0.091	0.088	0.021
	-0.3	0.072	0.098	0.028	0.092	0.032	0.011	0.045	0.070	0.109	0.074
	-0.1	0.033	0.024	0.084	0.047	0.038	0.003	0.095	0.041	0.087	0.001
	0.1	0.022	0.077	0.020	0.004	0.027	0.019	0.060	0.026	0.023	0.009
	0.3	0.021	0.014	0.057	0.011	0.006	0.000	0.030	0.019	0.022	0.004
	0.5	0.003	0.035	0.008	0.031	0.025	0.015	0.071	0.047	0.002	0.034
	0.7	0.007	0.008	0.001	0.036	0.038	0.039	0.039	0.018	0.011	0.073
	0.9	0.010	0.014	0.016	0.020	0.030	0.014	0.006	0.019	0.001	0.033

Table F.10. Short Glass Fiber end-gated plaque gate orientation error (A33) at 00% Width.											
A33		**x/L_g**									
		-0.9	**-0.7**	**-0.5**	**-0.3**	**-0.1**	**0.1**	**0.3**	**0.5**	**0.7**	**0.9**
z/L_g	**-0.9**	0.000	0.054	0.006	0.095	0.066	0.039	0.002	0.008	0.018	0.019
	-0.7	0.055	0.064	0.111	0.106	0.179	0.106	0.008	0.046	0.023	0.002
	-0.5	0.010	0.019	0.006	0.044	0.064	0.136	0.073	0.051	0.067	0.019
	-0.3	0.032	0.081	0.029	0.007	0.020	0.063	0.088	0.056	0.065	0.095
	-0.1	0.070	0.011	0.029	0.025	0.030	0.035	0.077	0.023	0.055	0.022
	0.1	0.083	0.036	0.068	0.040	0.055	0.035	0.033	0.002	0.038	0.019
	0.3	0.018	0.048	0.041	0.070	0.047	0.036	0.008	0.048	0.029	0.009
	0.5	0.026	0.052	0.003	0.116	0.062	0.007	0.117	0.026	0.008	0.017
	0.7	0.005	0.052	0.135	0.133	0.085	0.098	0.078	0.069	0.021	0.069
	0.9	0.066	0.026	0.007	0.092	0.074	0.100	0.022	0.036	0.002	0.076

Gate: 00% of Width – SGF A_{ij} Error

Table F.11. Short Glass Fiber end-gated plaque gate orientation error (A13) at 00% Width.											
A13		**x/L$_g$**									
		-0.9	**-0.7**	**-0.5**	**-0.3**	**-0.1**	**0.1**	**0.3**	**0.5**	**0.7**	**0.9**
z/L$_g$	**-0.9**	0.007	0.007	0.012	0.003	0.009	0.002	0.003	0.004	0.003	0.014
	-0.7	0.030	0.017	0.005	0.007	0.025	0.028	0.031	0.003	0.015	0.014
	-0.5	0.005	0.014	0.036	0.027	0.017	0.001	0.012	0.010	0.003	0.025
	-0.3	0.064	0.004	0.021	0.002	0.020	0.001	0.001	0.011	0.014	0.005
	-0.1	0.009	0.036	0.026	0.047	0.020	0.012	0.008	0.005	0.007	0.000
	0.1	0.029	0.023	0.021	0.031	0.012	0.030	0.006	0.008	0.012	0.003
	0.3	0.023	0.036	0.028	0.038	0.012	0.009	0.015	0.018	0.004	0.003
	0.5	0.005	0.011	0.003	0.028	0.032	0.018	0.018	0.004	0.000	0.001
	0.7	0.012	0.022	0.008	0.005	0.009	0.014	0.003	0.008	0.001	0.012
	0.9	0.028	0.033	0.033	0.000	0.005	0.006	0.004	0.025	0.003	0.035

Table F.12. Short Glass Fiber end-gated plaque gate orientation error (A23) at 00% Width.											
A23		**x/L$_g$**									
		-0.9	**-0.7**	**-0.5**	**-0.3**	**-0.1**	**0.1**	**0.3**	**0.5**	**0.7**	**0.9**
z/L$_g$	**-0.9**	0.005	0.005	0.010	0.034	0.030	0.032	0.019	0.014	0.014	0.014
	-0.7	0.018	0.005	0.023	0.026	0.047	0.034	0.013	0.028	0.021	0.009
	-0.5	0.017	0.013	0.007	0.019	0.021	0.043	0.024	0.020	0.001	0.012
	-0.3	0.029	0.012	0.012	0.014	0.012	0.016	0.045	0.008	0.005	0.024
	-0.1	0.006	0.002	0.014	0.023	0.006	0.022	0.019	0.015	0.001	0.012
	0.1	0.003	0.025	0.011	0.003	0.017	0.006	0.007	0.010	0.008	0.005
	0.3	0.005	0.006	0.007	0.027	0.019	0.019	0.004	0.008	0.033	0.003
	0.5	0.006	0.016	0.028	0.026	0.012	0.004	0.015	0.002	0.001	0.000
	0.7	0.006	0.004	0.001	0.025	0.028	0.029	0.032	0.020	0.009	0.019
	0.9	0.007	0.013	0.010	0.018	0.024	0.014	0.004	0.016	0.004	0.023

Gate: 50% of Width – SGF A_{ij} Data

Table F.13. Short Glass Fiber end-gated plaque gate orientation data (A11) at 50% Width.

A11		x/L_g									
		-0.9	-0.7	-0.5	-0.3	-0.1	0.1	0.3	0.5	0.7	0.9
z/L_g	-0.9	0.113	0.161	0.162	0.225	0.232	0.351	0.549	0.463	0.503	0.564
	-0.7	0.036	0.071	0.117	0.218	0.199	0.295	0.529	0.580	0.668	0.734
	-0.5	0.052	0.090	0.180	0.297	0.384	0.504	0.714	0.651	0.495	0.271
	-0.3	0.029	0.055	0.139	0.217	0.378	0.424	0.515	0.391	0.189	0.069
	-0.1	0.053	0.051	0.077	0.116	0.273	0.404	0.388	0.194	0.106	0.035
	0.1	0.025	0.032	0.088	0.101	0.191	0.295	0.252	0.174	0.072	0.055
	0.3	0.022	0.029	0.042	0.101	0.106	0.217	0.185	0.081	0.036	0.043
	0.5	0.043	0.047	0.042	0.090	0.210	0.203	0.125	0.067	0.058	0.035
	0.7	0.067	0.038	0.059	0.066	0.057	0.056	0.083	0.066	0.068	0.080
	0.9	0.125	0.127	0.202	0.108	0.106	0.138	0.135	0.122	0.169	0.108

Table F.14. Short Glass Fiber end-gated plaque gate orientation data (A12) at 50% Width.

A12		x/L_g									
		-0.9	-0.7	-0.5	-0.3	-0.1	0.1	0.3	0.5	0.7	0.9
z/L_g	-0.9	-0.011	-0.005	-0.008	-0.032	-0.018	-0.011	0.074	0.039	0.050	0.025
	-0.7	0.004	-0.003	0.012	0.013	0.007	0.015	0.113	0.137	0.214	0.162
	-0.5	-0.009	-0.007	0.027	0.085	0.067	0.181	0.267	0.303	0.276	0.186
	-0.3	0.004	-0.005	0.049	0.122	0.208	0.230	0.291	0.291	0.205	0.037
	-0.1	-0.013	-0.001	0.063	0.081	0.215	0.294	0.249	0.176	0.141	0.013
	0.1	0.013	0.009	-0.005	0.033	0.096	0.184	0.141	0.218	0.073	0.008
	0.3	-0.005	-0.015	-0.035	-0.024	-0.059	0.052	0.151	0.047	0.025	0.002
	0.5	-0.013	-0.025	-0.023	-0.003	-0.071	-0.022	-0.001	0.027	0.007	0.016
	0.7	-0.033	-0.005	-0.016	-0.013	-0.010	-0.017	-0.014	-0.004	0.006	0.022
	0.9	-0.029	-0.018	0.000	0.000	-0.018	-0.007	-0.015	-0.009	0.010	0.011

Gate: 50% of Width – SGF A_{ij} Data

Table F.15. Short Glass Fiber end-gated plaque gate orientation data (A22) at 50% Width.

A22		x/L_g									
		-0.9	-0.7	-0.5	-0.3	-0.1	0.1	0.3	0.5	0.7	0.9
z/L_g	-0.9	0.065	0.038	0.055	0.045	0.017	0.044	0.044	0.017	0.034	0.037
	-0.7	0.155	0.099	0.070	0.070	0.082	0.058	0.060	0.074	0.100	0.070
	-0.5	0.122	0.077	0.110	0.082	0.085	0.113	0.130	0.194	0.212	0.245
	-0.3	0.098	0.040	0.184	0.195	0.211	0.255	0.301	0.349	0.370	0.350
	-0.1	0.041	0.072	0.247	0.365	0.335	0.367	0.403	0.413	0.374	0.296
	0.1	0.116	0.175	0.285	0.292	0.307	0.427	0.425	0.513	0.274	0.293
	0.3	0.110	0.115	0.139	0.170	0.266	0.321	0.392	0.219	0.111	0.308
	0.5	0.169	0.100	0.082	0.116	0.113	0.128	0.130	0.093	0.081	0.213
	0.7	0.147	0.054	0.037	0.069	0.053	0.052	0.064	0.048	0.050	0.179
	0.9	0.061	0.048	0.049	0.035	0.058	0.046	0.035	0.047	0.087	0.161

Table F.16. Short Glass Fiber end-gated plaque gate orientation data (A33) at 50% Width.

A33		x/L_g									
		-0.9	-0.7	-0.5	-0.3	-0.1	0.1	0.3	0.5	0.7	0.9
z/L_g	-0.9	0.821	0.800	0.782	0.730	0.751	0.605	0.407	0.520	0.463	0.399
	-0.7	0.809	0.830	0.813	0.712	0.718	0.647	0.410	0.347	0.232	0.196
	-0.5	0.826	0.833	0.710	0.621	0.531	0.383	0.155	0.154	0.293	0.484
	-0.3	0.873	0.906	0.676	0.588	0.411	0.321	0.185	0.260	0.442	0.581
	-0.1	0.907	0.877	0.676	0.520	0.392	0.229	0.208	0.393	0.520	0.668
	0.1	0.859	0.793	0.627	0.607	0.502	0.278	0.322	0.312	0.655	0.652
	0.3	0.867	0.856	0.819	0.729	0.628	0.461	0.423	0.700	0.852	0.649
	0.5	0.788	0.853	0.876	0.794	0.677	0.669	0.745	0.840	0.861	0.752
	0.7	0.786	0.908	0.904	0.865	0.890	0.892	0.853	0.886	0.883	0.741
	0.9	0.814	0.826	0.748	0.857	0.836	0.816	0.830	0.831	0.743	0.732

Gate: 50% of Width – SGF A_{ij} Data

Table F.17. Short Glass Fiber end-gated plaque gate orientation data (A13) at 50% Width.

A13		x/L_g									
		-0.9	**-0.7**	**-0.5**	**-0.3**	**-0.1**	**0.1**	**0.3**	**0.5**	**0.7**	**0.9**
z/L_g	**-0.9**	-0.013	-0.011	-0.039	-0.013	-0.009	-0.030	0.102	0.114	0.082	0.097
	-0.7	0.000	-0.016	0.017	0.005	0.020	0.038	0.115	0.144	0.148	0.230
	-0.5	-0.016	-0.005	0.020	0.067	0.081	0.181	0.136	0.165	0.219	0.156
	-0.3	0.006	0.001	0.029	0.087	0.167	0.149	0.130	0.122	0.133	0.026
	-0.1	-0.022	-0.003	0.017	0.056	0.119	0.137	0.082	0.084	0.066	0.003
	0.1	0.010	0.004	-0.010	0.015	0.085	0.052	0.028	0.081	0.028	-0.014
	0.3	-0.004	-0.010	-0.018	-0.005	-0.031	-0.005	0.029	0.014	0.020	-0.005
	0.5	-0.018	-0.014	-0.030	-0.011	-0.105	-0.041	-0.019	0.013	0.000	0.023
	0.7	-0.030	0.001	-0.021	-0.018	-0.017	-0.040	-0.011	-0.012	0.018	0.028
	0.9	-0.053	-0.022	0.010	-0.011	-0.020	-0.011	-0.024	-0.023	0.023	0.004

Table F.18. Short Glass Fiber end-gated plaque gate orientation data (A23) at 50% Width.

A23		x/L_g									
		-0.9	**-0.7**	**-0.5**	**-0.3**	**-0.1**	**0.1**	**0.3**	**0.5**	**0.7**	**0.9**
z/L_g	**-0.9**	0.062	0.047	0.063	0.051	0.027	0.053	0.051	0.033	0.052	0.051
	-0.7	0.089	0.085	0.064	0.073	0.078	0.071	0.063	0.073	0.072	0.080
	-0.5	0.084	0.062	0.088	0.066	0.089	0.101	0.074	0.112	0.158	0.165
	-0.3	0.066	0.035	0.097	0.119	0.156	0.144	0.151	0.157	0.213	0.225
	-0.1	0.040	0.054	0.110	0.153	0.183	0.159	0.164	0.192	0.189	0.144
	0.1	0.074	0.097	0.142	0.149	0.209	0.202	0.191	0.183	0.133	0.158
	0.3	0.063	0.061	0.101	0.131	0.162	0.219	0.173	0.146	0.082	0.152
	0.5	0.082	0.075	0.066	0.077	0.103	0.129	0.109	0.079	0.071	0.126
	0.7	0.088	0.046	0.039	0.060	0.047	0.044	0.061	0.054	0.048	0.106
	0.9	0.057	0.040	0.055	0.038	0.057	0.050	0.046	0.051	0.080	0.107

Gate: 50% of Width – SGF A_{ij} Error

Table F.19. Short Glass Fiber end-gated plaque gate orientation error (A11) at 50% Width.											
A11		**x/L$_g$**									
		-0.9	**-0.7**	**-0.5**	**-0.3**	**-0.1**	**0.1**	**0.3**	**0.5**	**0.7**	**0.9**
z/L$_g$	**-0.9**	0.004	0.032	0.041	0.025	0.017	0.034	0.023	0.036	0.011	0.019
	-0.7	0.002	0.011	0.014	0.024	0.015	0.023	0.026	0.024	0.016	0.010
	-0.5	0.005	0.009	0.011	0.032	0.045	0.046	0.022	0.034	0.033	0.028
	-0.3	0.006	0.008	0.018	0.023	0.022	0.029	0.021	0.034	0.021	0.024
	-0.1	0.002	0.016	0.045	0.051	0.064	0.046	0.015	0.011	0.004	0.024
	0.1	0.005	0.009	0.016	0.026	0.040	0.018	0.015	0.009	0.008	0.014
	0.3	0.005	0.012	0.013	0.028	0.027	0.027	0.011	0.010	0.014	0.015
	0.5	0.005	0.021	0.035	0.024	0.034	0.019	0.012	0.016	0.017	0.027
	0.7	0.004	0.018	0.011	0.030	0.012	0.007	0.015	0.016	0.024	0.019
	0.9	0.012	0.018	0.037	0.028	0.038	0.027	0.033	0.070	0.052	0.020

Table F.20. Short Glass Fiber end-gated plaque gate orientation error (A12) at 50% Width.											
A12		**x/L$_g$**									
		-0.9	**-0.7**	**-0.5**	**-0.3**	**-0.1**	**0.1**	**0.3**	**0.5**	**0.7**	**0.9**
z/L$_g$	**-0.9**	0.004	0.006	0.004	0.010	0.007	0.003	0.004	0.006	0.009	0.014
	-0.7	0.008	0.009	0.007	0.012	0.007	0.006	0.006	0.005	0.011	0.018
	-0.5	0.002	0.008	0.011	0.015	0.027	0.011	0.014	0.016	0.019	0.011
	-0.3	0.004	0.007	0.015	0.020	0.044	0.042	0.017	0.015	0.021	0.007
	-0.1	0.001	0.011	0.015	0.026	0.069	0.036	0.030	0.016	0.008	0.010
	0.1	0.003	0.013	0.024	0.037	0.016	0.030	0.021	0.016	0.004	0.004
	0.3	0.005	0.010	0.019	0.030	0.023	0.012	0.014	0.011	0.015	0.022
	0.5	0.003	0.021	0.002	0.017	0.011	0.017	0.008	0.006	0.009	0.020
	0.7	0.011	0.006	0.009	0.005	0.012	0.006	0.004	0.006	0.014	0.008
	0.9	0.009	0.005	0.006	0.003	0.006	0.003	0.007	0.013	0.014	0.010

Gate: 50% of Width – SGF A_{ij} Error

Table F.21. Short Glass Fiber end-gated plaque gate orientation error (A22) at 50% Width.

A22		x/L_g									
		-0.9	**-0.7**	**-0.5**	**-0.3**	**-0.1**	**0.1**	**0.3**	**0.5**	**0.7**	**0.9**
z/L_g	**-0.9**	0.015	0.004	0.006	0.007	0.003	0.011	0.005	0.019	0.007	0.025
	-0.7	0.029	0.006	0.012	0.009	0.009	0.009	0.015	0.023	0.015	0.022
	-0.5	0.009	0.011	0.018	0.016	0.020	0.006	0.023	0.014	0.012	0.021
	-0.3	0.021	0.019	0.023	0.026	0.015	0.025	0.030	0.022	0.012	0.035
	-0.1	0.010	0.015	0.032	0.027	0.037	0.058	0.035	0.019	0.022	0.072
	0.1	0.005	0.039	0.028	0.018	0.055	0.033	0.025	0.023	0.037	0.052
	0.3	0.021	0.019	0.008	0.019	0.006	0.015	0.018	0.016	0.034	0.059
	0.5	0.020	0.025	0.020	0.010	0.017	0.012	0.016	0.009	0.021	0.032
	0.7	0.016	0.010	0.011	0.006	0.008	0.011	0.008	0.019	0.022	0.044
	0.9	0.013	0.006	0.005	0.006	0.005	0.012	0.010	0.014	0.006	0.022

Table F.22. Short Glass Fiber end-gated plaque gate orientation error (A33) at 50% Width.

A33		x/L_g									
		-0.9	**-0.7**	**-0.5**	**-0.3**	**-0.1**	**0.1**	**0.3**	**0.5**	**0.7**	**0.9**
z/L_g	**-0.9**	0.021	0.037	0.042	0.032	0.019	0.036	0.023	0.049	0.014	0.023
	-0.7	0.028	0.014	0.022	0.029	0.016	0.034	0.015	0.024	0.021	0.029
	-0.5	0.010	0.020	0.026	0.024	0.039	0.048	0.036	0.052	0.037	0.019
	-0.3	0.022	0.027	0.038	0.028	0.021	0.032	0.028	0.041	0.026	0.033
	-0.1	0.009	0.022	0.050	0.043	0.032	0.067	0.046	0.022	0.021	0.053
	0.1	0.004	0.048	0.037	0.038	0.052	0.038	0.035	0.027	0.037	0.066
	0.3	0.030	0.025	0.015	0.023	0.030	0.029	0.015	0.027	0.047	0.066
	0.5	0.026	0.037	0.043	0.029	0.045	0.032	0.029	0.023	0.031	0.045
	0.7	0.014	0.027	0.026	0.033	0.018	0.016	0.023	0.035	0.041	0.044
	0.9	0.024	0.022	0.036	0.033	0.036	0.030	0.036	0.059	0.053	0.027

Gate: 50% of Width – SGF A_{ij} Error

Table F.23. Short Glass Fiber end-gated plaque gate orientation error (A13) at 50% Width.											
A13		**x/L$_g$**									
		-0.9	**-0.7**	**-0.5**	**-0.3**	**-0.1**	**0.1**	**0.3**	**0.5**	**0.7**	**0.9**
z/L$_g$	**-0.9**	0.007	0.013	0.008	0.013	0.030	0.005	0.019	0.009	0.013	0.014
	-0.7	0.005	0.009	0.009	0.015	0.016	0.008	0.017	0.008	0.014	0.014
	-0.5	0.003	0.006	0.009	0.017	0.019	0.012	0.020	0.022	0.020	0.007
	-0.3	0.005	0.006	0.010	0.016	0.014	0.014	0.007	0.007	0.010	0.004
	-0.1	0.001	0.009	0.018	0.010	0.031	0.006	0.004	0.009	0.005	0.006
	0.1	0.003	0.008	0.018	0.019	0.008	0.014	0.009	0.009	0.002	0.005
	0.3	0.003	0.003	0.007	0.018	0.028	0.014	0.014	0.008	0.004	0.010
	0.5	0.003	0.008	0.003	0.021	0.011	0.016	0.008	0.004	0.010	0.009
	0.7	0.005	0.003	0.006	0.006	0.009	0.005	0.004	0.006	0.013	0.006
	0.9	0.006	0.004	0.006	0.005	0.018	0.008	0.011	0.018	0.014	0.005

Table F.24. Short Glass Fiber end-gated plaque gate orientation error (A23) at 50% Width.											
A23		**x/L$_g$**									
		-0.9	**-0.7**	**-0.5**	**-0.3**	**-0.1**	**0.1**	**0.3**	**0.5**	**0.7**	**0.9**
z/L$_g$	**-0.9**	0.013	0.005	0.004	0.005	0.005	0.007	0.005	0.014	0.005	0.015
	-0.7	0.009	0.004	0.006	0.006	0.006	0.009	0.012	0.011	0.006	0.011
	-0.5	0.004	0.005	0.009	0.009	0.008	0.008	0.011	0.011	0.013	0.009
	-0.3	0.006	0.009	0.010	0.009	0.013	0.015	0.013	0.005	0.012	0.009
	-0.1	0.010	0.006	0.015	0.015	0.026	0.013	0.011	0.014	0.012	0.016
	0.1	0.004	0.019	0.011	0.016	0.029	0.008	0.013	0.011	0.014	0.021
	0.3	0.009	0.008	0.005	0.016	0.006	0.004	0.006	0.011	0.018	0.013
	0.5	0.007	0.006	0.011	0.009	0.009	0.009	0.009	0.006	0.018	0.011
	0.7	0.005	0.005	0.005	0.004	0.004	0.007	0.007	0.011	0.015	0.011
	0.9	0.008	0.005	0.004	0.006	0.003	0.007	0.009	0.009	0.005	0.010

Gate: 90% of Width – SGF A_{ij} Data

Table F.25. Short Glass Fiber end-gated plaque gate orientation data (A11) at 90% Width.

A11		x/L_g									
		-0.9	**-0.7**	**-0.5**	**-0.3**	**-0.1**	**0.1**	**0.3**	**0.5**	**0.7**	**0.9**
z/L_g	**-0.9**	0.077	0.125	0.095	0.215	0.161	0.328	0.351	0.519	0.585	0.834
	-0.7	0.031	0.056	0.087	0.140	0.316	0.509	0.740	0.760	0.693	0.743
	-0.5	0.025	0.068	0.107	0.112	0.453	0.662	0.695	0.556	0.367	0.168
	-0.3	0.061	0.053	0.059	0.184	0.345	0.635	0.535	0.253	0.083	0.040
	-0.1	0.047	0.048	0.054	0.062	0.136	0.420	0.404	0.130	0.047	0.044
	0.1	0.037	0.066	0.046	0.047	0.064	0.257	0.202	0.122	0.057	0.062
	0.3	0.025	0.066	0.049	0.033	0.063	0.072	0.150	0.075	0.049	0.062
	0.5	0.055	0.124	0.100	0.058	0.061	0.046	0.099	0.068	0.064	0.063
	0.7	0.069	0.214	0.291	0.163	0.090	0.091	0.087	0.069	0.064	0.062
	0.9	0.076	0.208	0.196	0.209	0.171	0.173	0.098	0.148	0.096	0.075

Table F.26. Short Glass Fiber end-gated plaque gate orientation data (A12) at 90% Width.

A12		x/L_g									
		-0.9	**-0.7**	**-0.5**	**-0.3**	**-0.1**	**0.1**	**0.3**	**0.5**	**0.7**	**0.9**
z/L_g	**-0.9**	0.004	-0.004	-0.006	-0.023	-0.016	0.003	0.008	0.105	0.116	0.150
	-0.7	-0.002	0.006	0.007	0.005	0.031	0.106	0.188	0.286	0.310	0.253
	-0.5	0.013	-0.027	0.051	0.026	0.158	0.281	0.333	0.304	0.307	0.180
	-0.3	0.004	0.001	0.033	0.059	0.188	0.367	0.346	0.206	0.168	0.018
	-0.1	-0.003	-0.007	0.003	0.024	0.090	0.322	0.254	0.110	0.058	-0.019
	0.1	0.014	0.020	-0.017	0.026	0.020	0.230	0.140	0.081	0.019	-0.007
	0.3	0.001	-0.001	-0.029	-0.002	0.000	0.002	0.050	-0.010	0.011	-0.016
	0.5	-0.014	-0.075	-0.049	-0.018	-0.032	-0.009	0.005	-0.028	-0.012	-0.011
	0.7	-0.033	-0.090	-0.043	-0.004	-0.028	-0.015	-0.019	-0.008	-0.004	-0.017
	0.9	-0.060	-0.054	-0.040	-0.031	-0.040	-0.033	-0.038	-0.017	-0.009	-0.020

Gate: 90% of Width – SGF A_{ij} Data

Table F.27. Short Glass Fiber end-gated plaque gate orientation data (A22) at 90% Width.

A22		x/L_g									
		-0.9	**-0.7**	**-0.5**	**-0.3**	**-0.1**	**0.1**	**0.3**	**0.5**	**0.7**	**0.9**
z/L_g	**-0.9**	0.086	0.035	0.022	0.054	0.017	0.047	0.030	0.064	0.038	0.036
	-0.7	0.206	0.068	0.040	0.043	0.037	0.070	0.075	0.118	0.169	0.134
	-0.5	0.168	0.109	0.124	0.077	0.079	0.142	0.170	0.192	0.357	0.349
	-0.3	0.252	0.102	0.105	0.105	0.164	0.239	0.277	0.356	0.579	0.383
	-0.1	0.173	0.078	0.107	0.074	0.115	0.320	0.306	0.465	0.494	0.200
	0.1	0.211	0.141	0.076	0.028	0.120	0.354	0.462	0.455	0.196	0.225
	0.3	0.236	0.152	0.102	0.061	0.059	0.134	0.290	0.106	0.104	0.102
	0.5	0.136	0.139	0.108	0.059	0.064	0.064	0.039	0.076	0.061	0.114
	0.7	0.132	0.127	0.084	0.054	0.059	0.044	0.047	0.062	0.054	0.074
	0.9	0.083	0.062	0.079	0.046	0.064	0.041	0.076	0.028	0.040	0.041

Table F.28. Short Glass Fiber end-gated plaque gate orientation data (A33) at 90% Width.

A33		x/L_g									
		-0.9	**-0.7**	**-0.5**	**-0.3**	**-0.1**	**0.1**	**0.3**	**0.5**	**0.7**	**0.9**
z/L_g	**-0.9**	0.836	0.840	0.884	0.732	0.822	0.625	0.619	0.417	0.377	0.130
	-0.7	0.763	0.876	0.873	0.817	0.647	0.421	0.185	0.122	0.138	0.123
	-0.5	0.806	0.823	0.769	0.812	0.468	0.196	0.135	0.252	0.277	0.482
	-0.3	0.687	0.845	0.836	0.711	0.491	0.126	0.189	0.392	0.338	0.577
	-0.1	0.780	0.874	0.840	0.863	0.748	0.260	0.290	0.405	0.459	0.757
	0.1	0.752	0.792	0.878	0.925	0.816	0.389	0.336	0.423	0.747	0.713
	0.3	0.739	0.782	0.849	0.906	0.878	0.794	0.560	0.819	0.847	0.836
	0.5	0.809	0.736	0.793	0.883	0.875	0.890	0.862	0.856	0.874	0.823
	0.7	0.799	0.660	0.625	0.783	0.850	0.864	0.865	0.870	0.882	0.864
	0.9	0.841	0.730	0.725	0.744	0.765	0.785	0.826	0.824	0.864	0.884

Gate: 90% of Width – SGF A_{ij} Data

Table F.29. Short Glass Fiber end-gated plaque gate orientation data (A13) at 90% Width.

A13		x/L_g									
		-0.9	**-0.7**	**-0.5**	**-0.3**	**-0.1**	**0.1**	**0.3**	**0.5**	**0.7**	**0.9**
z/L_g	**-0.9**	0.003	-0.002	-0.016	-0.059	-0.049	0.010	0.029	0.109	0.130	0.125
	-0.7	-0.010	0.001	0.005	0.003	0.069	0.164	0.147	0.157	0.194	0.157
	-0.5	0.006	-0.020	0.017	0.019	0.226	0.201	0.161	0.282	0.181	0.087
	-0.3	-0.025	-0.001	0.006	0.069	0.189	0.140	0.178	0.133	0.053	0.008
	-0.1	-0.016	-0.013	-0.005	0.011	0.084	0.171	0.184	0.045	0.009	-0.019
	0.1	-0.003	0.016	-0.025	0.039	0.018	0.134	0.070	-0.017	0.014	-0.005
	0.3	-0.008	-0.004	-0.027	-0.007	0.002	-0.014	0.013	-0.017	-0.008	-0.021
	0.5	-0.024	-0.062	-0.069	-0.023	-0.029	-0.015	0.011	-0.038	-0.025	-0.007
	0.7	-0.030	-0.104	-0.042	-0.014	-0.048	-0.032	-0.020	-0.005	0.001	-0.020
	0.9	-0.044	-0.070	-0.069	-0.049	-0.057	-0.050	-0.045	-0.051	-0.035	-0.021

Table F.30. Short Glass Fiber end-gated plaque gate orientation data (A23) at 90% Width.

A23		x/L_g									
		-0.9	**-0.7**	**-0.5**	**-0.3**	**-0.1**	**0.1**	**0.3**	**0.5**	**0.7**	**0.9**
z/L_g	**-0.9**	0.064	0.038	0.027	0.052	0.029	0.054	0.041	0.058	0.047	0.030
	-0.7	0.089	0.050	0.044	0.051	0.052	0.078	0.058	0.068	0.104	0.069
	-0.5	0.096	0.064	0.074	0.064	0.095	0.098	0.082	0.164	0.188	0.150
	-0.3	0.079	0.078	0.045	0.091	0.154	0.094	0.146	0.222	0.176	0.177
	-0.1	0.099	0.058	0.070	0.060	0.106	0.180	0.174	0.201	0.200	0.136
	0.1	0.101	0.088	0.054	0.029	0.098	0.215	0.204	0.180	0.117	0.097
	0.3	0.086	0.104	0.073	0.050	0.056	0.109	0.193	0.090	0.056	0.084
	0.5	0.078	0.098	0.093	0.052	0.055	0.058	0.034	0.065	0.053	0.079
	0.7	0.081	0.105	0.086	0.063	0.061	0.052	0.046	0.050	0.048	0.059
	0.9	0.059	0.066	0.074	0.060	0.071	0.048	0.070	0.033	0.041	0.043

Gate: 90% of Width – SGF A_{ij} Error

Table F.31. Short Glass Fiber end-gated plaque gate orientation error (A11) at 90% Width.											
A11		**x/L$_g$**									
		-0.9	**-0.7**	**-0.5**	**-0.3**	**-0.1**	**0.1**	**0.3**	**0.5**	**0.7**	**0.9**
z/L$_g$	**-0.9**	0.030	0.019	0.015	0.034	0.056	0.021	0.039	0.020	0.036	0.027
	-0.7	0.013	0.037	0.048	0.046	0.033	0.040	0.023	0.026	0.022	0.022
	-0.5	0.013	0.038	0.039	0.056	0.021	0.050	0.036	0.007	0.063	0.027
	-0.3	0.007	0.009	0.050	0.076	0.025	0.029	0.012	0.035	0.033	0.029
	-0.1	0.022	0.005	0.038	0.053	0.037	0.016	0.026	0.029	0.017	0.019
	0.1	0.007	0.017	0.064	0.047	0.041	0.026	0.030	0.023	0.015	0.022
	0.3	0.016	0.050	0.054	0.074	0.054	0.095	0.059	0.019	0.007	0.014
	0.5	0.008	0.033	0.051	0.051	0.035	0.022	0.024	0.023	0.016	0.020
	0.7	0.013	0.020	0.028	0.065	0.039	0.035	0.026	0.036	0.027	0.012
	0.9	0.016	0.021	0.013	0.029	0.022	0.056	0.040	0.003	0.035	0.040

Table F.32. Short Glass Fiber end-gated plaque gate orientation error (A12) at 90% Width.											
A12		**x/L$_g$**									
		-0.9	**-0.7**	**-0.5**	**-0.3**	**-0.1**	**0.1**	**0.3**	**0.5**	**0.7**	**0.9**
z/L$_g$	**-0.9**	0.006	0.006	0.016	0.011	0.007	0.009	0.010	0.015	0.029	0.037
	-0.7	0.004	0.024	0.015	0.016	0.013	0.030	0.028	0.027	0.042	0.020
	-0.5	0.004	0.011	0.023	0.013	0.016	0.020	0.020	0.013	0.018	0.012
	-0.3	0.008	0.017	0.033	0.036	0.045	0.051	0.037	0.019	0.015	0.028
	-0.1	0.009	0.023	0.016	0.067	0.022	0.018	0.009	0.021	0.017	0.011
	0.1	0.013	0.028	0.064	0.049	0.015	0.030	0.022	0.015	0.015	0.011
	0.3	0.012	0.010	0.027	0.066	0.024	0.015	0.017	0.023	0.009	0.022
	0.5	0.013	0.013	0.020	0.034	0.021	0.017	0.004	0.018	0.011	0.017
	0.7	0.015	0.020	0.018	0.027	0.013	0.017	0.011	0.004	0.003	0.008
	0.9	0.010	0.014	0.009	0.023	0.021	0.011	0.007	0.014	0.005	0.018

Gate: 90% of Width – SGF A_{ij} Error

Table F.33. Short Glass Fiber end-gated plaque gate orientation error (A22) at 90% Width.											
A22		**x/L$_g$**									
		-0.9	**-0.7**	**-0.5**	**-0.3**	**-0.1**	**0.1**	**0.3**	**0.5**	**0.7**	**0.9**
z/L$_g$	**-0.9**	0.012	0.020	0.015	0.019	0.009	0.013	0.010	0.015	0.012	0.010
	-0.7	0.027	0.045	0.019	0.007	0.014	0.012	0.005	0.006	0.009	0.008
	-0.5	0.057	0.067	0.020	0.035	0.024	0.025	0.014	0.005	0.015	0.012
	-0.3	0.045	0.060	0.080	0.055	0.016	0.026	0.030	0.020	0.028	0.041
	-0.1	0.068	0.038	0.087	0.053	0.049	0.027	0.035	0.006	0.043	0.037
	0.1	0.052	0.057	0.067	0.022	0.042	0.045	0.052	0.019	0.031	0.043
	0.3	0.062	0.058	0.022	0.048	0.060	0.037	0.043	0.014	0.030	0.077
	0.5	0.026	0.037	0.050	0.043	0.028	0.025	0.016	0.024	0.020	0.046
	0.7	0.018	0.041	0.031	0.044	0.019	0.018	0.012	0.011	0.007	0.024
	0.9	0.016	0.035	0.037	0.040	0.031	0.013	0.009	0.022	0.011	0.043

Table F.34. Short Glass Fiber end-gated plaque gate orientation error (A33) at 90% Width.											
A33		**x/L$_g$**									
		-0.9	**-0.7**	**-0.5**	**-0.3**	**-0.1**	**0.1**	**0.3**	**0.5**	**0.7**	**0.9**
z/L$_g$	**-0.9**	0.032	0.042	0.012	0.026	0.067	0.019	0.048	0.023	0.040	0.033
	-0.7	0.026	0.043	0.033	0.047	0.040	0.035	0.023	0.024	0.023	0.029
	-0.5	0.050	0.071	0.026	0.085	0.047	0.056	0.030	0.005	0.054	0.031
	-0.3	0.044	0.069	0.108	0.112	0.047	0.028	0.016	0.037	0.016	0.055
	-0.1	0.068	0.049	0.147	0.092	0.055	0.018	0.026	0.030	0.032	0.026
	0.1	0.061	0.059	0.140	0.067	0.072	0.073	0.070	0.025	0.034	0.053
	0.3	0.057	0.051	0.066	0.108	0.074	0.079	0.046	0.030	0.026	0.084
	0.5	0.023	0.045	0.058	0.018	0.019	0.013	0.035	0.038	0.034	0.054
	0.7	0.029	0.049	0.064	0.079	0.039	0.028	0.041	0.042	0.032	0.032
	0.9	0.018	0.024	0.046	0.048	0.026	0.060	0.031	0.022	0.044	0.074

Gate: 90% of Width – SGF A_{ij} Error

Table F.35. Short Glass Fiber end-gated plaque gate orientation error (A13) at 90% Width.											
A13		**x/L$_g$**									
		-0.9	**-0.7**	**-0.5**	**-0.3**	**-0.1**	**0.1**	**0.3**	**0.5**	**0.7**	**0.9**
z/L$_g$	**-0.9**	0.014	0.008	0.013	0.018	0.005	0.015	0.023	0.018	0.027	0.039
	-0.7	0.004	0.014	0.025	0.025	0.007	0.028	0.027	0.028	0.020	0.012
	-0.5	0.004	0.004	0.017	0.014	0.022	0.031	0.034	0.029	0.015	0.005
	-0.3	0.006	0.015	0.020	0.013	0.029	0.035	0.042	0.018	0.015	0.017
	-0.1	0.005	0.020	0.010	0.014	0.018	0.015	0.030	0.018	0.011	0.007
	0.1	0.006	0.025	0.030	0.029	0.036	0.025	0.005	0.009	0.008	0.008
	0.3	0.007	0.013	0.017	0.034	0.031	0.037	0.013	0.009	0.012	0.015
	0.5	0.010	0.015	0.013	0.020	0.030	0.040	0.013	0.016	0.008	0.010
	0.7	0.009	0.011	0.023	0.018	0.013	0.008	0.004	0.006	0.005	0.006
	0.9	0.010	0.016	0.006	0.037	0.031	0.038	0.024	0.015	0.005	0.014

Table F.36. Short Glass Fiber end-gated plaque gate orientation error (A23) at 90% Width.											
A23		**x/L$_g$**									
		-0.9	**-0.7**	**-0.5**	**-0.3**	**-0.1**	**0.1**	**0.3**	**0.5**	**0.7**	**0.9**
z/L$_g$	**-0.9**	0.014	0.008	0.013	0.019	0.004	0.013	0.025	0.014	0.025	0.038
	-0.7	0.004	0.014	0.029	0.023	0.008	0.030	0.030	0.035	0.021	0.012
	-0.5	0.004	0.004	0.015	0.016	0.023	0.039	0.027	0.026	0.014	0.007
	-0.3	0.006	0.016	0.016	0.011	0.026	0.036	0.033	0.023	0.014	0.016
	-0.1	0.005	0.026	0.008	0.014	0.018	0.017	0.025	0.020	0.012	0.009
	0.1	0.008	0.027	0.024	0.026	0.028	0.022	0.005	0.009	0.010	0.010
	0.3	0.007	0.015	0.020	0.037	0.027	0.035	0.012	0.009	0.013	0.012
	0.5	0.010	0.014	0.016	0.019	0.035	0.043	0.014	0.017	0.010	0.011
	0.7	0.009	0.012	0.024	0.021	0.013	0.007	0.004	0.005	0.007	0.005
	0.9	0.012	0.019	0.005	0.037	0.030	0.038	0.029	0.015	0.005	0.014

Gate: 00% of Width – LGF R_{ij} Data

Table F.37. Long Glass Fiber end-gated plaque gate orientation data (R11) at 00% Width.											
R11		**x/L$_g$**									
		-0.9	**-0.7**	**-0.5**	**-0.3**	**-0.1**	**0.1**	**0.3**	**0.5**	**0.7**	**0.9**
z/L$_g$	**-0.9**	0.428	0.393	0.291	0.262	0.359	0.332	0.320	0.249	0.201	0.242
	-0.7	0.520	0.440	0.365	0.318	0.339	0.164	0.144	0.064	0.058	0.176
	-0.5	0.434	0.224	0.224	0.233	0.245	0.142	0.068	0.066	0.049	0.095
	-0.3	0.301	0.225	0.183	0.242	0.147	0.112	0.072	0.039	0.058	0.040
	-0.1	0.394	0.249	0.201	0.188	0.101	0.097	0.077	0.049	0.050	0.039
	0.1	0.602	0.390	0.212	0.187	0.123	0.152	0.087	0.071	0.040	0.024
	0.3	0.387	0.311	0.380	0.261	0.224	0.186	0.127	0.071	0.041	0.025
	0.5	0.535	0.497	0.328	0.238	0.301	0.261	0.155	0.094	0.117	0.027
	0.7	0.497	0.479	0.369	0.280	0.270	0.246	0.164	0.122	0.039	0.023
	0.9	0.579	0.528	0.375	0.309	0.326	0.270	0.207	0.190	0.119	0.151

Table F.38. Long Glass Fiber end-gated plaque gate orientation data (R12) at 00% Width.											
R12		**x/L$_g$**									
		-0.9	**-0.7**	**-0.5**	**-0.3**	**-0.1**	**0.1**	**0.3**	**0.5**	**0.7**	**0.9**
z/L$_g$	**-0.9**	0.003	0.004	0.029	0.028	0.017	0.036	0.018	0.007	0.001	0.016
	-0.7	0.073	0.057	0.042	0.030	0.022	0.036	-0.031	0.014	0.045	0.144
	-0.5	-0.075	-0.049	-0.033	-0.055	-0.151	-0.042	-0.003	0.036	0.054	0.097
	-0.3	-0.068	-0.059	-0.141	-0.068	-0.043	-0.050	-0.005	0.004	0.045	0.044
	-0.1	0.169	-0.020	-0.090	-0.035	0.054	0.039	-0.003	0.003	0.025	-0.008
	0.1	0.040	0.142	0.053	0.062	0.124	0.110	0.049	0.046	0.017	0.004
	0.3	0.240	0.152	0.199	0.185	0.165	0.162	0.103	0.058	0.030	0.014
	0.5	0.038	0.083	0.110	0.092	0.133	0.178	0.086	0.101	0.056	0.013
	0.7	0.000	-0.050	-0.043	0.032	0.054	0.041	0.041	0.049	0.022	0.027
	0.9	0.024	0.015	0.027	0.001	0.019	0.007	0.004	0.005	0.019	0.079

Gate: 00% of Width – LGF R_{ij} Data

Table F.39. Long Glass Fiber end-gated plaque gate orientation data (R22) at 00% Width.											
R22		**x/L$_g$**									
		-0.9	**-0.7**	**-0.5**	**-0.3**	**-0.1**	**0.1**	**0.3**	**0.5**	**0.7**	**0.9**
z/L$_g$	**-0.9**	0.033	0.056	0.040	0.070	0.069	0.091	0.052	0.049	0.059	0.088
	-0.7	0.112	0.056	0.102	0.125	0.111	0.108	0.176	0.368	0.417	0.254
	-0.5	0.200	0.217	0.208	0.211	0.315	0.210	0.258	0.348	0.422	0.266
	-0.3	0.329	0.392	0.372	0.434	0.440	0.409	0.388	0.453	0.449	0.319
	-0.1	0.288	0.366	0.371	0.396	0.425	0.482	0.322	0.369	0.482	0.199
	0.1	0.120	0.341	0.272	0.273	0.476	0.406	0.365	0.345	0.418	0.261
	0.3	0.341	0.261	0.317	0.301	0.312	0.304	0.403	0.327	0.401	0.155
	0.5	0.133	0.132	0.155	0.167	0.187	0.237	0.199	0.244	0.203	0.132
	0.7	0.057	0.052	0.057	0.083	0.093	0.089	0.087	0.083	0.072	0.128
	0.9	0.051	0.036	0.042	0.065	0.058	0.062	0.036	0.042	0.057	0.114

Table F.40. Long Glass Fiber end-gated plaque gate orientation data (R33) at 00% Width.											
R33		**x/L$_g$**									
		-0.9	**-0.7**	**-0.5**	**-0.3**	**-0.1**	**0.1**	**0.3**	**0.5**	**0.7**	**0.9**
z/L$_g$	**-0.9**	0.539	0.551	0.670	0.667	0.572	0.577	0.629	0.701	0.740	0.670
	-0.7	0.368	0.504	0.533	0.558	0.549	0.728	0.680	0.569	0.526	0.570
	-0.5	0.366	0.559	0.568	0.556	0.439	0.648	0.674	0.585	0.529	0.638
	-0.3	0.370	0.383	0.444	0.324	0.413	0.478	0.540	0.508	0.493	0.641
	-0.1	0.318	0.386	0.428	0.415	0.473	0.421	0.601	0.582	0.468	0.762
	0.1	0.279	0.269	0.516	0.540	0.402	0.442	0.548	0.583	0.542	0.715
	0.3	0.272	0.429	0.303	0.438	0.465	0.509	0.470	0.602	0.557	0.821
	0.5	0.331	0.371	0.518	0.595	0.512	0.502	0.647	0.662	0.679	0.841
	0.7	0.446	0.470	0.574	0.637	0.637	0.666	0.749	0.796	0.889	0.849
	0.9	0.370	0.435	0.582	0.626	0.616	0.668	0.757	0.768	0.824	0.735

Gate: 00% of Width – LGF R_{ij} Data

Table F.41. Long Glass Fiber end-gated plaque gate orientation data (R13) at 00% Width.											
R13		**x/L_g**									
		-0.9	**-0.7**	**-0.5**	**-0.3**	**-0.1**	**0.1**	**0.3**	**0.5**	**0.7**	**0.9**
z/L_g	**-0.9**	-0.021	0.036	0.069	0.040	0.002	0.055	0.043	0.033	0.020	0.008
	-0.7	0.094	0.072	0.032	0.047	0.044	0.036	-0.034	0.017	0.024	0.053
	-0.5	-0.010	0.000	-0.003	-0.001	-0.062	-0.006	0.012	0.032	0.025	0.069
	-0.3	0.003	0.004	-0.051	-0.029	-0.008	0.000	-0.004	0.005	0.023	0.032
	-0.1	0.120	0.003	-0.055	0.004	0.051	0.027	-0.001	0.004	0.018	-0.010
	0.1	0.051	0.085	0.038	0.060	0.044	0.070	0.035	0.041	0.011	0.010
	0.3	0.129	0.099	0.102	0.096	0.145	0.113	0.048	0.032	0.013	0.007
	0.5	0.027	0.042	0.083	0.104	0.106	0.131	0.059	0.069	0.055	0.014
	0.7	-0.009	-0.067	-0.067	0.050	0.044	0.063	0.050	0.049	0.023	0.020
	0.9	0.065	0.041	0.038	0.006	0.028	0.007	0.022	0.023	0.023	0.060

Table F.42. Long Glass Fiber end-gated plaque gate orientation data (R23) at 00% Width.											
R23		**x/L_g**									
		-0.9	**-0.7**	**-0.5**	**-0.3**	**-0.1**	**0.1**	**0.3**	**0.5**	**0.7**	**0.9**
z/L_g	**-0.9**	0.041	0.057	0.050	0.059	0.059	0.074	0.052	0.044	0.046	0.080
	-0.7	0.100	0.073	0.105	0.100	0.086	0.084	0.124	0.143	0.146	0.123
	-0.5	0.163	0.157	0.165	0.139	0.146	0.125	0.128	0.200	0.182	0.183
	-0.3	0.204	0.236	0.164	0.199	0.221	0.190	0.188	0.167	0.162	0.151
	-0.1	0.152	0.239	0.200	0.190	0.231	0.231	0.181	0.197	0.179	0.133
	0.1	0.113	0.189	0.173	0.167	0.172	0.193	0.187	0.207	0.169	0.110
	0.3	0.214	0.193	0.168	0.143	0.220	0.170	0.182	0.141	0.137	0.084
	0.5	0.132	0.131	0.128	0.136	0.137	0.153	0.122	0.134	0.138	0.052
	0.7	0.062	0.064	0.065	0.074	0.077	0.086	0.078	0.072	0.061	0.058
	0.9	0.061	0.048	0.039	0.059	0.048	0.055	0.043	0.047	0.052	0.084

Gate: 00% of Width – LGF R_{ij} Error

Table F.43. Long Glass Fiber end-gated plaque gate orientation error (R11) at 00% Width.

R11		x/L_g									
		-0.9	-0.7	-0.5	-0.3	-0.1	0.1	0.3	0.5	0.7	0.9
z/L_g	-0.9	0.008	0.056	0.015	0.060	0.022	0.017	0.028	0.037	0.050	0.001
	-0.7	0.034	0.061	0.083	0.069	0.117	0.089	0.007	0.036	0.028	0.034
	-0.5	0.006	0.028	0.022	0.032	0.088	0.068	0.026	0.049	0.031	0.001
	-0.3	0.053	0.041	0.080	0.112	0.063	0.066	0.041	0.020	0.041	0.021
	-0.1	0.120	0.047	0.061	0.093	0.003	0.047	0.017	0.024	0.038	0.025
	0.1	0.072	0.137	0.118	0.041	0.043	0.016	0.037	0.037	0.019	0.011
	0.3	0.049	0.077	0.025	0.115	0.060	0.047	0.053	0.040	0.018	0.017
	0.5	0.029	0.011	0.006	0.119	0.059	0.011	0.057	0.022	0.009	0.020
	0.7	0.001	0.066	0.160	0.110	0.039	0.075	0.040	0.077	0.009	0.006
	0.9	0.096	0.059	0.014	0.075	0.074	0.111	0.016	0.021	0.001	0.041

Table F.44. Long Glass Fiber end-gated plaque gate orientation error (R12) at 00% Width.

R12		x/L_g									
		-0.9	-0.7	-0.5	-0.3	-0.1	0.1	0.3	0.5	0.7	0.9
z/L_g	-0.9	0.009	0.003	0.008	0.015	0.007	0.017	0.010	0.009	0.007	0.017
	-0.7	0.037	0.017	0.026	0.034	0.043	0.056	0.052	0.011	0.018	0.000
	-0.5	0.012	0.034	0.063	0.051	0.029	0.017	0.009	0.009	0.001	0.026
	-0.3	0.103	0.034	0.036	0.056	0.047	0.000	0.008	0.030	0.022	0.010
	-0.1	0.028	0.059	0.095	0.110	0.033	0.007	0.012	0.019	0.004	0.008
	0.1	0.013	0.005	0.036	0.041	0.005	0.046	0.000	0.000	0.010	0.014
	0.3	0.018	0.016	0.064	0.042	0.010	0.008	0.000	0.022	0.015	0.004
	0.5	0.041	0.046	0.022	0.023	0.006	0.044	0.043	0.018	0.001	0.006
	0.7	0.008	0.021	0.014	0.010	0.004	0.011	0.002	0.009	0.000	0.019
	0.9	0.018	0.012	0.003	0.006	0.016	0.016	0.006	0.022	0.010	0.046

Gate: 00% of Width – LGF R_{ij} Error

Table F.45. Long Glass Fiber end-gated plaque gate orientation error (R22) at 00% Width.

R22		x/L_g									
		-0.9	-0.7	-0.5	-0.3	-0.1	0.1	0.3	0.5	0.7	0.9
z/L_g	-0.9	0.008	0.013	0.022	0.060	0.057	0.063	0.032	0.028	0.029	0.026
	-0.7	0.035	0.010	0.045	0.059	0.085	0.061	0.005	0.098	0.000	0.037
	-0.5	0.020	0.002	0.014	0.023	0.007	0.103	0.079	0.107	0.120	0.024
	-0.3	0.093	0.132	0.040	0.120	0.037	0.012	0.058	0.090	0.128	0.094
	-0.1	0.040	0.032	0.104	0.062	0.046	0.004	0.109	0.053	0.111	0.002
	0.1	0.025	0.095	0.026	0.005	0.031	0.024	0.080	0.035	0.033	0.011
	0.3	0.028	0.017	0.081	0.017	0.007	0.000	0.043	0.023	0.025	0.005
	0.5	0.004	0.049	0.010	0.044	0.032	0.019	0.088	0.052	0.002	0.044
	0.7	0.008	0.009	0.002	0.048	0.056	0.051	0.048	0.023	0.015	0.093
	0.9	0.012	0.020	0.022	0.030	0.035	0.015	0.009	0.023	0.001	0.046

Table F.46. Long Glass Fiber end-gated plaque gate orientation error (R33) at 00% Width.

R33		x/L_g									
		-0.9	-0.7	-0.5	-0.3	-0.1	0.1	0.3	0.5	0.7	0.9
z/L_g	-0.9	0.001	0.068	0.007	0.120	0.078	0.047	0.003	0.009	0.021	0.025
	-0.7	0.070	0.072	0.128	0.128	0.203	0.149	0.012	0.062	0.028	0.003
	-0.5	0.014	0.026	0.008	0.055	0.081	0.171	0.104	0.058	0.090	0.023
	-0.3	0.040	0.091	0.040	0.008	0.026	0.078	0.099	0.071	0.087	0.114
	-0.1	0.080	0.015	0.043	0.031	0.043	0.043	0.093	0.029	0.072	0.027
	0.1	0.097	0.043	0.092	0.046	0.074	0.040	0.043	0.002	0.052	0.022
	0.3	0.021	0.060	0.056	0.098	0.067	0.047	0.010	0.063	0.043	0.012
	0.5	0.033	0.060	0.003	0.163	0.091	0.008	0.145	0.030	0.011	0.024
	0.7	0.007	0.075	0.158	0.158	0.095	0.126	0.088	0.100	0.024	0.099
	0.9	0.084	0.039	0.008	0.104	0.109	0.127	0.024	0.044	0.002	0.087

Gate: 00% of Width – LGF R_{ij} Error

Table F.47. Long Glass Fiber end-gated plaque gate orientation error (R13) at 00% Width.

R13		x/L_g									
		-0.9	-0.7	-0.5	-0.3	-0.1	0.1	0.3	0.5	0.7	0.9
z/L_g	-0.9	0.010	0.009	0.014	0.004	0.011	0.003	0.003	0.004	0.003	0.017
	-0.7	0.043	0.021	0.008	0.010	0.030	0.038	0.038	0.004	0.018	0.018
	-0.5	0.007	0.019	0.050	0.032	0.020	0.002	0.016	0.014	0.004	0.029
	-0.3	0.094	0.005	0.030	0.003	0.027	0.001	0.002	0.014	0.017	0.006
	-0.1	0.010	0.047	0.030	0.064	0.022	0.016	0.010	0.007	0.009	0.000
	0.1	0.038	0.028	0.027	0.039	0.016	0.037	0.009	0.011	0.014	0.004
	0.3	0.030	0.044	0.036	0.054	0.014	0.012	0.017	0.024	0.006	0.005
	0.5	0.007	0.014	0.003	0.033	0.043	0.023	0.020	0.005	0.000	0.002
	0.7	0.013	0.032	0.010	0.006	0.013	0.017	0.004	0.011	0.001	0.016
	0.9	0.031	0.044	0.038	0.000	0.006	0.007	0.005	0.031	0.004	0.043

Table F.48. Long Glass Fiber end-gated plaque gate orientation error (R23) at 00% Width.

R23		x/L_g									
		-0.9	-0.7	-0.5	-0.3	-0.1	0.1	0.3	0.5	0.7	0.9
z/L_g	-0.9	0.005	0.007	0.015	0.039	0.035	0.040	0.021	0.019	0.016	0.016
	-0.7	0.024	0.006	0.029	0.032	0.054	0.039	0.019	0.033	0.023	0.010
	-0.5	0.022	0.017	0.009	0.022	0.025	0.048	0.033	0.026	0.001	0.017
	-0.3	0.041	0.016	0.016	0.016	0.016	0.020	0.052	0.009	0.006	0.029
	-0.1	0.008	0.003	0.020	0.031	0.008	0.025	0.022	0.021	0.001	0.016
	0.1	0.003	0.032	0.014	0.004	0.023	0.008	0.008	0.015	0.010	0.007
	0.3	0.008	0.007	0.008	0.039	0.025	0.024	0.006	0.012	0.049	0.004
	0.5	0.008	0.021	0.034	0.032	0.016	0.006	0.020	0.003	0.001	0.000
	0.7	0.007	0.005	0.002	0.031	0.035	0.038	0.041	0.023	0.012	0.027
	0.9	0.010	0.018	0.011	0.021	0.027	0.016	0.006	0.020	0.005	0.032

Gate: 50% of Width – LGF R_{ij} Data

Table F.49. Long Glass Fiber end-gated plaque gate orientation data (R11) at 50% Width.

R11		x/L_g									
		-0.9	**-0.7**	**-0.5**	**-0.3**	**-0.1**	**0.1**	**0.3**	**0.5**	**0.7**	**0.9**
z/L_g	**-0.9**	0.105	0.235	0.181	0.271	0.277	0.304	0.316	0.323	0.446	0.466
	-0.7	0.035	0.072	0.127	0.175	0.210	0.382	0.408	0.572	0.513	0.516
	-0.5	0.026	0.061	0.141	0.332	0.447	0.625	0.573	0.475	0.311	0.345
	-0.3	0.032	0.048	0.189	0.380	0.471	0.532	0.412	0.262	0.159	0.107
	-0.1	0.015	0.066	0.177	0.386	0.415	0.265	0.261	0.153	0.058	0.049
	0.1	0.020	0.048	0.120	0.239	0.247	0.296	0.208	0.104	0.033	0.036
	0.3	0.035	0.060	0.119	0.285	0.362	0.282	0.161	0.057	0.045	0.043
	0.5	0.023	0.062	0.178	0.234	0.247	0.233	0.102	0.048	0.054	0.059
	0.7	0.037	0.081	0.127	0.199	0.122	0.147	0.084	0.112	0.088	0.053
	0.9	0.075	0.118	0.202	0.220	0.196	0.185	0.221	0.257	0.215	0.118

Table F.50. Long Glass Fiber end-gated plaque gate orientation data (R12) at 50% Width.

R12		x/L_g									
		-0.9	**-0.7**	**-0.5**	**-0.3**	**-0.1**	**0.1**	**0.3**	**0.5**	**0.7**	**0.9**
z/L_g	**-0.9**	0.026	0.035	0.009	0.005	0.003	0.015	0.013	0.017	0.050	0.068
	-0.7	0.019	0.029	0.032	0.033	0.029	0.065	0.118	0.204	0.258	0.244
	-0.5	0.011	0.019	0.074	0.113	0.150	0.229	0.287	0.298	0.229	0.227
	-0.3	0.004	0.041	0.093	0.198	0.214	0.301	0.293	0.237	0.171	0.121
	-0.1	0.007	0.015	0.104	0.126	0.067	0.184	0.230	0.162	0.066	0.002
	0.1	0.009	0.007	0.018	0.077	0.150	0.183	0.162	0.098	0.026	-0.006
	0.3	-0.010	-0.052	-0.060	-0.044	0.071	0.135	0.131	0.048	0.031	-0.015
	0.5	0.000	-0.055	-0.036	-0.001	0.053	0.088	0.050	0.011	0.031	-0.004
	0.7	-0.032	-0.048	-0.015	0.032	0.020	0.043	0.014	0.031	0.050	0.018
	0.9	-0.021	-0.014	0.011	0.012	0.014	0.015	0.027	0.021	0.053	0.055

Gate: 50% of Width – LGF R_{ij} Data

Table F.51. Long Glass Fiber end-gated plaque gate orientation data (R22) at 50% Width.											
R22		**x/L_g**									
		-0.9	**-0.7**	**-0.5**	**-0.3**	**-0.1**	**0.1**	**0.3**	**0.5**	**0.7**	**0.9**
z/L_g	**-0.9**	0.062	0.037	0.029	0.027	0.028	0.033	0.034	0.054	0.041	0.063
	-0.7	0.100	0.070	0.061	0.036	0.048	0.055	0.090	0.131	0.179	0.157
	-0.5	0.094	0.080	0.153	0.128	0.152	0.152	0.234	0.275	0.215	0.228
	-0.3	0.110	0.142	0.204	0.278	0.317	0.314	0.374	0.299	0.266	0.394
	-0.1	0.093	0.184	0.343	0.349	0.372	0.397	0.324	0.298	0.207	0.404
	0.1	0.098	0.258	0.347	0.351	0.341	0.238	0.250	0.216	0.177	0.368
	0.3	0.144	0.191	0.232	0.162	0.116	0.160	0.190	0.108	0.160	0.347
	0.5	0.173	0.114	0.126	0.110	0.081	0.092	0.077	0.065	0.098	0.307
	0.7	0.151	0.074	0.063	0.030	0.040	0.043	0.038	0.056	0.138	0.267
	0.9	0.094	0.038	0.035	0.025	0.026	0.032	0.032	0.043	0.065	0.161

Table F.52. Long Glass Fiber end-gated plaque gate orientation data (R33) at 50% Width.											
R33		**x/L_g**									
		-0.9	**-0.7**	**-0.5**	**-0.3**	**-0.1**	**0.1**	**0.3**	**0.5**	**0.7**	**0.9**
z/L_g	**-0.9**	0.833	0.728	0.790	0.702	0.695	0.663	0.650	0.623	0.513	0.471
	-0.7	0.865	0.858	0.813	0.789	0.742	0.564	0.502	0.297	0.309	0.327
	-0.5	0.880	0.858	0.706	0.540	0.400	0.223	0.193	0.250	0.474	0.427
	-0.3	0.858	0.810	0.607	0.342	0.212	0.154	0.213	0.439	0.575	0.499
	-0.1	0.892	0.750	0.480	0.265	0.214	0.339	0.415	0.548	0.734	0.547
	0.1	0.882	0.695	0.532	0.410	0.412	0.466	0.541	0.680	0.791	0.596
	0.3	0.821	0.750	0.650	0.553	0.523	0.557	0.649	0.835	0.795	0.610
	0.5	0.804	0.824	0.696	0.655	0.673	0.675	0.821	0.887	0.848	0.634
	0.7	0.813	0.846	0.811	0.771	0.839	0.810	0.878	0.832	0.774	0.680
	0.9	0.831	0.844	0.762	0.756	0.778	0.782	0.746	0.700	0.721	0.722

Gate: 50% of Width – LGF R_{ij} Data

Table F.53. Long Glass Fiber end-gated plaque gate orientation data (R13) at 50% Width.											
R13		**x/L$_g$**									
		-0.9	**-0.7**	**-0.5**	**-0.3**	**-0.1**	**0.1**	**0.3**	**0.5**	**0.7**	**0.9**
z/L$_g$	**-0.9**	0.027	0.033	0.005	0.022	0.011	0.049	0.029	0.052	0.122	0.109
	-0.7	0.012	0.019	0.035	0.063	0.058	0.092	0.138	0.172	0.209	0.186
	-0.5	0.010	0.014	0.065	0.115	0.114	0.122	0.143	0.168	0.143	0.153
	-0.3	-0.007	0.023	0.085	0.111	0.091	0.084	0.125	0.130	0.097	0.069
	-0.1	0.008	0.017	0.070	0.072	0.054	0.070	0.111	0.084	0.043	0.005
	0.1	0.008	0.009	0.031	0.040	0.080	0.106	0.099	0.060	0.022	-0.002
	0.3	-0.005	-0.022	-0.036	-0.017	0.071	0.109	0.087	0.034	0.018	0.004
	0.5	0.002	-0.028	-0.028	0.016	0.061	0.104	0.054	0.007	0.023	0.005
	0.7	-0.016	-0.023	-0.015	0.044	0.027	0.059	0.028	0.033	0.036	0.010
	0.9	-0.029	-0.026	0.025	0.040	0.016	0.036	0.054	0.043	0.068	0.046

Table F.54. Long Glass Fiber end-gated plaque gate orientation data (R23) at 50% Width.											
R23		**x/L$_g$**									
		-0.9	**-0.7**	**-0.5**	**-0.3**	**-0.1**	**0.1**	**0.3**	**0.5**	**0.7**	**0.9**
z/L$_g$	**-0.9**	0.056	0.036	0.033	0.032	0.036	0.039	0.040	0.047	0.052	0.064
	-0.7	0.055	0.050	0.048	0.040	0.052	0.058	0.088	0.102	0.125	0.108
	-0.5	0.057	0.051	0.090	0.111	0.105	0.091	0.119	0.153	0.132	0.132
	-0.3	0.051	0.080	0.137	0.152	0.139	0.124	0.165	0.156	0.154	0.182
	-0.1	0.060	0.100	0.193	0.165	0.175	0.158	0.151	0.163	0.131	0.175
	0.1	0.056	0.120	0.209	0.210	0.207	0.145	0.149	0.128	0.102	0.175
	0.3	0.078	0.093	0.151	0.119	0.104	0.107	0.119	0.069	0.084	0.148
	0.5	0.088	0.066	0.089	0.094	0.076	0.088	0.069	0.048	0.070	0.147
	0.7	0.085	0.040	0.045	0.036	0.036	0.043	0.039	0.047	0.094	0.124
	0.9	0.063	0.035	0.035	0.031	0.029	0.032	0.038	0.043	0.062	0.105

Gate: 50% of Width – LGF R_{ij} Error

Table F.55. Long Glass Fiber end-gated plaque gate orientation error (R11) at 50% Width.

R11		x/L_g									
		-0.9	-0.7	-0.5	-0.3	-0.1	0.1	0.3	0.5	0.7	0.9
z/L_g	-0.9	0.005	0.044	0.050	0.029	0.024	0.039	0.028	0.043	0.014	0.021
	-0.7	0.003	0.016	0.016	0.033	0.021	0.029	0.032	0.033	0.019	0.012
	-0.5	0.007	0.012	0.015	0.040	0.061	0.052	0.031	0.047	0.040	0.037
	-0.3	0.008	0.011	0.022	0.027	0.025	0.033	0.030	0.040	0.023	0.028
	-0.1	0.003	0.022	0.051	0.068	0.073	0.055	0.023	0.012	0.006	0.033
	0.1	0.007	0.011	0.023	0.033	0.051	0.022	0.020	0.012	0.010	0.019
	0.3	0.007	0.014	0.015	0.041	0.036	0.034	0.015	0.014	0.017	0.021
	0.5	0.007	0.023	0.046	0.031	0.041	0.027	0.017	0.021	0.020	0.036
	0.7	0.006	0.021	0.016	0.044	0.017	0.009	0.021	0.024	0.030	0.022
	0.9	0.017	0.025	0.047	0.040	0.047	0.036	0.039	0.078	0.064	0.022

Table F.56. Long Glass Fiber end-gated plaque gate orientation error (R12) at 50% Width.

R12		x/L_g									
		-0.9	-0.7	-0.5	-0.3	-0.1	0.1	0.3	0.5	0.7	0.9
z/L_g	-0.9	0.006	0.008	0.005	0.012	0.010	0.003	0.005	0.009	0.012	0.016
	-0.7	0.010	0.012	0.009	0.014	0.011	0.008	0.008	0.007	0.013	0.022
	-0.5	0.002	0.010	0.015	0.021	0.034	0.014	0.018	0.021	0.023	0.014
	-0.3	0.005	0.009	0.019	0.028	0.062	0.049	0.020	0.021	0.026	0.009
	-0.1	0.002	0.015	0.022	0.031	0.077	0.048	0.035	0.020	0.011	0.013
	0.1	0.005	0.017	0.029	0.052	0.023	0.036	0.026	0.022	0.005	0.006
	0.3	0.006	0.011	0.022	0.043	0.026	0.014	0.019	0.013	0.017	0.025
	0.5	0.005	0.027	0.003	0.022	0.017	0.022	0.010	0.007	0.012	0.026
	0.7	0.013	0.010	0.010	0.006	0.013	0.008	0.005	0.009	0.017	0.009
	0.9	0.010	0.006	0.009	0.005	0.008	0.004	0.008	0.017	0.017	0.013

Gate: 50% of Width – LGF R_{ij} Error

Table F.57. Long Glass Fiber end-gated plaque gate orientation error (R22) at 50% Width.

R22		x/L_g									
		-0.9	**-0.7**	**-0.5**	**-0.3**	**-0.1**	**0.1**	**0.3**	**0.5**	**0.7**	**0.9**
z/L_g	**-0.9**	0.020	0.006	0.007	0.009	0.005	0.013	0.006	0.024	0.008	0.031
	-0.7	0.036	0.008	0.017	0.011	0.012	0.013	0.018	0.030	0.018	0.026
	-0.5	0.010	0.014	0.024	0.020	0.023	0.009	0.031	0.020	0.018	0.032
	-0.3	0.026	0.025	0.032	0.039	0.017	0.032	0.038	0.026	0.016	0.047
	-0.1	0.013	0.020	0.046	0.033	0.053	0.084	0.052	0.022	0.025	0.082
	0.1	0.006	0.050	0.033	0.025	0.070	0.043	0.035	0.030	0.045	0.078
	0.3	0.029	0.024	0.008	0.025	0.007	0.017	0.020	0.023	0.038	0.077
	0.5	0.027	0.028	0.023	0.012	0.019	0.017	0.018	0.012	0.027	0.041
	0.7	0.018	0.015	0.016	0.007	0.010	0.014	0.011	0.023	0.027	0.060
	0.9	0.017	0.008	0.007	0.007	0.006	0.016	0.013	0.019	0.009	0.026

Table F.58. Long Glass Fiber end-gated plaque gate orientation error (R33) at 50% Width.

R33		x/L_g									
		-0.9	**-0.7**	**-0.5**	**-0.3**	**-0.1**	**0.1**	**0.3**	**0.5**	**0.7**	**0.9**
z/L_g	**-0.9**	0.024	0.043	0.048	0.036	0.025	0.040	0.030	0.063	0.019	0.029
	-0.7	0.037	0.018	0.027	0.039	0.018	0.038	0.021	0.029	0.028	0.035
	-0.5	0.014	0.024	0.037	0.031	0.058	0.057	0.042	0.061	0.053	0.022
	-0.3	0.031	0.033	0.050	0.039	0.028	0.039	0.039	0.051	0.034	0.039
	-0.1	0.011	0.028	0.063	0.051	0.039	0.096	0.052	0.030	0.024	0.077
	0.1	0.006	0.058	0.042	0.050	0.060	0.055	0.047	0.038	0.052	0.085
	0.3	0.036	0.036	0.021	0.032	0.041	0.038	0.021	0.034	0.055	0.081
	0.5	0.029	0.050	0.052	0.039	0.052	0.039	0.033	0.032	0.044	0.061
	0.7	0.021	0.036	0.030	0.044	0.026	0.019	0.026	0.043	0.053	0.051
	0.9	0.031	0.028	0.051	0.037	0.046	0.041	0.044	0.088	0.066	0.036

Gate: 50% of Width – LGF R_{ij} Error

Table F.59. Long Glass Fiber end-gated plaque gate orientation error (R13) at 50% Width.											
R13		**x/L$_g$**									
		-0.9	**-0.7**	**-0.5**	**-0.3**	**-0.1**	**0.1**	**0.3**	**0.5**	**0.7**	**0.9**
z/L$_g$	**-0.9**	0.010	0.018	0.011	0.017	0.035	0.006	0.021	0.011	0.017	0.017
	-0.7	0.007	0.010	0.012	0.017	0.019	0.009	0.024	0.010	0.017	0.020
	-0.5	0.003	0.008	0.012	0.021	0.026	0.016	0.026	0.031	0.023	0.010
	-0.3	0.006	0.007	0.013	0.020	0.017	0.018	0.010	0.008	0.014	0.004
	-0.1	0.001	0.011	0.023	0.014	0.035	0.007	0.005	0.012	0.007	0.009
	0.1	0.005	0.011	0.022	0.026	0.011	0.015	0.013	0.011	0.003	0.006
	0.3	0.003	0.004	0.011	0.024	0.041	0.017	0.016	0.010	0.006	0.014
	0.5	0.004	0.010	0.004	0.027	0.014	0.020	0.011	0.005	0.012	0.012
	0.7	0.006	0.004	0.007	0.008	0.011	0.008	0.006	0.008	0.017	0.007
	0.9	0.008	0.006	0.007	0.007	0.021	0.009	0.014	0.026	0.016	0.007

Table F.60. Long Glass Fiber end-gated plaque gate orientation error (R23) at 50% Width.											
R23		**x/L$_g$**									
		-0.9	**-0.7**	**-0.5**	**-0.3**	**-0.1**	**0.1**	**0.3**	**0.5**	**0.7**	**0.9**
z/L$_g$	**-0.9**	0.017	0.006	0.005	0.008	0.006	0.010	0.005	0.016	0.008	0.017
	-0.7	0.010	0.004	0.008	0.008	0.009	0.010	0.017	0.015	0.007	0.014
	-0.5	0.006	0.006	0.011	0.013	0.010	0.009	0.012	0.013	0.016	0.012
	-0.3	0.007	0.012	0.011	0.010	0.019	0.020	0.018	0.007	0.013	0.011
	-0.1	0.012	0.009	0.018	0.020	0.030	0.016	0.015	0.016	0.014	0.018
	0.1	0.005	0.022	0.014	0.019	0.033	0.011	0.015	0.013	0.020	0.025
	0.3	0.012	0.011	0.006	0.019	0.008	0.006	0.006	0.013	0.020	0.020
	0.5	0.010	0.008	0.015	0.011	0.013	0.012	0.012	0.009	0.022	0.014
	0.7	0.007	0.005	0.007	0.006	0.006	0.008	0.008	0.016	0.022	0.013
	0.9	0.010	0.006	0.006	0.007	0.005	0.009	0.012	0.014	0.007	0.013

Gate: 90% of Width – LGF R_{ij} Data

Table F.61. Long Glass Fiber end-gated plaque gate orientation data (R11) at 90% Width.											
R11		**x/L$_g$**									
		-0.9	**-0.7**	**-0.5**	**-0.3**	**-0.1**	**0.1**	**0.3**	**0.5**	**0.7**	**0.9**
z/L$_g$	**-0.9**	0.119	0.221	0.313	0.378	0.398	0.440	0.458	0.610	0.618	0.687
	-0.7	0.079	0.217	0.373	0.411	0.508	0.585	0.650	0.687	0.641	0.675
	-0.5	0.058	0.182	0.356	0.474	0.560	0.581	0.596	0.575	0.441	0.436
	-0.3	0.046	0.160	0.259	0.431	0.453	0.564	0.408	0.297	0.197	0.093
	-0.1	0.092	0.164	0.200	0.400	0.382	0.392	0.286	0.205	0.090	0.050
	0.1	0.045	0.182	0.291	0.374	0.380	0.272	0.268	0.172	0.066	0.039
	0.3	0.084	0.221	0.341	0.382	0.350	0.446	0.280	0.165	0.067	0.047
	0.5	0.066	0.195	0.341	0.405	0.508	0.381	0.209	0.126	0.076	0.051
	0.7	0.066	0.197	0.235	0.338	0.263	0.270	0.265	0.193	0.156	0.070
	0.9	0.076	0.251	0.220	0.271	0.299	0.354	0.382	0.341	0.265	0.143

Table F.62. Long Glass Fiber end-gated plaque gate orientation data (R12) at 90% Width.											
R12		**x/L$_g$**									
		-0.9	**-0.7**	**-0.5**	**-0.3**	**-0.1**	**0.1**	**0.3**	**0.5**	**0.7**	**0.9**
z/L$_g$	**-0.9**	0.030	0.029	0.022	0.028	0.016	0.022	0.053	0.092	0.096	0.075
	-0.7	0.027	0.110	0.113	0.108	0.122	0.097	0.151	0.167	0.196	0.225
	-0.5	0.033	0.104	0.144	0.153	0.161	0.177	0.257	0.327	0.296	0.311
	-0.3	0.020	0.083	0.170	0.098	0.119	0.283	0.265	0.281	0.247	0.124
	-0.1	0.031	0.067	0.090	0.079	0.120	0.226	0.251	0.201	0.152	0.047
	0.1	0.003	-0.036	-0.044	0.016	0.149	0.134	0.184	0.192	0.097	0.011
	0.3	0.018	-0.036	-0.083	-0.024	0.061	0.103	0.184	0.154	0.072	0.039
	0.5	-0.033	-0.041	-0.060	0.039	0.083	0.126	0.089	0.091	0.062	0.032
	0.7	-0.028	-0.031	-0.011	0.041	0.036	0.055	0.072	0.071	0.054	0.052
	0.9	-0.024	-0.005	0.024	0.039	0.026	0.027	0.027	0.042	0.050	0.069

Gate: 90% of Width – LGF R_{ij} Data

Table F.63. Long Glass Fiber end-gated plaque gate orientation data (R22) at 90% Width.											
R22		**x/L$_g$**									
		-0.9	**-0.7**	**-0.5**	**-0.3**	**-0.1**	**0.1**	**0.3**	**0.5**	**0.7**	**0.9**
z/L$_g$	**-0.9**	0.057	0.054	0.071	0.051	0.039	0.037	0.055	0.053	0.044	0.045
	-0.7	0.123	0.177	0.129	0.096	0.101	0.093	0.094	0.091	0.134	0.117
	-0.5	0.222	0.353	0.199	0.183	0.171	0.184	0.219	0.275	0.289	0.297
	-0.3	0.248	0.402	0.359	0.220	0.301	0.316	0.380	0.378	0.448	0.367
	-0.1	0.322	0.438	0.451	0.301	0.335	0.349	0.397	0.317	0.556	0.424
	0.1	0.318	0.474	0.353	0.322	0.240	0.274	0.273	0.390	0.476	0.287
	0.3	0.259	0.371	0.266	0.219	0.220	0.181	0.267	0.310	0.323	0.321
	0.5	0.221	0.262	0.210	0.173	0.135	0.161	0.143	0.156	0.163	0.224
	0.7	0.139	0.114	0.093	0.083	0.064	0.069	0.083	0.092	0.090	0.174
	0.9	0.062	0.068	0.060	0.073	0.070	0.036	0.037	0.054	0.064	0.122

Table F.64. Long Glass Fiber end-gated plaque gate orientation data (R33) at 90% Width.											
R33		**x/L$_g$**									
		-0.9	**-0.7**	**-0.5**	**-0.3**	**-0.1**	**0.1**	**0.3**	**0.5**	**0.7**	**0.9**
z/L$_g$	**-0.9**	0.824	0.725	0.616	0.571	0.564	0.522	0.487	0.337	0.338	0.268
	-0.7	0.798	0.606	0.498	0.493	0.392	0.322	0.256	0.222	0.225	0.208
	-0.5	0.720	0.465	0.445	0.343	0.269	0.235	0.184	0.150	0.269	0.267
	-0.3	0.706	0.438	0.382	0.350	0.246	0.120	0.212	0.324	0.356	0.540
	-0.1	0.586	0.398	0.350	0.299	0.283	0.259	0.317	0.479	0.353	0.526
	0.1	0.638	0.345	0.355	0.304	0.380	0.455	0.459	0.437	0.458	0.674
	0.3	0.656	0.409	0.393	0.398	0.430	0.373	0.452	0.525	0.610	0.632
	0.5	0.714	0.543	0.449	0.422	0.357	0.458	0.648	0.718	0.761	0.726
	0.7	0.795	0.689	0.672	0.579	0.673	0.660	0.652	0.716	0.753	0.755
	0.9	0.862	0.680	0.720	0.655	0.631	0.610	0.581	0.605	0.671	0.735

Gate: 90% of Width – LGF R_{ij} Data

Table F.65. Long Glass Fiber end-gated plaque gate orientation data (R13) at 90% Width.											
R13		**x/L_g**									
		-0.9	**-0.7**	**-0.5**	**-0.3**	**-0.1**	**0.1**	**0.3**	**0.5**	**0.7**	**0.9**
z/L_g	**-0.9**	0.035	0.035	0.000	0.019	0.052	0.033	0.114	0.125	0.148	0.095
	-0.7	0.016	0.084	0.102	0.119	0.109	0.111	0.148	0.177	0.161	0.151
	-0.5	0.024	0.035	0.125	0.104	0.120	0.141	0.164	0.155	0.156	0.158
	-0.3	0.012	0.045	0.101	0.080	0.081	0.129	0.135	0.153	0.126	0.067
	-0.1	0.018	0.052	0.067	0.115	0.124	0.132	0.129	0.138	0.057	0.032
	0.1	0.003	-0.001	0.030	0.077	0.135	0.091	0.106	0.098	0.045	0.010
	0.3	0.010	-0.006	-0.022	0.026	0.055	0.042	0.115	0.099	0.037	0.015
	0.5	-0.008	-0.021	-0.015	0.082	0.069	0.087	0.085	0.072	0.052	0.020
	0.7	-0.021	-0.021	-0.025	0.018	0.044	0.076	0.073	0.073	0.055	0.040
	0.9	-0.018	-0.007	0.044	0.025	0.015	0.043	0.058	0.049	0.075	0.061

Table F.66. Long Glass Fiber end-gated plaque gate orientation data (R23) at 90% Width.											
R23		**x/L_g**									
		-0.9	**-0.7**	**-0.5**	**-0.3**	**-0.1**	**0.1**	**0.3**	**0.5**	**0.7**	**0.9**
z/L_g	**-0.9**	0.055	0.046	0.049	0.045	0.043	0.050	0.065	0.055	0.053	0.048
	-0.7	0.074	0.118	0.102	0.087	0.081	0.084	0.081	0.081	0.101	0.077
	-0.5	0.099	0.137	0.142	0.118	0.124	0.113	0.134	0.125	0.159	0.151
	-0.3	0.130	0.196	0.173	0.126	0.139	0.126	0.180	0.208	0.215	0.181
	-0.1	0.127	0.202	0.167	0.155	0.185	0.204	0.197	0.199	0.201	0.167
	0.1	0.130	0.197	0.155	0.184	0.178	0.192	0.159	0.177	0.211	0.147
	0.3	0.139	0.193	0.173	0.136	0.175	0.136	0.144	0.171	0.170	0.130
	0.5	0.109	0.178	0.141	0.142	0.105	0.132	0.115	0.108	0.111	0.118
	0.7	0.089	0.086	0.089	0.076	0.062	0.071	0.073	0.077	0.082	0.111
	0.9	0.046	0.062	0.052	0.064	0.060	0.050	0.045	0.052	0.069	0.084

Gate: 90% of Width – LGF R_{ij} Error

Table F.67. Long Glass Fiber end-gated plaque gate orientation error (R11) at 90% Width.

R11		x/L_g									
		-0.9	-0.7	-0.5	-0.3	-0.1	0.1	0.3	0.5	0.7	0.9
z/L_g	-0.9	0.034	0.029	0.022	0.039	0.066	0.026	0.054	0.023	0.041	0.038
	-0.7	0.014	0.048	0.065	0.054	0.046	0.053	0.032	0.037	0.025	0.028
	-0.5	0.015	0.042	0.055	0.076	0.027	0.074	0.051	0.011	0.086	0.036
	-0.3	0.010	0.011	0.074	0.088	0.033	0.040	0.017	0.050	0.038	0.039
	-0.1	0.026	0.006	0.052	0.069	0.041	0.022	0.030	0.036	0.025	0.028
	0.1	0.010	0.022	0.080	0.060	0.061	0.034	0.038	0.030	0.021	0.027
	0.3	0.018	0.057	0.062	0.097	0.067	0.107	0.069	0.023	0.008	0.019
	0.5	0.012	0.047	0.063	0.064	0.040	0.032	0.027	0.028	0.019	0.027
	0.7	0.014	0.029	0.035	0.086	0.051	0.052	0.036	0.043	0.031	0.017
	0.9	0.018	0.027	0.019	0.038	0.032	0.081	0.045	0.004	0.051	0.049

Table F.68. Long Glass Fiber end-gated plaque gate orientation error (R12) at 90% Width.

R12		x/L_g									
		-0.9	-0.7	-0.5	-0.3	-0.1	0.1	0.3	0.5	0.7	0.9
z/L_g	-0.9	0.009	0.009	0.019	0.014	0.009	0.012	0.013	0.019	0.033	0.045
	-0.7	0.005	0.029	0.018	0.019	0.015	0.042	0.042	0.033	0.048	0.026
	-0.5	0.005	0.016	0.031	0.018	0.019	0.024	0.023	0.019	0.026	0.014
	-0.3	0.009	0.024	0.041	0.051	0.067	0.060	0.043	0.021	0.017	0.032
	-0.1	0.010	0.026	0.024	0.080	0.031	0.026	0.011	0.023	0.026	0.013
	0.1	0.018	0.039	0.084	0.072	0.021	0.036	0.030	0.020	0.022	0.014
	0.3	0.014	0.012	0.039	0.076	0.029	0.021	0.021	0.028	0.013	0.033
	0.5	0.015	0.015	0.029	0.043	0.030	0.024	0.006	0.021	0.014	0.019
	0.7	0.020	0.022	0.027	0.032	0.015	0.020	0.014	0.005	0.004	0.012
	0.9	0.011	0.016	0.013	0.029	0.027	0.015	0.010	0.018	0.008	0.025

Gate: 90% of Width – LGF R_{ij} Error

Table F.69. Long Glass Fiber end-gated plaque gate orientation error (R22) at 90% Width.

R22		x/L_g									
		-0.9	-0.7	-0.5	-0.3	-0.1	0.1	0.3	0.5	0.7	0.9
z/L_g	-0.9	0.015	0.024	0.020	0.022	0.013	0.014	0.012	0.022	0.014	0.013
	-0.7	0.032	0.051	0.022	0.010	0.017	0.015	0.006	0.008	0.013	0.010
	-0.5	0.064	0.081	0.030	0.045	0.035	0.029	0.018	0.006	0.017	0.015
	-0.3	0.059	0.074	0.091	0.075	0.021	0.038	0.039	0.024	0.034	0.053
	-0.1	0.081	0.055	0.129	0.061	0.070	0.040	0.045	0.008	0.050	0.052
	0.1	0.076	0.081	0.087	0.029	0.047	0.052	0.059	0.023	0.040	0.056
	0.3	0.070	0.069	0.027	0.060	0.072	0.047	0.053	0.018	0.046	0.095
	0.5	0.030	0.045	0.057	0.048	0.031	0.033	0.024	0.030	0.024	0.065
	0.7	0.026	0.046	0.039	0.050	0.022	0.023	0.016	0.016	0.008	0.027
	0.9	0.022	0.042	0.046	0.051	0.045	0.018	0.010	0.030	0.016	0.051

Table F.70. Long Glass Fiber end-gated plaque gate orientation error (R33) at 90% Width.

R33		x/L_g									
		-0.9	-0.7	-0.5	-0.3	-0.1	0.1	0.3	0.5	0.7	0.9
z/L_g	-0.9	0.042	0.048	0.017	0.036	0.075	0.027	0.054	0.030	0.054	0.046
	-0.7	0.033	0.063	0.046	0.061	0.048	0.049	0.028	0.029	0.033	0.033
	-0.5	0.057	0.081	0.031	0.099	0.056	0.064	0.043	0.006	0.072	0.039
	-0.3	0.050	0.077	0.147	0.143	0.052	0.037	0.023	0.045	0.020	0.069
	-0.1	0.081	0.058	0.170	0.112	0.069	0.023	0.037	0.035	0.045	0.032
	0.1	0.073	0.070	0.163	0.088	0.095	0.082	0.090	0.036	0.039	0.065
	0.3	0.074	0.068	0.075	0.146	0.088	0.090	0.068	0.039	0.038	0.105
	0.5	0.034	0.053	0.069	0.022	0.023	0.015	0.048	0.055	0.042	0.070
	0.7	0.034	0.068	0.073	0.099	0.051	0.037	0.048	0.059	0.038	0.042
	0.9	0.026	0.035	0.055	0.064	0.036	0.073	0.044	0.027	0.055	0.098

Gate: 90% of Width – LGF R_{ij} Error

Table F.71. Long Glass Fiber end-gated plaque gate orientation error (R13) at 90% Width.

R13		x/L_g									
		-0.9	-0.7	-0.5	-0.3	-0.1	0.1	0.3	0.5	0.7	0.9
z/L_g	-0.9	0.017	0.011	0.019	0.024	0.006	0.018	0.032	0.020	0.032	0.052
	-0.7	0.005	0.018	0.037	0.029	0.009	0.040	0.038	0.041	0.024	0.016
	-0.5	0.004	0.005	0.021	0.020	0.028	0.045	0.038	0.038	0.017	0.007
	-0.3	0.007	0.023	0.024	0.017	0.034	0.042	0.047	0.026	0.019	0.019
	-0.1	0.006	0.030	0.011	0.021	0.025	0.020	0.035	0.026	0.016	0.010
	0.1	0.009	0.031	0.034	0.033	0.040	0.032	0.007	0.012	0.011	0.012
	0.3	0.009	0.017	0.024	0.049	0.035	0.051	0.015	0.012	0.016	0.017
	0.5	0.013	0.017	0.018	0.024	0.042	0.049	0.017	0.019	0.011	0.015
	0.7	0.013	0.014	0.028	0.025	0.015	0.010	0.005	0.008	0.008	0.006
	0.9	0.014	0.023	0.008	0.042	0.039	0.042	0.033	0.018	0.006	0.019

Table F.72. Long Glass Fiber end-gated plaque gate orientation error (R23) at 90% Width.

R23		x/L_g									
		-0.9	-0.7	-0.5	-0.3	-0.1	0.1	0.3	0.5	0.7	0.9
z/L_g	-0.9	0.015	0.014	0.012	0.013	0.005	0.010	0.007	0.012	0.013	0.005
	-0.7	0.010	0.024	0.018	0.012	0.011	0.011	0.007	0.012	0.007	0.008
	-0.5	0.018	0.008	0.014	0.018	0.009	0.023	0.025	0.024	0.015	0.007
	-0.3	0.023	0.010	0.032	0.020	0.022	0.026	0.022	0.022	0.010	0.008
	-0.1	0.017	0.011	0.031	0.011	0.015	0.014	0.024	0.010	0.012	0.008
	0.1	0.014	0.010	0.036	0.029	0.019	0.015	0.015	0.017	0.022	0.024
	0.3	0.021	0.015	0.029	0.038	0.049	0.036	0.018	0.018	0.013	0.037
	0.5	0.018	0.025	0.032	0.032	0.015	0.024	0.012	0.027	0.012	0.024
	0.7	0.015	0.025	0.027	0.029	0.014	0.019	0.010	0.021	0.007	0.014
	0.9	0.009	0.026	0.029	0.032	0.025	0.016	0.010	0.020	0.013	0.029